12-2013

Modeling, Design, Packaging and Experimental Analysis of Liquid-Phase Shear-Horizontal Surface Acoustic Wave

Thomas B. Pollard

MODELING, DESIGN, PACKAGING AND EXPERIMENTAL ANALYSIS OF LIQUID-PHASE SHEAR-HORIZONTAL SURFACE ACOUSTIC WAVE SENSORS

By Thomas B. Pollard

B.S. University of Maine, 2003

M.S. University of Maine, 2010

A DISSERTATION

Submitted in Partial Fulfillment of the

Requirements for the Degree of

Doctor of Philosophy

(in Electrical & Computer Engineering)

The Graduate School

The University of Maine

December 2013

Advisory Committee:

Mauricio Pereira da Cunha, Professor of Electrical and Computer Engineering, Advisor

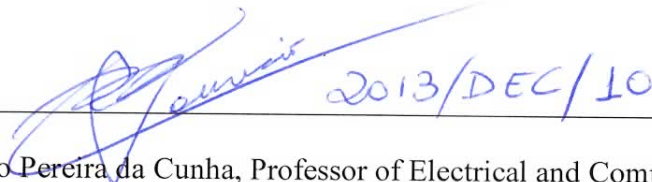Donald H. Hummels, Professor of Electrical and Computer Engineering

Paul J. Millard, Associate Professor of Chemical and Biological Engineering

David J. Neivandt, Associate Professor of Chemical and Biological Engineering

John F. Vetelino, Professor of Electrical and Computer Engineering

DISSERTATION ACCEPTANCE STATEMENT

On behalf of the Graduate Committee for Thomas B. Pollard, I affirm that this manuscript is the final and accepted dissertation. Signatures of all committee members are on file with the Graduate School at the University of Maine, 42 Stodder Hall, Orono, Maine.

2013/DEC/10

_____

Dr. Mauricio Pereira da Cunha, Professor of Electrical and Computer Engineering

(September 25th 2013)

LIBRARY RIGHTS STATEMENT

In presenting this dissertation in partial fulfillment of the requirements for an advanced degree at The University of Maine, I agree that the Library shall make it freely available for inspection. I further agree that permission for "fair use" copying of this dissertation for scholarly purposes may be granted by the Librarian. It is understood that any copying or publication of this dissertation for financial gain shall not be allowed without my written permission.

Signature:

Date: 12/10/13

MODELING, DESIGN, PACKAGING AND EXPERIMENTAL ANALYSIS OF LIQUID-PHASE SHEAR-HORIZONTAL SURFACE ACOUSTIC WAVE SENSORS

By Thomas B. Pollard

Dissertation Advisor: Dr. Mauricio Pereira da Cunha

An Abstract of the Dissertation Presented
in Partial Fulfillment of the Requirements for the
Degree of Doctor of Philosophy
(in Electrical & Computer Engineering)
December 2013

Recent advances in microbiology, computational capabilities, and microelectromechanical-system fabrication techniques permit modeling, design, and fabrication of low-cost, miniature, sensitive and selective liquid-phase sensors and lab-on-a-chip systems. Such devices are expected to replace expensive, time-consuming, and bulky laboratory-based testing equipment. Potential applications for devices include: fluid characterization for material science and industry; chemical analysis in medicine and pharmacology; study of biological processes; food analysis; chemical kinetics analysis; and environmental monitoring. When combined with liquid-phase packaging, sensors based on surface-acoustic-wave (SAW) technology are considered strong candidates. For this reason such devices are focused on in this work; emphasis placed on device modeling and packaging for liquid-phase operation. Regarding modeling, topics considered include mode excitation efficiency of transducers; mode sensitivity based on

guiding structure materials/geometries; and use of new piezoelectric materials. On packaging, topics considered include package interfacing with SAW devices, and minimization of packaging effects on device performance.

In this work novel numerical models are theoretically developed and implemented to study propagation and transduction characteristics of sensor designs using wave/constitutive equations, Green's functions, and boundary/finite element methods. Using developed simulation tools that consider finite-thickness of all device electrodes, transduction efficiency for SAW transducers with neighboring uniform or periodic guiding electrodes is reported for the first time. Results indicate finite electrode thickness strongly affects efficiency. Using dense electrodes, efficiency is shown to approach 92% and 100% for uniform and periodic electrode guiding, respectively; yielding improved sensor detection limits. A numerical sensitivity analysis is presented targeting viscosity using uniform-electrode and shear-horizontal mode configurations on potassium-niobate, langasite, and quartz substrates. Optimum configurations are determined yielding maximum sensitivity. Results show mode propagation-loss and sensitivity to viscosity are correlated by a factor independent of substrate material. The analysis is useful for designing devices meeting sensitivity and signal level requirements. A novel, rapid and precise microfluidic chamber alignment/bonding method was developed for SAW platforms. The package is shown to have little effect on device performance and permits simple macrofluidic interfacing. Lastly, prototypes were designed, fabricated, and tested for viscosity and biosensor applications; results show ability to detect as low as 1% glycerol in water and surface-bound DNA crosslinking.

DEDICATION

This dissertation is dedicated to my Bumpas:

two outstanding and unique role models

with wonderful characters I've always tried to emulate

ACKNOWLEDGMENTS

First, I would like to thank my dissertation advisor, Dr. Mauricio Pereira da Cunha, for his mentorship and this research and intellectual-growth opportunity he provided. I thoroughly enjoyed long and fruitful discussions with him on the subject and I am very grateful for his tremendous insight and guidance. I would like to thank Dr. John Vetelino for the initial work opportunity at LASST as an undergraduate that introduced me to the world of research, which eventually led me down this path. I would also like to thank the other members of my advisory committee, Dr. Donald Hummels, Dr. Paul Millard, and Dr. David Neivandt, for their insight, assistance and carefully review this work. Next, I would like to thank my fellow MAL graduate students that helped me all along the way and made the overall journey extremely fun: Jeremy Thiele, Tom Kenny, Bennett Meulendyk, Eric Berkenpas, Peter Davulis, and Dana Tucker. I would also like to thank ECE/LASST faculty and staff, and in particular, Janice Gomm, George Bernhardt, Mike Call, and Eric Martin for all their help over the years. I would like to thank Joe Arsenault for his help reviewing this dissertation, and Environetix Technologies for giving me time to complete the requirements.

Next, I would like to thank my mother, father, step-mother, two sisters and extended family who have always been pillars of support that provided encouragement over the entire process. I am truly lucky to have such an amazing family.

Most importantly, I would like to thank my wife, Sarah, for her endless encouragement, aid in getting this dissertation out, patience, and sacrifice.

TABLE OF CONTENTS

LIST OF TABLES

LIST OF FIGURES

xiii

CHAPTER 1

INTRODUCTION, MOTIVATION AND BACKGROUND

1.1. Introduction and Motivation

Liquid-phase sensors are currently being researched and developed for applications in the areas of: (i) fluid characterization, in terms of viscoelastic, density, dielectric, and conductivity properties for material science and industry in process- and quality-control; (ii) chemical analysis in the area of medicine and pharmacology, biological processes, food analysis, and chemical kinetics; and (iii) environmental monitoring applications such as detection of pathogens or toxic chemicals. Bench-top devices and instruments are typically employed to address many of the aforementioned needs. In particular, fluidic physical properties are typically measured using devices such as: hydrometers, pycnometers, and analytical balances; Zahn cups and Stormer viscometers (Newtonian-fluids), rheometers for characterization non-Newtonian behavior; and parallel-plate impedance analysis devices, e.g. a Schering Bridge, for electrical property characterization [1]. In terms of liquid-phase chemical and biological sensing, techniques and equipment such as fluorescence microscopy, chemiluminescence, surface plasmon resonance, liquid chromatography, and electrochemical analysis are commonly applied [2].

With the recent technological advances in microelectronics and microelectromechanical systems (MEMS) fabrication techniques, microbiology, and computational capabilities it has become possible to model, design, and fabricate low-cost, miniature, sensitive and selective candidate liquid phase sensing platforms and lab-on-a-chip systems [3]. Such devices are expected to eventually replace expensive, time-consuming, and bulky laboratory based testing equipment. Additional potential advantages over use of standard instruments also include reduced required reagent volumes, lower power consumption, faster analysis, portability, and batch fabrication compatibility. In spite of these advantages, significant design challenges emerge as devices move towards the micro- and nano-scale dimensions. Packaging devices for liquid-phase operation becomes challenging, and in particular microfluidic to macrofluidic interfacing, fluidic chamber design, and integration with a sensor device. Compared to the macro-scale, fluids at the micro-scale may behave drastically different as effects such as surface tension and viscosity begin to dominate. In particular, fluids at micro- and nano-scale regimes typically exhibit a low Reynolds number, which is a measure of the ratio of inertial forces to viscous forces [4]. Therefore the design of microfluidic flow cells becomes non-trivial as problems such as bubble entrapment, nucleation, and chamber filling prevent reproducible sample exposure and analysis by the sensor transducers. Other concerns regarding the use of micro- and nano-scale devices may include device fabrication reproducibility and overall sensor robustness.

Since the 1980's acoustic wave devices began to be explored as candidate liquid-phase sensor platforms. Devices based on this technology consist of electromechanical transducers affixed to a piezoelectric material. Due to the piezoelectric effect the electric field within the material is linked to mechanical fields i.e. stress and displacement. Via application of an electrical signal to a transducer, electromechanical modes are excited in the substrate. In terms of sensing, a measurand interacts with the piezoelectric material and modifies properties of the device's characteristic mode(s). Another transducer, or the same, can be used to detect the modes and measure propagation properties such as phase velocity and attenuation, or characteristic resonance frequencies. The variation in the mode properties may then be related to a measurand, upon the usage of a device calibration curve. Acoustic wave devices are typically fabricated using batch photolithographic techniques, and are typically as small as a few mm^2, portable, and are considered highly sensitive sensing platforms [5].

In this dissertation, liquid-phase sensors based on one type of acoustic wave is studied extensively. More specifically, the candidate sensor platform considered in this work is based on a pure shear-horizontal surface acoustic wave (SHSAW) device; a technology which is reviewed in Section 1.2. In brief, such a device (see Figure 1.1) is typically configured as a delay-line for liquid-phase sensor applications and consists of two transducers spaced some distance apart and positioned along a specific orientation on the surface of a piezoelectric substrate. Through application of an electrical signal to one of the transducers, a SHSAW mode is launched and propagates along the substrate surface across the delay/sensing region and is then detected by another transducer.

3

Applying a fluid analyte to the device delay/sensing region causes properties of the mode supported in that region to be altered, such as phase velocity and attenuation, which is detected by the output transducer. Devices based on the SHSAW mode are applicable to liquid-phase sensor applications due to the reduced mode dampening from fluid surface loading as compared to devices based on other surface wave modes, such as a Rayleigh type. A more thorough discussion on modes relevant to liquid-phase sensing is given in Section 1.2.
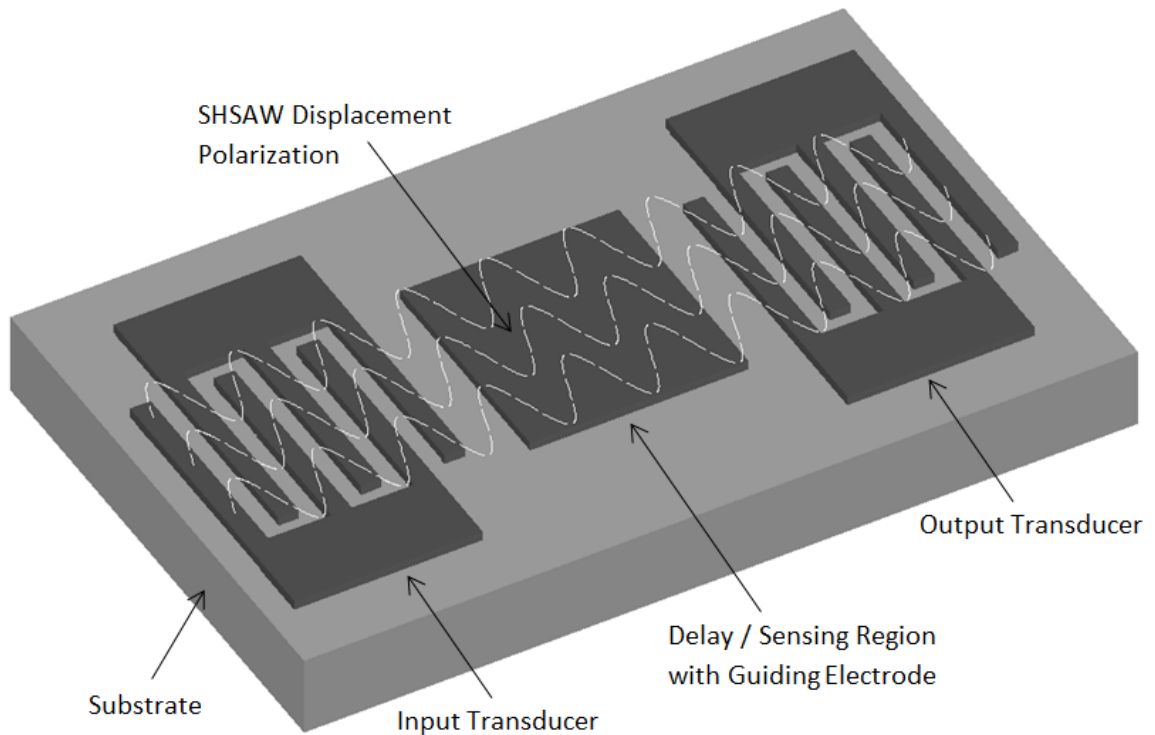
Figure 1.1. Diagram of a typical SHSAW device.

SHSAW devices have transducers positioned on the same side of the substrate as the fluid/substrate interface and therefore require packaging to isolate transducers in order to prevent dielectric or electric shorting by high-permittivity or conducting fluid analytes, respectively. The packaging at the same time must permit fluid contact with device delay/sensing region. Because of this requirement, packaging devices becomes challenging as the chamber sealing area between the delay path and transducer regions is typically relatively small (few wavelengths). Furthermore, the attachment of a chamber may also negatively affect the device response via introducing effects such as mode scattering, dampening, and reflection at this interface.

The motivation for this work was to improve SHSAW device design through the development of new modeling tools and analyses aiming at increasing sensor performance. In addition, this work sought to further study and implement improved SHSAW liquid-phase device packaging techniques in order to enhance the overall sensor performance, reproducibility, and fabrication simplicity.

1.2. Acoustic Wave Liquid-Phase Sensor Technology Background

Acoustic wave devices based on the piezoelectric effect are typically fabricated by depositing thin-film electrodes, acting as transducers, on the surface(s) of a piezoelectric substrate. The transducers are used excite and/or detect electromechanical modes supported in the material via the piezoelectric effect (discussed in greater detail below). When configured as sensors, perturbations in the surrounding environment (i.e. modification of the physical boundary conditions) cause the characteristics of modes supported in the material to be altered, such as phase velocity and/or level of attenuation. The sensed signal, represented as a change in the time/phase, frequency, or amplitude properties of the device, is directly measured using external electrical equipment connected to the transducer(s). The mode perturbations can be mechanical in nature, e.g. surface mass, stiffness, and viscous loading; or electrical in nature, e.g. resulting from modification of the surrounding dielectric or conductivity properties. As mentioned briefly above, electrical mode excitation and detection by transducers occurs as a result of the piezoelectric properties of the substrate. In particular, a material is said to be piezoelectric if upon application of a mechanical force the body becomes electrically polarized (direct effect), and conversely upon application of an electric field the body becomes mechanically deformed (inverse effect) [6]. The direct effect was discovered by the brothers Pierre and Jacques Curie in 1880, however the inverse effect was predicted shortly afterwards by Gabriel Lippmann in 1881 and was later confirmed in 1882 by the Curie brothers [7]. Over the period of 1914-1918, Paul Langevin demonstrated one of the first real-world uses of the technology through application of piezoelectric transducers towards submarine detection [8]. A few years later in 1921 Walter Cady demonstrated for

the first time the use of quartz resonators for stabilization of oscillators and narrow band filter applications [7]. Later with the invention of the interdigital transducer by White and Voltmer (discussed in greater detail later) acoustic wave technology was applied to various signal processing applications, including: matched filters, compressors, convolvers, and delay lines [9,10]. Today acoustic wave filters find widespread use in high-volume low-cost consumer applications such as television, global positioning systems, wireless local area networks, and mobile phones [11].

In addition to the large number of signal processing applications, over the past thirty years acoustic wave technology has also been considered for liquid-phase sensing applications. Earlier sensing devices were initially considered for solid-phase sensing or gravimetric applications (reported in late 1950's) and were based on use of the quartz crystal microbalance (QCM) [12]. The QCM device consists of a polished parallel plate resonator, configured much like a parallel plate capacitor, consisting of piezoelectric substrate and thin (100's nm) electrodes positioned atop each face. As a result of the piezoelectric effect, bulk acoustic wave(s) (BAW) mode(s) are generated within the body via applying an electrical signal to the transducer electrodes. As the BAW is generated, the acoustic energy becomes contained between the two surfaces and the device resonates at frequencies where the fields satisfy the boundary conditions (under fundamental mode operation substrate is ½ BAW wavelengths thick). Typical fundamental operating frequencies for QCM devices range from hundreds of kHz up to tens of MHz; the upper limit is governed by the crystals thicknesses, in terms of robustness, and surface finish quality. Early QCM devices were shown to display resonance frequency with high

sensitivity to surface mass loading. For instance in [12] an accuracy of 10^{-10} g is reported. Today commercial sensing systems based on QCM devices are employed all over the world for measurement of deposited thin-film thickness in vacuum deposition systems. The degree the device resonant frequency shifts due to mass surface loading was first successfully approximated by the Sauerbrey Equation [12]:

$$\Delta f = -\frac{\Delta m_d \cdot f_0^2}{\rho \cdot v} ,$$

(1.1)

where:
- Δf is the change in resonant frequency,
- Δm_d is the surface mass change per unit area,
- f_0 is the operating frequency,
- ρ is the density of the piezoelectric material,
- v is the velocity of the acoustic wave in the material.

One very important property of (1.1) of is that the device sensitivity, given as $\Delta f/f_0$, is proportional to the device operating frequency. This indicates that devices made on reduced thickness substrates will tend to have higher sensitivity compared to their thicker counterparts. It was not until the 1980's that such devices were considered for liquid-phase sensing applications. In particular, it was shown that QCM devices could achieve stable oscillation under a liquid-loaded surface condition using a temperature compensated AT-cut QCM [13]. This ability is attributed to the QCM's excitation of a thickness-shear mode (TSM). Such a mode has particle displacement components only along the plane of the crystal surface which results in minimal coupling to the adjacent fluid and avoids severe mode dampening through compression wave excitation into the fluid [14,15]. The Sauerbrey Equation did not accurately predict resonance frequency

8

changes under liquid-loaded conditions, which were mainly ascribed to viscous coupling to the liquid. Such a problem was first addressed by the work of Kanazawa and Gordon in 1985, which proposed a relationship for the change in resonance frequency due to the viscosity-density product of a Newtonian fluid [5]:

$$\Delta f = -f_0^{3/2} \cdot \left(\frac{\eta_l \cdot \rho_l}{\pi \cdot \eta_q \cdot \rho_q} \right)^{1/2} ,$$

(1.2)

where:
- Δf is the change in resonant frequency,
- f_0 is the operating frequency,
- η_l and ρ_l are the viscosity and density of the fluid respectively,
- η_q and ρ_q are the viscosity and density of the piezoelectric respectively.

Equation (1.2) indicates that the device response in terms of sensing is mainly governed by the fluid analyte square-root viscosity-density product. In addition the device sensitivity is proportional to the square-root of device operating frequency. The work of [5] was later expanded for similar quartz resonator devices in [16] to include resonance frequency shift due to dielectric and conductivity properties of fluids.

Similar to a QCM device, the lateral field excited (LFE) device has recently been considered for liquid-phase sensing applications [17,18]. In the case of AT-cut quartz, both QCM and LFE device configurations can excite the TSM mode, but unlike the QCM configuration, the LFE has both electrodes positioned on the same side of the piezoelectric crystal (separated by a parallel gap). The other side of crystal is typically left electrically unshielded to allow probing of electrical properties of the fluid in addition to viscosity and density properties [17].

Another more recent member of the bulk acoustic wave liquid-phase sensor family is the thin-film bulk acoustic resonator (FBAR) [19]. Recently, the ability to deposit thin piezoelectric films on the order of hundreds of nanometers, which support excitation of the TSM, have opened up the possibility of using such devices for liquid-phase sensor applications [20,21]. Such devices can be thought of as scaled down versions of the QCM device, and are based on the formation of a resonating structure via the deposition of thin-film piezoelectric materials on non-piezoelectric substrates such as silicon. Typical deposited piezoelectric materials used in the fabrication of these devices include zinc-oxide (ZnO) and aluminum-nitride (AlN). There are two main methods used to fabricate the resonant cavities of FBAR devices: (i) a periodic super-lattice consisting of materials with large differences in acoustic impedances is first deposited on a silicon substrate, followed by deposition of the bottom electrode, a piezoelectric film, and a top electrode respectively; or (ii) the bottom electrode is deposited on silicon followed by a deposition of the piezoelectric and top electrode respectively, next the bulk silicon is removed from the underside of the structure forming a membrane cavity. An advantage of FBAR based devices over QCMs is the fact that the fabrication techniques can be compatible with complementary metal-oxide semiconductor (CMOS) processing, which may lead to fully integrated sensors. Another advantage is the capability of operating at much higher frequency; from hundreds of MHz to a few GHz. Increased operation frequency is anticipated to yield devices with greater sensitivity according to (1.1) and (1.2). A current disadvantage is the relatively low obtainable quality factor (Q) of such devices compared to QCM, which have been reported as 156 and 2000 [21] under liquid-loaded conditions for the TSM FBAR and QCM devices, respectively. Although the

10 MHz QCM Q reported is about 13 times larger than that that for the 790 MHz TSM FBAR under liquid loading conditions, the devices was still able to detect mass changes down to 2.3 ng/cm^2, which is about two times lower than that reported for the QCM [21].

The other family of acoustic wave devices considered for liquid-phase sensing applications is based on guided acoustic modes, which are typically generated and detected by transducers located at the surface of a piezoelectric material. Such devices are expected to yield higher sensitivity compared to QCM and LFE devices because of increased operating frequency, in accordance with (1.1) and (1.2), which range from hundreds MHz to a few GHz. The theoretical basis for such devices began over a century ago. In particular, Lord Rayleigh discovered the existence of a surface acoustic wave (SAW) mode which is guided by the surface of an elastic solid that exhibits an energy profile exponentially decaying into the bulk [22]. Later studies by Lamb, Stoneley, and Love expanded the knowledge in the field with the discovery of modes propagating in finite-thickness elastic plates, at the interface of two elastics solids, and at the interface of finite-thickness elastic layer and solid, respectively [23,24,25]. Such works were focused on the area of geodynamics. In 1965 with the invention of the interdigital transducer (IDT) by White and Voltmer, an efficient means for excitation and detection of the aforementioned modes was demonstrated on piezoelectric materials [26]. The IDT consists of a periodic arrangement of electrodes having alternating polarity in a comb-like structure. Such structures are typically fabricated using standard microelectronic photolithography and thin-film deposition techniques. For liquid-phase sensors based on SAW devices, sustained propagation of the acoustic mode is required at the liquid/solid

interface in order to accurately measure mode perturbations associated with the fluid measurand. Such a scenario was first considered by Campbell and Jones in 1970, where the authors studied the propagation loss of SAW modes at the boundary between a piezoelectric crystal and fluid medium (air and water loading reported) [15]. In their work it was shown that strong propagation loss of the SAW mode occurs through the launching of a compression wave into the fluid due resulting from the mode displaying a particle displacement component normal to the surface. Around the same time, the existence of piezoelectrically coupled SAW modes with particle displacements only within the plane of the crystal surface and transverse to the propagation direction were shown to exist along particular crystallographic orientations of piezoelectric materials that exhibited no counterpart in isotropic homogeneous solids [27]. The discovery of such a mode has been credited to three or more different groups around the globe working independently [28] and is commonly referred to as the Bleustein-Gulyaev-Shimizu (BGS) wave [27,29,30]. General methods were developed in the early 1970's to classify substrate orientations in terms of crystallographic symmetries for generic substrates [31]. In particular, orientations of elastic solids were separated into 5 symmetry types. Each type displayed unique behavior regarding field polarization and piezoelectric coupling within the substrate along particular propagation directions. The individual types specify which mechanical and electrical field components are coupled to each other within the substrate, and are determined given the substrate constants, orientation, and propagation direction. The symmetry types consist of: (i) *Symmetry Type 1*, which is the most general symmetry and presents coupling in all three dimensions between electrical and mechanical fields in the piezoelectric substrate; (ii) *Symmetry Type 2* is similar to *Symmetry Type 1* with the

12

exception that mechanical and electrical fields are decoupled (e.g. generic orientations of non-piezoelectric crystals); (iii) *Symmetry Type 3* presents decoupling of two sets of fields in which one set exhibits piezoelectrically-active pure Rayleigh polarization (elliptical particle motion in the sagittal plane) and the other set is purely mechanical with pure transverse shear polarization (direction transverse to the sagittal plane); (iv) *Symmetry Type 4* also presents the decoupling of two sets of fields in which one set exhibits piezoelectrically-active pure transverse shear polarization and the other set is purely mechanical with pure Rayleigh polarization; lastly (v) *Symmetry Type 5* also presents decoupling of fields and presents both piezoelectrically-inactive pure Rayleigh and transverse shear polarizations (e.g. isotropic substrates). Based on the rotated material elastic, dielectric, and piezoelectric constants, criteria were given to determine the corresponding symmetry type in [31]. It should be mentioned that the properties of the symmetry type classifications do not require a half-space consideration. Under half-space conditions not all solutions are guaranteed to support a guided wave. For example, in an isotropic half-space (*Symmetry Type 5*) a pure SHSAW mode solution does not exist for the purely transverse shear solution, although a purely mechanical SHBAW mode is supported. In the work by Lardat *et al.* in 1971, pure orientations falling under *Symmetry Types 3* and *4* could be predicted based on crystallographic point groups [32]. In particular, the authors stated that pure Rayleigh coupling occurs when the sagittal plane is a plane of symmetry, and pure shear coupling occurs when the perpendicular to the sagittal plane is a binary axis.

The first attempts to build liquid-phase sensors on piezoelectric substrates using devices incorporating IDTs began in the late 1980's and early 1990's [33,34,35,36,37]. One early reported sensor was applied to fluidic density characterization and pressure monitoring using a Lamb mode device [34]. The sensor was built on a silicon substrate through deposition of a silicon nitride film, ground plane, piezoelectric zinc oxide layer, and IDT electrodes respectively, followed by removal of bulk silicon from the device underside. Although the Lamb wave mode considered displayed particle displacement components normal to the substrate surface, the device was still able to operate under liquid loading conditions in an oscillator configuration. The authors attributed this to the fact that the phase velocity of the Lamb wave mode is below the compression wave phase velocity supported by the fluid, and is hence cut-off. Another device reported around this time was based on the acoustic plate modes (APM) on lithium niobate, and was proposed for monitoring antigen/antibody reactions [35]. The APM is a mode excited and detected with IDTs and is guided by the entire thickness of the crystal. Devices based on plate modes are interesting because the fluid interface does not come into contact with IDTs since they are on opposite sides, and hence avoids possible direct dielectric and conductive electrical shorting of IDTs from fluids and also permits simple packaging methods. Another liquid-phase sensor platform based on a Love mode was also reported around this time and utilized a *Symmetry Type 4* orientation of quartz that was combined with a polymer guiding layer [36]. The use of polymer over-layer was shown to convert shallow propagating BAW energy to a guided Love mode, which displayed increased sensitivity to fluid viscosity. The degree of sensitivity was also studied as a function of guiding layer thickness and tended to increase with layer thickness. Devices based on the

14

pseudo SAW (PSAW) mode in lithium tantalate were also investigated for liquid-phase sensing applications at this time because the particle displacement associated with the mode is predominantly shear, which results in the mode not being heavily damped by the fluid [33]. A few proposed devices were used to monitor fluid conductivity and pH [33,37]. In the case of PSAWs, there is intrinsic propagation loss associated with the mode because of energy leakage to BAW. Much work has been devoted to the search of orientations which support these modes and display low propagation loss because such modes typically display higher phase velocity then SAWs [38] resulting in increased device operating frequency for a given fabrication requirement. More recently devices based on the BGS mode have also begun to be considered as possible liquid-phase sensors because of displaying minimal dampening by the fluid analyte and ease of device fabrication. Two particular works investigated the BGS mode on new piezoelectric materials, e.g. potassium niobate and the LGX family of crystals which include lagasite, laganite, and langatate, that exhibit very high electromechanical coupling and existence of temperature compensated orientations, respectively [39,40].

This work focuses on the modeling, design, fabrication, and testing of acoustic liquid-phase sensor platforms fabricated on *Symmetry Type 4* piezoelectric orientations. Examples of general *Symmetry Type 4* piezoelectric orientations include quartz, Euler Angles (0°, θ, 90°); langasite, Euler Angles (0°, θ, 90°); and potassium niobate, Euler Angles (ϕ, 90°, 0°). Specific orientations explored in this work include quartz, Euler Angles (0°, 132.75°, 90°); langasite, Euler Angles (0°, 22°, 90°); and potassium niobate, Euler Angles (0°, 90°, 0°). From here on, the use of shear horizontal SAW (SHSAW) will

be used to encompass Love and BGS modes, since they have particle displacements which are shear with respect to the propagation direction and horizontal with respect to the surface normal. In general, SHSAW modes can exist on *Symmetry Type 4* orientations of piezoelectric materials when combined with isotropic materials, which may be used to form electrodes and guiding structures. Some of the particular challenges in the use of SHSAW technology for liquid-phase sensing are evaluation of mode excitation and propagation properties, and development of appropriate packaging techniques which permit liquid-phase operation. The next few sections of this chapter discuss these issues individually with regard to SHSAW platforms, but it should be noted that many of the techniques used in this work to addresses these challenges are not limited to *Symmetry Type 4* orientations.

1.3. Acoustic Wave Device Modeling Background

For SHSAW liquid-phase sensors both propagation and transduction must be carefully considered in the device design process. The SHSAW propagation analysis of candidate structures must be performed with and without consideration of the fluidic interaction. It is desirable to characterize mode properties for structures under liquid-loaded surface conditions in order to determine the potential mode sensitivity, quantify the degree of acoustic energy loss to viscoelastic fluid loading, and to determine the penetration depth of acoustic energy into the sensing platform and fluid.

The SHSAW may be ideal for liquid-phase sensing, but if not efficiently excitable the device is not of practical use, as the signal-to-noise-ratio becomes very poor. Spurious

acoustic signals also excited/detected by the IDTs that are insensitive to the fluid analyte, such as shear horizontal bulk wave (SHBAW), may begin to dominate the overall device response, masking all information regarding the fluid interaction with the SHSAW. Therefore in addition to studying SHSAW propagation, it becomes equally important to study mode transduction/detection as well.

1.3.1. SHSAW Propagation Modeling

Modern computational capabilities allow the use of numerical techniques to handle the characterization and modeling of SHSAW propagation properties. In particular, a number of models have been developed over the years to address propagation properties in structures relevant to SHSAW liquid-phase sensor devices [15,41,14,16,42,43]. In particular, the method proposed in [15] permits the calculation of modes propagating at the interface of semi-infinite piezoelectric materials and ideal fluids, and in particular uses an exact analysis method based on wave equations, but also considered a perturbation approach. Because of the ideal fluid assumption made, no viscosity effects were considered, and only fluid compression was taken into account. A later work [41] extended the methods used in [15] to include fluid dynamic viscosity effects and studied propagation in similar structures as [15]. The authors in [14] studied viscous loading for the BGS modes on a cadmium sulfide (CdS) substrate when a free surface is brought into contact with a fluid. Approximate analytical expressions were derived for the fractional change of mode phase velocity and propagation-loss given fluid density, viscosity, piezoelectric substrate constants, and operating frequency. The work presented in [16] considered both viscous and electrical properties of fluids on an AT-cut

17

crystal with one electrical free surface in contact with the fluid. In [42] the authors proposed the use of experimental techniques and theoretical transmission line models to evaluate mass sensitivity for a Love mode on ST-90° quartz. Recently [43] reported on propagation and excitation characteristics of a semi-infinite piezoelectric / zero-thickness electrode periodic grating / viscous fluid structure, which neglecting fluid conductivity and dielectric properties. The authors in [43] provided a slightly modified formalism compared to [41] regarding the treatment of viscosity, in which they also include a compressive viscosity factor.

In this dissertation, a wave-equation model is implemented that permits study of SHSAW mode properties (relevant to liquid-phase sensing) for structures consisting of a semi-infinite piezoelectric, *n* uniform finite thickness layers, and a semi-infinite viscous fluid, respectively. To the best knowledge of the author, for the first time a numerical sensitivity analysis is presented based on use of the full-wave model while considering finite-thickness effects of layers at the substrate / liquid interface. The motivation for this effort was to quantitatively determine achievable sensitivity parameters as a function of crystal substrate material and orientation, and layer materials and thickness. More information regarding this topic can be found in Section 3.3

1.3.2. SHSAW Excitation Modeling

It is very important to consider the IDT excitation/detection properties in addition to propagation properties since practical devices usually excite spurious modes, such as the SHBAW, that reduces the overall device signal-to-noise ratio. The SHSAW delay line

sensor configuration targeted in this work consists of input and output IDTs separated by a sensing region. Such devices are susceptible to the excitation and detection of spurious SHBAW, mode diffraction, and electromagnetic feed-through [44].

Significant contributions to SAW device modeling can be found in the literature since the conception of the IDT. Review material are given in [9,44]. In terms of liquid-phase sensors targeted in this work, it is shown that it is important to consider the fraction of IDT input power converted to the mode of interest as compared to other modes. The most rigorous reported models to date, and discussed below, are able to include finite-thickness electrode mass/stiffness effects, bulk acoustic wave, electrostatic effects, and SAW modes in the overall device analysis. A number of numerical techniques have been implemented to address boundary-value problems based upon the underlying linear partial differentials equations that describe electromechanical wave excitation and propagation in materials. For instance, SAW device models has been proposed based on methods such as the boundary element method (BEM) [45], combined finite element method (FEM) and BEM methods [46], direct FEM [47], and finite difference time-domain (FDTD) [48] techniques. The first reported BEM model applied to surface acoustic wave problem was presented in [45]. The model was based upon forming integral equations through computation of spectral-domain Green's functions and application of the Fourier transform. Some of the assumptions made in [45] included no field variations along the IDT aperture dimension, quasi-static treatment of the electromagnetic wave, and that electrodes are considered to have zero-thickness and are perfect electrical conductors. The formalism was well suited for finite IDT structures

with surrounding electrode-free regions that extended infinitely in both directions, as well as for structures consisting of finite IDT structures with surrounding uniform electrode ground planes extending infinitely in both directions. After solving the boundary problem, analysis of the results allow extraction of far-field SAW and BAW behavior including input power partitioning, SAW amplitude, BAW radiation pattern into the substrate bulk, and overall IDT input impedance. The work in [45] also performed an analysis on a *Symmetry Type 4* orientation of lead zirconate titanate (PZT), and showed that use of a guiding electrode placed in the device delay path region can dramatically increase the excitation efficiency for the respective BGS mode. Almost twenty years after the work in [45], the method was expanded in [46] and [49] to include finite-thickness effects of IDT electrodes via coupling a FEM and normal mode analysis to the BEM models, respectively. These works ignored the thickness of surrounding semi-infinite guiding electrodes. The problem of dealing with finite thickness of the guiding electrodes arises because in the FEM/BEM formalism, surface normal components of stress and the electric charge density are considered sources of waves and extend infinitely. In order to solve for the distribution of sources at the surface, basis function expansions are used for finite width electrodes, but no such convergent basis has been reported for semi-infinite extending electrodes. Even with this limitation, valuable insight regarding IDT SHSAW excitation could be gained for the study of *Symmetry Type 4* orientations. In publications by the author of this dissertation [50,51] SHSAW orientations of potassium niobate and langasite were studied considering infinitesimally thin guiding electrodes, and also apply to liquid-phase sensing applications as reported in this dissertation. In a more recent work published by the author of this dissertation [52] it was identified that the finite thickness

of long guiding electrodes must be included in the analysis in order to accurately extract from simulation the transduction and propagation properties applicable to sensor platforms.

An alternative to FEM/BEM techniques is direct FEM analysis of the electrodes and piezoelectric substrate. Such methods have been developed and applied for the simulation of SAW devices [47,53,54,55], and are well poised for structures with limited dimensions, since the entire domain must be discretized, thus not permitting far-field behavior of modes to be analyzed directly. Recently absorbing boundary conditions, enforced at the discretized domain edges that make the model appear more as if it is infinite in extent (reduce domain edge reflections), have begun to be implemented in FEM models [55]. This boundary condition method may allow extraction of far-field SHSAW mode behavior, but no work has been reported regarding this application. Other device simulation models reported that are based on FDTD techniques can be found in [48,56]. This method is similar to FEM in that the domain must be discretized, but rather than assuming sinusoidal time variation, temporal partial derivatives are approximated by finite differences of fields as a result of small stepping in time. It may be possible to use this technique to determine far-field SHSAW behaviors by running simulations in time up to a point before computational domain edge effects cause interference with mode amplitude extraction, e.g. reflections due to the computational domain boundaries may interact with the launching IDT and prevent accurate estimation of the IDT input power that would be observed had the model extended infinitely.

An alternative to modeling finite length IDT structures is analysis of infinite periodic array of grating electrodes positioned upon a piezoelectric material. Such analysis methods allow the characterization of SAW grating modes, and also permit the study of excitation properties of infinite IDT structures. An advantage of periodic analysis compared to simulation of finite structures is that computation time is dramatically reduced because only one period of the array needs to be studied with FEM/BEM, according to Floquet theory [44]. The method of Floquet analysis is applicable to the FEM/BEM and FEM methods discussed and are used to study an individual period or array. One such early work [57] discusses a method to determine grating mode characteristics while also considering bulk acoustic wave interactions; however this work neglected the loading effects from finite thickness electrodes. A later work expanded these concepts to include loading effects of finite-thickness electrodes [58]. This particular analysis allowed calculation of the harmonic admittance for the grating structure, which is the ratio of current entering an electrode over one period to voltage (the entire structure is driven sinusoidally in space and time, i.e. adjacent electrodes in the array have a constant increasing applied voltage phase shift and are also driven sinusoidally in time). In [59], which also neglected electrode loading effects, the harmonic admittance was used to compute mutual admittance of a periodic structure using the inverse Fourier series. The mutual admittance technique allows the calculation of the current entering any electrode in the array when a voltage is applied to one electrode in the array; all other electrodes are assumed grounded. Based on the mutual admittance and superposition principle, the technique allows the analysis of an arbitrary arrangement of driven electrodes within an infinitely periodic electrode structure. The

method also permits the separation of the SAW mode from bulk wave and electrostatic contributions. The methods in [58] and [59] were combined in this dissertation for the analysis of SHSAW transduction efficiency by IDTs considering finite-thickness electrodes on a *Symmetry Class 4* orientation of potassium niobate, langasite, and quartz [50,60,52]. The main results of the this work showed that through the use of thick gratings consisting of dense materials such as gold, almost 100% of the IDT input power can be transduced into the grating mode. This important result showed that efficient transduction of SHSAW modes can be achieved using heavy electrodes and is applicable to the design of efficient liquid-phase sensor platforms, that display improved signal-to-noise ratio via reduction of spurious signal excitation and detection.

1.4. Liquid-Phase Packaging Background

For SHSAW liquid-phase sensors, the employed device packaging that permits liquid-phase operation must minimally interfere with the sensing platform, prevent IDT shorting, provide some level of device protection, and facilitate easy micro- to macro-fluidic connections. In addition, it is highly beneficial if the sensor packaging process is compatible with batch fabrication techniques. A number of solutions have been reported for acoustic wave devices, which have typically borrowed fabrication techniques initially developed for MEMS devices. One such proposed technique [61] makes use of the ultra-thick high aspect-ratio photoresist SU-8 to form fluid containment walls around IDTs on prefabricated Love mode device. A quartz cap was manually placed on top of the structures and glued in place, leaving the sensing region open for fluid introduction via pipette. A similar reported method used SU-8 to cover the entire surface of a SHSAW

device forming a Love mode guiding layer, followed by SU-8 patterning of containment walls and attachment of a glass cap [62]. The use of the first SU-8 layer was two-fold; first to provide Love mode guiding, and second to improve adhesion of SU-8 walls to the device since in general SU-8 poorly adheres to quartz and silicon [63]. In another technique involving use of SU-8 [64], microfluidic chambers were fabricated using SU-8 on a poly(methyl methacrylate) (PMMA) substrate due to the superior adhesion that PMMA has with SU-8 when compared to glass and silicon. Next an optical adhesive NOA-73 was applied to the patterned SU-8 sealing-channels and then brought into contact with the SAW device and cured — bonding the two structures. In another SAW packaging work [65], a liquid-phase lithium tantalate platform was packaged with a polymeric chamber fabricated using a 3D photopolymerisation process of a copolymer based on acrylate. The packaging method required the chamber to be pressed to the sensor platform in order to produce a seal. The inventors of a commercially available Love wave liquid-phase sensor platform, S-sens® K5 biosensor system (Nanofilm Surface Analysis - Goettingen, Germany), reported a packaging method based on hot-embossing of thermoplastic-elastomeric polymers [66]. In this case the fluidic chamber walls are located outside of the IDT regions, such that fluid is exposed to the top of the entire Love mode device including IDTs, and the silicon dioxide guiding layer is used to prevent IDT shorting from conductive fluids.

The use of poly(dimethylsiloxane) (PDMS) or silicone rubber has been considered for microfluidic systems and MEMS in biological sensing applications since the late 1990's. Microfluidic devices are fabricated from this material through molding

techniques, and are typically used in rapid prototyping applications. The use of PDMS is attractive in liquid-phase sensor applications because it is inexpensive, easy to mold, flexible, optically transparent, compatible with bio-reagents, impermeable to water, and able to covalently bond to various surfaces [67]. A study on the solvent compatibility of PDMS can be found in [68]. Fabrication of molds used to form microfluidic structures are typically made through bulk micromachining of silicon, patterning of SU-8 on silicon or glass, and more recently by processing SU-8 on PMMA substrates due to increased adhesion and mold robustness [69]. Two instances of PDMS packaged SHSAW devices were reported in the literature [70,71]. In [70] PDMS microfluidic chips were molded using an SU-8 process and designed to have containment walls protecting the IDT of quartz Love mode device. Upon oxygen plasma exposure the devices where manually brought into contact and bonded covalently. Fluidic tubes were connected to the device by insertion into pre-bored holes. No mention of an alignment technique was reported. In [71] a similar packaging technique is used for a polymer coated quartz Love mode device. Here the microfluidic chip was not permanently attached to the device, but was sealed through applying slight pressure. Again no mention of alignment is given. In this work, a packaging technique is proposed which is similar to the two previous techniques, but also provides a rapid alignment technique that allows the microfluidic chip to be properly aligned to the SHSAW device before permanent attachment takes place. The proposed technique is compatible with wafer-scale batch fabrication techniques and allows rapid attachment placement and accuracy within ±10 μm.

1.5. Rationale

The literature review discussed so far in this chapter revealed that additional investigation of SHSAW based liquid-phase sensors was required regarding mode excitation and propagation analysis, sensor modeling under fluid loading conditions, and liquid-phase packaging development.

In terms of SHSAW propagation analysis, further study was required to quantify achievable sensor performance under fluid loading conditions. A thorough comparison of performance metrics was necessary, such as mode sensitivity, based on various guiding layer configurations and substrate materials. In addition to propagation analysis, additional work was required to quantify achievable SHSAW mode excitation efficiency of transducers while considering various substrates, guiding configurations, and transducer design parameters. In terms of sensor packaging, it was identified that there was a strong need to improve methods for SHSAW device encapsulation permitting liquid-phase operation. In particular, additional methods for simpler, more robust and repeatable packaging of SHSAW devices was desired.

1.6. Objectives and Approach

The main objectives of this dissertation included: (i) the identification of key SHSAW sensor design parameters and the quantification of their impact on sensor performance; (ii) extraction of key parameters for candidate SHSAW sensor designs; (iii) the improvement of liquid-phase packaging techniques for SHSAW devices; and (iv) the

verification of models used in this work and the liquid-phase sensing performance of the prototype SHSAW sensors designed.

The approach taken to achieve objective (i) included developing an analytical SHSAW sensor response model and deriving the expected sensor response in terms of key sensor design parameters (e.g. IDT center-to-center length, sensing region length, SHSAW temperature and analyte sensitivities, SHSAW complex slowness, and ratio of spurious signal detected to desired signal) and properties of the analyte (this work focused on the analysis of viscosity). In regards to accomplishing objective (ii), the approach chosen included theoretically developing and numerically implementing SHSAW propagation and excitation modeling tools, along with post-processing routines, for the extraction of some of the aforementioned key design parameters. The method taken to accomplish objective (iii) included combining and enhancing promising reported SHSAW and MEMS liquid-phase packaging methods. Lastly, to achieve objective (iv), the approach selected involved designing, fabricating, and testing prototype SHSAW designs in liquid-phase sensing applications, and comparing the measured data with calculations based on the proposed models.

1.7. Organization

The remaining chapters of this dissertation are outlined as follows. Chapter 2 discusses the theoretical background of the modeling tools developed and implemented in this work, which were used for the determination of SHSAW propagation and excitation properties. Chapter 3 presents at the beginning a simplified model of the expected

response of the liquid-phase sensor design topology considered. Based on the model, key sensor design parameters (e.g. IDT center-to-center length, sensing region length, SHSAW temperature and analyte sensitivities, SHSAW complex slowness, and ratio of spurious signal detected to desired signal) are identified and expressions are developed that permit sensor performance quantification based on said parameters. Afterwards, key parameters are calculated for a variety of device designs (consideration of various orientations, IDT pairs, film thickness, guiding layer configurations, etc.) using the numerical models discussed in Chapter 2. Chapter 4 reports on the SHSAW packaging methods implemented in this work and also on the design of sensor prototypes. In Chapter 5 experimental liquid-phase sensor measurements are reported demonstrating two potential applications for the developed devices; i.e. fluid viscosity sensing and biosensing. Chapter 6 is dedicated to summary, conclusions, and suggestions for future work.

CHAPTER 2

**THEORETICAL DEVELOPMENT OF ACOUSTIC WAVE MODELING TOOLS
AND NUMERICAL CONSIDERATIONS**

2.1. Introduction

This chapter presents the theoretical formalism of the modeling tools used extensively in this work towards the design and evaluation of candidate liquid-phase SAW sensor platforms. The implemented tools allow the study of design considerations relevant to SAW-based liquid-phase sensing platform devices, including: evaluation of acoustic wave (AW) mode properties based on various considered boundary conditions (application of guiding structures, effect of liquid-loading, etc.); and analysis of mode(s) excitation via interdigital transducer (IDT) simulation as a function of IDT surrounding boundary conditions. Propagation studies are carried out through evaluation of numerically computed Green's functions for the geometric structures considered (procedure described in this chapter). Mode properties such as phase velocity, penetration depth, coupling, propagation loss may be evaluated using the techniques presented in this chapter. IDT simulation and evaluation is carried out using numerical tools based on an implemented combined finite element and boundary element method (FEM/BEM) model (described in this chapter), which relies heavily on the computation of Green's functions.

Computation of spectral-domain Green's functions is considered first, as such functions are useful to identify and characterize AW modes, and in addition are required by the BEM model. Before describing the characteristics of such functions, an overview

of the matrix method proposed by Adler [38] for determining such functions is given. Adler's method is used to solve the linear quasi-static partial differential equations that describe the electromechanical fields in a piezoelectric material under time-harmonic and plane-wave propagation assumptions. The solution of the most general case shows that the fields within a piezoelectric continuum are represented as a superposition of eight partial modes, with a specified equal sinusoidal x- and y-spatial variation. Each eigenvalue of a derived matrix, **A** from Alder's method, gives the z-variation of a partial mode, while the associated eigenvector defines the corresponding field structure. Under the additional assumption of a semi-infinite body (i.e., a half-space extending to infinity in one of the + or - z directions), four of the partial modes are shown to have zero amplitude, as there is no reflecting surface or source of energy deep within the body, prompting an investigation into how to select valid partial modes with non-zero amplitude.

Presented next is a theoretical analysis of spectral-domain Green's function numerical computation for a semi-infinite piezoelectric / stress-free dielectric (i.e. vacuum) media problem. It is shown that evaluation of spectral-domain Green's functions permits identification of propagating modes by locating simple poles in the complex slowness plane. A novel application of a numerical computation method for the half-space problem is presented, and application of the method yields proper partial mode selection when sinusoidal x-directed spatial variation is considered a complex quantity. The method performs proper analytic continuation of partial modes into the complex slowness plane [72] using a numerical technique based on evaluation of

eigenvalue/eigenvector partial derivatives, with respect to x-directed slowness. The proposed numerical technique can be used to ensure proper identification of lossy/attenuating modes such as pseudo and high-velocity-pseudo acoustic waves (PSAW/HVPSAW). Analytic continuation of Green's functions into the complex slowness plane is also advantageous for BEM analysis, as will be shown.

After discussion of proper partial mode selection for the half-space problem, numerical calculation of Green's functions is considered for the cases of a semi-infinite vacuum atop a piezoelectric half-space, and for an n-layer problem, which permits identification of characteristic modes and the ability to analyze electrical responses of devices incorporating finite-thickness homogeneous layers. Lastly, the theory behind the FEM/BEM modeling tools implemented in this work is presented. These tools permit time-harmonic full-wave analysis (consideration of SAW/BAW/evanescent modes) of IDT structures atop piezoelectric half-space media (vacuum on other side) for both finite and infinitely periodic structures. The FEM/BEM tools were used in this work for the design of SHSAW liquid-phase sensor platform prototypes.

2.2. Matrix Method Analysis

Analyzing the intrinsic coupling between electrical and mechanical quantities of piezoelectric materials involves combining Newton's equation of motion and Maxwell's electromagnetic equations. Following [73], the piezoelectric constitutive equations are given as (2.1) using a matrix notation for tensor fields. (Note: In this dissertation,

boldface variables denote vectors or matrices; italicized variables, scalars; and the superscript T, a matrix/vector transpose operation.)

$$\mathbf{T} = \mathbf{c}^E \mathbf{S} - \mathbf{e}^T \mathbf{E}$$
$$\mathbf{D} = \boldsymbol{\varepsilon}^s \mathbf{E} - \mathbf{e}\mathbf{S}$$

(2.1)

where:

- $\mathbf{T} = \begin{bmatrix} T_1 & T_2 & T_3 & T_4 & T_5 & T_6 \end{bmatrix}^T$ is the stress vector,

- $\mathbf{S} = \begin{bmatrix} S_1 & S_2 & S_3 & S_4 & S_5 & S_6 \end{bmatrix}^T$ is the strain vector,

- $\mathbf{E} = \begin{bmatrix} E_1 & E_2 & E_3 \end{bmatrix}^T$ is the electric field vector,

- $\mathbf{D} = \begin{bmatrix} D_1 & D_2 & D_3 \end{bmatrix}^T$ is the electric displacement vector,

- $\mathbf{c}^E$ is the 6x6 elastic constant matrix under constant electric field,

- $\boldsymbol{\varepsilon}^s$ is the 3x3 dielectric permittivity matrix under constant strain, and

- $\mathbf{e}$ is the 3x6 piezoelectric constant matrix.

The strain vector may be written in terms of displacement components:

$$\mathbf{S} = \nabla_{6x3}\mathbf{u},$$

(2.2)

where:

- $\mathbf{u} = \begin{bmatrix} u_1 & u_2 & u_3 \end{bmatrix}^T$ is the displacement vector, and

- $\nabla_{6x3} = \begin{bmatrix} \partial/\partial x & 0 & 0 & 0 & \partial/\partial z & \partial/\partial y \\ 0 & \partial/\partial y & 0 & \partial/\partial z & 0 & \partial/\partial x \\ 0 & 0 & \partial/\partial z & \partial/\partial y & \partial/\partial x & 0 \end{bmatrix}^T$ is the 6x3 gradient operator.

Newton's equation of motion will be considered here only in the symmetric case where the limit of volume goes to zero:

$$\nabla_{3x6} \cdot \mathbf{T} = -\omega^2 \rho \mathbf{u},$$

(2.3)

where:

- ρ is the mass density of the material, and

- $\nabla_{3x6} \cdot = \begin{bmatrix} \frac{\partial}{\partial x} & 0 & 0 & 0 & \frac{\partial}{\partial z} & \frac{\partial}{\partial y} \\ 0 & \frac{\partial}{\partial y} & 0 & \frac{\partial}{\partial z} & 0 & \frac{\partial}{\partial x} \\ 0 & 0 & \frac{\partial}{\partial z} & \frac{\partial}{\partial y} & \frac{\partial}{\partial x} & 0 \end{bmatrix}$ is the 3x6 divergence operator.

Of particular interest for this work are quasi-acoustic modes, which typically propagate 10^5 times slower than quasi-electromagnetic waves in a piezoelectric material, as is well known. Thus Maxwell's equations may be treated under quasi-static conditions [73] (i.e. $\nabla \times E = 0$). Under this assumption, the electric field in the body is given as

$$\mathbf{E} = -\nabla_{3x1}\phi,$$

(2.4)

where:

- ϕ is the electric potential, and

- $\nabla_{3x1} = \begin{bmatrix} \frac{\partial}{\partial x} & \frac{\partial}{\partial y} & \frac{\partial}{\partial z} \end{bmatrix}^{\mathrm{T}}$ is 3x1 gradient operator.

Finally, recall that Gauss's Law for a source free medium is

$$\nabla_{1x3} \cdot \mathbf{D} = 0,$$

(2.5)

where:

- c is the 1x3 divergence operator.

Note that if the material has finite conductivity then an equivalent complex dielectric permittivity matrix is used, where: $\varepsilon^s \rightarrow \varepsilon^s - j/\omega\,\boldsymbol{\sigma}$, and $\boldsymbol{\sigma}$ is the 3x3 conductivity matrix.

Using a method similar to [38], sinusoidal time variation is given as $e^{j\omega t}$ and x-directed (resp. y-directed) sinusoidal spatial variation as $e^{-j\omega s_x x}$ (resp. $e^{-j\omega s_y y}$), where ω is radian frequency and s_x (resp. s_y) is the x-directed (resp. y-directed) inverse velocity or slowness. As a result, the partial derivatives $\partial/\partial t$, $\partial/\partial x$, and $\partial/\partial y$ involve multiplication by $j\omega$, $-j\omega s_x$, and $-j\omega s_y$, respectively. Using these expressions for the partial derivatives given in (2.1) - (2.5) and combining equations permits construction of a first-order matrix ordinary differential equation (ODE):

$$\frac{\partial \boldsymbol{\tau}(z)}{\partial z} = j\omega \mathbf{A}\boldsymbol{\tau}(z), \tag{2.6}$$

where:

- $\boldsymbol{\tau} = \begin{bmatrix} T_5 & T_4 & T_3 & D_3 & j\omega u_1 & j\omega u_3 & j\omega u_3 & j\omega\phi \end{bmatrix}^{\mathrm{T}}$,

- $\mathbf{A} = \begin{bmatrix} \mathbf{A}^{11} & \mathbf{A}^{12} \\ \mathbf{A}^{21} & \mathbf{A}^{22} \end{bmatrix}$,

- $\mathbf{A}^{11} = s_x \boldsymbol{\Gamma}^{13}\mathbf{X} + s_y \boldsymbol{\Gamma}^{23}\mathbf{X}$,

- $\mathbf{A}^{12} = \rho \mathbf{I}_4 - s_x^2 \left(\boldsymbol{\Gamma}^{11} - \boldsymbol{\Gamma}^{13}\mathbf{X}\boldsymbol{\Gamma}^{31} \right) - s_y s_x \left(\boldsymbol{\Gamma}^{12} - \boldsymbol{\Gamma}^{13}\mathbf{X}\boldsymbol{\Gamma}^{32} - \boldsymbol{\Gamma}^{23}\mathbf{X}\boldsymbol{\Gamma}^{31} + \boldsymbol{\Gamma}^{21} \right) - s_y^2 \left(\boldsymbol{\Gamma}^{22} - \boldsymbol{\Gamma}^{23}\mathbf{X}\boldsymbol{\Gamma}^{32} \right)$,

- $\mathbf{A}^{21} = \mathbf{X}$,

- $\mathbf{A}^{22} = s_x \mathbf{X}\boldsymbol{\Gamma}^{31} + s_y \mathbf{X}\boldsymbol{\Gamma}^{32}$,

- $\mathbf{X} = \left[\boldsymbol{\Gamma}^{33} \right]^{-1}$,

- $\mathbf{I}_4 = \begin{bmatrix} 1 & 0 & 0 & 0 \\ 0 & 1 & 0 & 0 \\ 0 & 0 & 1 & 0 \\ 0 & 0 & 0 & 0 \end{bmatrix}$, and

- $\boldsymbol{\Gamma}^{ik} = \begin{bmatrix} c_{1i1k}^{E} & c_{1i2k}^{E} & c_{1i3k}^{E} & e_{k1i} \\ c_{2i1k}^{E} & c_{2i2k}^{E} & c_{2i3k}^{E} & e_{k2i} \\ c_{3i1k}^{E} & c_{3i2k}^{E} & c_{3i3k}^{E} & c_{k3i} \\ e_{i1k} & e_{i2k} & e_{i3k} & -\varepsilon_{ik}^{s} \end{bmatrix}$,

(Voigt notation: 11→1, 22→2, 33→3, 12→6, 21→6, 13→5, 31→5, 23→4, 32→4).

34

This ODE system describes the field variation in a body with respect to z, given the fields at any point in the material and specified sinusoidal x and y field variations. A full derivation of this solution is given in Appendix A.

It should be mentioned that the analysis presented here generalizes the method in [38]. In [38] the ratio of x- to y-slowness is fixed and dependent on the pre-material-coordinate-system-rotation angle about the surface normal. The method used here permits independent specification of sinusoidal x and y variation. Analysis using independently specifiable complex x and y spatial variation allows independent complex slowness to be specified, which cannot be obtained from [38] as the ratio of x- to y-slowness is fixed.

A well-known solution to ODEs of the form (2.6) is given by

$$\boldsymbol{\tau}(z) = e^{j\omega \mathbf{A} z} \cdot \boldsymbol{\tau}(z = 0). \tag{2.7}$$

It is often convenient to rewrite (2.7) in normal mode form using the Jordan matrix decomposition $\mathbf{A} = \mathbf{PJP}^{-1}$, where $\mathbf{P}$ is an invertible matrix and $\mathbf{J}$ is a matrix in Jordan canonical form [74]. Substituting the Jordan decomposition of $\mathbf{A}$ into (2.7) yields

$$\boldsymbol{\tau}(z) = \mathbf{P}e^{j\omega \mathbf{J} z}\mathbf{c}, \tag{2.8}$$

where:

- $\mathbf{c} = \mathbf{P}^{-1}\boldsymbol{\tau}(0)$ is an 8x1 vector of normal mode weights.

It can furthermore be shown that the matrix exponential term in (2.8) can be expressed as a direct sum of exponential matrices for individual Jordan blocks [74]; i.e.

$$
\begin{aligned}
e^{j\omega \mathbf{J}z} &= e^{j\omega \mathbf{J}_1 z} \oplus e^{j\omega \mathbf{J}_2 z} \oplus \cdots \oplus e^{j\omega \mathbf{J}_n z} \\
&= e^{j\omega \lambda_1 z} e^{j\omega \mathbf{N}_1 z} \oplus e^{j\omega \lambda_2 z} e^{j\omega \mathbf{N}_2 z} \oplus \cdots \oplus e^{j\omega \lambda_n z} e^{j\omega \mathbf{N}_n z}
\end{aligned}
\tag{2.9}
$$

where

- The direct sum of arbitrary matrices $\mathbf{M}_i$ ($i = 1$ to n) is defined as

$$
\mathbf{M}_1 \oplus \mathbf{M}_2 \oplus \cdots \oplus \mathbf{M}_n =
\begin{bmatrix}
\mathbf{M}_1 & \mathbf{0} & \cdots & \mathbf{0} \\
\mathbf{0} & \mathbf{M}_2 & \ddots & \vdots \\
\vdots & \ddots & \ddots & \mathbf{0} \\
\mathbf{0} & \cdots & \mathbf{0} & \mathbf{M}_n
\end{bmatrix},
$$

- $\mathbf{J}_i$ is the ith Jordan block of $\mathbf{A}$,
- λ_i is the eigenvalue of $\mathbf{A}$ corresponding to the ith Jordan block,
- $\mathbf{N}_i = \mathbf{J}_i - \lambda_i \mathbf{I}$, and

$$
\bullet \; e^{j\omega \mathbf{N}_i z} = \sum_{k=0}^{n} \frac{(j\omega \mathbf{N}_i z)^k}{k!} =
\begin{bmatrix}
1 & j\omega z & \frac{(j\omega z)^2}{2} & \cdots & \frac{(j\omega z)^n}{n!} \\
0 & 1 & \ddots & \ddots & \vdots \\
\vdots & \ddots & \ddots & \ddots & \frac{(j\omega z)^2}{2} \\
0 & 0 & \ddots & 1 & j\omega z \\
0 & 0 & \cdots & 0 & 1
\end{bmatrix}, \text{ where } \mathbf{N}_i \text{ is } n \times n.
$$

Usually all Jordan blocks are 1×1 and the eigenvalues of $\mathbf{A}$ are distinct, in which case numerical Jordan decomposition is performed using standard eigen-decomposition. Diagonal entries of $\mathbf{J}$ assume the eigenvalues and columns of $\mathbf{P}$ assume the corresponding eigenvectors. Thus (2.8) simplifies to

$$
\boldsymbol{\tau}(z) = \begin{bmatrix} \mathbf{v}_1 e^{j\omega \lambda_1 z} & \mathbf{v}_2 e^{j\omega \lambda_2 z} & \cdots & \mathbf{v}_8 e^{j\omega \lambda_8 z} \end{bmatrix} \begin{bmatrix} c_1 & c_2 & \cdots & c_8 \end{bmatrix}^{\text{T}},
\tag{2.10}
$$

where:

- $\mathbf{v}_i$ is the ith eigenvector of $\mathbf{A}$, and λ_i is the ith eigenvalue of $\mathbf{A}$.

36

Given (2.10), fields within the piezoelectric continuum are represented as a weighted superposition of eight partial modes having time and space variation $e^{j\omega\left(t - s_x x + s_y y + \lambda_i z\right)}$. The z-directed slowness component for the ith partial mode is thus given by $s_z^i = -\lambda_i$.

As an illustration, Figure 2.1 shows the computed real and imaginary parts of s_z^i obtained for the ST-X orientation of quartz, Euler Angles (0°, 132.75°, 0°), as function of s_x; $s_y = 0$. Note that bold points correspond to valid partial modes for a $-z$-directed half-space (to be discussed further in Section 2.3). It can be seen from the figure that the slowness surfaces for the three bulk acoustic wave modes can also be constructed from the presented analysis. In particular, the bulk wave slowness surface is obtained by plotting $\Re\{s_z^i\}$ when $\Im\{s_z^i\} = 0$ as a function of s_x.
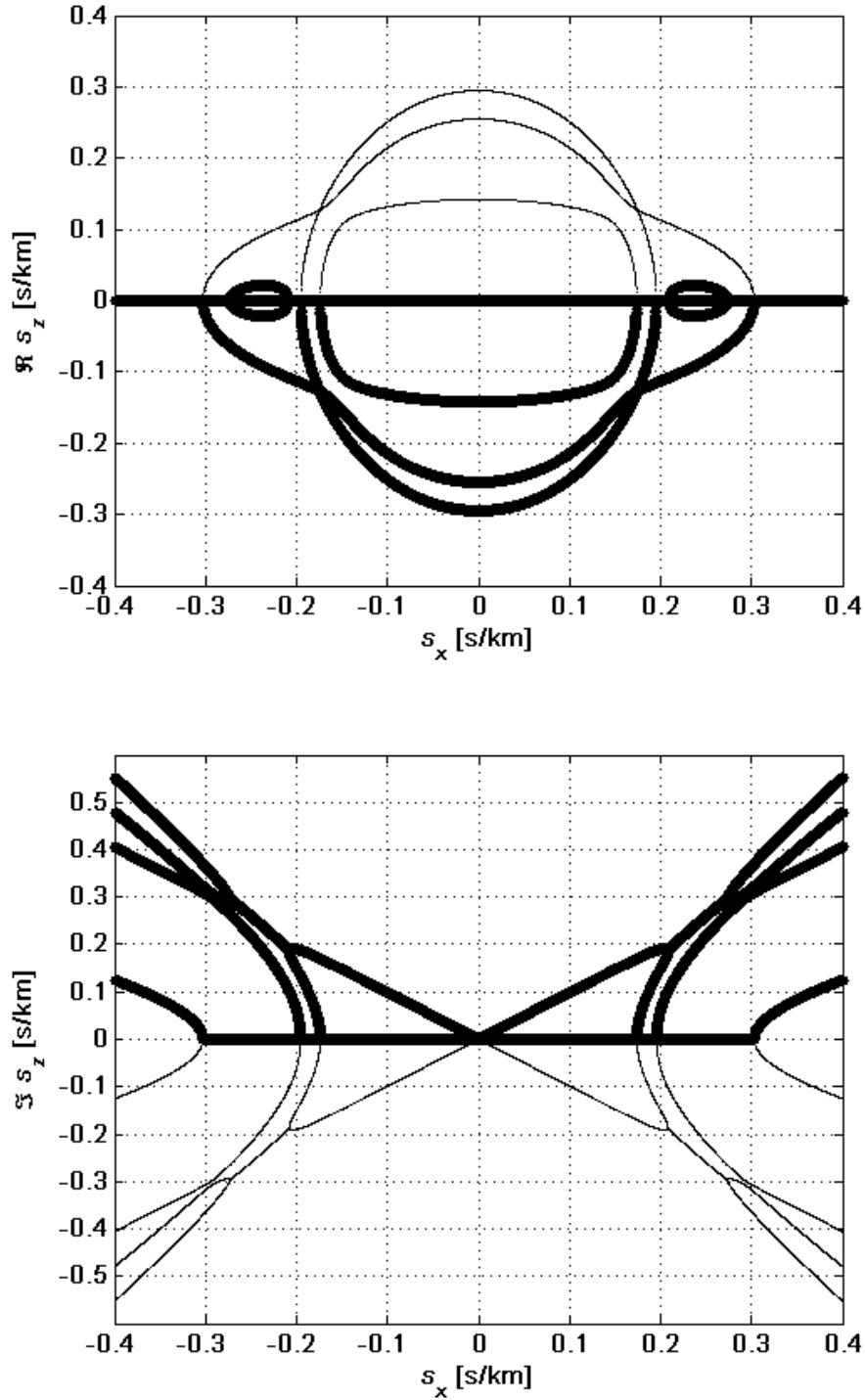
Figure 2.1. *z*-directed slowness for the 8 partial modes as a function s_x for ST-X quartz, Euler Angles (0°, 132.75°, 0°); $s_y = 0$. Bold points indicate the valid partial modes for a –*z*-directed half-space.

In cases where matrix $\mathbf{A}$ has repeated eigenvalues, Jordan blocks of order greater than 1 may be required. Such a situation occurs when s_x and s_y are both taken to be zero (e.g. a BAW device with electrodes positioned on top and bottom surfaces of a crystal extending infinitely in x- and y-directions) and field variation is limited to the z-direction. The sub-blocks of matrix $\mathbf{A}$ are: $\mathbf{A}^{11} = $ zero-matrix, $\mathbf{A}^{12} = \rho\mathbf{I}_4$, $\mathbf{A}^{21} = \mathbf{X}$, and $\mathbf{A}^{22} = $ zero-matrix. It can be shown that the overall $\mathbf{A}$ matrix is "defective" [74] and has a repeat eigenvalue of zero, with a single corresponding eigenvector. The situation requires use of $\begin{bmatrix} 0 & 1 \\ 0 & 0 \end{bmatrix}$ as the Jordan block for the zero eigenvalue case and use of a generalized eigenvector for $\mathbf{P}$ to be full rank and invertible. It can be shown that a valid generalized eigenvector is $\mathbf{g}_0 = \begin{bmatrix} nullspace\ \{\mathbf{I}_4\mathbf{X}\} & \mathbf{0}_{1x4} \end{bmatrix}^{\mathrm{T}}$. The nullspace vector may be found numerically using a singular value decomposition algorithm after enforcing that the smallest singular value is zero. It follows that the non-generalized eigenvector must be $\mathbf{v}_0 = (\mathbf{A} - \lambda_0\mathbf{I})\mathbf{g}_0 = \mathbf{A}\mathbf{g}_0 = \begin{bmatrix} \mathbf{0}_{1x7} & c_0 \end{bmatrix}^{\mathrm{T}}$, where $c_0 = \begin{bmatrix} x_{41} & x_{42} & x_{43} & x_{44} & \mathbf{0}_{1x4} \end{bmatrix}\mathbf{g}_0$. As the matrix exponential of the zero-eigenvalue Jordan block can be shown to be

$e^{j\omega z \begin{bmatrix} 0 & 1 \\ 0 & 0 \end{bmatrix}} = \begin{bmatrix} 1 & j\omega z \\ 0 & 1 \end{bmatrix}$, the resulting fields in the body are given by

$$\boldsymbol{\tau}(z) = \begin{bmatrix} \mathbf{v}_0 & (\mathbf{v}_0 j\omega z + \mathbf{g}_0) & \mathbf{v}_3 e^{j\omega\lambda_3 z} & \cdots & \mathbf{v}_8 e^{j\omega\lambda_8 z} \end{bmatrix} \cdot \begin{bmatrix} c_1 & c_2 & c_3 & \cdots & c_8 \end{bmatrix}^{\mathrm{T}}, \quad (2.11)$$

where:
- $\mathbf{v}_i$ is the ith eigenvector of $\mathbf{A}$, where vectors 3 through 8 correspond to non-zero eigenvalues (and, in this case, to the three bulk wave partial modes),
- λ_i is the ith eigenvalue of $\mathbf{A}$, where values 3 through 8 are non-zero eigenvalues,
- $\mathbf{v}_0$ is the non-generalized eigenvector for the zero eigenvalue, and
- $\mathbf{g}_0$ is the generalized eigenvector for the zero eigenvalue.

39

It can further be shown that elements of non-generalized eigenvectors relating to the electric displacement field D_3 are zero since the partial derivative of D_3 with respect to z is zero, by the $\mathbf{A}$ matrix and structure of $\mathbf{v}_0$. Therefore D_3 is uniform in the material and depends only on $\mathbf{g}_0$ and the partial mode weight c_2.

From (2.11) the fields within the body are determined to consist of six partial modes related to BAW modes having sinusoidal z-dependence and are uniform along x and y. The remaining two partial modes are pseudo-static: one is uniform along x, y and z; the other is uniform along x and y and varies linearly with respect to z. Pseudo-static partial modes physically represent the constant stress and z-directed electric displacement fields generated by one or more uniform charge source sheets located in an x-y plane in the continuum. The resulting electric potential (- integral of electric field) for pseudo-static partial modes thus varies linearly with respect to z.

Use of Jordan blocks with order larger than 1 are also required in instances where eigenvalues transition from a complex quantity to purely real or vice-versa with respect to x and y slowness (assuming lossless materials). These conditions occur at points where the slowness surface normal vector is directed along $\left[s_x \hat{\mathbf{s}}_x \quad s_y \hat{\mathbf{s}}_y \quad 0 \hat{\mathbf{s}}_z \right]^{\mathrm{T}}$ in three-dimensional slowness space (the variables with hats represent unit-normal vectors pointing along the s_x, s_y and s_z axes, respectively). The situation indicates the transition of a partial mode from a growth/decay mode with respect to z to one that does not does not grow/decay, or vice-versa. An example will now be given in the case of acoustic wave propagation in an isotropic media.

It is well known that the slowness surfaces of the longitudinal and two orthogonal transverse modes are spherical with radii equal to $\sqrt{\dfrac{\rho}{c_{11}}}$ and $\sqrt{\dfrac{\rho}{c_{44}}}$, respectively. Thus, for an isotropic solid, the eigenvalues of the **A** matrix associated with purely acoustic fields are

$$\left[\sqrt{\frac{\rho}{c_{11}}-s_x^2-s_y^2} \quad -\sqrt{\frac{\rho}{c_{11}}-s_x^2-s_y^2} \quad \sqrt{\frac{\rho}{c_{44}}-s_x^2-s_y^2} \quad -\sqrt{\frac{\rho}{c_{44}}-s_x^2-s_y^2} \quad \sqrt{\frac{\rho}{c_{44}}-s_x^2-s_y^2} \quad -\sqrt{\frac{\rho}{c_{44}}-s_x^2-s_y^2}\right].$$

Note that the transverse modes (terms involving c_{44}) have repeated eigenvalues but will not require use of generalized eigenvectors as a full set of eigenvectors can be obtained given mode orthogonality. It may however be difficult to obtain the two orthogonal eigenvectors using a numerical eigen-decomposition algorithm directly. Instead, the orthogonal vectors can be found using a singular value decomposition algorithm.

In the cases $s_x^2 + s_y^2 = \dfrac{\rho}{c_{11}}$ or $s_x^2 + s_y^2 = \dfrac{\rho}{c_{44}}$, where repeated eigenvalues are associated with the longitudinal, shear horizontal, and shear vertical modes, i.e. at a point where the normal to slowness curve is directed along direction $\left[s_x\hat{\mathbf{s}}_x \quad s_y\hat{\mathbf{s}}_y \quad 0\hat{\mathbf{s}}_z\right]^{\mathrm{T}}$, use of a generalized eigenvector will be required. For example, consider the shear-horizontal bulk acoustic wave evaluated at $s_y = 0$ and $s_x = \sqrt{\dfrac{\rho}{c_{44}}}$, which yields a repeated eigenvalue of 0. A solution to (2.8) for the fields T_4 and $j\omega u_2$ can be shown to be

$$\left[T_4 \quad j\omega u_2\right]^{\mathrm{T}} = \left[c_2 c_{44} \quad c_1 + c_2 j\omega z\right]^{\mathrm{T}} e^{-j\omega\sqrt{\frac{\rho}{c_{44}}}x}.$$ Observe the linear z-dependence of the $j\omega u_2$ field observed under uniform T_4, with respect to the z-direction. Also note the possible existence of zero T_4 throughout the continuum under uniform $j\omega u_2$ with respect

to z in the body. For non-isotropic and/or piezoelectric media, where analytical analysis is not possible or practical, conditions for when generalized eigenvectors are required may be determined by computing eigenvalue partial derivative singularities with respect to s_x or s_x, (discussed in Section 2.3).

2.3. Semi-Infinite Media: Proper Partial Mode Selection

Section 2.2 presented normal mode analysis in unbounded piezoelectric media. In the study of surface acoustic wave (SAW) devices, where excitation takes place at the interface between two materials (typically at the interface of air or vacuum and a piezoelectric), it is common to treat both materials as semi-infinite half-spaces since, in practice, the majority of mode energy in SAW applications is typically contained to within a few wavelengths of the interface. In addition, the backside of the crystal substrate is often left unpolished or intentionally roughened to scatter energy associated with deep penetrating modes in turn associated with bulk acoustic waves (BAWs). As a result, the crystal appears semi-infinite from the interface point of view.

Under the unbounded media assumption, the fields in the continuum are a linear superposition of eight partial-modes. In the case of semi-infinite media, the number of allowable partial-modes is cut in half as wave sources exist only at the interface (i.e. $z = 0$) and the body contains no internal reflecting interface. Like electromagnetic wave propagation on a semi-infinite transmission line with a single source at one end, power is carried in only one direction—away from the source. If the transmission line is truncated and terminated with non-matched impedance, forward and reverse propagating waves

will establish fields within the transmission line, as a reflective interface (impedance discontinuity) is now present. The analogous piezoelectric half-space situation raises the question as to which of the eight partial modes should be selected for inclusion in the analysis. The answer to this question requires qualitative reasoning to determine under what conditions a particular partial mode makes physical sense in a semi-infinite material.

Partial mode selection criterion will first be considered for purely real values of s_x and s_y, i.e. when there is no propagation loss/growth of partial modes along the x or y direction. In the case of a transmission line, one would select the partial mode that carries power away from the source. In the situation of propagation in semi-infinite media it follows that one should choose to keep bulk-type propagating partial modes, i.e. partial modes with purely real eigenvalues that carry power away from the interface towards the bulk. The sign of the z-directed Poynting vector associated with a particular bulk-type partial mode will determine whether the partial mode carries energy away from the surface towards the bulk.

Under the quasi-static approximation the time average spatial-domain Poynting vector in a piezoelectric material [73] is given by (2.12). Note that the order of conjugation for the product of electrical terms was chosen to be opposite in this work for simplicity; it can easily be shown using conjugation properties that the overall result is unaffected by this modification.

$$\overline{S}_x = -\frac{1}{2}\Re\left\{\left[\overline{T}_1 \quad \overline{T}_6 \quad \overline{T}_5 \quad \overline{D}_1\right]\left[\overline{j\omega u_1} \quad \overline{j\omega u_2} \quad \overline{j\omega u_3} \quad \overline{j\omega\phi}\right]^H\right\},$$

$$\overline{S}_y = -\frac{1}{2}\Re\left\{\left[\overline{T}_6 \quad \overline{T}_2 \quad \overline{T}_4 \quad \overline{D}_2\right]\left[\overline{j\omega u_1} \quad \overline{j\omega u_2} \quad \overline{j\omega u_3} \quad \overline{j\omega\phi}\right]^H\right\}, \qquad (2.12)$$

$$\overline{S}_z = -\frac{1}{2}\Re\left\{\left[\overline{T}_5 \quad \overline{T}_4 \quad \overline{T}_3 \quad \overline{D}_3\right]\left[\overline{j\omega u_1} \quad \overline{j\omega u_2} \quad \overline{j\omega u_3} \quad \overline{j\omega\phi}\right]^H\right\},$$

where:

- superscript H denotes conjugate transpose, and
- S_x, S_y, and S_z are the x-, y-, and z-directed Poynting vectors, respectively.

Therefore, for the ith partial mode, the z-directed Poynting vector is given from (2.12),

(2.8), and (2.10) as $S_z^i = -\frac{1}{2}|c_i|^2\Re\left\{\left[P_{1i} \quad P_{2i} \quad P_{3i} \quad P_{4i}\right]\left[P_{5i} \quad P_{6i} \quad P_{7i} \quad P_{8i}\right]^H\right\}$, where P_{ji} is

j^{th} element of the ith partial mode eigenvector. As only the sign of the real part of

z-directed Poynting vector is sought, no knowledge of the partial mode weights, c_i, is

required. The partial mode will be considered valid and will be included in the analysis of

the semi-infinite body if the sign of (2.12) corresponding to the z-direction is negative,

given a half-space occupying $z <= 0$.

In the case of non-bulk type partial modes, which occurs when the eigenvalue is

not purely real, the partial modes are denoted as growing or decaying type partial modes

and exhibit field amplitude z-variation exponentially increasing or decreasing. Only the

partial modes that decay with depth $\Im\{\lambda\} < 0$ are considered valid for the semi-infinite

body, since increasing Poynting vector magnitude is not physically possible as $z \rightarrow -\infty$,

given that the Poynting vector in the x and y directions are constant with respect to x and

y and all wave sources are considered to be at the interface or above.

Analysis of a semi-infinite body assuming a specified x or y partial mode decay or growth rate, i.e. complex x- and or y-slowness, is required when trying to verify existence of PSAW and HVPSAW modes. In particular, these modes display fields that decay along the propagation direction along the interface, since one or two downward propagating BAW modes are coupled to the solution, respectively [75]. Proper partial mode selection rules under complex x- and or y-slowness are difficult to define insofar as the modes do not resemble familiar plane-wave BAWs or evanescent waves that decay or grow only in z. Standard techniques for determining proper selection of partial modes [44] involve first calculating partial mode eigenvalues by considering only the real part of the slowness, then determining the number of bulk-type, N_{BAW}, and decaying-type, N_{DECAY}, partial modes required using the selection criteria given in the previous paragraph. The eigenvalues are then computed at the desired complex slowness point. Based on the set of partial modes that grow with depth, the N_{BAW} with the slowest growth rates are selected. Of the remaining number of required partial modes to include, N_{DECAY} are chosen from the decaying partial mode set having the fastest decay rates. Such a selection criterion cannot guarantee proper partial mode selection, unlike the case considering purely real slowness. In particular, the standard technique was on occasion seen to fail in this work as propagation loss (relative shift into the complex plane) becomes larger, as indicated by observing the boundary condition function solution used for PSAW/HVSPSAW identification becoming discontinuous at points along a line extending into the imaginary slowness axis that is perpendicular to the real slowness axis.

A more robust selection process is needed to guarantee proper selection of partial modes. According to [72], proper partial mode selection should result from analytically continuing the valid partial modes from the real slowness axis into the complex plane since all required information regarding the solutions to the boundary problem can be derived from evaluation on just the real slowness axis. In particular, given the proper set of partial modes and their corresponding eigen-solutions (eigenvalues and eigenvectors of **A**) determined for a purely real slowness, the proper partial mode and corresponding eigen-solution sets for the half-space upon shifting into the complex plane should be chosen such that eigen-solutions are analytically continued from the real slowness axis into the complex plane. The strategy is based on the theory of analytic functions. Using a Taylor series expansion, a partial mode's eigenvalue can be determined in the complex plane given the eigenvalue on the real slowness axis and value of all partial derivatives at that point. Using a slowness stepping algorithm into the complex slowness plane, the continuation of eigenvalues associated with a given partial mode is performed by starting on the real slowness axis, choosing valid partial modes, then taking a number of small steps into the complex plane (relative to the variation of the eigenvalue in the complex plane) such that a small error in predicted (via Taylor series) and actual (computed) eigen-values and -vectors occurs. Once arriving at the desired complex slowness point, the stepping algorithm ends and the proper set of partial modes is determined.

The authors of [72] appear to neglect partial derivatives in the Taylor series expansion/comparison stepping approach, and it has been observed in this work that eigenvalues can cross in the complex plane, making knowledge of slopes needful for

determining proper continuation. By contrast, the stepping method used in this dissertation includes higher order partial derivatives as well. The method requires numerical evaluation of eigenvalue partial derivatives with respect to x and y slowness. While the theory of computing eigenvalue n^{th}-order partial derivatives has been reported in the literature [76] to determine eigenmode sensitivities, to the best of the author's knowledge, the technique has not before been applied to partial mode selection in piezoelectric half-space problems.

The following analysis is concerned with computing n^{th} order eigenvalue and eigenvector partial derivatives. The formalism will be developed with respect to x-directed slowness; s_y is assumed to be 0. Computation of partial derivatives with respect to y-directed slowness proceeds analogously. It is further assumed that Jordan decomposition results in a complete eigenvector basis, i.e. $\mathbf{P}$ is full rank and contains no generalized eigenvectors, which is the case except for finitely many s_x values. From the definition of the Jordan decomposition of $\mathbf{A}$, it can be shown that $\mathbf{AP} - \mathbf{PJ}$ = zero-vector. Taking the nth partial derivative of this equation with respect to some variable in $\mathbf{A}$, in this case s_x, and applying Leibniz rule [77] yields

$$\frac{\partial^n (\mathbf{AP} - \mathbf{PJ})}{\partial s_x^n} = \sum_{k=0}^{n} \binom{n}{k} \left(\frac{\partial^{n-k} \mathbf{A}}{\partial s_x^{n-k}} \cdot \frac{\partial^k \mathbf{P}}{\partial s_x^k} - \frac{\partial^k \mathbf{P}}{\partial s_x^k} \cdot \frac{\partial^{n-k} \mathbf{J}}{\partial s_x^{n-k}} \right) = \text{zero-vector}. \tag{2.13}$$

Solving for the nth partial derivative of $\mathbf{J}$ with respect to s_x, and making appropriate substitutions result in

$$\frac{\partial^n \mathbf{J}}{\partial s_x^n} = \mathbf{J}\mathbf{C}^n - \mathbf{C}^n\mathbf{J} + \mathbf{H}^n,$$

(2.14)

where

- $\mathbf{C}^n$ is an 8x8 matrix to be determined,

- $\mathbf{H}^n = \mathbf{Z}^n + \sum_{k=1}^{n-1} \binom{n}{k}\left(\mathbf{Z}^{n-k}\mathbf{C}^k - \mathbf{C}^k \frac{\partial^{n-k}\mathbf{J}}{\partial s_x^{n-k}}\right)$,

- $\mathbf{Z}^m = \mathbf{P}^{-1}\frac{\partial^m \mathbf{A}}{\partial s_x^m}\mathbf{P}$, and

- $\frac{\partial^k \mathbf{P}}{\partial s_x^k} = \mathbf{P}\mathbf{C}^k$.

The nth partial derivatives of $\mathbf{A}$ are determined from the constitutive equations of (2.6). Thus the nth partial derivatives of $\mathbf{J}$ and $\mathbf{P}$ can be determined recursively once $\mathbf{C}^k$ is known for $k = 1$ to n.

To determine $\mathbf{C}^n$, note first it can be shown that $diag\left\{\frac{\partial^n \mathbf{J}}{\partial s_x^n}\right\} = diag\left\{\mathbf{H}^n\right\}$ when Jordan blocks all have rank 1 and all off-diagonal entries of $\mathbf{J}$ are zero. Then from (2.14) one finds $C_{ij}^n = \frac{H_{ij}^n}{J_{jj} - J_{ii}}$ $(i \neq j)$. For diagonal entries of $\mathbf{C}^n$, the equation $\frac{\partial^n \mathbf{P}}{\partial s_x^n} = \mathbf{P}\mathbf{C}^n$ will prove useful following a discussion of $\mathbf{P}$, the matrix of eigenvectors. In general eigenvectors are not uniquely determined since any non-zero scaling yields another valid solution. If instead eigenvectors are scaled such that one of the fields associated with an eigenvector is held constant with respect to s_x, then eight equations may be formed using

48

the definition of the nth partial derivative of **P** with respect to s_x given above, which allows determination of a unique solution for $\mathbf{C}^n$. From these equations, diagonal entries of $\mathbf{C}^n$ are given by $C_{ii}^n = -\dfrac{P_{rows(i)j}C_{ji}^n}{P_{rows(i)i}}$, where j is summed from 1 to 8 ($i \neq j$), and $rows(i)$ is the row index of the ith eigenvector which is held constant with respect to s_x. As mentioned at the end of Section 2.2, a search for eigenvalue partial derivatives singularities with respect to s_x can be performed using this method to determine s_x points where a generalized eigenvector is required.

Finally, the special case when generalized eigenvectors are encountered in the **A** matrix decomposition is treated, so to determine the proper selection of partial modes for a half-space under these circumstances.

For the sub-case of zero x- and y-directed slowness, i.e. no field variation along the x and y directions, one can choose three valid bulk-type partial modes based on the Poynting vector analysis presented previously.

For the sub-case of pseudo-static partial modes associated with repeated zero-eigenvalues, it is convenient to consider a finite-thickness piezoelectric layer, sandwiched by two zero-thickness perfect conductors with opposite polarity atop a semi-infinite piezoelectric body embedded in free space (Figure 2.2).
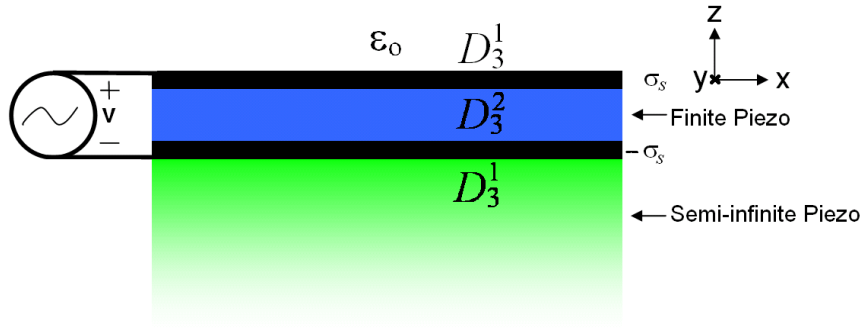
Figure 2.2. Finite-thickness piezoelectric sandwiched by two zero-thickness perfect conductors with opposite polarity atop a semi-infinite piezoelectric.

The following boundary conditions apply: surface normal components of stress (i.e. T_5, T_4, and T_3), displacement components, and electrical potential are continuous across boundaries; $D_3^1 - D_3^1 = \sigma_s$, where σ_s is the source charge density at the top interface. Charge conservation requires that the charge at the free-space/finite-piezo interface be equal and opposite in sign to the charge at the finite-piezo/semi-infinite-piezo interface. From the discussion leading to expression (2.11) describing the fields in the body of Figure 2.2, the D_3 field in each material will be constant with respect to z. It can also be shown from charge conservation and Gauss's Law that D_3 above the finite layer is equal to D_3 below the finite layer. Additionally, since the net charge above the semi-infinite piezoelectric is zero it follows that D_3^1 equals zero, which can be shown using Coulomb's law and charge superposition. (In detail: only one partial mode yields finite D_3 in each body and at the same time has zero associated strain since $\partial/\partial x = \partial/\partial y = \partial/\partial z = 0$, therefore $D_3 = \varepsilon_{33}E_3$ in each material and it follows that the situation can be treated like a simple dielectric stack regarding D_3, E_3, and σ_s.) Since D_3^1 is equal to zero, according to (2.11) the partial mode weight c_2 in the semi-infinite piezoelectric must be zero. As a

50

result, the pseudo-static partial mode based on the non-generalized eigenvector is considered valid for any configuration above the interface when the total source charge above the semi-infinite body is zero (charge conservation), and the partial mode based on the generalized eigenvector is considered invalid.

Proceeding to the sub-case when generalized eigenvector(s) are required for non-zero s_x and s_y, recall that such situations occur at points where the tangent of a bulk-type partial mode slowness surface is directed along $\begin{bmatrix} s_x\hat{\mathbf{s}}_x & s_y\hat{\mathbf{s}}_y & 0\hat{\mathbf{s}}_z \end{bmatrix}^{\mathrm{T}}$. Furthermore, it can be shown that the direction of power flow for the bulk-type partial mode is along the surface, since the power flow direction coincides with the slowness surface normal [73]. Therefore, as this bulk-type partial mode does not carry energy toward the surface from the bulk, it can be deemed valid for the semi-infinite body, and thus the partial mode based on the generalized eigenvector is considered invalid for the semi-infinite half-space. Practically speaking, it is the field behavior in a semi-infinite body near, not at, exact slowness points (where generalized eigenvectors are encountered) that need to be evaluated; hence this partial mode selection criterion is generally not encountered numerically, but was included for the sake of completeness.

2.4. Calculation of Spectral-Domain Green's Functions

The Green's function calculation procedure to be presented herein is used to characterize SAW device excitation and propagation for the semi-infinite media problem. The functions derived are used in conjunction with BEM models for numerical evaluation of SAW device electrical responses. Calculation of Green's functions is also shown to

permit identification of acoustic modes. The geometry considered in this section is shown in Figure 2.3.
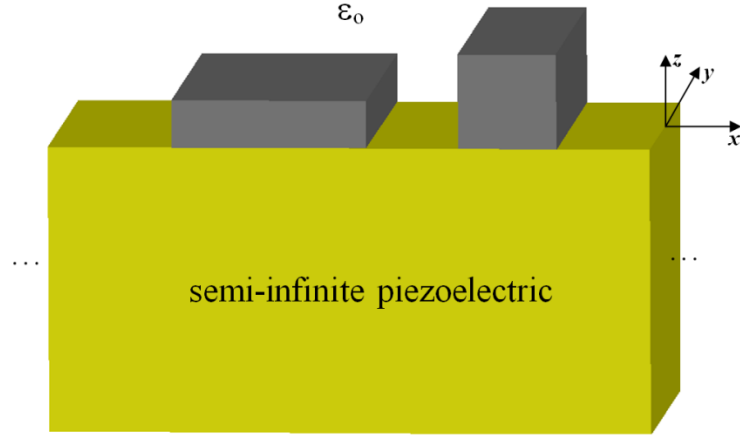
Figure 2.3. Geometry of the problem considered in this section.

In the figure, the semi-infinite piezoelectric media occupies the space z < 0. Arbitrarily sized electrodes are positioned at the interface of the piezoelectric and vacuum, and are considered to extend infinitely along the *y*-direction (no field variation along *y* is assumed). In the electrical sense, electrodes are considered to have zero thickness and be perfect conductors such that charge sources are considered to exist only at $z = 0$; however, in the acoustical sense, electrodes are treated as having finite thickness. Also, wave fronts generated by the structure are assumed to travel only in the *x-z* plane.

The Green's functions described in this section relate the resulting fields $[u_1 \ u_2 \ u_3 \ \phi]^{\text{T}}$ at a semi-infinite media interface, subject to interface source distributions of $[T_5 \ T_4 \ T_3 \ \sigma]^{\text{T}}$, where σ is the source surface charge density at the interface, i.e. $D_3^{0+} - D_3^{0-}$ at the interface. Interfacial boundary conditions must be imposed in the spatial-domain using the FEM/BEM model, i.e. enforcement of electric potential, and continuity of

52

surface normal stress and displacement; however, the analyses given in previous sections of this chapter consider propagation in finite and semi-infinite media in the spectral-domain, i.e. assumed sinusoidal field variation given by s_x. Thus transformation of the Green's functions using Fourier analysis is performed to convert the problem into the spatial-domain, where boundary conditions can be imposed and a solution obtained. The Fourier transform pair adopted in this work is given by

$$\overline{f}(x) = \int_{-\infty}^{\infty} f(k_x) e^{-jk_x x} dk_x$$

$$f(k_x) = \frac{1}{2\pi} \int_{-\infty}^{\infty} \overline{f}(x) e^{jk_x x} dx$$

(2.15)

where:

• $k_x = \omega\, s_x$ is the x-directed wave number, and

• f is any particular field at the interface.

The bar above a variable denotes spatial-domain representation. Using (2.15), a particular field at an interface is expressed as the infinite superposition of weighted sinusoidal varying fields. Thus, if displacement and potential fields can be related to stress and charge fields in the spectral-domain, then by (2.15) the fields in the spatial-domain can be related as well. Individual spectral components of $[u_1\ u_2\ u_3\ \phi]^{\mathrm{T}}$ and $[T_5\ T_4\ T_3\ \sigma]^{\mathrm{T}}$ at the interface are related by the spectral-domain Green's functions, $\mathbf{G}$, which have the form

$$\left[j\omega u_1(k_x) \quad j\omega u_2(k_x) \quad j\omega u_3(k_x) \quad j\omega\phi(k_x) \right]^{\mathrm{T}} = \mathbf{G}\!\left(\frac{k_x}{\omega}\right) \cdot \left[T_5(k_x) \quad T_5(k_x) \quad T_5(k_x) \quad \sigma(k_x) \right]^{\mathrm{T}}, \quad (2.16)$$

and can be shown to be functions of $k_x/\omega = s_x$ only (non-dispersive) for the lossless semi-infinite media problem considered. Applying (2.15) to (2.16) and simplifying generates the spatial-domain Green's functions:

53

$$\overline{\mathbf{G}}(\omega\, x) = \frac{1}{2\pi j} \int\limits_{-\infty}^{\infty} \mathbf{G}(s_x) e^{-js_x\omega\, x} ds_x \tag{2.17}$$

where

$$\bullet \; \left[\overline{u_1}(x) \quad \overline{u}_2(x) \quad \overline{u}_3(x) \quad \overline{\phi}(x)\right]^{\mathrm{T}} = \int\limits_{-\infty}^{\infty} \overline{\mathbf{G}}(\omega\, x - \omega\, x') \cdot \left[\overline{T}_5(x') \quad \overline{T}_5(x') \quad \overline{T}_5(x') \quad \overline{\sigma}(x')\right]^{\mathrm{T}} dx'.$$

The spatial-domain Green's functions thus describe the impulse response on the structure, in terms of the displacement and electrical potential fields along the interface, that results from a single impulse line-distribution extending along y of either one component of surface normal stress or charge density located at $(x = 0, z = 0)$. The rest of this section will discuss numerical computation of the spectral-domain Green's functions and their properties.

Recall that the surface charge density at the interface is given by the difference in surface normal electrical displacement: $\sigma(x, z = 0) = D_3(x, z = 0^+) - D_3(x, z = 0^-)$. With this relationship and use of the linearity property of the Fourier transform, the coupling of two independent semi-infinite media spectral-domain analyses (based on the Matrix Method described in the previous sections) is achieved and subsequently used to yield the spectral-domain Green's functions. For spectral analysis of the semi-infinite vacuum, the Matrix Method can be applied as well, assuming a non-piezoelectric material with dielectric permittivity ε_o and arbitrary stiffness and density. Since the vacuum is non-piezoelectric, the arbitrarily chosen stiffness and density do not influence the relationship between electric potential and D_3 in the vacuum and are only included so that the analysis can make use of existing software written for arbitrary materials. The results of the Matrix Method in the spectral-domain for the vacuum can be summarized as

54

$[D_3 \quad j\omega\phi]^{\mathrm{T}} = \mathbf{v}_{electrical} \cdot e^{j\omega\lambda_{electrical} z} c_{electrical}$, which are the eigenvector ($\mathbf{v}_{electrical}$), eigenvalue ($\lambda_{electrical}$), and partial mode weight ($c_{electrical}$) obtained from Jordan decomposition of the **A** matrix associated with the electrical fields in the vacuum. Equation (2.17) states that the electrical fields consist of only one partial mode. Thus, at the interface, $D_3(k_x, z = 0^+) = \mathbf{v}_{electrical}(1)/\mathbf{v}_{electrical}(2)j\omega\phi(k_x, z = 0)$, where (1) and (2) indicate first and second vector elements. It can be shown analytically that $\lambda_{electrical} = jSign\{\mathrm{Re}\{s_x\}\}s_x$ by using Laplace's equation and guaranteeing that the eigenvalue is correctly continued into the complex plane. Furthermore, using (2.4) and (2.5) it can be shown that $\mathbf{v}_{electrical}(1)/\mathbf{v}_{electrical}(2) = -j\varepsilon_o Sign\{\mathrm{Re}\{s_x\}\}s_x$. Therefore the electric displacement in an infinitesimal neighborhood about the vacuum/piezoelectric interface is given by

$$D_3^+(k_x, z = 0) = -j\varepsilon_o Sign\{\mathrm{Re}\{s_x\}\}s_x j\omega\phi(k_x, z = 0)$$

(for a vacuum half-space occupying z > 0).

(2.18)

Next, the resulting Matrix Method analysis for semi-infinite piezoelectric media is considered. In previous sections it was shown that the fields in the body are represented as the superposition of four partial modes in the spectral-domain, and at the interface $z = 0$ are given by

$$[T_5 \quad T_4 \quad T_3 \quad D_3^- \quad j\omega u_1 \quad j\omega u_3 \quad j\omega u_3 \quad j\omega\phi]_{z=0}^{\mathrm{T}} = \mathbf{P}_{8x4} \cdot [c_1 \quad c_2 \quad c_3 \quad c_4]^{\mathrm{T}}.$$

(2.19)

Substitution of (2.18) into (2.19) and applying the definition of charge density yields

$$\begin{bmatrix} T_5 & T_4 & T_3 & \sigma & j\omega u_1 & j\omega u_3 & j\omega u_3 & j\omega\phi \end{bmatrix}^{\mathrm{T}}_{z=0} = \mathbf{M}_{8x4} \cdot \begin{bmatrix} c_1 & c_2 & c_3 & c_4 \end{bmatrix}^{\mathrm{T}}, \quad (2.20)$$

where:

- $\mathbf{M}$ is initially set equal to $\mathbf{P}$, then
- $\mathbf{M}(4,:)$ is set to $-j\varepsilon_o sign\{real(s_x)\}s_x\,\mathbf{M}(8,:) - \mathbf{M}(4,:)$ (Matlab index notation).

The spectral-domain Green's functions defined by (2.16) may then be directly computed using

$$\mathbf{G}\left(\frac{k_x}{\omega} = s_x\right) = \mathbf{M}_{low}\mathbf{M}_{up}^{-1}, \quad (2.21)$$

where:

- $\mathbf{M}_{low} = \mathbf{M}(5:8,:)$ (Matlab index notation), and
- $\mathbf{M}_{up} = \mathbf{M}(1:4,:)$ (Matlab index notation).

In general the number of electrically coupled Green's functions is 16, which occurs for piezoelectric orientations classified as *Symmetry Type 1* [31]. For some orientations and materials classified by higher Symmetry Types, the number of electrically coupled Green's functions is reduced to 1 for *Symmetry Type 2* (only $j\omega\phi$ and σ coupled), 9 for *Symmetry Type 3* (pure Rayleigh polarization, only $j\omega u_1$, $j\omega u_3$, $j\omega\phi$, and T_5, T_4, σ coupled), 4 for *Symmetry Type 4* (pure shear-horizontal polarization; $j\omega u_2$, $j\omega\phi$, and T_4, σ coupled), and 1 for *Symmetry Type 5* (only $j\omega\phi$ and σ coupled). As an example, two of the spectral-domain Green's functions for the popular ST-X *Symmetry Type 1* orientation of quartz, Euler Angles (0°, 132.75°, 0°), are shown in Figure 2.4 as a function of s_x. The Green's functions for other Symmetry Types and those that relate other fields follow the same general behavior but are not all considered here strictly to

save space. It should be noted that the nomenclature regarding naming specific Green's functions within the matrix follows G_{ab}, which represents the Green's function that relates field b to field a at the interface.
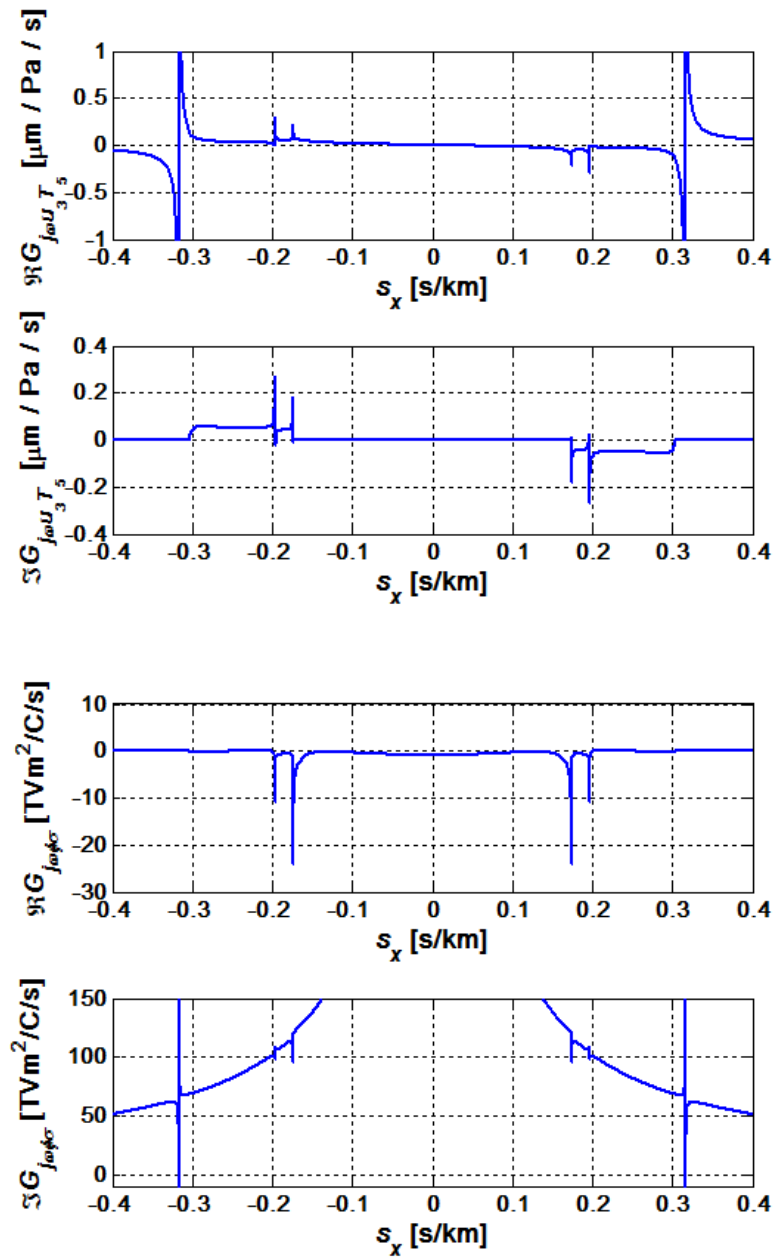
Figure 2.4. Real and imaginary components for 2 of the 16 spectral-domain Green's functions for ST-X quartz, Euler Angles (0°, 132.75°, 0°). Top two plots give the relation between the T_5 and $j\omega u_3$ fields whereas the bottom two plots give the relation between the σ and $j\omega\phi$ fields.

The plots in Figure 2.4 show the real and imaginary components for 2 of the 16 spectral-domain Green's functions obtained for the considered ST-X orientation of quartz. In particular, the two figures on top give the relation between the T_5 and $j\omega u_3$ fields whereas the bottom two plots give the relation between the σ and $j\omega\phi$ fields. Immediately one notes the $\propto \frac{1}{\sqrt{s_x^2}}$ behavior near $s_x \approx 0$ seen only for the purely electrical Green's function. This behavior is always observed for the purely electrical Green's function but does not manifest in other Green's functions, such as those relating mixed mechanical and electrical fields. This behavior appears for any Symmetry Type. The origin of this singularity is attributed to the use of the quasi-static approximation in the formalism; physically speaking this singularity captures the electrostatic behavior of charges located on the semi-infinite surface [45] and is responsible for the static capacitance of structures. Another interesting observation is the existence in both plots of simple poles located at $s_x = \pm 0.31655510$ s/km. Poles do not always appear in Green's functions for arbitrary materials and orientations, but if a pole is observed in any one particular Green's function, it can also exist in all the Green's functions (note the pole residue or weight can be zero for some Green's functions if those particular fields that the Green's function describes are not coupled to the mode). In particular, the simple pole behavior represents the existence of a SAW mode that propagates in $\pm x$ directions. This mode satisfies the stress- and charge-free boundary conditions of the semi-infinite media problem. As to why the mode manifests as a simple pole, if one assumes the spatial-domain Green's function portion associated with the $\pm x$-traveling SAW is $\propto e^{\mp jk_o x}H(\pm x)$ (where k_o is the complex wavenumber of the SAW and H is the Heaviside step function),

then it can be shown, upon transformation into the spectral domain using (2.15) and taking the limit as SAW propagation loss goes to zero, that the spectral contribution of the $\pm x$-traveling SAW is $\propto \dfrac{1}{k \pm k_o}$. The assumptions made here are valid and appropriate since the far-field SAW behavior is captured and all materials in reality exhibit a finite degree of loss. Thus, if one identifies simple poles in a Green's function, a free surface SAW mode exists and will have phase velocity equal to the inverse of the slowness location for which the pole is encountered. (In this work SAW modes are identified numerically using a Green's function pole search algorithm.)

Yet another interesting observation from the Green's functions in Figure 2.4, though difficult to discern directly, involves derivative discontinuities at a finite number of slowness points; specifically, at $s_x = \pm 0.1739$, 0.1954, and 0.3031 s/km. Recalling Figure 2.1 these slowness points indicate where the normal to the slowness curve points along the s_x-axis. In other words, as one sweeps s_x these points occur when one or more of the semi-infinite media partial modes included in the analysis transition from decaying-type to bulk-type or vice-versa. Such points are called bulk-wave cut-off slowness points and are useful for setting lower slowness search bounds for a SAW mode, since, to prevent propagation loss, no true SAW solution can contain bulk-type partial modes.

For Green's functions calculations used to determine the existence of PSAW and HVPSAW modes, simple poles also appear as in a true SAW mode, though shifted into the complex s_x-plane to account for propagation-loss resulting from bulk-wave(s)

60

coupling. When the propagation-loss of PSAW and HVPSAW is very low, the pole is shifted only slightly off the real s_x-axis; as a result, the poles become more easily identifiable from the real s_x-axis. Bulk-wave cut-off slowness points prove useful for setting search bounds for PSAW and HVPSAW modes, which may lie between consecutive bulk-wave cut-off slowness points. In the Green's functions shown in Figure 2.4, a strong blip is observed near $s_x = 0.19620$, suggesting that a pole may be located nearby in the complex slowness plane. Also note that the blip lies between bulk-wave cut-off points, another clue that a complex pole may exist nearby. To verify whether the blip is indeed caused by a complex pole, a search in the complex-slowness plane is performed. If a simple pole is found in the complex plane then a PSAW or HVPSAW mode is identified satisfying the stress- and charge-free boundary conditions of the semi-infinite media problem; the phase velocity and propagation-loss of the mode are determined from the pole's location in the complex slowness plane. For example, Figure 2.5 shows the Green's function relating the T_5 and $j\omega u_3$ fields for the same quartz substrate and orientation considered above, evaluated in the complex slowness plane near the region of the observed blip. The same Green's function evaluated on the real s_x-axis is given for comparison. For the case involving complex slowness, the imaginary part of s_x is constant with respect to the real part and equal to -0.0002896739 s/km. Figure 2.5 shows that the blip observed on the purely real s_x-axis is indeed due to a complex simple pole located at $s_x = 0.1962022608 - 0.0002896739j$ s/km. This indicates the existence of a PSAW mode that exhibits propagation loss equal to -0.0805 dB/λ. The observed simple pole behavior associated with the PSAW can be seen in the other 15 Green's functions as well, but is not shown here to save space.
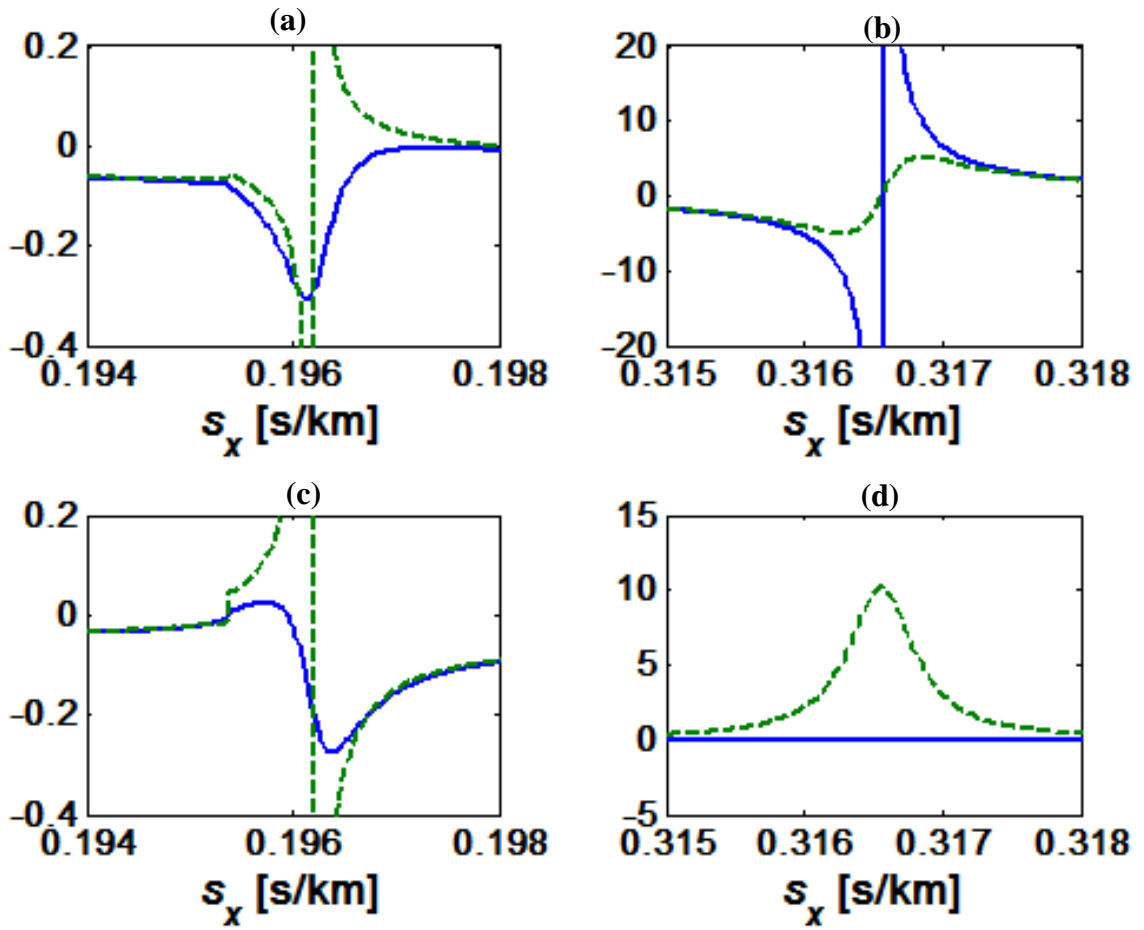
Figure 2.5. Real (a-b) and imaginary (c-d) components of spectral-domain Green's function for ST-X quartz, Euler Angles (0°, 132.75°, 0°) relating T_5 and $j\omega u_3$ fields; along real s_x-axis (solid), in the complex plane (dashed) with imaginary part of $s_x = -0.0002896739$ s/km. True SAW and PSAW simple poles are evident.

In addition, though difficult to see in Figure 2.5 (observed best in (c) for the dashed curve), the Green's functions display a discontinuity for the case of complex slowness located at real part of $s_x = 0.1954$ s/km, which corresponds to a bulk-wave cut-off slowness point. The bulk-wave cut-off slowness points define the starting points of branch cut-lines extending into the complex slowness plane of the Green's functions (lines where the Green's functions are multivalued and become discontinuous [78]). The

bulk-wave cut-off slowness points, or starting points of the branch cut-lines, may or may not be branch point singularities [78]. For instance, in the presented example none of the bulk-wave cut-off slowness points are branch point singularities, as the Green's functions are finite at these points. But such singularities may be encountered, for example in the case of the purely mechanical shear-horizontal Green's function relating T_4 and $j\omega u_2$ for the isotropic half-space problem. Such singular points satisfy the stress- and charge-free boundary conditions for a free surface and in literature are typically denoted as exceptional waves [79,80]. Although the singularity points satisfy the stress- and charge-free boundary condition, the mode structure associated with these singularities in the spatial-domain is fundamentally different than that of a purely propagating mode associated with a simple pole. In particular, this mode will have far-field amplitude $\propto \frac{1}{x^p}$, where $p > 0$. For example, again considering the purely mechanical shear-horizontal fields for an isotropic half-space, the spectral domain Green's function relating

T_4 to $j\omega u_2$ can be shown to be $-\dfrac{1}{c_{44}\sqrt{s_c^2 - s_x^2}}$ for $s_x^2 > s_c^2$ and $+\dfrac{1}{c_{44}\sqrt{s_c^2 - s_x^2}}$ for $s_x^2 < s_c^2$,

where $s_c^2 = \dfrac{\rho}{c_{44}}$ (-z half-space). Notice the branch point singularities at $s_x = \pm s_c$ indicating the existence of an exceptional wave. Using (2.17) it can be shown the resulting spatial-domain Green's function relating T_4 and u_2 fields is

$\dfrac{-j}{2c_{44}}\left(J_0(s_c|\omega x|) - jY_0(s_c|\omega x|)\right)$, where J_0 and Y_0 are the zero-order Bessel functions of the first and second kind respectively, which combine to form the conjugate of a Hankel function of the first kind. Using asymptotic approximations of Bessel functions, the

far-field u_2 field generated by a T_4 line-impulse located at $x = 0$ is given by

$\dfrac{-j}{c_{44}\sqrt{2\pi s_c |\omega x|}} e^{j\frac{\pi}{4}} e^{-js_c|\omega x|}$. Now notice that what is defined as an exceptional wave does not

propagate directly, but has amplitude that falls off as $\dfrac{1}{\sqrt{x}}$ in the far-field. In fact the

Green's function relating the pure shear fields in the isotropic half-space can be shown to

represent excitation of a pure shear cylindrical bulk wave in the semi-infinite isotropic

half-space. To the best of the author's knowledge, the analysis presented here for

explaining properties of exceptional waves based on pure shear horizontal wave

excitation in an isotropic half-space has not been previously reported in the literature.

Regarding other properties of Green's functions, for semi-infinite piezoelectric

media all Green's functions are $\propto \dfrac{1}{s_x}$ as $|s_x|$ becomes large. As a recap of the behavior

observed for Green's functions, Figure 2.6 shows some situations encountered regarding

behavior in the complex slowness plane.
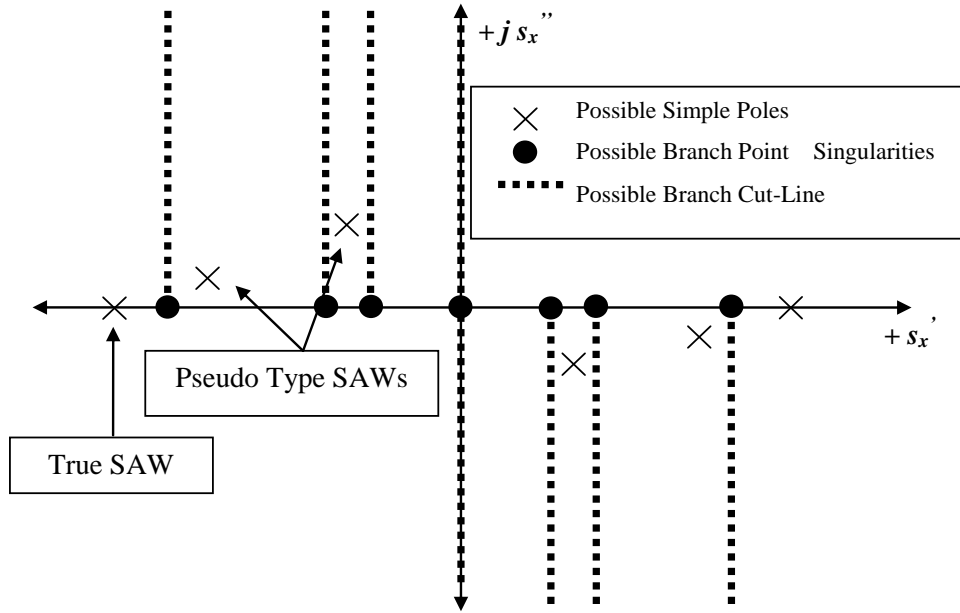
Figure 2.6. Possible structure of Green's functions in the complex slowness plane.

Using methods such as contour integration and residue theory [78], spatial-domain Green's functions can be determined from the spectral-domain Green's function structure given in Figure 2.6, by applying (2.17). To numerically compute such a transform, one must subtract out contributions due to singularities along integration paths and then add their respective analytical transforms to the numerically computed transform of the residual bound portion [45]. Lastly, it should be noted that simple poles in the inverse purely electric Green's function, $(G_{j\omega\phi\sigma}(s_x))^{-1}$, indicates the existence of a SAW mode that satisfies a stress-free and short-circuited electric potential boundary condition, which can be shown using a modified Green's function formalism that relates alterative field sets at the interface, e.g. functions that relate $\left[\overline{T}_5(x) \ \ \overline{T}_4(x) \ \ \overline{T}_3(x) \ \ \overline{E}_1(x) \right]^{\mathrm{T}}$ to

$$\left[\overline{u}_1(x) \ \ \overline{u}_2(x) \ \ \overline{u}_3(x) \ \ \int \overline{\sigma}(x)dx \right]^{\mathrm{T}} \text{[45,46]}.$$

2.5. Addition of Finite-Thickness Layers

In Section 2.4 the theoretical analysis of spectral-domain Green's function numerical computation was presented for a semi-infinite piezoelectric / stress-free dielectric (i.e. vacuum) media problem. It was shown that through evaluation of the spectral-domain Green's functions, propagating modes can be identified by locating poles in the complex slowness plane. In this subsection a similar analysis is presented that considers n homogeneous finite-thickness layers forming a sandwich structure between two semi-infinite media. Incorporating finite-thickness layers in acoustic wave (AW) devices finds many practical applications [81], including mode temperature compensation, mode trapping or guiding, improved IDT SAW mode transduction/detection, device passivation, and electromechanical coupling to non-piezoelectric media. Figure 2.7 shows the generalized body studied in this section.
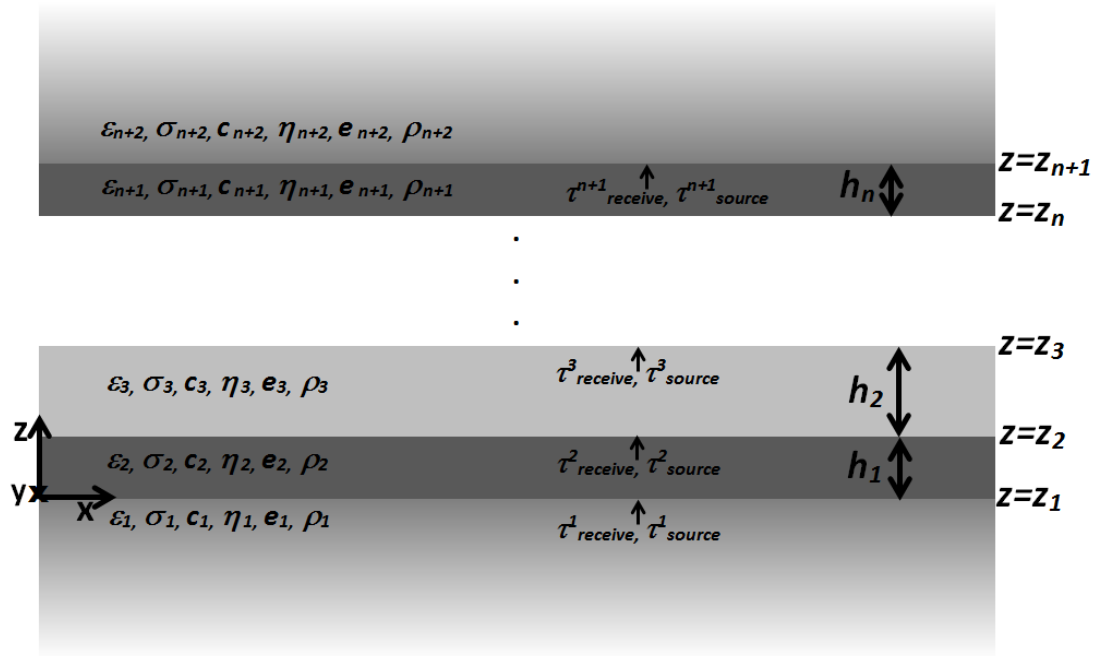
Figure 2.7. *n*-layer structure considered.

The structure in Figure 2.7 consists of n finite thickness layers sandwiched between two semi-infinite bodies, forming $n+1$ interfaces. Field vectors at the mth interface, denoted as $\boldsymbol{\tau}^m_{receive}$ and $\boldsymbol{\tau}^m_{source}$, are defined as

$$\boldsymbol{\tau}^m_{source} = \left[t_5(z_m) \quad t_4(z_m) \quad t_3(z_m) \quad \sigma(z_m) \right]^{\text{T}},$$

$$= \left[T_5(z_m^+) \quad T_4(z_m^+) \quad T_3(z_m^+) \quad D_3(z_m^+) \right]^{\text{T}} - \left[T_5(z_m^-) \quad T_4(z_m^-) \quad T_3(z_m^-) \quad D_3(z_m^-) \right]^{\text{T}},$$

and

$$\boldsymbol{\tau}^m_{recieve} = \left[j\omega u_1(z_m) \quad j\omega u_2(z_m) \quad j\omega u_3(z_m) \quad j\omega \phi(z_m) \right]^{\text{T}}.$$

The source vector represents interfacial stress and charge sources and provides structure excitation. The receive vector represents the continuous fields at the interface for any given source distribution. The results of the analysis presented in this section will yield the spectral-domain Green's functions of this system, denoted as $\mathbf{G}(k_x,\omega)$ and defined by

$$
\begin{bmatrix}
\boldsymbol{\tau}^1_{receive} \\
\boldsymbol{\tau}^2_{receive} \\
\vdots \\
\boldsymbol{\tau}^{n+1}_{receive}
\end{bmatrix}
= \mathbf{G}(k_x,\omega)
\begin{bmatrix}
\boldsymbol{\tau}^1_{source} \\
\boldsymbol{\tau}^2_{source} \\
\vdots \\
\boldsymbol{\tau}^{n+1}_{source}
\end{bmatrix}.
\tag{2.22}
$$

Note the dispersive nature of the problem due to finite thickness media. Using (2.15), the spatial-domain fields may be written in terms of the spatial-domain representation of the Green's functions, given by

$$
\begin{bmatrix}
\overline{\boldsymbol{\tau}^1_{receive}}(x) \\
\overline{\boldsymbol{\tau}^2_{receive}}(x) \\
\vdots \\
\overline{\boldsymbol{\tau}^{n+1}_{receive}}(x)
\end{bmatrix}
= \int_{-\infty}^{\infty} \overline{\mathbf{G}}(x-x',\omega)
\begin{bmatrix}
\overline{\boldsymbol{\tau}^1_{source}}(x') \\
\overline{\boldsymbol{\tau}^2_{source}}(x') \\
\vdots \\
\overline{\boldsymbol{\tau}^{n+1}_{source}}(x')
\end{bmatrix} dx',
\tag{2.23}
$$

where:

- $\overline{\mathbf{G}}(x,\omega) = \dfrac{1}{2\pi} \int_{-\infty}^{\infty} \mathbf{G}(k_x,\omega) e^{-jk_x x} dk_x$.

67

Based on (2.23), AW device analysis can be performed using BEM and FEM techniques for the *n*-layer structure considered. In other words, analysis may be performed for arbitrarily positioned infinitesimally thin perfect conducting electrodes and stress sources located at any interface subject to electric potential and displacement boundary conditions.

Now that the problem has been defined, attention will be turned to numerical analysis of the spectral-domain Green's function for the *n*-layer system. Considering the first material, $m = 1$ (i.e. semi-infinite substrate extending to $-\infty$), based on results derived in Sections 2.3 and 2.4, the field relationships at the first interface are given by

$$\left[T_5\left(z_1^-\right) \quad T_4\left(z_1^-\right) \quad T_3\left(z_1^-\right) \quad D_3\left(z_1^-\right)\right]^{\mathrm{T}} = \mathbf{G}_{neg}^{-1}\boldsymbol{\tau}_{receive}^1, \tag{2.24}$$

where:

- $\mathbf{P}_n$ is the eigenvector matrix for the nth material,
- $\mathbf{G}_{neg}^{-1} = \mathbf{P}_1\left(1:4, indsKept\right)\cdot\left(\mathbf{P}_1\left(5:8, indsKept\right)\right)^{-1}$ (Matlab index notation),
- and *indsKept* is the vector indices of the valid partial-modes included.

Next, the field relationships at opposite sides of finite-thickness layers are computed, given as $\mathbf{H}_m$ in (2.25), for the layers $m = 1$ to n:

$$\mathbf{H}_m = \begin{bmatrix} \mathbf{P}_{m+1}(1:4,:) \\ \mathbf{P}_{m+1}(1:4,:) \cdot e^{j\omega \mathbf{J}_{m+1} h_m} \end{bmatrix} \begin{bmatrix} \mathbf{P}_{m+1}(5:8,:) \\ \mathbf{P}_{m+1}(5:8,:) \cdot e^{j\omega \mathbf{J}_{m+1} h_m} \end{bmatrix}^{-1} \tag{2.25}$$

(Matlab index notation),

where:

- $\begin{bmatrix} T_5(z_m^+) & T_4(z_m^+) & T_3(z_m^+) & D_3(z_m^+) & T_5(z_{m+1}^-) & T_4(z_{m+1}^-) & T_3(z_{m+1}^-) & D_3(z_{m+1}^-) \end{bmatrix}^{\mathrm{T}} =$

$\mathbf{H}_m \begin{bmatrix} \begin{bmatrix} \boldsymbol{\tau}_{receive}^m \end{bmatrix}^{\mathrm{T}} & \begin{bmatrix} \boldsymbol{\tau}_{receive}^{m+1} \end{bmatrix}^{\mathrm{T}} \end{bmatrix}^{\mathrm{T}}$,

- $\begin{bmatrix} \begin{bmatrix} \boldsymbol{\tau}_{receive}^m \end{bmatrix}^{\mathrm{T}} & \begin{bmatrix} \boldsymbol{\tau}_{receive}^{m+1} \end{bmatrix}^{\mathrm{T}} \end{bmatrix}^{\mathrm{T}} = \begin{bmatrix} \mathbf{P}_{m+1}(5:8,:) \\ \mathbf{P}_{m+1}(5:8,:) \cdot e^{j\omega \mathbf{J}_{m+1} h_m} \end{bmatrix}_{8x8} \mathbf{c}_{m+1}$,

- $\begin{bmatrix} T_5(z_m^+) & T_4(z_m^+) & T_3(z_m^+) & D_3(z_m^+) & T_5(z_{m+1}^-) & T_4(z_{m+1}^-) & T_3(z_{m+1}^-) & D_3(z_{m+1}^-) \end{bmatrix}^{\mathrm{T}} =$

$\begin{bmatrix} \mathbf{P}_{m+1}(1:4,:) \\ \mathbf{P}_{m+1}(1:4,:) \cdot e^{j\omega \mathbf{J}_{m+1} h_m} \end{bmatrix}_{8x8} \mathbf{c}_{m+1}$.

It is important to mention that numerical evaluation of (2.25) can become unstable due to the matrix exponential terms and that fact that $\mathbf{J}$ will contain eigenvalues corresponding to growing and decaying partial modes. In this work (2.25) was computed numerically by factoring the exponential matrix into two diagonal-matrix factors, namely decaying and non-decaying factors with respect to layer thickness, given as $\mathbf{R}$ and $\mathbf{T}$, respectively, such that $e^{j\omega \mathbf{J}_{m+1} h_m} = \mathbf{RT}$.

Equation (2.25) can be rewritten as

$$\mathbf{H}_m = \begin{bmatrix} \mathbf{P}_{m+1}(1:4,:)\mathbf{T}^{-1} \\ \mathbf{P}_{m+1}(1:4,:)\mathbf{R} \end{bmatrix} \mathbf{TT}^{-1} \begin{bmatrix} \mathbf{P}_{m+1}(5:8,:)\mathbf{T}^{-1} \\ \mathbf{P}_{m+1}(5:8,:)\mathbf{R} \end{bmatrix}^{-1}$$
$$= \begin{bmatrix} \mathbf{P}_{m+1}(1:4,:)\mathbf{T}^{-1} \\ \mathbf{P}_{m+1}(1:4,:)\mathbf{R} \end{bmatrix} \begin{bmatrix} \mathbf{P}_{m+1}(5:8,:)\mathbf{T}^{-1} \\ \mathbf{P}_{m+1}(5:8,:)\mathbf{R} \end{bmatrix}^{-1},$$

(2.26)

which is numerically more stable as $\mathbf{T}^{-1}$ can be computed using simple analytical expressions and given that the matrix inverse term is better conditioned for acoustically thick layers. Next, the semi-infinite substrate extending to $+\infty$ is considered, yielding the field relationships for the $n+1$ interface, given as

$$\begin{bmatrix} T_5(z_{n+1}^+) & T_4(z_{n+1}^+) & T_3(z_{n+1}^+) & D_3(z_{n+1}^+) \end{bmatrix}^{\mathrm{T}} = \mathbf{G}_{pos}^{-1}\boldsymbol{\tau}_{receive}^{n+1},$$

(2.27)

where:

- $\mathbf{G}_{pos}^{-1} = \mathbf{P}_{n+2}(1:4, indsKept)(\mathbf{P}_{n+2}(5:8, indsKept))^{-1}$ (Matlab index notation),

- and *indsKept* is the indices of the valid partial-modes included.

Note that if either of the two semi-infinite materials is stress-free media, e.g. vacuum, the media is first treated as an isotropic material with arbitrarily chosen c_{11}, c_{44}, and ρ to make use of developed software routines for arbitrary media. Furthermore, all elements of $\mathbf{G}^{-1}_{neg}$ or $\mathbf{G}^{-1}_{pos}$ are set to zero except the element relating the electrical quantities, i.e. $\mathbf{G}^{-1}_{neg}(4,4)$ and $\mathbf{G}^{-1}_{pos}(4,4)$.

The interface source vectors are given by

If $n > 0$

- $\boldsymbol{\tau}_{source}^1 = \left[\left(\mathbf{H}_1^{11} - \mathbf{G}_{neg}^{-1}\right) \quad \mathbf{H}_1^{12}\right]\left[\left[\boldsymbol{\tau}_{receive}^1\right]^{\mathrm{T}} \quad \left[\boldsymbol{\tau}_{receive}^2\right]^{\mathrm{T}}\right]^{\mathrm{T}}$

- for $m = 2$ to n

$$\boldsymbol{\tau}_{source}^m = \left[-\mathbf{H}_{m-1}^{21} \quad \left(\mathbf{H}_m^{11} - \mathbf{H}_{m-1}^{22}\right) \quad \mathbf{H}_m^{12}\right]\left[\left[\boldsymbol{\tau}_{receive}^{m-1}\right]^{\mathrm{T}} \quad \left[\boldsymbol{\tau}_{receive}^m\right]^{\mathrm{T}} \quad \left[\boldsymbol{\tau}_{receive}^{m+1}\right]^{\mathrm{T}}\right]^{\mathrm{T}} \quad (2.28)$$

- $\boldsymbol{\tau}_{source}^{n+1} = \left[-\mathbf{H}_n^{21} \quad \left(\mathbf{G}_{pos}^{-1} - \mathbf{H}_n^{22}\right)\right]\left[\left[\boldsymbol{\tau}_{receive}^n\right]^{\mathrm{T}} \quad \left[\boldsymbol{\tau}_{receive}^{n+1}\right]^{\mathrm{T}}\right]^{\mathrm{T}}$

If $n = 0$

- $\boldsymbol{\tau}_{source}^1 = \left(\mathbf{G}_{pos}^{-1} - \mathbf{G}_{neg}^{-1}\right)\boldsymbol{\tau}_{receive}^1$

where:

- $\left(\mathbf{H}_m\right)_{8x8} = \begin{bmatrix} \left(\mathbf{H}_m^{11}\right)_{4x4} & \left(\mathbf{H}_m^{12}\right)_{4x4} \\ \left(\mathbf{H}_m^{21}\right)_{4x4} & \left(\mathbf{H}_m^{22}\right)_{4x4} \end{bmatrix}$.

Using (2.28), the n-layer system inverse Green's function, given by

$$\begin{bmatrix} \boldsymbol{\tau}_{source}^1(k_x) \\ \boldsymbol{\tau}_{source}^2(k_x) \\ \vdots \\ \boldsymbol{\tau}_{source}^{n+1}(k_x) \end{bmatrix} = \mathbf{G}^{-1}(k_x, \omega) \cdot \begin{bmatrix} \boldsymbol{\tau}_{receive}^1(k_x) \\ \boldsymbol{\tau}_{receive}^2(k_x) \\ \vdots \\ \boldsymbol{\tau}_{receive}^{n+1}(k_x) \end{bmatrix}, \quad (2.29)$$

may be constructed. The system Green's function may be computed by a matrix inversion if desired.

For standard applications, stress source terms are zero (normal components of stress are continuous) at interfaces between any two solid media, but are not assumed as such herein to account for possible finite stresses located at interfaces between a solid and vacuum produced by placing finite electrodes at the interface. This situation is required

for BEM coupling to finite electrode FEM analysis, as discussed in Section 2.6. Other interface boundary conditions may be applied to the n-layer system as well, such as the addition of perfect conducting infinitesimally thin ground planes (shorted interfaces) or the absence in one or more layers of infinitesimally thin charges (open interfaces), which results in setting interface electric potential or charge sources to zero, respectively. As with the treatment of the vacuum / semi-infinite piezoelectric problem in Section 2.4, allowable modes for the structure are identified through simple-pole searching of the modified Green's functions that have taken into account the imposed boundary conditions (e.g. shorted or open interfaces).

2.6. Finite FEM/BEM Model Theory

The FEM/BEM model implemented in this work and used for the simulation of finite length electrical structures atop a semi-infinite piezoelectric body is based on original works as reported in [45,46 ,82]. In [45] a BEM model was reported for the simulation of finite-length electrical structures atop a semi-infinite piezoelectric, which factored in SAW, BAW, and evanescent mode excitation and detection (a full-wave simulation tool), but the mechanical loading of the electrodes was neglected, which is usually a good first-order approximation when electrodes are very thin relative to wavelength, the substrate has relatively high piezoelectric coupling, and electrode materials have similar acoustic properties as the substrate (i.e. similar stiffness and density). In later reports [46,82] models were extended to include the mass/stiffness of the loading effects of electrodes in order to improve model accuracy, based on FEM modeling of electrodes coupled to the BEM substrate model. Interest in including the

FEM extension to BEM models increased as the benefits of using thicker and more exotic substrate and/or electrode materials were discovered (e.g. increased mode trapping and electrode reflectivity, improved device temperature compensation). The primary difference between [46] and [82] was in the method whereby the electrode/substrate interfacial charge density and stress were represented. In [82] the to-be-determined interfacial charge and stress at interfaces are represented by weighted rectangular pulses, whereas, in [46], the to-be-determined interfacial charge and stress at particular substrate/electrode interfaces are represented by weighted orthogonal Chebyshev polynomials of the first kind. The latter technique proved more efficient than the first due to the reduced number of global unknowns required for achieving solution convergence. For this reason the particular basis function for charge and stress representation reported in [46] was implemented in this work, although herein a novel FEM/BEM theoretical model is presented that is independent of basis function choice. Thus, implementation of other basis functions, which may be found more efficiently numerically for a particular problem, can easily be implemented without re-deriving the entire model. Also new to this work, as discussed in this section, is inclusion of possible incident free-surface mode analysis on finite structures that incorporate effects of mass/stiffness electrode loading. This extension allows directed scattering parameter extraction for arbitrary structures, which may be used in conjunction with simpler and more rapid simulation models such as equivalent-circuit, coupling of modes (COM), and P-matrix models [83,44]. While this capability was added, it was not deployed for this project. It has however found uses in projects, e.g. for the design of resonators in UMaine's current high-temperature harsh-environment sensor research project.

The following arbitrary-basis-function FEM/BEM theoretical analysis assumes that all fields follow sinusoidal time variation, given as $e^{j\omega t}$; that field variation is limited only along the x- and z- directions; and that all basis functions have existent Fourier transforms (i.e. a spatial- to spectral- domain representation). In Section 2.4 it was shown that spectral-domain Green's functions relate spectral components of interfacial stress and charge to interfacial time derivative displacement and electric potential (cf. (2.16)). Using the definition of Fourier transform pair in (2.15), the spatial-domain representation of displacement and electric potential may be given as

$$\left[\overline{u_1}(x) \quad \overline{u_2}(x) \quad \overline{u_3}(x) \quad \overline{\phi}(x)\right]^{\mathrm{T}} = \frac{1}{j\omega} \int_{-\infty}^{\infty} \mathbf{G}\left(\frac{k_x}{\omega}\right) \left[T_5(k_x) \quad T_5(k_x) \quad T_5(k_x) \quad \sigma(k_x)\right]^{\mathrm{T}} e^{-jk_x x} dk_x \ . \tag{2.30}$$

Equation (2.30) represents the driven response of the system, but does not include possible incident free-surface SAW, PSAW, and HVPSAW mode contributions, which have no associated surface normal stress or charge, but do have associated surface displacement and electric potential. To include incident mode analysis into the model, the left-hand-side of (2.30) must also include the terms:

$$\sum_m A_m^+ \mathbf{v}_m^+ e^{-jk_o^m x} + \sum_m A_m^- \mathbf{v}_m^- e^{jk_o^m x}, \tag{2.31}$$

where:

- A_m^+ is the complex valued electric potential at $x = 0$ for the mth free-surface mode traveling in the $+x$ direction,

- A_m^- is the complex valued electric potential at $x = 0$ for the mth free-surface mode traveling in the $-x$ direction,

- $\mathbf{v}^{m+}$ is the vector $\left[\dfrac{u_1(x=0)}{\phi(x=0)} \quad \dfrac{u_2(x=0)}{\phi(x=0)} \quad \dfrac{u_3(x=0)}{\phi(x=0)} \quad 1 \right]^{\text{T}} = \left[v_1^{m+} \quad v_2^{m+} \quad v_3^{m+} \quad v_4^{m+} \right]^{\text{T}}$ at the interface associated with the mth free-surface mode traveling in the $+x$ direction,

- $\mathbf{v}^{m-}$ is the vector $\left[\dfrac{u_1(x=0)}{\phi(x=0)} \quad \dfrac{u_2(x=0)}{\phi(x=0)} \quad \dfrac{u_3(x=0)}{\phi(x=0)} \quad 1 \right]^{\text{T}} = \left[v_1^{m-} \quad v_2^{m-} \quad v_3^{m-} \quad v_4^{m-} \right]^{\text{T}}$ at the interface associated with the mth free-surface mode traveling in the $-x$ direction,

- and k_o^m is the complex wavenumber for the mth free-surface mode.

Given these equations, the first step in the BEM analysis for the semi-infinite body is to discretize the problem so as to solve the system of integral equations given by (2.30) with the inclusion of the terms in (2.31) on the left-hand-side. The spatial-domain representation of interfacial stress and charge density are represented by finite sums of arbitrary basis functions; note that any particular basis function is assumed non-zero over one electrode/substrate interface. The total spatial-domain interface stress and charge is now given by:

75

$$\overline{T}_5(x) = \sum_{s=1}^{N_1} w_1^s \overline{f}_1^s(x)$$,

$$\overline{T}_4(x) = \sum_{s=1}^{N_2} w_2^s \overline{f}_2^s(x)$$,

(2.32)

$$\overline{T}_3(x) = \sum_{s=1}^{N_3} w_3^s \overline{f}_3^s(x)$$,

$$\overline{\sigma}(x) = \sum_{s=1}^{N_4} w_4^s \overline{f}_4^s(x)$$,

where:

- N_p is the total number of basis functions for the pth source field,

- w_p^s is the sth basis function's unknown weight for the pth source field,

- and $\overline{f}_p^s$ is the sth basis function spatial-domain representation for the pth source field.

Using the linearity property of the Fourier transform, the spectral-domain representation of (2.32) is given by

$$T_5(k_x) = \sum_{s=1}^{N_1} w_1^s f_1^s(k_x)$$,

$$T_4(k_x) = \sum_{s=1}^{N_2} w_2^s f_2^s(k_x)$$,

(2.33)

$$T_3(k_x) = \sum_{s=1}^{N_3} w_3^s f_3^s(k_x)$$,

$$\sigma(k_x) = \sum_{s=1}^{N_4} w_4^s f_4^s(k_x)$$.

The number of total unknowns for the problem now equals the total number of basis function weights, given by $N = N_1 + N_2 + N_3 + N_4$. To form a solvable square matrix

system, N equations are formed using (2.30). In particular, a Galerkin variational method [84] is used to form the N equations by multiplying (2.30), including (2.31), by the same N basis functions used for stress and charge representation, followed by integrating the result over the entire interface. Substituting (2.33) into (2.30), including (2.31) and applying the Galerkin variational method yields the square matrix system of equations:

$$
\begin{bmatrix} \mathbf{c}_1 \\ \mathbf{c}_2 \\ \mathbf{c}_3 \\ \mathbf{c}_4 \end{bmatrix} - \sum_m A_m^+ \begin{bmatrix} \mathbf{p}_1^{m+} \\ \mathbf{p}_2^{m+} \\ \mathbf{p}_3^{m+} \\ \mathbf{p}_4^{m+} \end{bmatrix} - \sum_m A_m^- \begin{bmatrix} \mathbf{p}_1^{m-} \\ \mathbf{p}_2^{m-} \\ \mathbf{p}_3^{m-} \\ \mathbf{p}_4^{m-} \end{bmatrix} = \begin{bmatrix} \mathbf{Y}_{11} & \mathbf{Y}_{12} & \mathbf{Y}_{13} & \mathbf{Y}_{14} \\ \mathbf{Y}_{21} & \mathbf{Y}_{22} & \mathbf{Y}_{23} & \mathbf{Y}_{24} \\ \mathbf{Y}_{31} & \mathbf{Y}_{32} & \mathbf{Y}_{33} & \mathbf{Y}_{34} \\ \mathbf{Y}_{41} & \mathbf{Y}_{42} & \mathbf{Y}_{43} & \mathbf{Y}_{44} \end{bmatrix} \begin{bmatrix} \mathbf{w}_1 \\ \mathbf{w}_2 \\ \mathbf{w}_3 \\ \mathbf{w}_4 \end{bmatrix}, \tag{2.34}
$$

where:

- $\mathbf{c}_n = \begin{bmatrix} c_n^1 & c_n^2 & \dots & c_n^{N_n} \end{bmatrix}^{\mathrm{T}}$ where,

$$
c_n^r = \int_{-\infty}^{\infty} \bar{f}_n^r(x) g_n(x) dx = \int_{\Gamma_{nr}} \bar{f}_n^r(x) g_n(x) dx, \text{where } \Gamma_{nr} \text{ is the non-zero contour of } \bar{f}_n^r(x)
$$

and $g_1(x) = u_1(x),\ g_2(x) = u_2(x),\ g_3(x) = u_3(x),\ g_4(x) = \phi(x),$

- $\mathbf{p}_n^{m+} = \begin{bmatrix} p_n^{1m+} & p_n^{2m+} & \dots & p_n^{N_n m+} \end{bmatrix}^{\mathrm{T}}$ (incident mode portion: $+x$ traveling) where,

$$
p_n^{rm+} = v_n^{m+} \int_{\Gamma_{nr}} \bar{f}_n^r(x) e^{-jk_o^m x} dx = 2\pi\, v_n^{m+} f_n^r\!\left(-k_o^m\right),
$$

- $\mathbf{p}_n^{m-} = \begin{bmatrix} p_n^{1m-} & p_n^{2m-} & \dots & p_n^{N_n m-} \end{bmatrix}^{\mathrm{T}}$ (incident mode portion: $-x$ traveling) where,

$$
p_n^{rm-} = v_n^{m-} \int_{\Gamma_{nr}} \bar{f}_n^r(x) e^{jk_o^m x} dx = 2\pi\, v_n^{m-} f_n^r\!\left(k_o^m\right),
$$

- $\mathbf{w}_n = \begin{bmatrix} w_n^1 & w_n^2 & \dots & w_n^{N_n} \end{bmatrix}^{\mathrm{T}},$

- $\mathbf{Y}_{mn} = \begin{bmatrix} Y_{mn}^{11} & Y_{mn}^{12} & \cdots & Y_{mn}^{1N_n} \\ Y_{mn}^{21} & Y_{mn}^{22} & \ddots & \vdots \\ \vdots & \ddots & \ddots & \vdots \\ Y_{mn}^{N_m 1} & \cdots & \cdots & Y_{mn}^{N_m N_n} \end{bmatrix}$ where

$$
Y_{mn}^{rs} = \frac{2\pi}{j\omega} \int_{-\infty}^{\infty} G_{mn}\!\left(\frac{k_x}{\omega}\right) f_m^r(-k_x) f_n^s(k_x)\, dk_x = -2\pi j \int_{-\infty}^{\infty} G_{mn}(s_x) f_m^r(-\omega s_x) f_n^s(\omega s_x)\, ds_x.
$$

Generally the most time consuming and numerically challenging aspect of BEM analysis is evaluating the $\mathbf{Y}_{mn}$ matrix elements. The computation requires numerical evaluation of many integrals having infinite limits and integrands that may contain poles, display rapid oscillatory behavior, and converge slowly with increasing integration limits. Also, as devices to be simulated become larger, the number of basis functions increases; so the

number of integrations required (and so the simulation time) tends to be proportional to the square of the total number of basis functions. Rapidly converging basis functions sets are desirable in order to reduce the problem size while achieving adequate convergence. Semi-periodic structures tend to be faster to evaluate as many of the integrations are repeated and thus only need to be performed once. Also, slowness symmetry in the Green's function matrix and Green's functions themselves can be recognized quite often, further reducing the number of integrations required. In this work the model implemented minimizes the number of required integration evaluations by identifying repeated integrals. The integration method adopted in this work is discussed in Appendix B and assumes the same basis function set used for charge and stress as in [46].

Once the $\mathbf{Y}_{mn}$ elements have been computed, attention is turned to the evaluation of $\mathbf{c}_n$. The evaluation of entries of $\mathbf{c}_4$ is considered first, which involves computing integrals over an electrode's domain with integrands being each charge basis function multiplied by the corresponding basis function electrode's electric potential. In general, the absolute electric potential is never specified in a circuit; instead, reference potentials are applied by setting some electrode(s) to ground and others to be either floating or driven with defined potential difference between themselves and a ground. In order to apply this rule to the BEM model, the electric potential is rewritten as $\phi(x) = \phi_o + v(x)$, where ϕ_o is unknown reference potential with respect to a grounded electrode reference and $v(x)$ is the voltage potential difference with respect to the grounded electrodes. Substituting this form for electric potential into (2.34) introduces another unknown to the system, i.e. ϕ_o. To maintain a square matrix system, an additional equation is needed.

The selected equation ensures that the total sourcing charge at the interface is zero, which is another way of saying that the current entering the circuit equals the current exiting, since current density is equal to $j\omega\sigma$ under time harmonic excitation. As a result, it can be shown that $\sigma(k_x = 0) = \sum_{s=1}^{N_4} w_4^s f_4^s (k_x = 0) = 0$ by evaluating (2.15) at $k_x = 0$ and applying (2.33). This relationship, which included in the system of equations (2.34), is used in a novel way for evaluating the electrostatic singularity contribution to the $\mathbf{Y}_{44}$ elements by canceling the non-simple pole ($1/|s_x|$) behavior in the integrand near $s_x = 0$, thereby permitting evaluation by numerical integration. (Details of this analysis are presented in Appendix B.) If floating electrodes are included in the structure, more unknowns are introduced—namely the electrodes' respective voltages. As in the previous case, equations are added to maintain a square system. These equations can be constructed by stipulating that the total charge on each floating electrode is equal to zero, so that no net current enters or leaves a floating electrode.

Evaluation of $\mathbf{c}_1$, $\mathbf{c}_2$, and $\mathbf{c}_3$, is now considered. Evaluating these elements involve integrals of basis functions and electrode/interface displacement components, which cannot be found directly. For this situation a FEM analysis of the mechanical electrode effects is performed, relating the interface stress basis functions to $\mathbf{c}_1$, $\mathbf{c}_2$, and $\mathbf{c}_3$, given by

$$\begin{bmatrix} \mathbf{c}_1 \\ \mathbf{c}_2 \\ \mathbf{c}_3 \end{bmatrix} = \begin{bmatrix} \mathbf{F}_{11} & \mathbf{F}_{12} & \mathbf{F}_{13} \\ \mathbf{F}_{21} & \mathbf{F}_{22} & \mathbf{F}_{23} \\ \mathbf{F}_{31} & \mathbf{F}_{32} & \mathbf{F}_{33} \end{bmatrix} \begin{bmatrix} \mathbf{w}_1 \\ \mathbf{w}_2 \\ \mathbf{w}_3 \end{bmatrix}. \tag{2.35}$$

The FEM analysis theory yielding (2.35) is discussed in Appendix D. Combining (2.35) and the additional equations regarding charge conservation and unknown potentials with (2.34) yields the final system of equations to be solved:

$$
\begin{bmatrix} \mathbf{0} \\ \mathbf{0} \\ \mathbf{0} \\ \mathbf{c}'_4 \\ \mathbf{0} \end{bmatrix} - \sum_m A_m^+ \begin{bmatrix} \mathbf{p}_1^{m+} \\ \mathbf{p}_2^{m+} \\ \mathbf{p}_3^{m+} \\ \mathbf{p}_4^{m+} \\ \mathbf{0} \end{bmatrix} - \sum_m A_m^- \begin{bmatrix} \mathbf{p}_1^{m-} \\ \mathbf{p}_2^{m-} \\ \mathbf{p}_3^{m-} \\ \mathbf{p}_4^{m-} \\ \mathbf{0} \end{bmatrix} = \begin{bmatrix} \mathbf{Y}_{11}-\mathbf{F}_{11} & \mathbf{Y}_{12}-\mathbf{F}_{12} & \mathbf{Y}_{13}-\mathbf{F}_{13} & \mathbf{Y}_{14} & \mathbf{0} \\ \mathbf{Y}_{21}-\mathbf{F}_{21} & \mathbf{Y}_{22}-\mathbf{F}_{22} & \mathbf{Y}_{21}-\mathbf{F}_{23} & \mathbf{Y}_{24} & \mathbf{0} \\ \mathbf{Y}_{31}-\mathbf{F}_{31} & \mathbf{Y}_{32}-\mathbf{F}_{32} & \mathbf{Y}_{33}-\mathbf{F}_{33} & \mathbf{Y}_{34} & \mathbf{0} \\ \mathbf{Y}_{41} & \mathbf{Y}_{42} & \mathbf{Y}_{43} & \mathbf{Y}_{44} & \mathbf{Z}^{\mathrm{T}} \\ \mathbf{0} & \mathbf{0} & \mathbf{0} & \mathbf{Z} & \mathbf{0} \end{bmatrix} \begin{bmatrix} \mathbf{w}_1 \\ \mathbf{w}_2 \\ \mathbf{w}_3 \\ \mathbf{w}_4 \\ -\boldsymbol{\varphi} \end{bmatrix}, \quad (2.36)
$$

where:

- $\mathbf{c}'_4 = \begin{bmatrix} c'^1_n & c'^2_n & \cdots & c'^{N_4}_n \end{bmatrix}^{\mathrm{T}}$, and

$$
c'^r_4 = \int_{-\infty}^{\infty} \bar{f}_4^r(x)v(x)\,dx = \int_{\Gamma_{4r}} \bar{f}_4^r(x)v(x)\,dx = 2\pi\, v(x=\Gamma_{4r})f_4^r(k_x=0), \ \Gamma_{4r} \text{ is non-zero}
$$

domain of $\bar{f}_4^r(x)$, where $v(x=\Gamma_{4r})$ is set equal to zero if r corresponds to a floating or grounded electrode (floating electrode voltage accounted for on right-hand-side),

- $\mathbf{Z}$ is matrix accounting for charge conservation on total system and floating electrodes, where:

$$
\mathbf{Z} = \begin{bmatrix} \mathbf{Z}_{total} \\ \mathbf{Z}^1_{floating} \\ \vdots \\ \mathbf{Z}^{N_f}_{floating} \end{bmatrix}, \text{ and } N_f \text{ is the number of floating electrodes,}
$$

$$
\mathbf{Z}_{total} = \begin{bmatrix} 2\pi f_4^1(k_x=0) & 2\pi f_4^2(k_x=0) & \cdots & 2\pi f_4^{N_4}(k_x=0) \end{bmatrix},
$$

and $\mathbf{Z}^i_{floating}$ is the same form as $\mathbf{Z}_{total}$, but with terms set to zero if the column's corresponding basis function's domain does not correspond to the ith floating electrode's domain,

- and $\boldsymbol{\varphi}$ is the vector containing the reference electric potential and floating electrode voltages relative to ground, given by

$$
\boldsymbol{\varphi} = \begin{bmatrix} \phi_o & v^1_{floating} & \cdots & v^{N_f}_{floating} \end{bmatrix}^{\mathrm{T}},
$$

(Note that if no floating electrode are present the $\mathbf{Z}_{floating}$ and $v_{floating}$ terms are not including in the overall matrix system).

82

It may be appropriate to scale **Z** to improve the condition of the overall matrix, and doing so only inversely scales the unknown potential vector. Once system (2.36) is constructed, the basis function weights and unknown potential terms can be determined using techniques of linear algebraic analysis, subject to the structure boundary conditions and/or exciting incident mode(s). Knowing the basis function weights and potential terms allows the stress and charge distribution at an electrode/substrate interface to be determined, and from which total currents entering electrodes can be determined and therefore electrical impedance. In addition the basis functions weights also allow calculation of far-field parameters, such as exited SAW magnitude, phase and power, and excited BAW power and radiation pattern (see Appendix C). Such analyses are useful for evaluating expected performance of liquid-phase sensor platforms and will be discussed in greater detail in Chapter 3.

2.7. Periodic FEM/BEM Model Theory

In this section the FEM/BEM model used in this work for simulation of periodic electrode structures atop a piezoelectric half-space is discussed. The assumptions of Section 2.6 apply here, except that for the current case the electrode structures at the interface are required to be spaced periodically and extend infinitely in each direction (though the applied electrical signals in the structure are not necessarily periodic). This requirement permits evaluation of designs consisting of finite IDTs surrounded by synchronous grating electrodes extending infinitely in both directions. Attempting to model such a structure using the finite model presented in Section 2.6 would generate an infinite problem statement, since charge and stress at all interfaces must be considered.

The modeling theory presented here is based on methods presented in [57,59,58]. The method used in [57] involves a periodic grating mode dispersion analysis carried out using a periodic model permitting evaluation of stopband characteristics for short- and open- circuit gratings. The charge density of electrodes is expressed using a Chebyshev basis to accurately capture the singularity behavior of charges near electrode edges. However, the model neglects the mass loading of electrodes. In [59] the characteristics of harmonic and mutual admittances are studied. The method allows grating mode contributions to harmonic and mutual admittances to be separated from other effects such as BAW. But again, the effect of mass loading by electrodes is neglected. In [58] a model for harmonic and mutual admittances is presented which includes mass/stiffness loading effects of electrodes and also considers charge and stress basis functions of Chebyshev polynomials. In this case, however, the excitation efficiency of finite length transducers is not investigated.

The work of this dissertation combines and extends these models into a novel suite of useful tools suitable for studying transducer excitation efficiency of finite length transducers for SHSAW grating modes as a function of electrode thickness, using a periodic model for grating mode dispersion that expresses electrode charge density on a Chebyshev basis, incorporates charge and stress basis functions of Chebyshev polynomials, distinguishes mode contributions to harmonic and mutual admittances from BAW and other effects, and includes mass/stiffness loading effects of electrodes. The resulting model is designed for analyzing SHSAW liquid phase sensor platforms and is independent of basis function choice, a functionality that does not yet appear in the

literature. The significance of the novelty of the presented model can be seen by noting that, whenever better-suited basis functions are determined, the functions can be rapidly applied to the model without re-deriving the model theory. Another benefit of the presented model is that it allows the study of multiple, arbitrary-shaped electrodes per period, whereby single-phase unidirectional transducer (SPUDT) structures can be analyzed. SPUDT structures often have two or more electrodes with unequal dimensions per period.

Consider an infinite periodic structure with arbitrary electrode geometries per period driven harmonically such that, for any position in the structure, in the distance of one period, p, the applied voltage and current (V and I) are phase shifted by an amount $-2\pi\gamma$ (see Figure 2.8).
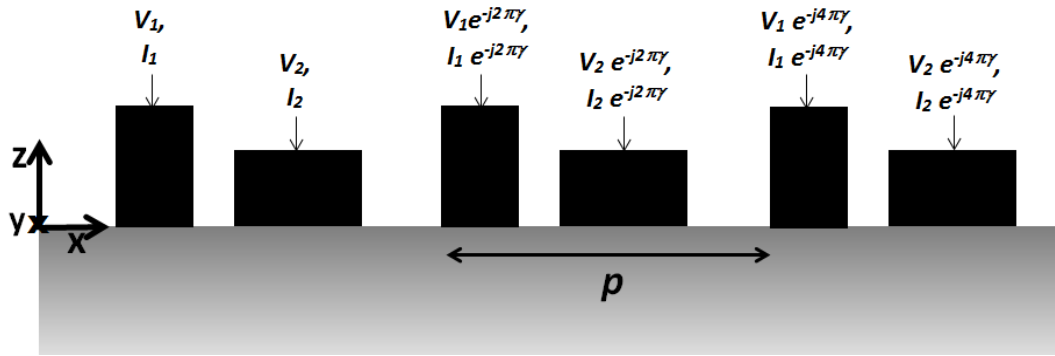
Figure 2.8. Infinite periodic structure considered driven harmonically.

According to Floquet theory [44], all fields in the structure follow an x spatial dependence of $e^{-j\beta x}$, where $\beta = \dfrac{2\pi\gamma}{p}$. As a result, multiplying any field in the material by $e^{-j\beta x}$ will be periodic with period p with respect to x. This important result implies

that only one period of the array needs to be studied to characterize the entire system. Any field at the interface can now be expressed as a Fourier series:

$$\bar{f}(x) = e^{-j\beta x} \sum_{k=-\infty}^{\infty} f^n e^{-j\frac{2\pi k}{p}x} = \sum_{k=-\infty}^{\infty} f^k e^{-j\beta_k x},$$

$$f^k = \frac{1}{p} \int_0^p \bar{f}(x) e^{j\beta_k x} dx,$$

(2.37)

where:

- $\beta_k = \beta + \dfrac{2\pi k}{p} = \omega s_k$.

Using (2.37) and (2.16) and noticing that the overall fields are composed of infinite sums of spectral-domain fields having wavenumbers given by β_k, it can be shown that interface displacements and electric potential are given by

$$\left[\bar{u}_1(x) \quad \bar{u}_2(x) \quad \bar{u}_3(x) \quad \bar{\phi}(x) \right]^{\mathrm{T}} = \frac{1}{j\omega} \sum_{k=-\infty}^{\infty} \mathbf{G}\left(\frac{\beta_k}{\omega} \right) \left[T_5^k \quad T_4^k \quad T_3^k \quad \sigma^k \right]^{\mathrm{T}} e^{-j\beta_k x},$$

(2.38)

where:

- $\left[T_5^k \quad T_4^k \quad T_3^k \quad \sigma_k \right]^{\mathrm{T}} = \dfrac{1}{p} \int_0^p \left[\bar{T}_5(x) \quad \bar{T}_4(x) \quad \bar{T}_3(x) \quad \bar{\sigma}(x) \right]^{\mathrm{T}} e^{j\beta_k x} dx.$

Using a similar basis function expansion for stress and charge to that found in Section 2.6 and comparing (2.37) and (2.15), it can be shown that the Fourier coefficients for stress and charge terms are given by:

86

$$T_5^k = \frac{2\pi}{p} \sum_{s=1}^{N_1} w_1^s f_1^s(\beta^k),$$

$$T_4^k = \frac{2\pi}{p} \sum_{s=1}^{N_2} w_2^s f_2^s(\beta^k),$$

$$T_3^k = \frac{2\pi}{p} \sum_{s=1}^{N_3} w_3^s f_3^s(\beta^k),$$

$$\sigma^k = \frac{2\pi}{p} \sum_{s=1}^{N_4} w_4^s f_4^s(\beta^k).$$

(2.39)

Using the Galerkin approach to form additional equations from (2.38), again as in Section 2.6, and including (2.39) results in:

$$\begin{bmatrix} \mathbf{c}_1 \\ \mathbf{c}_2 \\ \mathbf{c}_3 \\ \mathbf{c}_4 \end{bmatrix} = \begin{bmatrix} \mathbf{Y}_{11} & \mathbf{Y}_{12} & \mathbf{Y}_{13} & \mathbf{Y}_{14} \\ \mathbf{Y}_{21} & \mathbf{Y}_{22} & \mathbf{Y}_{23} & \mathbf{Y}_{24} \\ \mathbf{Y}_{31} & \mathbf{Y}_{32} & \mathbf{Y}_{33} & \mathbf{Y}_{34} \\ \mathbf{Y}_{41} & \mathbf{Y}_{42} & \mathbf{Y}_{43} & \mathbf{Y}_{44} \end{bmatrix} \begin{bmatrix} \mathbf{w}_1 \\ \mathbf{w}_2 \\ \mathbf{w}_3 \\ \mathbf{w}_4 \end{bmatrix},$$

(2.40)

where:

- $\mathbf{c}_n = \begin{bmatrix} c_n^1 & c_n^2 & \dots & c_n^{N_n} \end{bmatrix}^T$, where:

$c_n^r = \int_0^p \bar{f}_n^r(x) g_n(x) dx = \int_{\Gamma_{nr}} \bar{f}_n^r(x) g_n(x) dx$, Γ_{nr} is non-zero domain of $\bar{f}_n^r(x)$, and

$g_1(x) = u_1(x)$, $g_2(x) = u_2(x)$, $g_3(x) = u_3(x)$, $g_4(x) = \phi(x)$,

- $\mathbf{w}_n = \begin{bmatrix} w_n^1 & w_n^2 & \dots & w_n^{N_n} \end{bmatrix}^T$,

- $\mathbf{Y}_{mn} = \begin{bmatrix} Y_{mn}^{11} & Y_{mn}^{12} & \cdots & Y_{mn}^{1N_n} \\ Y_{mn}^{21} & Y_{mn}^{22} & \ddots & \vdots \\ \vdots & \ddots & \ddots & \vdots \\ Y_{mn}^{N_m 1} & \cdots & \cdots & Y_{mn}^{N_m N_n} \end{bmatrix}$, where $Y_{mn}^{rs} = -\frac{4\pi^2 j}{\omega p} \sum_{k=-\infty}^{\infty} G_{mn}\left(\frac{\beta^k}{\omega}\right) f_m^r(-\beta^k) f_n^s(\beta^k)$.

The FEM formalism used in Section 2.6 applies to this system. Charge conservation and reference potential only apply when $\beta = -\dfrac{2\pi\, k_{static}}{p}$, where k_{static} is an integer, since the $k = k_{static}$ term in the summation of (2.37) corresponds to a stationary term (no variation in x). Regarding the electrical potential field, this term is the reference potential, which must be constant with respect to x (all other terms in the sum display x variation).

A numerical difficulty occurs in the formulation given thus far. According to (2.40) the $Y_{44}^{r\,s}$ term is a summation with one term evaluated at $\beta^k = 0$, which occurs when $k = k_{static}$. This term presents a problem due to the singularity in $G_{44}\!\left(\dfrac{\beta^k}{\omega}\right)$ at $\dfrac{\beta^k}{\omega} = 0$. To deal with this situation numerically, the $k = k_{static}$ terms in $\mathbf{Y}_{41}$, $\mathbf{Y}_{42}$, $\mathbf{Y}_{43}$, and $\mathbf{Y}_{44}$ are omitted from the summation, represented as an additional unknown (an integrated reference potential term), and transferred to the other side of the equation. To maintain a square matrix system, an additional equation expressing charge conservation over a period is added to the system (which must be true if every period is identical in terms of its fields). Alternatively, if $\beta^k \neq -\dfrac{2\pi\, k}{p}$ for all k, the charge conservation equation is not required since, at some distance away (in terms of periods), equal and opposite charge/current on an electrode can be found, which automatically ensures charge conservation. In addition, the reference potential is zero since there are no constant terms with respect to x in the summations representing fields.

88

The analysis when floating electrodes are included in the structure is the same as that carried out in Section 2.6 and in general the system to be solved is

$$
\begin{bmatrix} \mathbf{0} \\ \mathbf{0} \\ \mathbf{0} \\ \mathbf{c}'_4 \\ \mathbf{0} \end{bmatrix} = \begin{bmatrix} \mathbf{Y}_{11}-\mathbf{F}_{11} & \mathbf{Y}_{12}-\mathbf{F}_{12} & \mathbf{Y}_{13}-\mathbf{F}_{13} & \mathbf{Y}_{14} & \mathbf{0} \\ \mathbf{Y}_{21}-\mathbf{F}_{21} & \mathbf{Y}_{22}-\mathbf{F}_{22} & \mathbf{Y}_{21}-\mathbf{F}_{23} & \mathbf{Y}_{24} & \mathbf{0} \\ \mathbf{Y}_{31}-\mathbf{F}_{31} & \mathbf{Y}_{32}-\mathbf{F}_{32} & \mathbf{Y}_{33}-\mathbf{F}_{33} & \mathbf{Y}_{34} & \mathbf{0} \\ \mathbf{Y}_{41} & \mathbf{Y}_{42} & \mathbf{Y}_{43} & \mathbf{Y}_{44} & \mathbf{Z}^t \\ \mathbf{0} & \mathbf{0} & \mathbf{0} & \mathbf{Z} & \mathbf{0} \end{bmatrix} \begin{bmatrix} \mathbf{w}_1 \\ \mathbf{w}_2 \\ \mathbf{w}_3 \\ \mathbf{w}_4 \\ -\boldsymbol{\varphi} \end{bmatrix},
\tag{2.41}
$$

where:

- $\mathbf{c}'_4 = \begin{bmatrix} c_n'^1 & c_n'^2 & \dots & c_n'^{N_4} \end{bmatrix}^\mathrm{T}$, where

$$
c_4'^r = \int_0^p \bar{f}_4^r(x)v(x)dx,
$$

- $\mathbf{Z}$ has the same form as given in (2.36),

  (Note total charge over a period is not to be conserved explicitly if $\beta^k \neq 0, \forall k$),

- $\boldsymbol{\varphi}$ has the same form as given in (2.36),

  (Note reference voltage term is not be included if $\beta^k \neq 0, \forall k$).

From the resulting basis function coefficients, all currents entering electrodes can be computed by multiplying the total electrode charge by $j\omega W$, where W is the electrode aperture. As is apparent from Figure 2.8, the ratio of current to voltage on an electrode is the same as that any integer number of periods away. This ratio is called the harmonic admittance of the structure and is generally computed as a function of frequency with fixed phase-shift, γ, or vice versa. For the structure depicted in Figure 2.8, the harmonic admittance is represented as a 2x2 matrix $\mathbf{Y}(f, \gamma)$, since there are two possibly driven electrodes per period. It is easy to show that $\mathbf{Y}(f, \gamma)$ is periodic with respect to γ, with period equal to 1. The elements of the matrix are determined using the same technique one would use to measure Y-parameters of a circuit; namely, by one-at-a-time setting an

electrode to 1 volt while setting the others to 0 volts and determining the resulting current on each electrode. When the structure in Figure 2.8 is further subject to a finite region of arbitrarily applied voltages, then, with reference to Figure 2.8, the voltage and current entering electrodes n periods to the right of the first are given by

$$\mathbf{I}_n(\omega,\gamma) = \mathbf{I}_0(\omega,\gamma)e^{-j2\pi\gamma n},$$

$$\mathbf{V}_n(\omega,\gamma) = \mathbf{V}_0(\omega,\gamma)e^{-j2\pi\gamma n},$$

(2.42)

where:

- $\mathbf{I}_n$ is the vector of currents on the electrodes for the nth period,

- $\mathbf{V}_n$ is the vector of voltages on the electrodes for the nth period.

The electrode currents on a single period are related to the voltages applied to the electrodes on the same period through the harmonic admittance matrix when driven harmonically such that $\mathbf{I}(\omega,\gamma) = \mathbf{Y}(\omega,\gamma)\mathbf{V}(\omega,\gamma)$ for any period. Now suppose instead of driving the structure harmonically the structure is driven by an arbitrary voltage distribution, $\mathbf{V}_n(\omega)$. Before proceeding, a Fourier and inverse Fourier series is defined for converting between the n and γ domains:

$$f(\omega,\gamma) = \sum_{n=-\infty}^{\infty} f_n(\omega)e^{j2\pi\gamma n},$$

$$f_n(\omega) = \int_{-1/2}^{1/2} f(\omega,\gamma)e^{-j2\pi\gamma n}d\gamma.$$

(2.43)

90

Using (2.43) the mutual admittance, $\mathbf{Y}_n(\omega)$, is defined by

$$\mathbf{Y}_n(\omega) = \int_{-1/2}^{1/2} \mathbf{Y}(\omega,\gamma) e^{-j2\pi\gamma n} d\gamma .$$ (2.44)

From $\mathbf{I}(\omega,\gamma) = \mathbf{Y}(\omega,\gamma)\mathbf{V}(\omega,\gamma)$ and use of (2.43) it can be shown that the current entering the mth period's electrode is given by

$$\mathbf{I}_m(\omega) = \sum_{n=-\infty}^{\infty} \mathbf{Y}_{m-n}(\omega)\mathbf{V}_n(\omega).$$ (2.45)

Thus given a finite-length driven voltage distribution along the interface (all other electrodes grounded), (2.45) determines the currents entering all electrodes. Note that the mutual admittance represents the current distribution on electrodes subject to driving the $n = 0$ electrode with unit potential; all other electrodes are considered at zero potential. For a considered structure, if the grounded electrodes of a finite-length IDT are not electrically connected to the surrounding electrodes, which are at zero potential, then the voltage distribution over the IDT electrodes is unknown as only the potential difference is specified. Therefore, in (2.45) $\mathbf{V}_n(\omega) \rightarrow \mathbf{V}_n(\omega) + \phi_{ref}(\omega)$ over the n IDT electrode indices. Including at extra equation, i.e. charge conservation on the IDT electrodes, enables the overall system to be solved, which results in determination of the IDT currents and reference potential, $\phi_{ref}(\omega)$, given the known potential difference applied to the IDT. Properties of the mutual admittance function relevant to SHSAW sensor platforms are discussed in Section 3.4.3.

CHAPTER 3

SHSAW MODELING FOR LIQUID-PHASE SENSING APPLICATIONS

3.1. Introduction

The overall purpose of chapter 3 is to: (i) identify key SHSAW sensor platform design parameters relevant to liquid-phase sensor applications; (ii) report on the use of the implemented modeling tools towards extraction of these parameters; and (iii) identify design trends that lead to high-performance SHSAW sensor platforms.

Section 3.2 begins with a discussion regarding why delay-line-based SAW devices where considered in this work over resonant-based sensors for the liquid-phase applications. Afterwards, a simplified model of a liquid-phase delay-line sensor is presented, and the overall expected measured sensor signal is estimated. Based on model, liquid-phase sensing platform specifications are established for sensitivity, signal-to-noise ratio, resolution, and dynamic range.

In Section 3.3, characteristics of SHSAW propagation, such as phase velocity, attenuation, and penetration depth are evaluated with and without liquid surface loading for both electrically open and shorted interface boundary conditions. Next, using implemented software a numerical viscosity sensitivity analysis is presented and results are discussed.

In Section 3.4, excitation/detection characteristics are evaluated for three IDT surrounding boundary conditions: (i) mechanically and electrically free surface, (ii) semi-infinite along the propagation direction, finite-thickness uniform guiding electrodes,

and (iii) semi-infinite along the propagation direction, periodic guiding grating electrodes. The latter two structures have not been previously reported in the literature in terms of achievable IDT power efficiency, defined as η_{SHSAW} (the ratio of total IDT SHSAW power excited to IDT input power). It is shown that guiding structures can significantly improve achievable η_{SHSAW} reducing spurious signal detection at the output IDT, and thus improving the signal-to-noise ratio for liquid-phase delay-line based SHSAW sensor platforms.

3.2. SHSAW Liquid-Phase Sensing Platforms

As the purpose of this investigations is ultimately to advance development of a reliable liquid-phase sensor design, SHSAW liquid-phase sensors based on delay-line devices and not platforms based on resonant structures are considered. A major factor that motivated this decision is that a given liquid analyte may contain conducting ions or have a dielectric constant greater than that of the substrate; therefore it is important to shield IDTs from the liquid to prevent electric or dielectric shorting of the device. Given the fact that in resonant-based devices IDTs are typically placed on the order of sub-wavelengths from reflective grating structures and other IDTs, the degree of accuracy consequently required for positioning and attachment of a fluidic chamber poses a significant challenge to reliable device packaging for liquid-phase operation. By contrast, in a delay-line device, the gaps between IDTs and delay regions, where chambers are sealed to the substrate, can be relatively large acoustically. In this work it is shown that devices based on delay-lines yield responses with small dependence on chamber

positioning. Less stringent packaging attachment positioning can considerably simplify

packaging considerations and permits higher device reproducibility.

3.2.1. Delay-Line Response Model

To identify key issues regarding design of SHSAW delay-line liquid-phase

sensors, an appropriate model of the situation is required. Figure 3.1 shows the general

topology of the delay-line structure under consideration (top) and an equivalent

scattering-matrix representation (bottom).
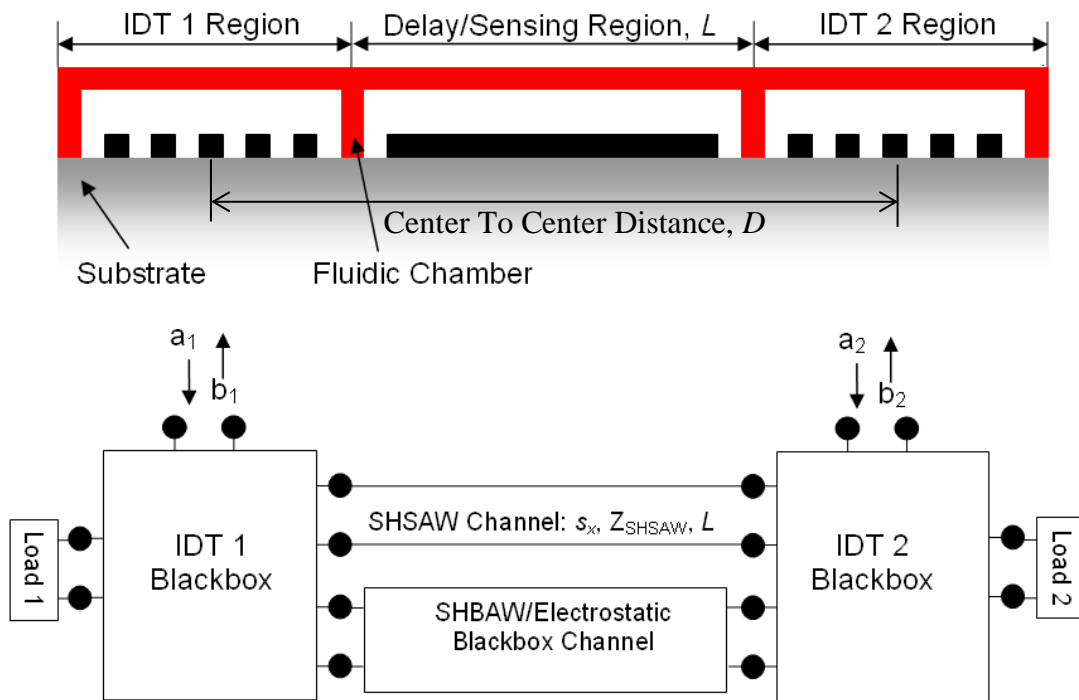
Figure 3.1. Topology and equivalent scattering-matrix representation for delay line
liquid-phase sensing platform under consideration.

The delay-line structure consists of two IDTs separated by a delay region. A fluidic

chamber is attached to the top of the device and has containment walls separating IDT

and delay regions. Configured as a liquid-phase sensor, it is assumed that only the delay region is exposed to the fluid analyte. The IDTs are considered 4-port black-box elements, where one port is the electrical port to be probed and the other ports are electromechanical. The outer electromechanical ports are terminated with loads. These loads represent energy storage effects and power lost to SHSAW and SHBAW propagating in the direction opposite to that of other IDT. The other two electromechanical ports permit coupling between input and output IDTs. Three types of coupling are considered: (i) electrostatic coupling between transducers; (ii) coupling due to SHBAW based on shallow propagation or reflection from bottom of substrate; and (iii) coupling via due to SHSAW propagating along the delay region interface.

In this analysis, cases (i) and (ii) are grouped together and are considered to be spurious signals. For case (iii), the SHSAW channel is modeled as a transmission line of length L with characteristic impedance Z_{SHSAW} and inverse propagation velocity or slowness given by s_x, which depends on properties of the fluid analyte, and is considered the sensing channel. In addition, complex multi-transit signals can also be detected; for instance detected SHSAW/BAW by the output IDT can regenerate SHSAW/BAW and then be detected again after reflection from the input IDT. Such multi-transit signals are also considered spurious.

The electrical response to be measured is given by the transmission coefficient $S_{21} = b_2/a_1$, which is determined when IDT 2 is terminated with system characteristic impedance and IDT 1 is driven with a source having system characteristic impedance. The overall transmission coefficient S_{21} is given by:

$$S_{21} = S_{21}^{SHSAW} + S_{21}^{Spurious} \tag{3.1}$$

where contributions due to the sensing and spurious channels are separated as

- S_{21}^{SHSAW}, the contribution due one-way propagation along the sensing channel,

- $S_{21}^{Spurious}$, the contributions due to the superposition of all spurious signals.

(Note that approximations for each term may be obtained experimentally via time-gating analysis if signals do not overlap in time.) For delay-line sensing applications, the phase of S_{21} is usually measured, tracked, and correlated to properties of the analyte. Therefore it becomes useful to define the maximum possible detection phase error, $|\phi_{error}|_{max}$, where ϕ_{error} is defined as the difference between the desired S_{21}^{SHSAW} phase value, ϕ_{SHSAW}, and overall detected S_{21} phase, ϕ_{21}. Figure 3.2 provides a geometric representation of the resulting phase error, where $\phi_{Spurious}$ is the phase of $S_{21}^{Spurious}$.
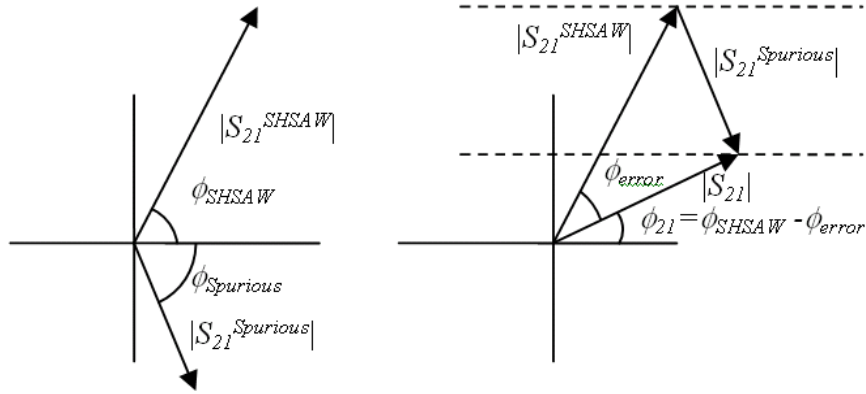
$$Law\ of\ Sines:\quad \frac{\left|S_{21}^{SHSAW}\right|}{\sin\left(\phi_{SHSAW} - \phi_{error} + \phi_{Spurious}\right)} = \frac{\left|S_{21}^{Spurious}\right|}{\sin\left(\phi_{error}\right)}$$

Figure 3.2. Maximum phase error due to the detection of spurious signal.

Applying the Law of Sines [85] to obtain an expression for ϕ_{error} and then determining either a maximum or minimum value by evaluating the expression at the point where its derivative with respect to $\phi_{Spurious}$ is zero, results in:

$$\left|\phi_{error}\right|_{max} = \tan^{-1}\left(\frac{\left|\dfrac{S_{21}^{spurious}}{S_{21}^{SHSAW}}\right|}{\sqrt{1-\left|\dfrac{S_{21}^{spurious}}{S_{21}^{SHSAW}}\right|^2}}\right) \approx \left|\frac{S_{21}^{spurious}}{S_{21}^{SHSAW}}\right| \quad for \quad \left|\frac{S_{21}^{spurious}}{S_{21}^{SHSAW}}\right| << 1 . \tag{3.2}$$

For the upcoming analysis in Section 3.2.2, it useful to express S_{21}^{SHSAW} as a function of the IDT center to center distance, D, and the delay-path length, L, which is the region that is sensitive to the analyte. Given that S_{21}^{SHSAW} consists of a contribution due to one-way SHSAW coupling, it can be expressed as:

$$S_{21}^{SHSAW} = \left|S_0^{SHSAW}\right| e^{j\phi_0^{SHSAW}} e^{\omega s_1''(D-L)} e^{-j\omega s_1'(D-L)} e^{\omega s_2''L} e^{-j\omega s_2'L} , \tag{3.3}$$

where:

- $\left|S_0^{SHSAW}\right|$ is the extrapolated magnitude of S_{21}^{SHSAW} as D goes to zero,

- ϕ_0^{SHSAW} is the extrapolated phase of the S_{21}^{SHSAW} as D goes to zero,

- s_1 is the complex SHSAW slowness in the IDT region, where $s_1' = \Re\{s_1\}$ and $s_1'' = \Im\{s_1\}$,

- s_2 is the complex SHSAW slowness in the delay region, where $s_2' = \Re\{s_2\}$ and $s_2'' = \Im\{s_2\}$.

The overall transmission phase is now given as:

$$\phi_{21} = \phi_0^{SHSAW} + \phi^{SHSAW} + \kappa \left| \phi_{error} \right|_{\max},$$ (3.4)

where:

- $\phi^{SHSAW} = -\omega s_1'(D-L) - \omega s_2' L$,

- $-1 \leq \kappa \leq 1$, and $\kappa \left| \phi_{error} \right|_{\max}$ represents the possible values of ϕ_{error}.

This relationship is used in Section 3.2.2 to study the theoretical sensitivity response, signal-to-noise ratio, resolution, and dynamic range of the proposed sensing system.

3.2.2. Sensitivity, Signal-To-Noise Ratio, Resolution, and Dynamic Range

Given a fixed operating frequency, two main phenomena are expected to cause a change in the value of ϕ_{21}, specifically changes in SHSAW slowness values, s_1 and s_2, and the propagation distances (*D-L*) and *L*. It should be noted that in the following analysis fluid viscosity is considered the measurand, but similar analyses can be performed for other parameters as well such as fluid density, conductivity, and dielectric parameters. With that said, the value s_2 is assumed to be dependent upon properties of the fluid viscosity and the device temperature, whereas s_1 is only considered dependent on temperature. Looking at the differential phase change of ϕ^{SHSAW} subject to differential changes in temperature and fluid viscosity permits a sensitivity analysis to be performed.

In particular, assuming the fluid viscosity and device temperature have infinitesimal changes given by $d\eta$ and dT respectively, given (3.3) the relative change in ϕ^{SHSAW} at a single frequency, is given by:

$$\frac{d\phi^{SHSAW}}{2\pi} = -\frac{(D-L)}{\lambda_1}\left(\frac{1}{s_1'}\frac{\partial s_1'}{\partial T} + \frac{1}{(D-L)}\frac{\partial(D-L)}{\partial T}\right)dT - \frac{L}{\lambda_2}\left(\frac{1}{s_2'}\frac{\partial s_2'}{\partial \eta}\right)d\eta - \frac{L}{\lambda_2}\left(\frac{1}{s_2'}\frac{\partial s_2'}{\partial T} + \frac{1}{L}\frac{\partial L}{\partial T}\right)dT, \quad (3.5)$$

where:

- $\lambda_1 = \dfrac{2\pi}{\omega s_1'}$, and $\lambda_2 = \dfrac{2\pi}{\omega s_2'}$.

Assuming that the normalized partial derivative terms w.r.t. temperature are equal for each region are equal, and $\lambda_1 \approx \lambda_2 = \lambda$, then:

$$\frac{d\phi^{SHSAW}}{2\pi} \approx -\frac{L}{\lambda}\frac{1}{s_2'}\frac{\partial s_2'}{\partial \eta}d\eta - \frac{D}{\lambda}\left(\frac{1}{s_2'}\frac{\partial s_2'}{\partial T} + \frac{1}{L}\frac{\partial L}{\partial T}\right)dT. \quad (3.6)$$

Equation (3.6) indicates that the normalized change of phase w.r.t. η is proportional to the normalized delay path distance L/λ. This suggest that L should be as large as possible to obtain higher change in detected signal, but given $S_{21}^{SHSAW} \propto e^{\omega s_x'' L}e^{-j\omega s_x' L}$, the level of signal at IDT 2 associated with S_{21}^{SHSAW} in dB is proportional to L/λ assuming SHSAW propagation loss, e.g. viscous loading. This is one important factor when determining an upper limit for L, as if the delay region becomes too long, the detected signal may fall into the noise level or into a region where spurious signals dominate, resulting in a larger phase error given by (3.2). The terms $\dfrac{1}{s_2'}\dfrac{\partial s_2'}{\partial \eta}$ and $\left(\dfrac{1}{s_2'}\dfrac{\partial s_2'}{\partial T} + \dfrac{1}{L}\dfrac{\partial L}{\partial T}\right)$ represent sensitivities towards viscosity and temperature, respectively. The sensitivity to temperature arises from finite temperature dependence of material stiffness, piezoelectric, dielectric, and

99

density constants, and the overall device physical length, i.e. thermal expansion. Assuming viscosity is the desired measurand, the signal-to-noise ratio of phase signal associated the SHSAW mode is therefore defined by:

$$SNR_{SHSAW} = \frac{L}{D} \left| \frac{S_\eta \Delta \eta}{S_T \Delta T} \right| = \frac{L}{D} \left| \frac{S_\eta \Delta \eta}{TCD\Delta T} \right|,$$ (3.7)

where:

- $S_\eta = \frac{1}{s'_2} \frac{\partial s'_2}{\partial \eta}$,

- $S_T = \frac{1}{s'_2} \frac{\partial s'_2}{\partial T} + \frac{1}{L} \frac{\partial L}{\partial T} = -\frac{1}{v_p} \frac{\partial v_p}{\partial T} + \frac{1}{L} \frac{\partial L}{\partial T} = -TCV + TCE = TCD$,

- TCV is temperature coefficient of velocity,

- TCE is temperature coefficient of expansion,

- TCD is temperature coefficient of delay.

Given (3.7), (3.6) is approximated by:

$$\frac{\Delta\phi^{SHSAW}}{2\pi} \approx -\frac{L}{\lambda} S_\eta \Delta \eta - \frac{D}{\lambda} TCD\Delta T,$$ (3.8)

Again considering viscosity as the measurand, the sensor resolution, $|\Delta\eta|_{min}$, is defined as the minimum detectable change in viscosity. An approximation for this term is now derived. Assume at time, t_1, a first measurement of ϕ_{21} is collected, and then at another time, t_2, an additional measurement of ϕ_{21} is conducted after the fluid viscosity changes. Further assume that the temperature of the devices fluctuates over time with amplitude given by $|\Delta T|_{max}$, and that the value of κ in (3.4) varies over time, as the detected spurious signal phase may depend on temperature as well. Let $|\phi_{min}|$ be the phase resolution of the measurement system. Given (3.4) and (3.8), it makes sense to neglect

100

$\Delta\phi_0^{SHSAW} = \phi_0^{SHSAW}(t_2) - \phi_0^{SHSAW}(t_1)$ as it is much smaller in magnitude than the contribution

the *TCD* term in (3.8). This assumption is valid given that $\dfrac{D}{\lambda}$ is typically on the order of

100 or more and that the phase change due to temperature associated with the delay

region is $2\pi\dfrac{D}{\lambda}TCD\Delta T$, whereas the phase change due to temperature associated with

ϕ_0^{SHSAW} is on the order of $2\pi TCD\Delta T$, which does not have a similar $\dfrac{D}{\lambda}$ factor. Equations

(3.9), (3.10), (3.11) give expressions for the maximum absolute phase changes associated

the following mechanisms; viscosity, temperature and phase error, respectively. Notice

the factor of 2 and the less-than or equal-to sign for (3.10) and (3.11) as the temperature

is assumed to be a random signal between $T - |\Delta T|_{max}$ and $T + |\Delta T|_{max}$, and κ is assumed

random and between -1 and 1.

$$\left|\frac{\phi_{21}(t_2)}{2\pi} - \frac{\phi_{21}(t_1)}{2\pi}\right|_{\eta} = \frac{L}{\lambda}|S_\eta||\Delta\eta|, \tag{3.9}$$

$$\left|\frac{\phi_{21}(t_2)}{2\pi} - \frac{\phi_{21}(t_1)}{2\pi}\right|_{T} \leq 2\frac{D}{\lambda}|TCD||\Delta T|_{max}, \tag{3.10}$$

$$\left|\frac{\phi_{21}(t_2)}{2\pi} - \frac{\phi_{21}(t_1)}{2\pi}\right|_{\phi_{error}} \leq 2\frac{|\phi_{error}|_{max}}{2\pi}. \tag{3.11}$$

In a worst case situation, where the phase response of viscosity is canceled by the

temperature and phase error responses, (3.9) must be greater than the sum of (3.10) and

(3.11) to guarantee a change viscosity is detected.

Therefore value of $|\Delta\eta|_{\min}$ is given by:

$$|\Delta\eta|_{\min} = 2\frac{D}{L}\frac{|TCD|}{|S_\eta|}|\Delta T|_{\max} + \frac{2}{|S_\eta|}\frac{\lambda}{L}\frac{|\phi_{error}|_{\max}}{2\pi}\,. \qquad (3.12)$$

Equation (3.12) assumes that the measurement equipment has perfect phase resolution, but in practice this is a finite value and is given by $|\phi_{\min}|$. Consequently the achievable value of $|\Delta\eta|_{\min}$ in practice is given as:

$$|\Delta\eta|_{\min} = 2\frac{D}{L}\frac{|TCD|}{|S_\eta|}|\Delta T|_{\max} + \frac{2}{|S_\eta|}\frac{\lambda}{L}\frac{|\phi_{error}|_{\max} + |\phi_{\min}|}{2\pi}\,. \qquad (3.13)$$

It should be mentioned that the value of $|\Delta\eta|_{\min}$ can also be thought of as the detection limit using the value of S_η in the limit of zero viscosity. Regarding the dynamic range of the sensor, this may be determined by finding regions of analyte parameters which yield sensor resolution guaranteed to be better than a given specification.

As a result of the analysis presented in this section it is apparent that optimal designs should present minimal *TCD*, acceptable sensitivity, and minimal excitation/detection of spurious signals.

3.3. SHSAW Propagation Characterization Towards Liquid-Phase Sensing

In this section propagation characteristics of the SHSAW mode relevant to liquid-phase sensing are discussed. SHSAW propagation characteristics are studied for platform devices having guiding structures located in delay regions. It is shown that guiding structures can dramatically improve the concentration of SHSAW energy near the interface and thus improve mode sensitivity to surface and interface perturbations. A

numerical SHSAW sensitivity analysis for viscosity is presented for uniform layered guiding situations to verify sensitivity improvement via guiding. In particular, Love mode structures are evaluated, which include a semi-infinite piezoelectric body, two guiding layers consisting of amorphous SiO_2 and Au, and a semi-infinite viscous fluid. The extracted sensitivity is determined as a function of each finite layer thickness for three piezoelectric materials and selected SHSAW orientations: potassium niobate (0°, 90°, 0°), quartz (0°, 132.75°, 90°) and langasite (0°, 22°, 90°).

3.3.1. Importance of SHSAW Guiding Structures

Using implemented software based on the theoretical development presented in Chapter 2, SHSAW mode properties are characterized for candidate substrate/layer configurations. Implemented software allows identification of modes for arbitrary materials, orientations, and uniform layered configurations and returns the complex valued slowness parameter of the mode. Additional routines were developed for computing the Poynting vector associated with a mode at any position in the body. Effective penetration depth of the mode was calculated using routines based on integration of x-directed (propagation direction) Poynting vector as a function of depth (see Appendix C).

Evaluation of three substrate materials and orientations are presented: potassium niobate ($KNbO_3$) Euler angles (0°, 90°, 0°), langasite (LGS) Euler angles (0°, 22°, 90°), and quartz Euler angles (0°, 132.75°, 90°). To demonstrate how altering the surface boundary condition influences properties of the SHSAW, four scenarios are considered:

(i) an electrically and mechanically free surface condition; (ii) an infinitesimally thin short-circuited and mechanically free surface condition; (iii) case (i) with addition of de-ionized (DI) water; and (iv) case (ii) with addition of DI water. Figure 3.3 shows the four scenarios considered. Propagation is assumed along the $+x$-direction, the z-axis is directed along the piezoelectric substrate normal with the origin at the interface, and all fields are assumed uniform along the y-direction. Characteristics of the SHSAW obtained using the implemented software routines for each of the four cases and three materials/orientations are given in Table 3.1, where v is the mode phase-velocity; α, the mode attenuation in units of dB/λ; d^+ the penetration depth above the interface; d^-, the penetration depth into the substrate; and quantity, P^+/P^-, given as the ratio of total x-directed power above the interface to that below the interface, respectively. The penetration depth is defined as the range of z from the interface to a point above or below the interface which accounts for 99% of the total power associated with the SHSAW mode above or below the interface, respectively.
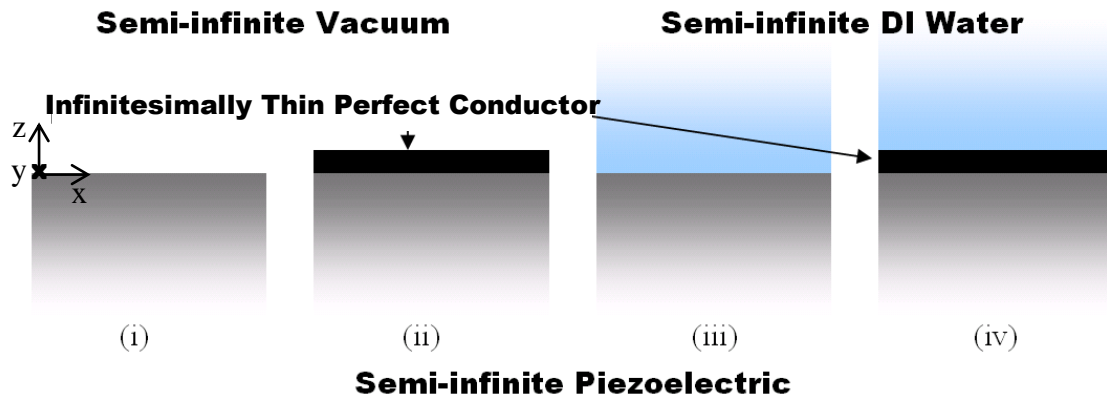
Figure 3.3. Four scenarios used to characterize SHSAW guiding.

In the cases including DI water loading, the overall mode becomes dispersive as the effective c_{44} stiffness coefficient of the fluid is given by $j\omega\eta$, where ω is radian frequency and η is the dynamic viscosity of DI water. For demonstration purposes, the simulations presented here were chosen to be evaluated at $\omega = 2 \cdot \pi \cdot 100 \cdot 10^6$ Hz, which is on the order of the operational frequency range of devices fabricated in this work. As a note, Appendix E presents the un-rotated material constants of each material considered in this dissertation. Figure 3.4 and Figure 3.5 plot the normalized x-directed Poynting vector as a function of distance in wavelengths from the interface for each case and material/orientation considered.

Case	Parameter	KNbO$_3$ (0°, 90°, 0°)	LGS (0°, 22°, 90°)	Quartz (0°, 132.75°, 90°)
(i)	v [m/s]	3801.06	2947.34	NA
	α [dB/λ]	0	0	NA
	d^+ [λ]	0.37	0.37	NA
	d^- [λ]	227	520	NA
	P^+/P^- [%]	-1.04 10^{-3}	-7.76 10^{-5}	NA
(ii)	v [m/s]	2863.67	2945.37	5008.80
	α [dB/λ]	0	0	0
	d^+ [λ]	0	0	0
	d^- [λ]	0.90	9.01	24.32
	P^+/P^- [%]	0	0	0
(iii)	v [m/s]	3711.27	2946.21	5008.78
	α [dB/λ]	9.46 10^{-3}	1.53 10^{-3}	1.12 10^{-3}
	d^+ [λ]	0.37	0.37	0.37
	d^- [λ]	3.13	11.97	22.22
	P^+/P^- [%]	-3.53	-2.01 10^{-2}	-8.66 10^{-4}
(iv)	v [m/s]	2862.62	2945.26	5008.73
	α [dB/λ]	2.00 10^{-2}	2.02 10^{-3}	1.19 10^{-3}
	d^+ [λ]	4.29 10^{-3}	4.17 10^{-3}	2.45 10^{-3}
	d^- [λ]	0.85	8.79	20.70
	P^+/P^- [%]	1.83$10^{-9}$	1.78 10^{-11}	2.14 10^{-12}

Table 3.1. SHSAW mode properties for 4 cases in Figure 3.3, for three substrate materials/orientations.

(e) case (i) [0°,132.75°,90°] quartz

(Mode Does Not Exist)
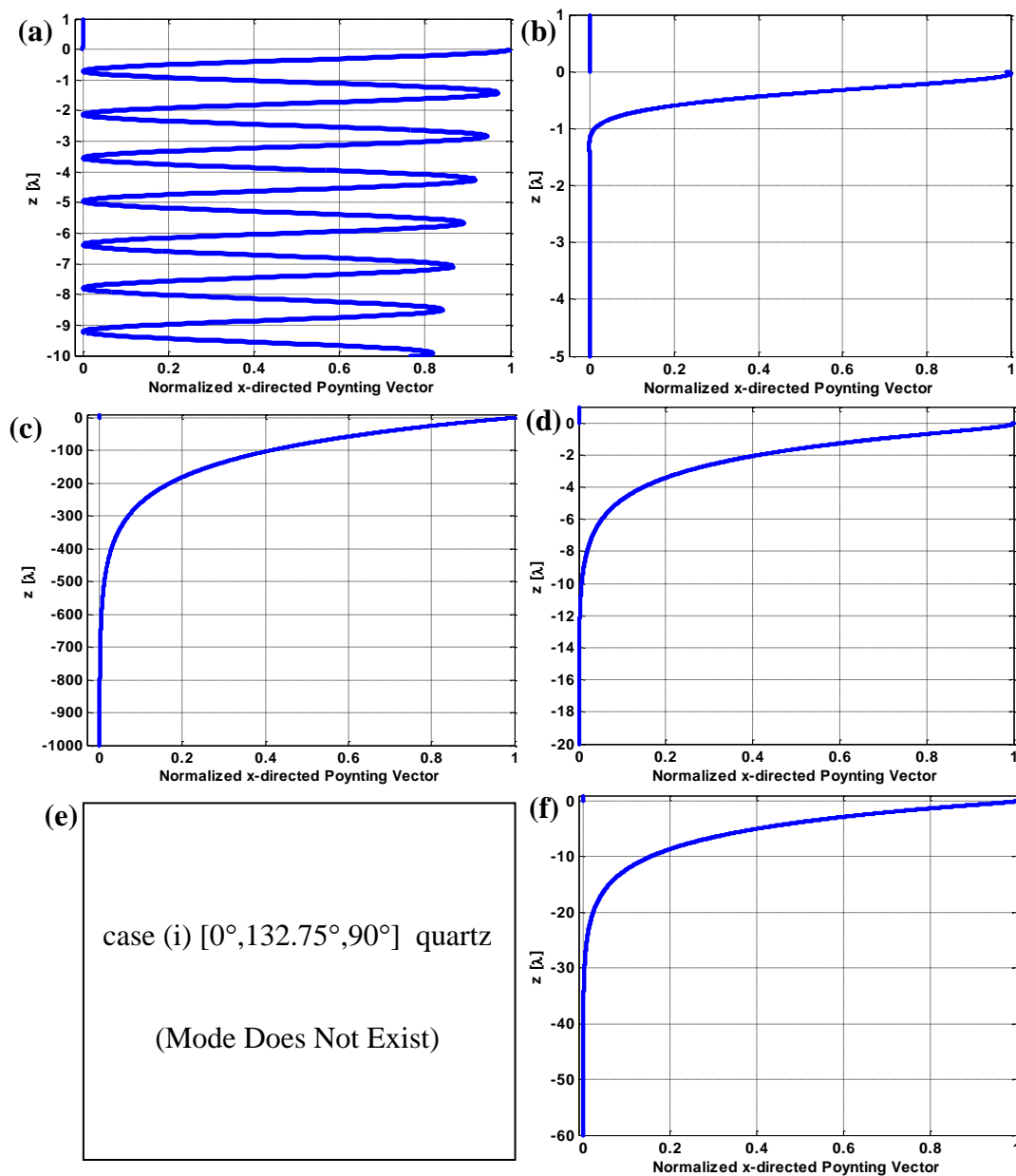
Figure 3.4. Normalized *x*-directed Poynting vector for cases (i) and (ii) demonstrating effect of addition of electrical guiding structure: (a) case (i) KNbO$_3$; (b) case (ii) KNbO$_3$; (c) case (i) LGS; (d) case (ii) LGS; (e) case (i) quartz; (f) case (ii) quartz.
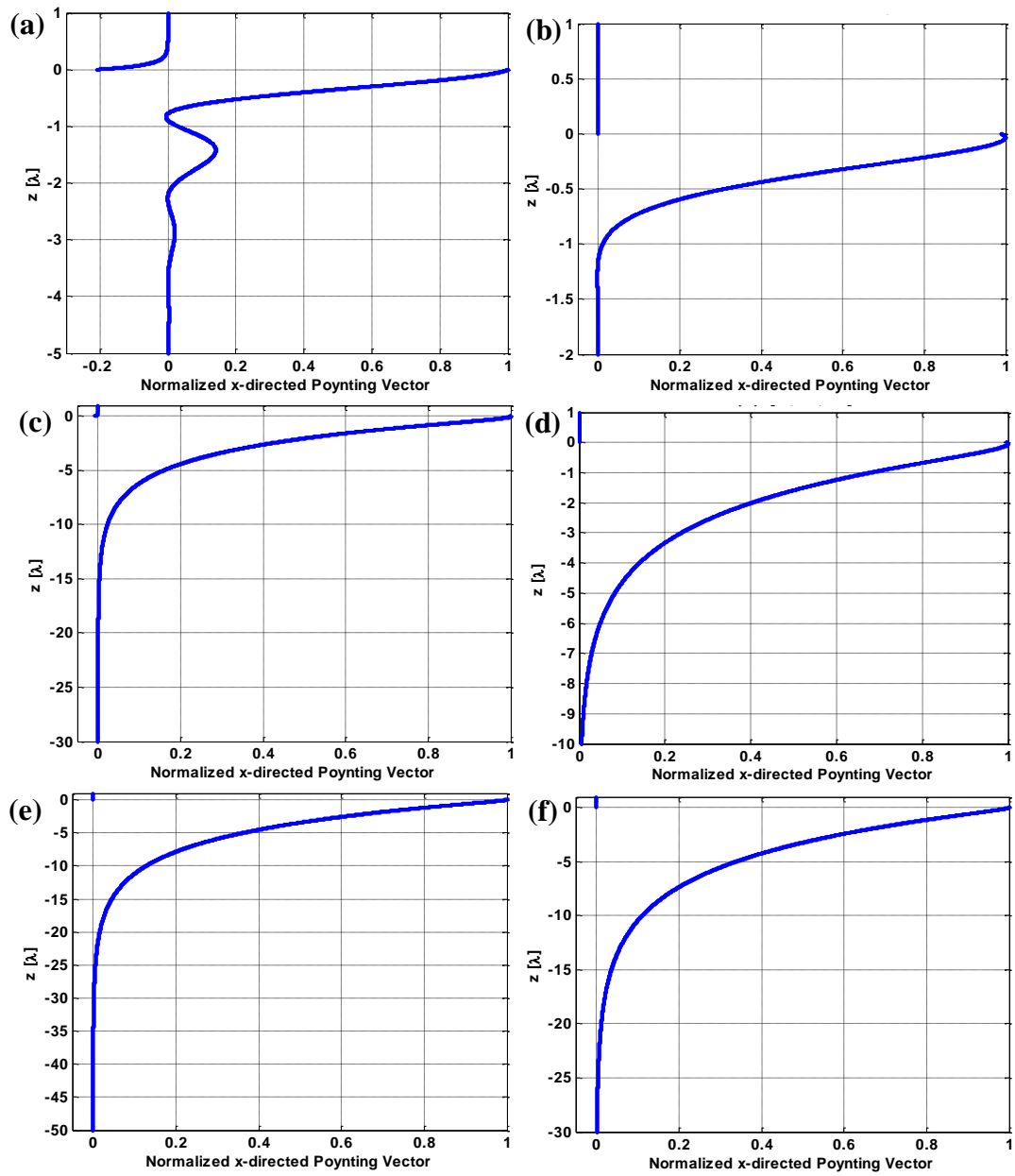
Figure 3.5. Normalized *x*-directed Poynting vector for cases (iii) and (iv) demonstrating effect of addition of electrical guiding structure: (a) case (iii) KNbO3; (b) case (iv) KNbO3; (c) case (iii) LGS; (d) case (iv) LGS; (e) case (iii) quartz; (f) case (iv) quartz.

Comparing cases (i) and (ii) shows the effect of short-circuiting the electric potential at the interface. For each material, the shorting effect results in energy concentration towards the interface. In the case of quartz no mechanically and electrically free boundary condition SHSAW solution exists, whereas a mode may be identified when short-circuiting the electric potential. Results of case (iii) indicate that fluid mechanical and dielectric loading has a similar guiding effect, though not as strong. Case (iv) presents the largest guiding effect, including mechanical loading and electric shorting effects. Slowing down the SHSAW mode generally results in a concentration of energy near the interface, consistent with the fact that the partial modes in each body tend to decay faster, with respect to z, for increased x-directed slowness. It is interesting to note negative P^+/P^- ratios for non-shorted interferences, although very small in magnitude. The reason why the sign of P^+ is negative is discussed in Appendix C, but it has to do with use of the quasi-static approximation. Alternatively in the case of interface shorting; no electrical fields are present above the interface, and only purely acoustic Poynting vector exists above the interface, in which the total integrated value is a positive quantity. Observed effects indicate that increased mode sensitivity will be achieved by using guiding structures, as energy becomes more concentrated near the analyte. The penetration depth into the fluid when electrical fields are shorted at the interface is also of note. In Chapter 2 it was shown that the eigenvalues associated with the two pure shear horizontal partial modes in an isotropic continuum are given by $\pm\sqrt{\dfrac{\rho}{c_{44}} - s_x^2}$; which if considering a viscous Newtonian fluid results in $\pm\sqrt{\dfrac{\rho}{j\omega\eta} - s_x^2}$, as $c_{44} = j\omega\eta$. If

$|s_x| \ll \dfrac{\rho}{\omega \eta}$ then the eigenvalues associated with the partial modes are approximately

given by $\pm \sqrt{\dfrac{\rho}{j\omega\eta}} = \pm \sqrt{\dfrac{\rho}{\omega\eta}} \dfrac{\sqrt{2}}{2}(1-j)$. For the considered semi-infinite fluid, the fields

associated with the valid partial mode must decay away from the interface. Therefore as

the fields in the fluid are proportional to e raised to the power of the eigenvalue

multiplied by $j\,\omega\,z$, only the negative square-root branch solution is considered valid.

Given that x-directed time average Poynting vector is -½ the real part of the product of T_4

and $(j\,\omega u_2)^*$ (see (2.12)), the z-dependence of the acoustic Poynting vector in the fluid is

given by $e^{-z\sqrt{\frac{2\omega\rho}{\eta}}}$. Integrating the x-directed Poynting vector w.r.t z allows penetration

depth to be estimated (d is the value of integration upper limit that yields 99% of total

integral, i.e. the value obtained as $d \rightarrow \infty$); which can be shown to result in

$d = -\ln(0.01) \cdot \sqrt{\dfrac{\eta}{2\omega\rho}}$. It should be noted that this value is exact for a BAW device

situation as s_x in that case is equal to zero. Given that relatively very little energy is

present in the fluid above d from the interface, whatever change occurs in the fluid above

the level d has very little effect on the overall wave velocity. Therefore we can define d

also as the effective sensor probing depth into the fluid. Figure 3.6 plots the effective

sensor probing depth into DI water versus device operating frequency. In this work,

device operating frequency of candidate designs are in on the order of 100-200 MHz, and

therefore the sensor platform devices are expected to be sensitive to interface

perturbations on the order of 125 to 90 nm, respectively; assuming the analyte fluidic

properties are similar to DI water.
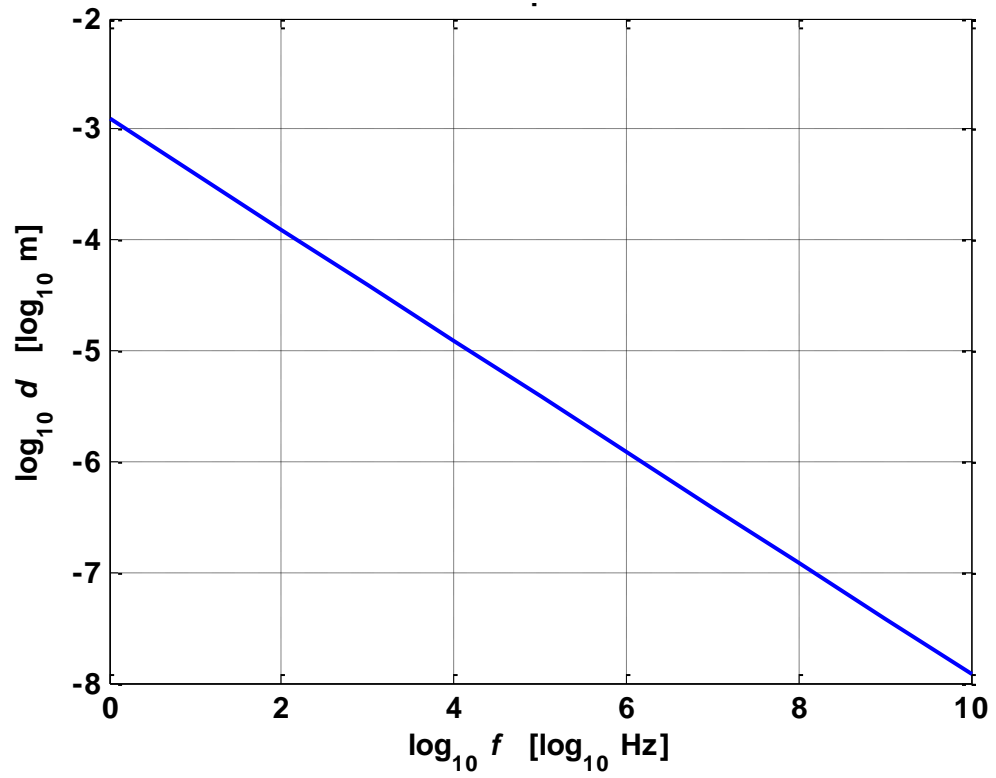
Figure 3.6. Effective sensor probing distance into DI water vs. operating frequency.

3.3.2. SHSAW Sensitivity Analysis For Viscosity Detection

In this section a numerical sensitivity evaluation is presented, which quantifies the effect of incorporating guiding layers on the SHSAW sensitivity to fluid viscosity. The analysis is based on use of the same software routines written for Section 3.3.1, but in this case the results of the analysis are applied to the outcomes in Section 3.2.2; i.e. definition of mode sensitivity. The structure topology studied is depicted in Figure 3.7.

Figure 3.7. Structure considered for numerical sensitivity analysis.

The structure in Figure 3.7 consists of a semi-infinite piezoelectric, finite thickness layer of amorphous SiO_2 having thickness h_{SiO2}, finite thickness layer of amorphous Au having thickness h_{Au}, and semi-infinite viscous DI water. The use of SiO_2 layers is included here in addition to Au to compare achievable sensitivity to reported Love mode liquid-phase sensor platforms using this topology. It should be of note that the results obtained when including no SiO_2 layer is the same of those obtained in the limit as $\omega \cdot h_{SiO2}$ goes to zero. Based on the partial mode and Green's function analysis for n-layer systems given in Chapter 2, it can be shown that the propagation characteristics of the structure in Figure 3.7 depend upon the following quantities: $\omega \cdot \eta$ where η is the dynamic viscosity of fluid half-space; ρ, the density of the fluid half-space; $\omega \cdot h_{Au}$; $\omega \cdot h_{SiO2}$; and the stiffness, density,

dielectric, and piezoelectric constants of the half-space piezoelectric and finite layers, a set denoted as X. If a SHSAW mode exists for this structure, the mode slowness, s_x, will depend as well on these parameters. The mode sensitivity with respect to $\omega \cdot \eta$, defined as $S_{\omega \eta}$, is given by:

$$S_{\omega \eta}\left(\omega \eta, \rho, \omega h_{SiO2}, \omega h_{Au}, X\right) = \frac{1}{s'_x\left(\omega \eta, \rho, \omega h_{SiO2}, \omega h_{Au}, X\right)} \frac{\partial s'_x\left(\omega \eta, \rho, \omega h_{SiO2}, \omega h_{Au}, X\right)}{\partial(\omega \eta)}, \quad (3.14)$$

where:

- $s_x = s'_x + js''_x$.

For a given operating frequency, f_0, the sensitivity to viscosity, S_η is given by:

$$S_\eta\left(\eta, \rho, h_{SiO2}, h_{Au}, X, \omega_0 = 2\pi f_0\right) = \omega_0 S_{\omega \eta}\left(\omega_0 \eta, \rho, \omega_0 h_{SiO2}, \omega_0 h_{Au}, X\right). \quad (3.15)$$

To keep the presented results regarding sensitivity to viscosity independent of operating frequency, $S_{\omega \eta}$ will be reported in this work. With (3.15) analysis of expected sensor parameters is achieved as described in Section 3.22; e.g. signal-to-noise ratio, resolution, and dynamic range. To evaluate (3.14) in this work, sensitivity was approximated by finding s_x for a given set of independent variable parameters, followed by applying a 1% increase in $\omega \cdot \eta$ and determining a new value of s_x. The partial derivative term in (3.14) was then approximated by computing $\Delta s'_x / \Delta(\omega \cdot \eta)$. The value of ρ for the fluid was chosen to be that of DI water, for consistency with Section 3.3.1. The sensitivity around two baseline values of $\omega \cdot \eta$ is evaluated, in particular 0.0005592 and 0.005592 GPa, which correspond to viscosity of DI water and a device operating frequency of 100 and 1000 MHz, respectively. To evaluate how guiding layers and piezoelectric substrate choice influences sensitivity and overall properties of the SHSAW mode, three SHSAW

materials/orientations are considered for a variety of $\omega \cdot h_{Au}$ and $\omega \cdot h_{SiO2}$ combinations: quartz (QTZ) Euler angles (0°, 132.75°, 90°), langasite (LGS) Euler angles (0°, 22°, 90°) and potassium niobate (KNB) Euler angles (0°, 90°, 0°). Figure 3.8, Figure 3.9, and Figure 3.10 show the determined $S_{\omega\eta}$ and corresponding SHSAW propagation loss due to viscous loading in dB/λ for the quartz, LGS, and KNB orientations considered, respectively, at $\omega \cdot \eta = 0.0005592$ GPa. In addition, Figure 3.11, Figure 3.12, and Figure 3.13 show the results of the same analysis, but with $\omega \cdot \eta = 0.005592$ GPa. It should noted that this analysis considered substrate materials/orientations with relatively low, medium, and high electromechanical coupling; i.e. QTZ, LGS, and KNB, respectively, to determine if coupling has any significant affect on achievable sensitivity.

Figure 3.8. QTZ, Euler Angles (0°, 132.75°, 90°), (a) sensitivity to $\omega \cdot \eta$, and (b) propagation loss, α. Parameters are plotted as functions of normalized SiO_2 and Au thicknesses; baseline $\omega \cdot \eta = 0.0005592$ GPa. Crosshatched areas indicate regions where no solution was obtained.

Figure 3.9. LGS, Euler Angles (0°, 22°, 90°), (a) sensitivity to $\omega \cdot \eta$, and (b) propagation loss, α. Parameters are plotted as functions of normalized SiO$_2$ and Au thicknesses; baseline $\omega \cdot \eta$ = 0.0005592 GPa. Crosshatched areas indicate regions where no solution was obtained.

Figure 3.10. KNB, Euler Angles $(0°, 90°, 0°)$, (a) sensitivity to $\omega \cdot \eta$, and (b) propagation loss, α. Parameters are plotted as functions of normalized SiO$_2$ and Au thicknesses; baseline $\omega \cdot \eta = 0.0005592$ GPa. Crosshatched areas indicate regions where no solution was obtained.
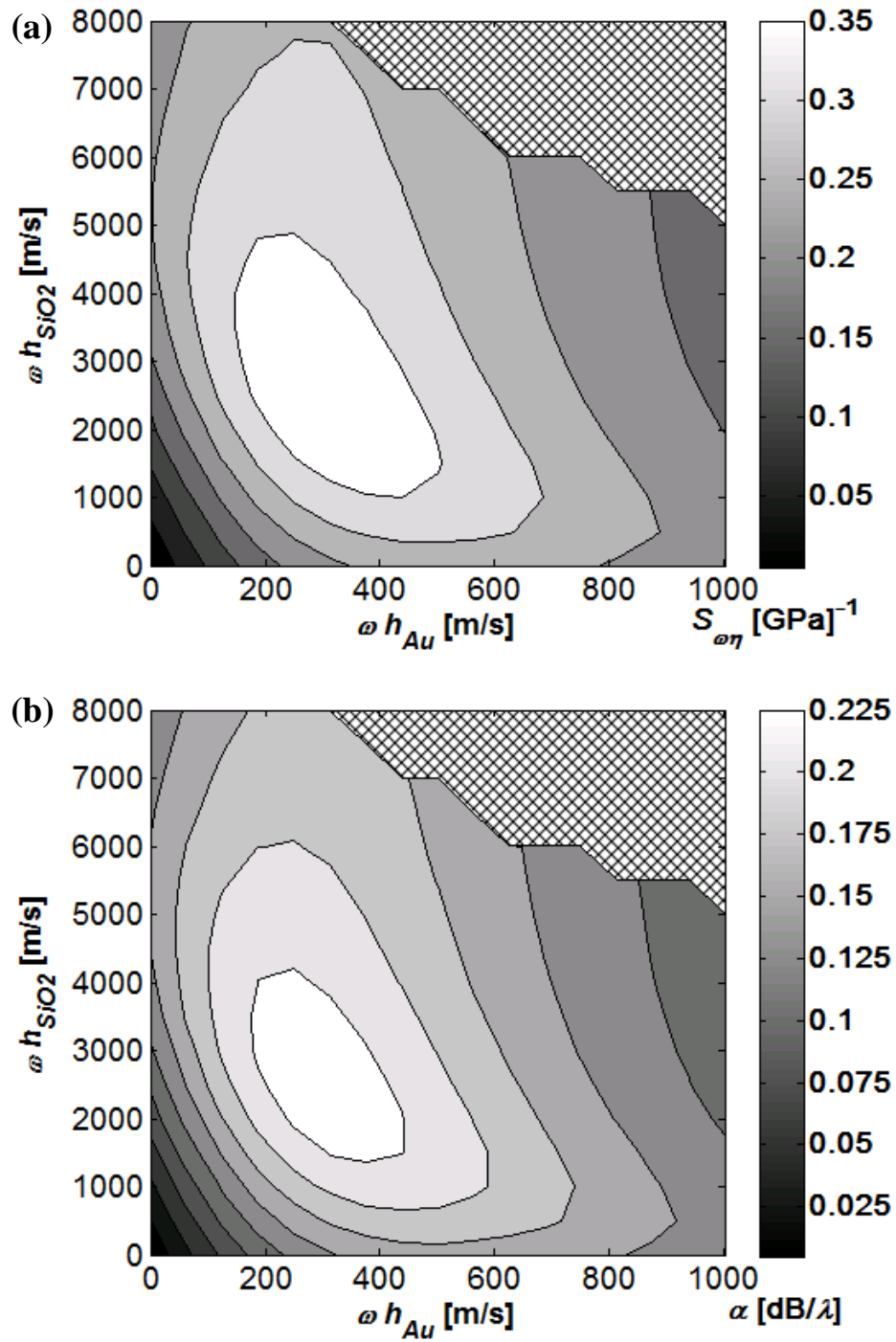
Figure 3.11. QTZ, Euler Angles (0°, 132.75°, 90°), (a) sensitivity to $\omega \cdot \eta$, and (b) propagation loss, α. Parameters are plotted as functions of normalized SiO$_2$ and Au thicknesses; baseline $\omega \cdot \eta = 0.005592$ GPa. Crosshatched areas indicate regions where no solution was obtained.
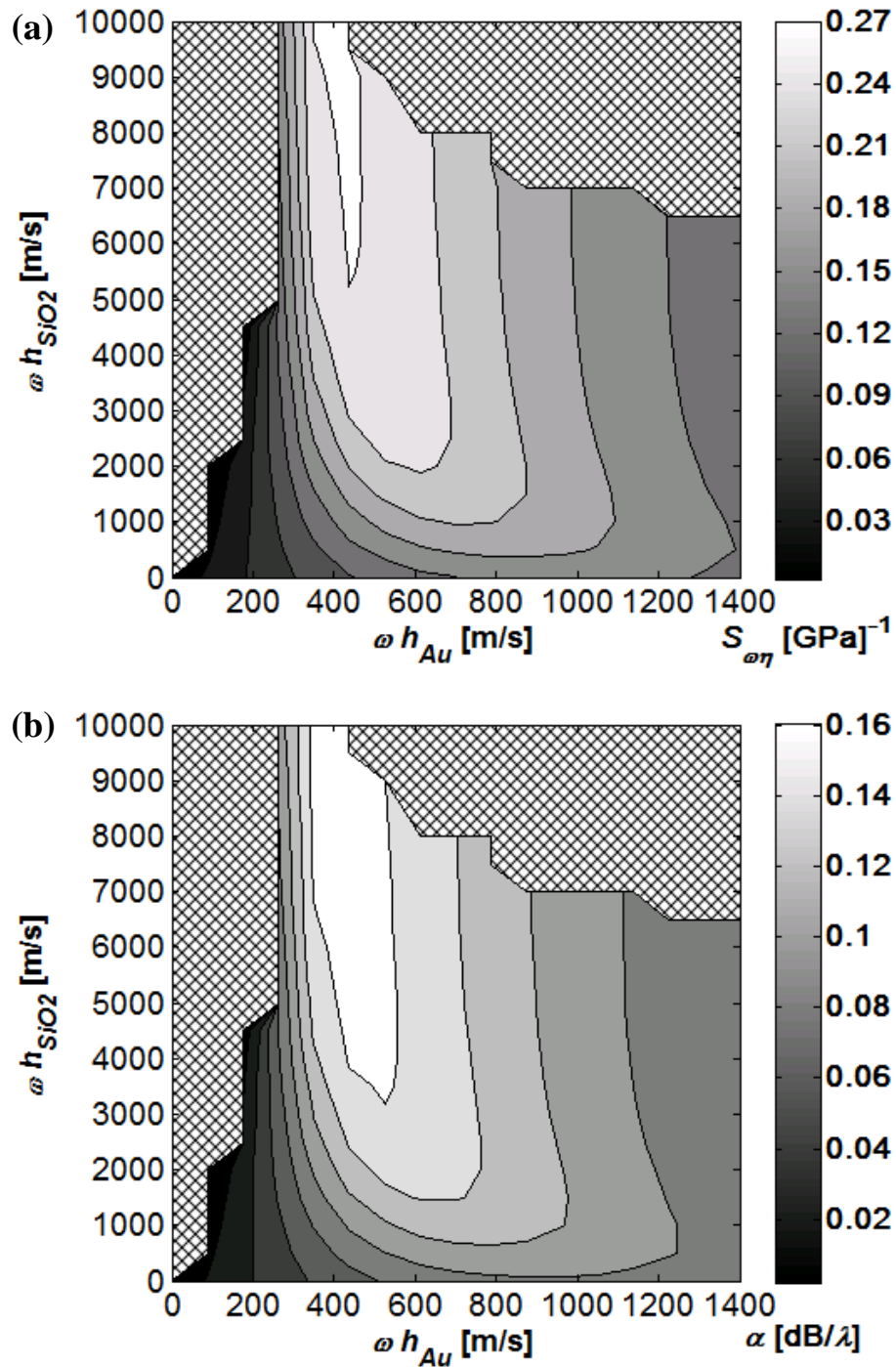
Figure 3.12. LGS, Euler Angles (0°, 22°, 90°), (a) sensitivity to $\omega \cdot \eta$, and (b) propagation loss, α. Parameters are plotted as functions of normalized SiO$_2$ and Au thicknesses; baseline $\omega \cdot \eta = 0.005592$ GPa. Crosshatched areas indicate regions where no solution was obtained.
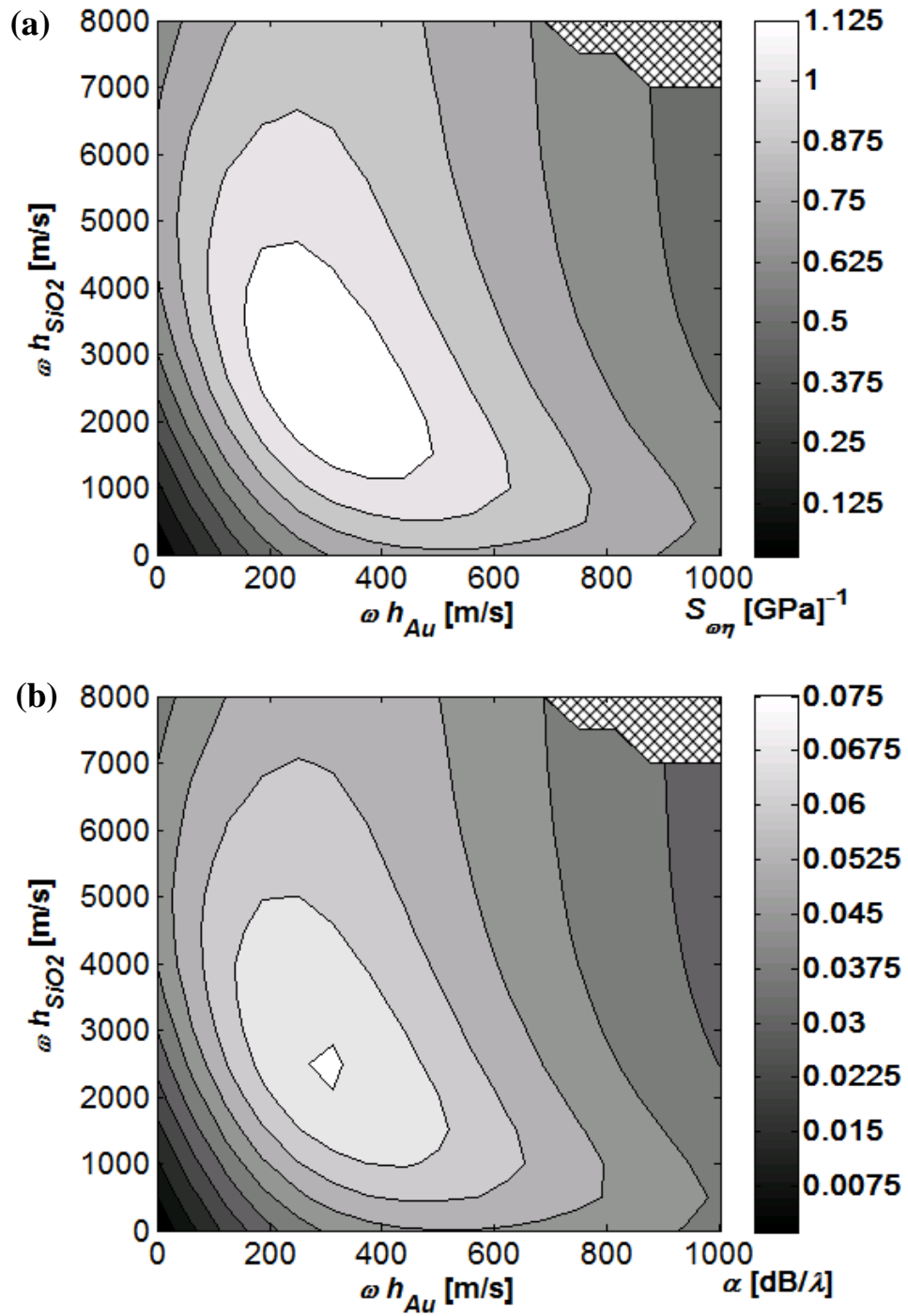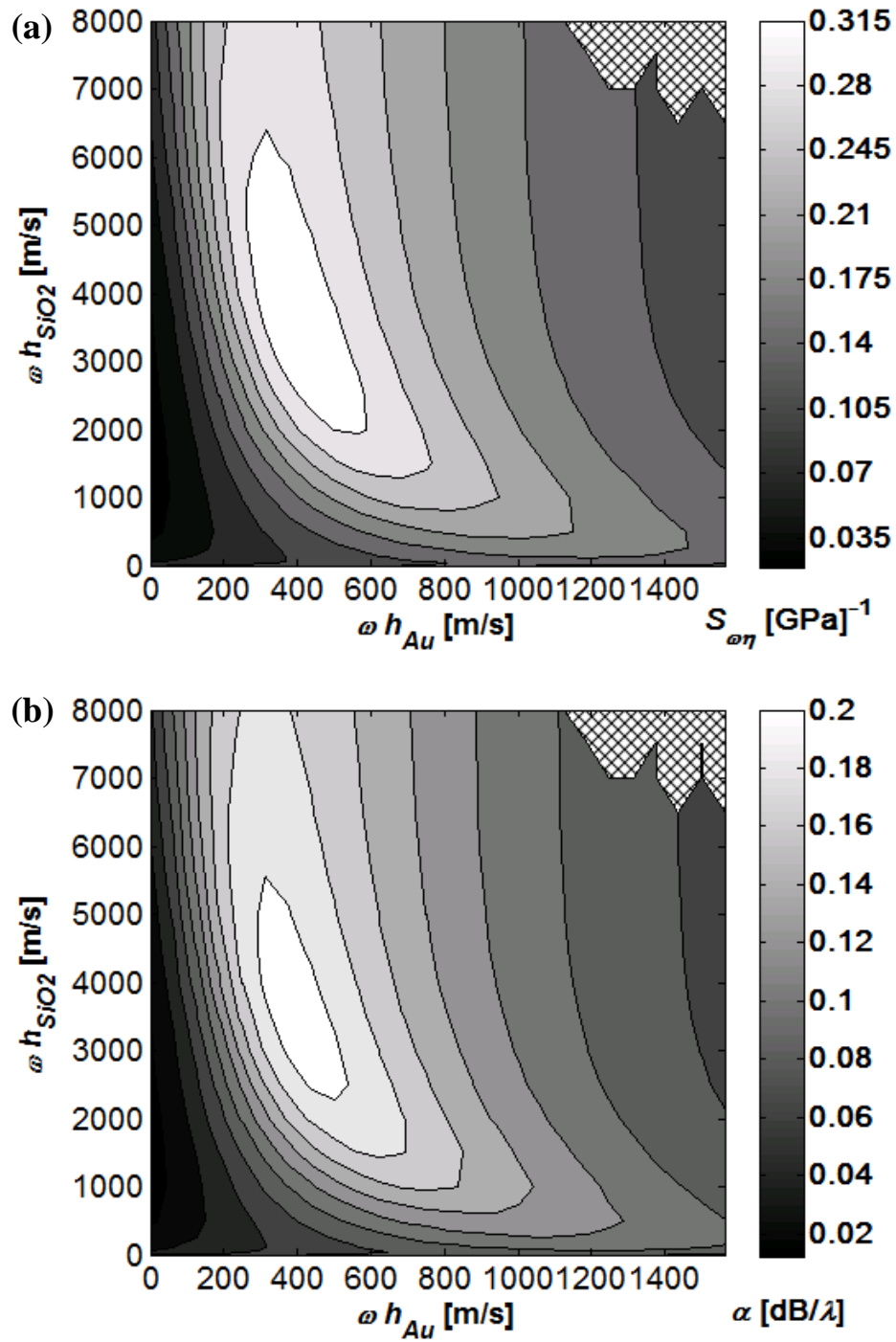
Figure 3.13. KNB, Euler Angles $(0°, 90°, 0°)$, (a) sensitivity to $\omega \cdot \eta$, and (b) propagation loss, α. Parameters are plotted as functions of normalized SiO_2 and Au thicknesses; baseline $\omega \cdot \eta = 0.005592$ GPa. Crosshatched areas indicate regions where no solution was obtained.
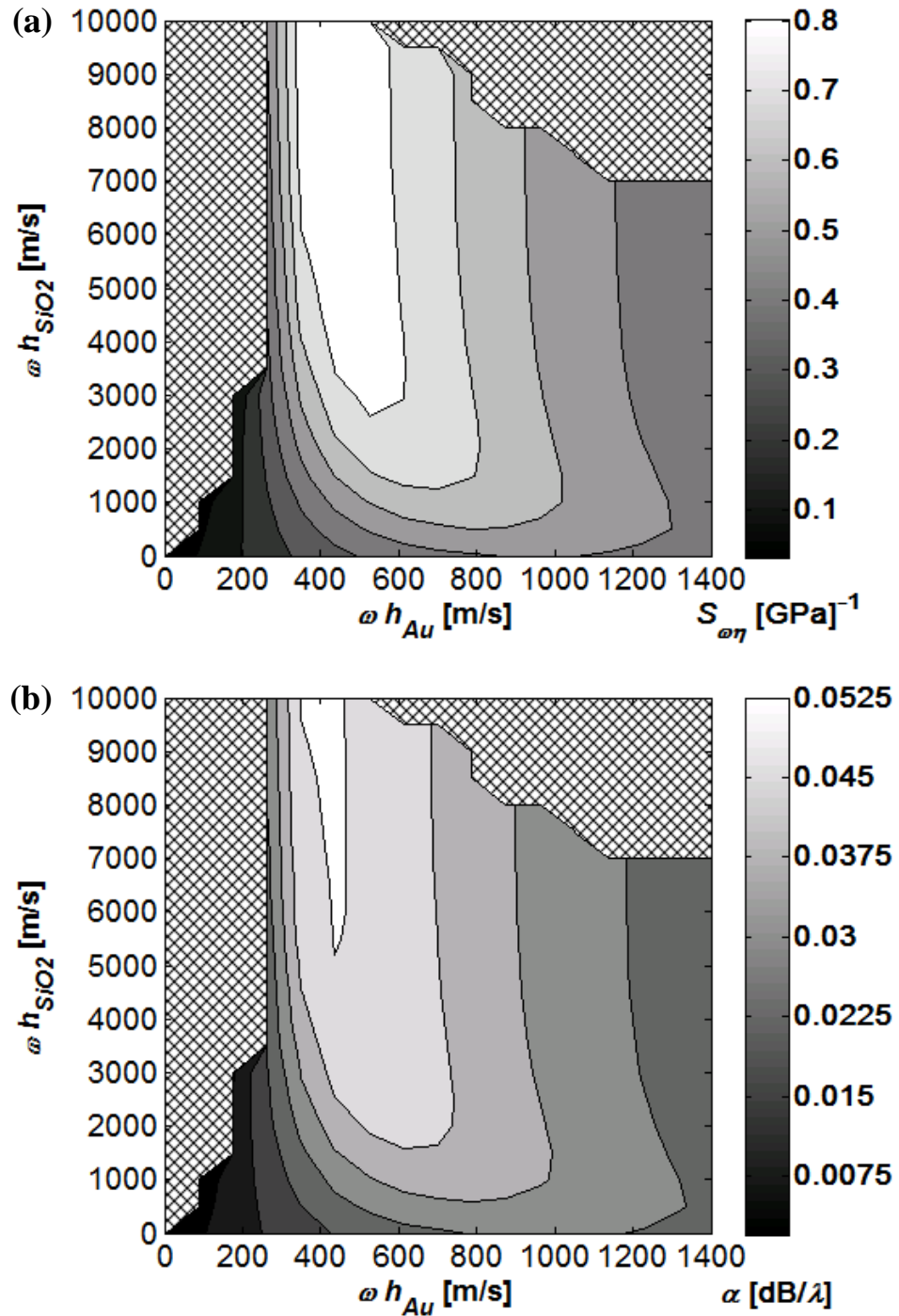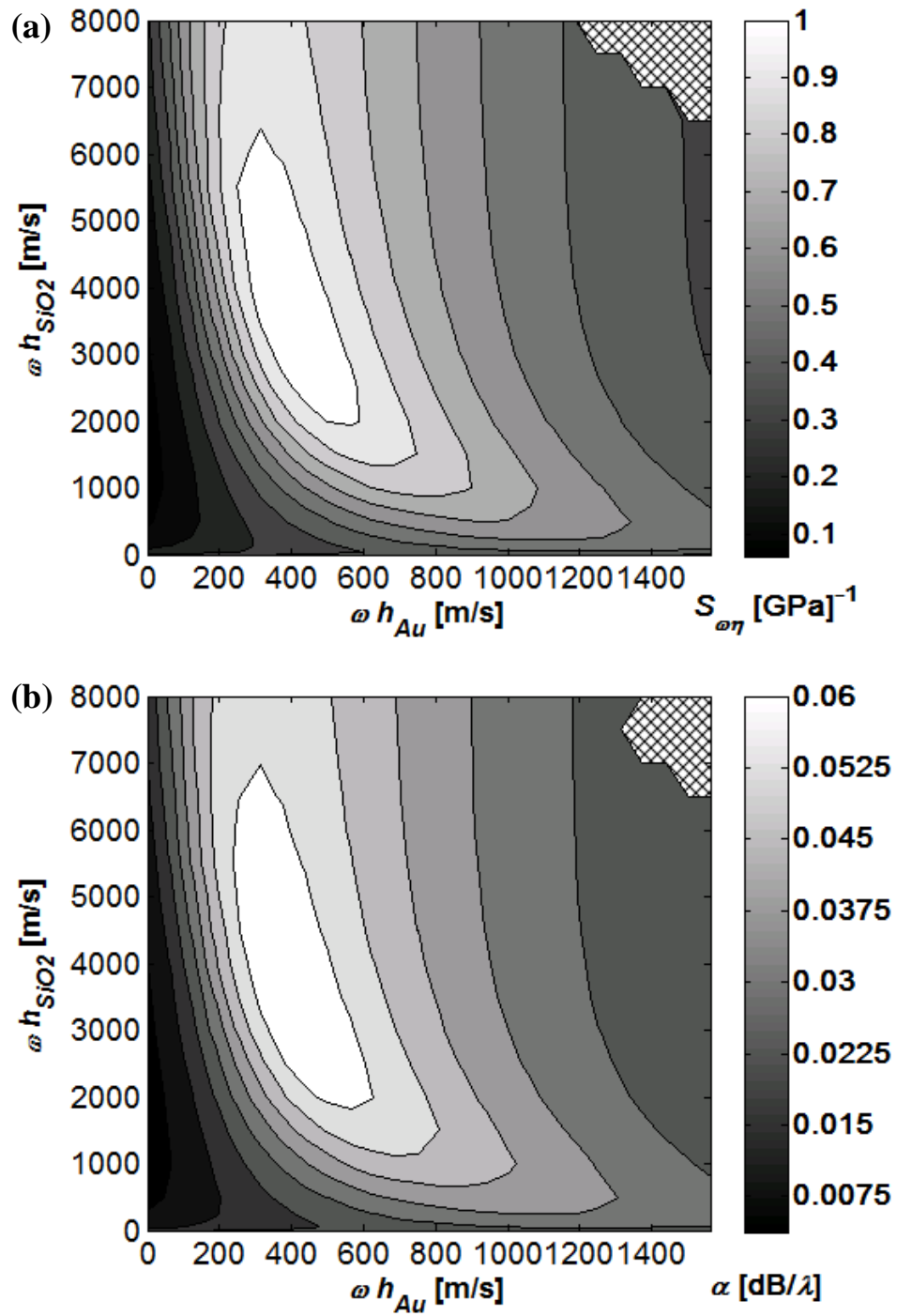
Crosshatched regions of figures indicate where no SHSAW mode is identified for corresponding values of h_{SiO2} and h_{Au}, as either the mode does not exist or is too weakly coupled piezoelectrically to be identified by the implemented Green's function pole searching algorithm. In all situations presented, optimal thicknesses of guiding SiO_2 and Au layers producing maximal SHSAW sensitivity to fluid viscosity are identified. In particular, for the QTZ case evaluated at $\omega \cdot \eta = 0.0005592$ GPa, a maximum sensitivity of 1.23 GPa^{-1} is achieved when $\omega \cdot h_{SiO2}$ and $\omega \cdot h_{Au}$ are approximately 2500 and 312.5 m/s, respectively. As for the SHSAW attenuation due to viscous loading, a maximal value of 0.0756 dB/λ is given for the same $\omega \cdot h_{SiO2}$ and $\omega \cdot h_{Au}$. For LGS evaluated at $\omega \cdot \eta = 0.0005592$ GPa, a maximum sensitivity of 0.87 GPa^{-1} is achieved when $\omega \cdot h_{SiO2}$ and $\omega \cdot h_{Au}$ are approximately 8000 and 437.5 m/s respectively; a maximum attenuation of 0.0532 dB/λ occurs for the same $\omega \cdot h_{SiO2}$ and $\omega \cdot h_{Au}$. For KNB evaluated at $\omega \cdot \eta = 0.0005592$ GPa, a maximum sensitivity of 1.08 GPa^{-1} is achieved when $\omega \cdot h_{SiO2}$ and $\omega \cdot h_{Au}$ are approximately 3500 and 375 m/s respectively; a maximum attenuation of 0.066 dB/λ occurs for the same $\omega \cdot h_{SiO2}$ and $\omega \cdot h_{Au}$. As for the effect of increasing $\omega \cdot \eta$ by a factor of 10 to 0.005592 GPa, in the QTZ case, a maximal sensitivity of 0.3885 GPa^{-1} occurs for the same $\omega \cdot h_{SiO2}$ and $\omega \cdot h_{Au}$ combination that maximized sensitivity when $\omega \cdot \eta = 0.0005592$ GPa. Attenuation maxima trend similarly and are observed at 0.239 dB/λ. For LGS, a maximal sensitivity of 0.274 GPa^{-1} is observed at the same $\omega \cdot h_{SiO2}$ and $\omega \cdot h_{Au}$ that maximized sensitivity when $\omega \cdot \eta = 0.0005592$ GPa. Maximal attenuation is 0.168 dB/λ. For KNB, a maximal sensitivity of 0.340 GPa^{-1} is observed at the same $\omega \cdot h_{SiO2}$ and $\omega \cdot h_{Au}$ that maximized sensitivity when $\omega \cdot \eta = 0.0005592$ GPa. Maximal

attenuation is 0.209 dB/λ. These results indicate that mode attenuation and sensitivity are highly correlated. In particular, Figure 3.14 shows the correlation between SHSAW attenuation and sensitivity to DI water viscosity after de-normalizing the reported $S_{\omega\eta}$ to S_η via multiplication by radian operating frequency.
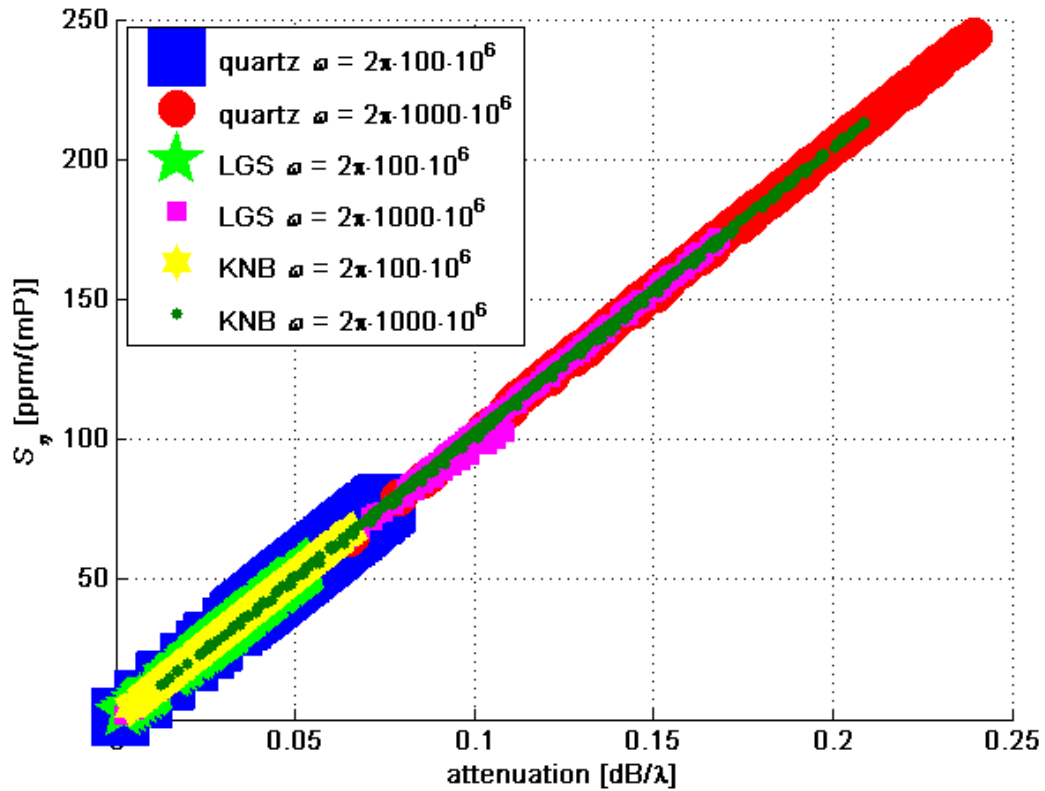
Figure 3.14. SHSAW sensitivity to DI water viscosity, S_η, as function of mode attenuation for QTZ Euler angles (0°, 132.75°, 90°), LGS Euler angles (0°, 22°, 90°), and KNB Euler angles (0°, 90°, 0°); data gathered using the same $S_{\omega\eta}$ data presented after de-normalized to operating frequencies of 100 and 1000 MHz.

Figure 3.14 suggests the tradeoffs involved in choosing materials for SHSAW liquid-phase viscosity sensing: materials providing higher viscosity sensitivity (in this case, quartz) involve increased mode attenuation per wavelength, a correlation that

appears to be independent of piezoelectric substrate material. A linear fit of Figure 3.14 data reveals the correlation relationship to be approximately 1000 ppm/(mP)/(dB/λ). When this relationship is used with the sensor resolution relationship given by (3.13), and assuming *TCD* to be small relative to viscosity sensitivity, or ΔT to be zero, then the sensor resolution is approximated by:

$$
\left| \Delta \eta \right|_{\min} \approx \frac{1000}{\alpha \cdot r} \frac{\tan^{-1}\left(\dfrac{Q(r) \cdot 10^{\frac{\alpha \cdot r}{20}}}{\sqrt{1 - Q(r)^2 \cdot 10^{\frac{2\alpha \cdot r}{20}}}} \right) + \left| \Delta \phi_{\min} \right|}{\pi} \ \text{[mP]},
\tag{3.16}
$$

where:

- r is length of delay region in units of wavelengths,
- α is the SHSAW attenuation in units of dB/λ,
- $Q(r) = \left| \dfrac{S_{21}^{spurious}}{S_{21}^{SHSAW}} \right|$ is the magnitude of spurious signal to SHSAW signal

  detected by output IDT without viscous fluid loading,

- $\left| \Delta \phi_{\min} \right|$ is the phase resolution of the measurement system in radians.

Figure 3.15 shows the expected viscosity resolution obtainable as a function of total attenuation due to viscous loss, $\alpha \cdot r$, and the magnitude of spurious signal to SHSAW detected without viscous loading, $Q(r)$, for $|\Delta \phi_{\min}|$ values of 0.1° and 1°. From Figure 3.15, optimal values of $\alpha \cdot r$ can be determined for a given $Q(r)$ in both cases. Crosshatched regions indicate where the detected spurious signal exceeds the detected SHSAW signal after considering signal attenuation due to viscous loading.
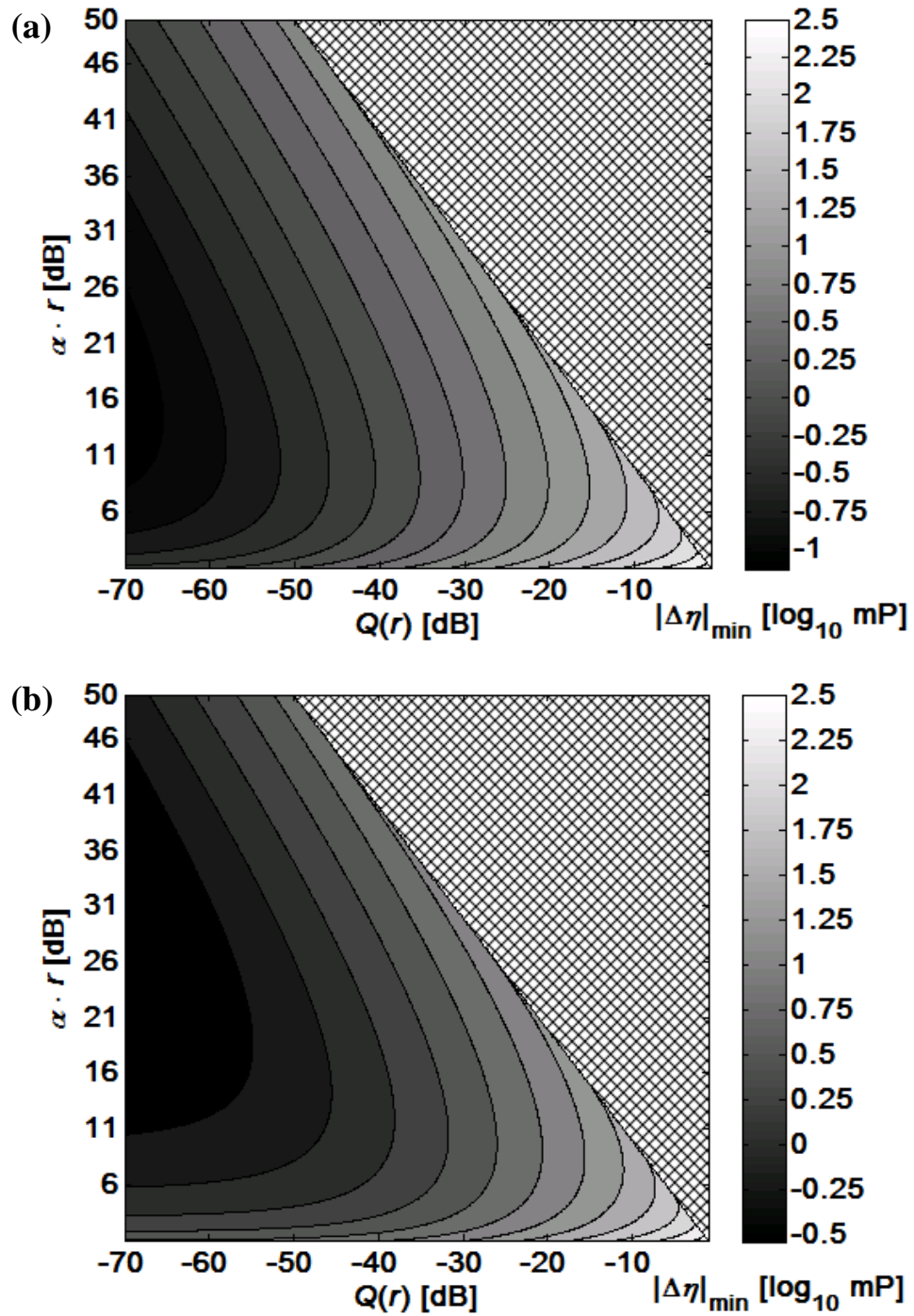
Figure 3.15. Expected sensor minimum detectable change in viscosity as function of SHSAW attenuation due to viscous loading and ratio of detected of spurious signal to SHSAW. In (a) $|\Delta\phi_{min}| = 0.1°$; (b) $|\Delta\phi_{min}| = 1°$.

Figure 3.15 indicates that viscosity sensor resolution based on delay-line SHSAW sensors can be at best around 0.1-1 mP with a realistic design (about ½ an order of magnitude improvement in resolution is attained if $|\Delta\phi_{min}| = 0.1°$ compared to $|\Delta\phi_{min}| = 1°$). This corresponds to approximately 1-10% of the nominal room temperature value of DI water viscosity (0.89 cP). It should be noted that this result neglects the effect of *TCD* and temperature variation, which will further decrease achievable resolution. In addition, this result indicates that achievable resolution is proportional to $Q(r)$ for a particular range and thereafter limited by $|\Delta\phi_{min}|$. To relax the requirements of $|\Delta\phi_{min}|$ and so reduce sensor interrogation cost, $Q(r)$ should be minimal. Note that $Q(r)$ in practical circumstances is not easily determined numerically as a function of IDT separation distance, but is used here to determine the maximum sensor resolution of a design, guaranteed to an have upper limit of $Q(r)$. Methods to improve $Q(r)$ for SHSAW delay-line devices by placing guiding structures alongside IDTs will be presented in the next section.

It should be mentioned that other reported viscosity sensitivity analysis techniques [86] apply perturbation theory, a less rigorous approach than the numerical method adopted in this work. A comparison of the methods may be given by means of a relevant example, establishing the approximate normalized phase and attenuation shifts due to viscous loading. These are proportional to the square-root of the radian frequency-viscosity-density product and a sensitivity parameter, given by *S*. In particular, the relationship developed in [86] is given by:

$$\Delta\alpha/\beta = \Delta\beta/\beta = S\sqrt{\omega\eta\rho/2} \qquad (3.17)$$

where:

- The complex propagation constant is given as $\gamma = \alpha + j\beta$,

- β is the unperturbed real propagation constant, and

- S is the device sensitivity parameter.

This result shows that mode attenuation and sensitivity are linearly related as observed using the numerical technique presented and the data shown in Figure 3.14. To verify the observed correlation using the model implemented in this dissertation, S must be related to the sensitivity-to-viscosity parameter, S_η (defined in (3.7)). Using (3.17) and the definition of S_η, it can be shown that relationship between sensitivity parameters is given by:

$$S = 2S_\eta\sqrt{\frac{2\eta}{\omega\rho}}. \qquad (3.18)$$

Substituting (3.18) into (3.17) and simplifying yields

$$\Delta\alpha/\beta = \Delta\beta/\beta = 2S_\eta\eta. \qquad (3.19)$$

With (3.19) it can be shown that the expected S_η is proportional to the mode attenuation in units of dB/λ by the factor $1/(80 \cdot \pi \cdot \eta \cdot \log_{10} e)$ after using the relationships $\beta = \dfrac{2\pi}{\lambda}$ and attenuation (in units of dB/λ) is given as $20\log_{10}\left(e^{\Delta\alpha\lambda}\right)$. Given the value of viscosity chosen for water and used for the presented numerical results, 8.9 mP, this factor is equal to 1029 ppm/mP/(dB/λ), which is relatively close to the approximate value of 1000 ppm/mP/(dB/λ) extracted from Figure 3.14. The two sensitivity techniques seem to agree well at least for fluids with properties close to DI water. It should be noted here in

passing that the authors in [86] also give a relationship, $S_m = \omega \cdot S$, between the device sensitivity parameter, S, and a mass sensitivity parameter, S_m, which will be applied in Chapter 5 to compare the performance of a device developed in this work to values reported in the literature.

3.4. SHSAW Excitation/Detection Characterization

In Sections 3.2 and 3.3 it was shown that the achievable performance of SHSAW delay-line based liquid-phase sensor platforms can be improved by increasing the level of detected SHSAW signal to spurious signal. In this section, IDT designs are studied in terms of better exciting the SHSAW mode of interest, reducing spurious signal excitation and detection, and consequently improving the performance of liquid-phase sensor platforms. In particular, designs are evaluated in terms the parameter, η_{SHSAW}, which is defined as input power transduced to the SHSAW mode relative to the total IDT input power. By reducing the SHBAW excited by an IDT a greater proportion of SHSAW signal should be detected by the output IDT, improving overall sensor performance. It is shown that the IDT surrounding boundary condition strongly affects achievable η_{SHSAW}. In particular, it is demonstrated that η_{SHSAW} can approach 100% by using guiding structures placed alongside the IDT. The analysis also shows finite thickness electrodes made of relatively dense materials play a strong role in improving η_{SHSAW}. Many of the results and modeling techniques presented in the section have been published by the author in [52]. Additional related publications authored or co-authored by the author of this document, of which some directly lead up to [52], include [87], [88], [89], [60], [90], [51], [91].

The analysis presented makes use of an implemented FEM/BEM simulation tool that is based on the finite and periodic model theory discussed in Chapter 2. Four IDT surrounding boundary conditions are considered (refer to Figure 3.16): (i) single IDT with finite thickness electrodes surrounded by an electrically and mechanically free surface; (ii) single IDT with finite thickness electrodes surrounded by one semi-infinitely long guiding electrodes having finite-thickness and placed on either side of IDT; (iii) single IDT with finite thickness electrodes surrounded by two semi-infinitely long guiding electrodes having finite-thickness and placed both sides of the IDT; and (iv) single IDT with finite-thickness electrodes surrounded two semi-infinitely long periodic guiding grating electrode structures having finite thickness and placed on both sides of the IDT.
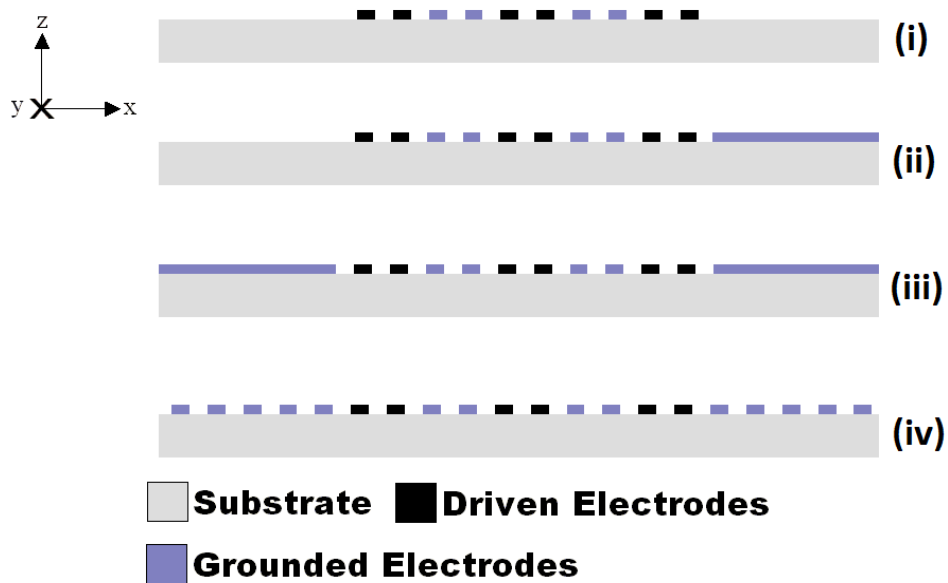
Figure 3.16. IDT surrounding boundary conditions considered for η_{SHSAW} evaluation.

Structures (i) and (iii) have been studied in previously reported work and explored in terms of η_{SHSAW} [45], but the authors neglected the effect of finite-thickness electrodes, which may be satisfactory given that the author studied pure shear excitation on a highly piezoelectric material, i.e. lead zirconate titanate (PZT), and the fact that at that time aluminum electrodes were typically employed, which are relatively much less dense than those considered in this work, e.g. Au. In this work a similar model was implemented, but also includes the effect of finite thickness of all electrodes, which is shown to be necessary for accurate estimation of η_{SHSAW} for the important cases of quartz and LGS substrates. Including finite-thickness electrode effects for case (i) involves a relatively straightforward combination of methods presented in [45] and [46]. For cases (ii) and (iii), incorporating the finite thickness of guiding electrodes proves challenging as the interfacial stress sources along the guiding electrode substrate interface extend infinitely and thus are not compatible with reported FEM/BEM models. In this work, for the first time, η_{SHSAW} for the case (ii) and (iii) structures, inducing finite thickness of guiding electrodes, is rigorously extracted using the implemented FEM/BEM model in conjunction with a novel acoustic matching technique. Details of the method are presented in Section 3.4.2. For the case (iv) structure, using an implemented periodic FEM/BEM model based on the theory developed in Chapter 2, η_{SHSAW} is reported for the first time, after extending the theory reported in [59]. In all three cases, η_{SHSAW} is studied as a function of substrate material/orientation, electrode material and thickness, and number of IDT transducer pairs. The results reported here were used to design IDT configurations of prototype liquid-phase sensing platforms targeting improved

129

performance by increasing SHSAW transduction and thus reducing spurious signal detection by an output IDT.

3.4.1. Surrounding Free Surface IDT Analysis

Using an implemented finite full-wave FEM/BEM model based on the formalism presented in Chapter 2, IDT structures with surrounding mechanically and electrically free surfaces were simulated in the frequency domain. The value of η_{SHSAW} was extracted from the numerical results based on methods presented in Appendix C. In particular, Appendix C presents the method used to calculate the excited SAW power present in the far-field far away from either side of the IDT. Given the total IDT input power, which is computed using the determined IDT conductance for a specified applied voltage, and the determined excited SAW power thus permits extraction of η_{SHSAW}. The extraction process is valid for general symmetry orientations, and is thus also valid for orientations that present pure shear horizontal coupling where some fields decouple electrically, i.e. T_5, T_3, $j\omega u_1$, and $j\omega u_3$. The method used to determine the IDT input impedance or admittance is described next.

Based on simulation results of an IDT, the charge and stress distributions at electrode/substrate interfaces are determined for a given electric potential applied to the IDT. Using the determined charge distribution, the admittance of the transducer is determined by calculating the total current entering the driven electrodes, which, using (2.33), is given by:

$$I = j\omega W \int_{-\infty}^{\infty} \sigma_{driven}(x)dx = j2\pi\omega W \sum_{s=drivenInds} w_4^s f_4^s (k_x = 0), \tag{3.20}$$

where:

- W is the device aperture,
- σ_{driven} is charge density on the driven electrodes,
- $drivenInds$ are charge density basis function indices for the driven electrodes.

Given a specified value of the peak voltage applied across the IDT, V, which is used to solve the model, the IDT input conductance and time average power entering the IDT are given, respectively, by:

$$Y_{in} = \frac{I}{V}, \tag{3.21}$$

and

$$P_{in} = \frac{1}{2}\Re\{Y_{in}\}|V|^2. \tag{3.22}$$

This concludes the η_{SHSAW} extraction presentation for the case (i) considered topology.

As an example, extracted η_{SHSAW} is presented for the pure shear horizontal orientation of langasite Euler angles (0°, 22°, 90°). (A similar analysis is not possible for the shear horizontal orientation of quartz Euler angles (0°, 132.75°, 90°) as no mechanically and electrically free SHSAW mode exists.) A similar analysis for KNbO$_3$ Euler angles (0°, 90°, 0°) published by the author [90] showed that under case (i) η_{SHSAW} varies between 1 and 2% for IDTs containing 1.5 to 5.5 wavelengths of active electrodes, while under case (iii) η_{SHSAW} is above 98% for the same considered IDTs. It should mentioned that in [90] the effect of electrode finite thickness on the guiding electrodes

131

was not included in the analysis as it was published relatively early in this dissertation work and the appropriate theory had yet to be developed.

The value of η_{SHSAW} is in general a function of IDT excitation frequency, but in this dissertation η_{SHSAW} is extracted only at the approximate frequency of maximum IDT conductance, where the IDT is typically operated and is generally most efficient regarding excitation of the SHSAW mode. To determine the approximate peak conductance frequency, the IDT impedance was calculated using the periodic FEM/BEM model described in Chapter 2, where semi-infinite synchronous periodic guiding grating electrode structures are alongside each side of the IDT. This technique was chosen because computation time is greatly reduced compared to finite device analysis. The frequency of maximum IDT conductance assuming surrounding guiding gratings is in general a very good approximation and typically was observed to fall within a few percent of the finite device IDT maximum conductance frequency. For the simulation results presented, IDT electrodes are assumed 4 μm in width, mark-to-space ratio of 1:1, and be of split-type, or + + - -, to reduce spurious triple transit detection in an actual 2-port device. The number of split-finger pairs, L_{eff}, under consideration was 4.5, 9.5, 19.5, 39.5, and 79.5, where as an example 2.5 pairs would have spatial voltage distribution on electrodes given as - - + + - - + + - -. Field dependence along the aperture dimension is assumed uniform, and therefore the η_{SHSAW} results are assumed independent of IDT aperture W. In terms of electrode metal material and thickness, for the simulations electrodes were assumed composed of isotropic Au with thicknesses equal to 750, 1500, 3000, or 6000 Å. Figure 3.17 plots the η_{SHSAW} extracted.
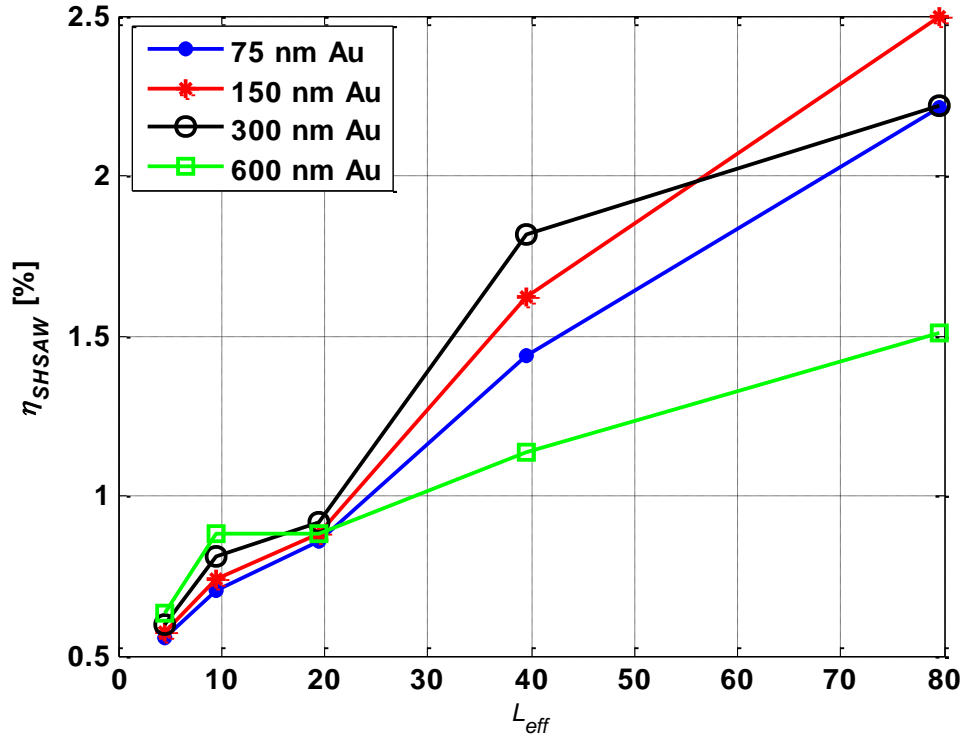
Figure 3.17. η_{SHSAW} for LGS Euler angles (0°, 22°, 90°) for IDTs with surrounding mechanically and electrically free surfaces vs. IDT length and Au thickness.

It is observed that in all cases less then 3% of IDT input power is transduced to the mode of interest, with the remaining energy being transduced to the spurious SHBAW. This result indicates incorporation of guiding structures is required for efficient delay-line platforms, as shown in the upcoming sections. Although the majority of input power is transduced to the SHBAW spurious mode, a few trends can be observed regarding η_{SHSAW} in Figure 3.17. In particular it is observed that increasing L_{eff} seems to increase efficiency for all cases of electrode metal thickness as the IDT becomes longer. In addition, it appears that using thicker IDT electrodes results in reduced η_{SHSAW} as the IDT becomes long and when the value of η_{SHSAW} begins to level out w.r.t. L_{eff}. The following discussion attempts to explain these results.

At the frequency $f = 1 / (4ps_g)$, where p is the periodicity of the electrodes in the IDT and s_g is the short-circuit grating mode slowness, the IDT conductance takes on a maximum value as the transducer becomes longer as excitation of the mode supported under the IDT region becomes constructive. The values of s_g (a function of f) and f which satisfy constructive interference depends on the electrode thickness as the mode is dispersive due to incorporation of electrodes with finite thickness. For the Au/LGS case studied here, s_g is always greater than the free surface SHSAW slowness (s_o) and increases with increasing electrode thickness as the total mass fixed to the surface increases. As the IDT becomes longer the wave sources σ and T_4 at the substrate/electrode interfaces become somewhat spatially periodic with period equal to 4p (by "somewhat" it is meant that the overall distribution is also multiplied by a finite-length window function). Therefore the IDT the spectral distribution of the sources takes on that of a windowed (due to finite L_{eff}) sum of harmonics, i.e. a sum of functions similar to sinc functions which are centered at $\pm s_x^n = \pm s_g + \dfrac{n}{f\,p}$ (see Chapter 2 Section 2.7 regarding the periodic model for more information on this). Therefore as the IDT becomes longer, the spectral distribution of the wave sources approach a series of Dirac delta functions located at $\pm s_x^n$. Given that s_o is closer to s_g compared to the SHBAW slowness region, it makes sense that as the IDT length begins to increase from a single electrode pair that η_{SHSAW} increases as the energy becomes more concentrated around s_g and s_o. At some point as L_{eff} becomes even larger, and the spectral energy becomes even further concentrated, η_{SHSAW} will level off as there is a finite difference between s_g and s_o. Given that this difference is greater for thicker films, it makes sense that the point at

which η_{SHSAW} begins to level off occurs faster w.r.t. L_{eff}. The author believes this is the reason why use of thicker electrodes results in reduced maximum achievable η_{SHSAW} as L_{eff} becomes very large. With this reasoning in mind, it would suggest that to achieve maximum η_{SHSAW} the supported mode along the delay regions should have the slowness value as the mode supported in the IDT region. In addition, if this condition is satisfied, η_{SHSAW} will improve faster, w.r.t increasing L_{eff}, if the two modes are further slowed away from the SHBAW slowness region. The results presented in the upcoming sections indicate that these theories are correct.

3.4.2. Surrounding Uniform Plate IDT Analysis

The extraction of η_{SHSAW} for IDTs with surrounding uniform guiding electrodes while considering the finite metal thickness of all electrodes in the structure was reported first by the author of this dissertation in [52]. Such an analysis had not been previously developed due to the added computational complexities encountered by including finite metal thickness of guiding electrodes as the unknown interfacial stress and charge sources extend infinitely along the substrate/electrode interface, which must be solved for. Reported theories used to solve for the interfacial source fields had only been applied to finite length electrodes. In this work it is shown that for liquid phase sensor applications it proves very important to take into account the thickness of all electrodes for accurate extraction η_{SHSAW}, as this value directly relates to the achievable sensor performance.

135

Simulating such a structure using a traditional finite FEM/BEM model requires solving for the stress and charge density sources located at the semi-infinite length electrode/substrate interface. However, convergent basis functions for representing these fields over a semi-infinite domain have not been reported in the literature. As a first attempt to solve this problem, new basis functions for the semi-infinite electrodes were explored in this work; in particular, basis functions consisting of associated orthogonal Laguerre polynomials [92] and a single sinusoidal basis were used to represent the combination of electrostatic effects, and evanescent and SHSBAW modes; and SHSAW field contributions, respectively. After many attempts using such basis function sets, including trying various Laguerre polynomial parameters, with implemented finite FEM/BEM models, it was determined such basis function sets does not provide adequate solution convergence.

As an alternative, truncating the length of the guiding electrode was considered, as it allows extraction of a rough estimate for η_{SHSAW}. Results however become inaccurate as electrode thickness increases due to stronger SHSAW reflection from the truncated electrode edge. Edge discontinuities cause reflected signals to be redetected at the IDT electrical port, prohibiting accurate extraction of the IDT input power that would be obtained if the truncated electrode were extended infinitely. Use of Fourier frequency-time analysis to obtain the time response of fields might overcome the error introduced by edge discontinuity, but such a method requires simulation at many frequencies, which is impractical from a computational perspective, as it may take hours to simulate a single frequency point for some of the longer devices considered in this

136

work. Another possibility involves simulation using models based on finite-difference time-domain analysis (FDTD) [56], which allows direct simulation in the time domain, or FEM with application of absorbing boundary conditions [54,55]. As an alternative, a frequency domain FEM/BEM model developed by the author, as described in this section, proved sufficient for excitation of η_{SHSAW}, and use of these two other potential methods were not further investigated.

To apply existing software models, particularly the already implemented finite-length FEM/BEM model used to simulate finite SAW devices without semi-infinite guiding electrodes, it was hypothesized that simulation of a modified finite structure that behaves as if the electrode extends infinitely is possible. Using transmission line matching concepts, a wave 'matching' scenario for the truncated electrode was envisioned. The 'matching' would effectively cancel the reflected SHSAW resulting from the structure discontinuity, so the device would behave as though the guiding electrode extends infinitely, in terms of the impedance 'seen' by the IDT. The simulation generates accurate information about the IDT input power and amplitude of the excited SHSAW along the guiding electrode region. Using a traditional transmission line quarter-wave transformer matching technique, this work shows that by adding an additional "matching electrode" placed directly after a long truncated guiding electrode, the reflected SHSAW at the discontinuity is canceled.

The modified structure considered for the analysis of cases (ii) in Figure 3.16 is depicted in Figure 3.18 (a).
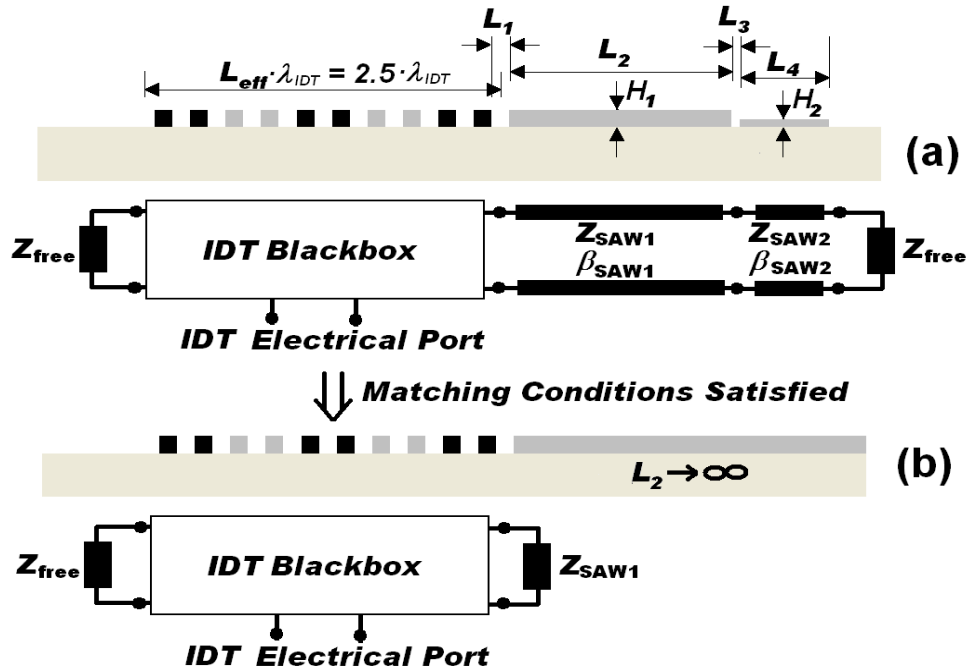
Figure 3.18. (a) Truncated structure simulated including a matching electrode and the analogous transmission line representation (where λ_{IDT} is the IDT periodicity). Represented in the figure, $L_{eff} = 2.5$; (b) equivalent structure and transmission line representation when quarter-wave transformer matching requirement is met.

Instead of studying a semi-infinite electrode, a long truncated electrode is used and followed by an additional "matching" electrode placed directly after the guiding structure. The uniform long guiding electrode cannot be simply truncated without the incorporation of the "matching" electrode because acoustic reflections from the electrode edge discontinuity normally interact strongly with the launching IDT making it difficult to estimate the IDT input power of the referred structure. Through the adjustment of the 'matching' electrode dimensions, namely the film thickness and length, the reflected SHSAW at the truncated electrode can be effectively canceled. As a result, the IDT input

admittance and the magnitude of the guided SHSAW mode along the truncated electrode region can be estimated as if the electrode extended infinitely. In addition to the structure simulated, Figure 3.18 (a) also shows an analogous transmission line representation. If the truncated electrode of length L_2 and thickness H_1 is long relative to wavelength, only the guided SHSAW is present at the surface far away from the IDT. Such a situation can be modeled as an electromagnetic wave propagating on a transmission line having characteristic impedance Z_{SAW1} and propagation constant $\beta_{SAW1} = \omega \cdot s_{SAW1}$, where ω is radian frequency and s_{SAW1} is the inverse velocity or slowness of the SHSAW for the analogous uniform-layer over a semi-infinite substrate propagation condition. The matching electrode of length L_4 and thickness H_2 is modeled in the same way, and has characteristic impedance Z_{SAW2} and propagation constant $\beta_{SAW2} = \omega \cdot s_{SAW2}$. The load impedance Z_{free} is analogous to the impedance looking towards the free surface. The matching technique employed in this work is analogous to transmission line quarter-wave transformer theory. It is shown that by altering H_2 that the effective Z_{SAW2} is modified, and by varying L_4 the effective electrical length is modified. Thus, by adjusting each parameter the quarter-wave transformer matching criterion:

$$Z_{SAW2} = \sqrt{Z_{SAW1} \cdot Z_{free}} \text{ , and } L_4 = \frac{\pi}{2 \cdot \beta_{SAW2}} (1 + 2 \cdot n), \qquad (3.23)$$

can be satisfied, where n is a non-negative integer. Under this condition, the SHSAW reflected power at the truncated electrode edge is cancelled at a particular frequency, and the structure behaves as if the electrode extends infinitely, as indicated in Figure 3.18 (b).

A case study is now presented to demonstrate the η_{SHSAW} calculation technique based on the structure defined in Figure 3.18. The split-finger IDT considered consists of 4 μm electrodes, $L_{eff} = 4.5$, IDT periodicity, $\lambda_{IDT} = 32$ μm, 1:1 mark-to-space ratio, $L_1 = 4$ μm, $L_2 = 800$ μm, $L_3 = 2$ μm, $L_4 =$ variable (varying from 33.5 to 36.5 μm), $H_1 = 300$ nm, and $H_2 =$ variable (varying from 190 to 260 nm). The IDT has acoustic aperture $W=1600$ μm and is oriented along quartz, Euler angles (0°, 132.75°, 90°). Using the implemented FEM/BEM tool and dimensions of the design considered in this case study, Chebyshev basis function in of orders up to 12, 100 and 20, for the 4 μm IDT electrodes, 800 μm uniform guiding electrode, and 35 μm matching electrode, respectively, were used. The analysis showed that polynomials of these orders were adequate to guarantee convergence within the IDT bandwidth. As the length of the guiding electrode increases, the dominant functional dependence of the stress and charge fields far away from the IDT and along the uniform guiding electrode resemble that of a SHSAW propagating wave. By expanding this field variation as a weighted series of the basis functions used for charge and stress representation, the respective coefficients can be determined using the orthogonality properties of the Chebyshev polynomials. Given the coefficients functional dependence with the polynomial order, an expression can be determined for the estimation of the required polynomial order to describe the SHSAW field behavior. This analysis showed that the required number of basis functions to describe the fields can be estimated by $ceiling\{1.25 \cdot \pi \cdot L_2/\lambda_g\}$, where λ_g is the SHSAW acoustic wavelength along the guiding electrode region.

The next step in the η_{SHSAW} calculation is the determination of the excitation frequency for the analysis. In this work, the frequency of maximum IDT conductance was selected as the excitation frequency. The structure given as case (iv) in Figure 3.16 was used for the determination of the approximate frequency of maximum IDT conductance, and yielded in this work, for the dimensions mentioned at the beginning of this section, a device center frequency of 150.8 MHz.

In order to proceed with the η_{SHSAW} calculation, the fields along the guiding electrode interface associated with SHSAW are extracted from the FEM/BEM results. In particular, P^+_{SHSAW} and P^-_{SHSAW}, which stand respectively for the power of the forward and backward SHSAW in the truncated electrode region, are extracted.

The FEM/BEM calculated fields along the truncated electrode interface include contributions from electrostatic effects, SHBAW, evanescent modes, and the SHSAW. The SHSAW surface normal component of stress, T_4, or the charge density, σ, can be extracted from the total contribution via Fourier transform spectral-domain fitting. For the SHSAW field fitting, T_4 was preferred over σ, as the electrostatic part of σ may have a significant contribution which makes it more difficult to extract the SHSAW contribution. Such an effect is not present in T_4, and the SHSAW contribution dominates the overall field behavior over the entire structure represented in Fig. 2.

The fitting procedure is performed as follows. Considering only the SHSAW, and neglecting any other field contribution due to electrostatics or other modes, the fitting technique assumes that T_4 along the truncated electrode/substrate interface is given as a

141

weighted sum of $+x$ and $-x$ propagating waves having velocity equal to that for the guided SHSAW, i.e.,

$$\overline{T_4}(x) = \left(T_4^+ e^{-j\beta_{SAW1}(x-c-a)} + T_4^- e^{j\beta_{SAW1}(x-c-a)}\right) \cdot [H(x-c+a)-H(x-c-a)], \qquad (3.24)$$

where c is the center position of the truncated electrode, a is the half-length of the truncated electrode and H is the Heaviside step function. T_4^+ and T_4^- are the unknown weights associated with the $+x$ and $-x$ propagating SHSAW, respectively. Using (2.15), the spectral-domain representation of (3.24) is given by:

$$T_4(k_x) = T_4^+ e^{j(k_x c + \beta_{SAW1}a)} \frac{\sin[a(k_x - \beta_{SAW1})]}{\pi(k_x - \beta_{SAW1})} + T_4^- e^{j(k_x c - \beta_{SAW1}a)} \frac{\sin[a(k_x + \beta_{SAW1})]}{\pi(k_x + \beta_{SAW1})}. \qquad (3.25)$$

An estimation of T_4^+ and T_4^- is obtained by fitting (3.25) at $k_x = \pm \beta_{SAW1}$ to the computed $\overline{T_4}(k_x)$ contribution considering only the $\overline{T_4}(x)$ field along the long guiding electrode, which is determined using (B.23) and (2.33) and the basis function weights resulting of the FEM/BEM analysis. Finally, the power associated with the forward and backward propagating SHSAW, P^+_{SHSAW} and P^-_{SHSAW}, are determined through integration of the x-directed Poynting vector along the entire z-axis, from $-\infty$ to the top surface of the electrode. The reflection coefficient looking into the matching electrode region, $|\Gamma_{SHSAW}| = |P^-_{SHSAW}/P^+_{SHSAW}|^{1/2}$, can also be estimated and is used and used to quantify the degree of matching achieved.

At the selected frequency and using the technique described above, simulations were performed for a combined range of L_4 and H_2. The thickness and length of the matching electrode were respectively varied over a range of $\pm 15\%$ and $\pm 5\%$ from their initial values. The thickness H_2 was varied first, as that requires only the FEM analysis

for the matching electrode to be recomputed, which typically runs much faster than the BEM analysis. When L_4 is modified only the affected $\mathbf{Y}_{mn}$ matrix elements of (2.34) are recomputed in order speed up the calculation.

For the example considered in this section, Figure 3.19 shows the computed $|\Gamma_{SHSAW}|$ for a variety of matching electrode lengths and thicknesses. As can be inferred from Figure 3.19, a matching condition is achieved when $L_4 = 34$ μm and $H_2 = 244.2$ nm. Using these dimensions of the matching electrode, the far-field SHSAW power is estimated using the calculated value of P^+_{SHSAW} as previously detailed in this section. In addition, the IDT input power is computed given the calculated IDT input conductance and the applied voltage. From P^+_{SHSAW} and P_{in} one calculates η_{SHSAW}.
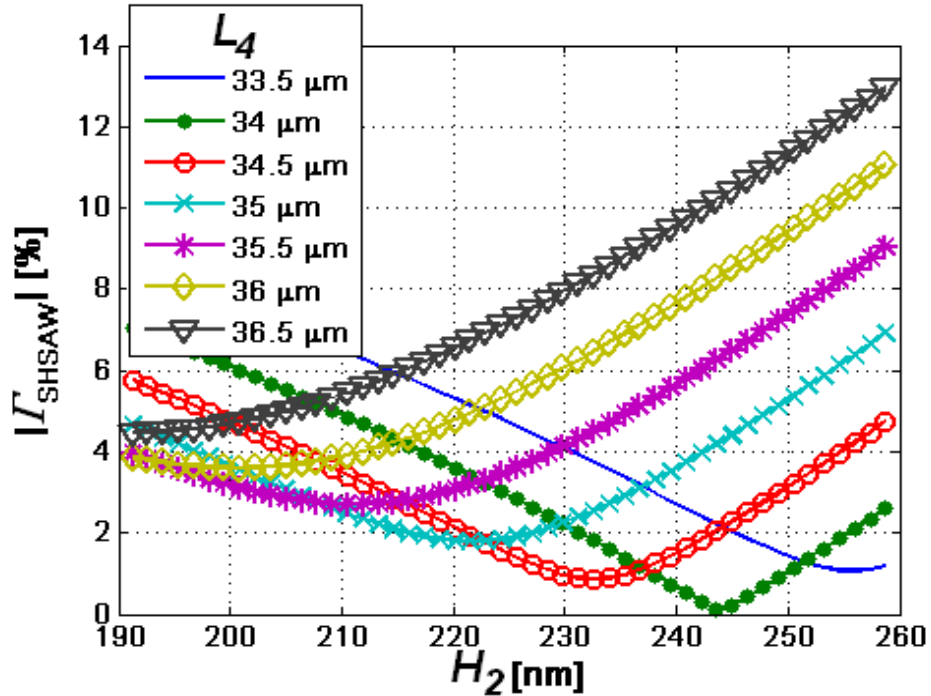
Figure 3.19. Magnitude of SHSAW reflection coefficient $|\Gamma_{SHSAW}|$ as a function of matching electrode length and thickness for the case study considered.

For the example discussed in this section, P^+_{SHSAW} = 2.549 μW (1V applied) and the IDT input admittance when matched equals 1.186e-5+j5.155e-4 S. The η_{SHSAW} for the structure in Figure 3.18 (b). is thus estimated to be 43%, with the entire SHSAW energy propagating under the long guiding electrode, since no SHSAW propagates to the other free surface side of the IDT for quartz Euler angles (0°, 132.75°, 90°) as the mode does not exist.

The effect of the matching electrode can be further appreciated in Figure 3.20, where T_4 along the electrode/substrate interface at the IDT and at the long uniform guiding electrode is plotted when the matching electrode is omitted and present, Figure 3.20 (a) and (b), respectively (1V applied). Figure 3.20 (c) plots T_4 near the matching electrode when the matching structure is present. As can be seen from Figure 3.20 (a), the omission of the matching electrode results in a standing wave along the long guiding electrode region. Alternatively, when the matching electrode with proper dimensions is included, no standing wave pattern is evident, which indicates a SHSAW matched condition. For the matched case, the field behavior along the long guiding electrode region resembles that of a SHSAW propagating wave under uniform media as one looks further away from the IDT. This indicates the SHSAW is dominant along the truncated electrode region and thus the field amplitudes can be considered as far-field values, thus appropriate to calculate η_{SHSAW}. In addition, it is interesting to note from Figure 3.20 (c), that the effective electrical length of the matching electrode is approximate 1 and ¼ wavelengths according to the stress variation, which is in accordance with the quarter-wave transformer requirement (3.23).
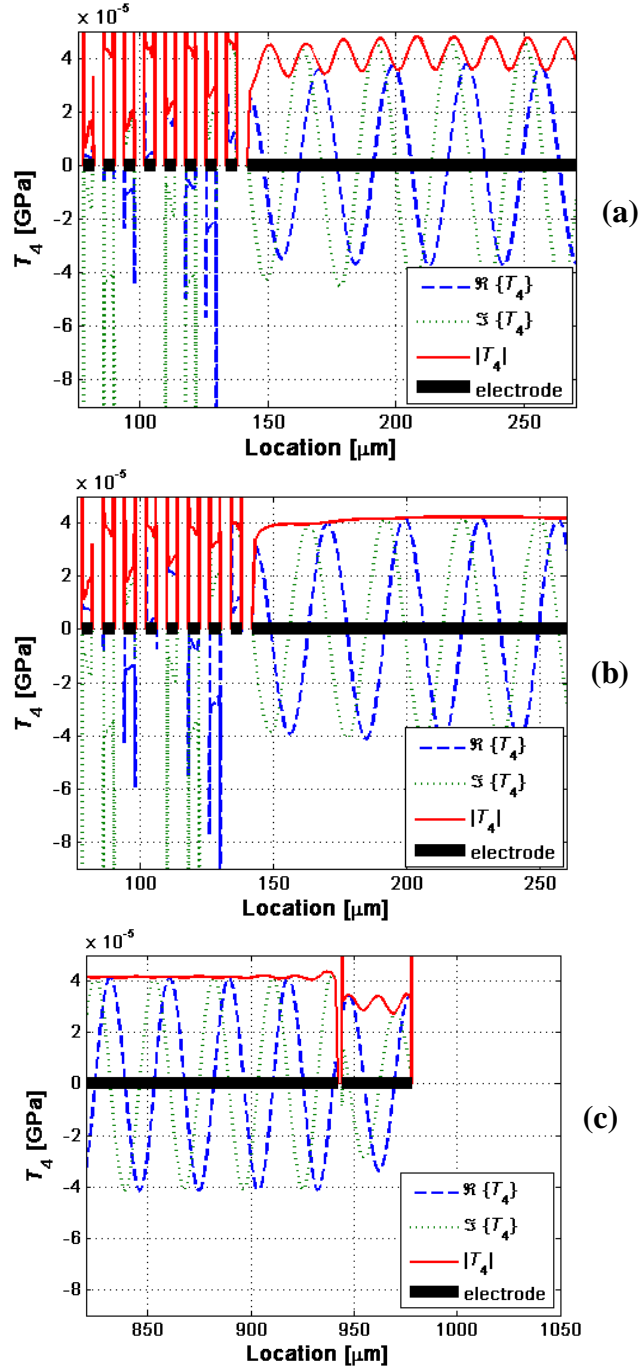
Figure 3.20. Resulting interfacial T_4 around the long guiding electrode region when (a) matching electrode is omitted, (close to IDT); (b) matching electrode included in the analysis, (close to IDT); (c) matching electrode included (close to the matching electrode). (1V applied).

It should be noted that if the guiding structure is considered on both sides of the IDT, case (iii) in Figure 3.16, the aforementioned analysis is performed twice to determine the required matching electrode dimensions for each side. Once both matching electrodes are determined, simulation is performed including both matching structures and η_{SHSAW} for each side is extracted using the technique previously described.

Based on the extraction technique just presented, η_{SHSAW} for finite-length split-finger IDTs with semi-infinite uniform guiding electrodes on one and both sides of the IDT were determined for various metallization thicknesses and number of IDT split-finger pairs. The analysis was carried out for quartz Euler angles (0°, 132.75°, 90°), Au metallization, split-finger IDT with 4 μm electrodes, $\lambda_{\text{IDT}} = 32$ μm, and mark-to-space ratio = 1:1; and with all guiding electrodes connected to the IDT ground. The structures studied consisted of IDTs with L_{eff} = 4.5, 9.5, 19.5, 39.5, and 79.5, and $H_1 = 75$, 150, 300, and 600 nm. L_1 and L_3 were chosen to be 4 μm and 2 μm, respectively. L_2 was selected as 800μm and 1200μm, and verified that the difference between extracted η_{SHSAW} was less than 1% for increased guided electrode length. Thus 800μm was adopted as a long enough guiding structure for this analysis such that if increased the extracted value of η_{SHSAW} would be affected by less than a percent. The percent variation is then considered the uncertainty for the η_{SHSAW} results presented in this section.
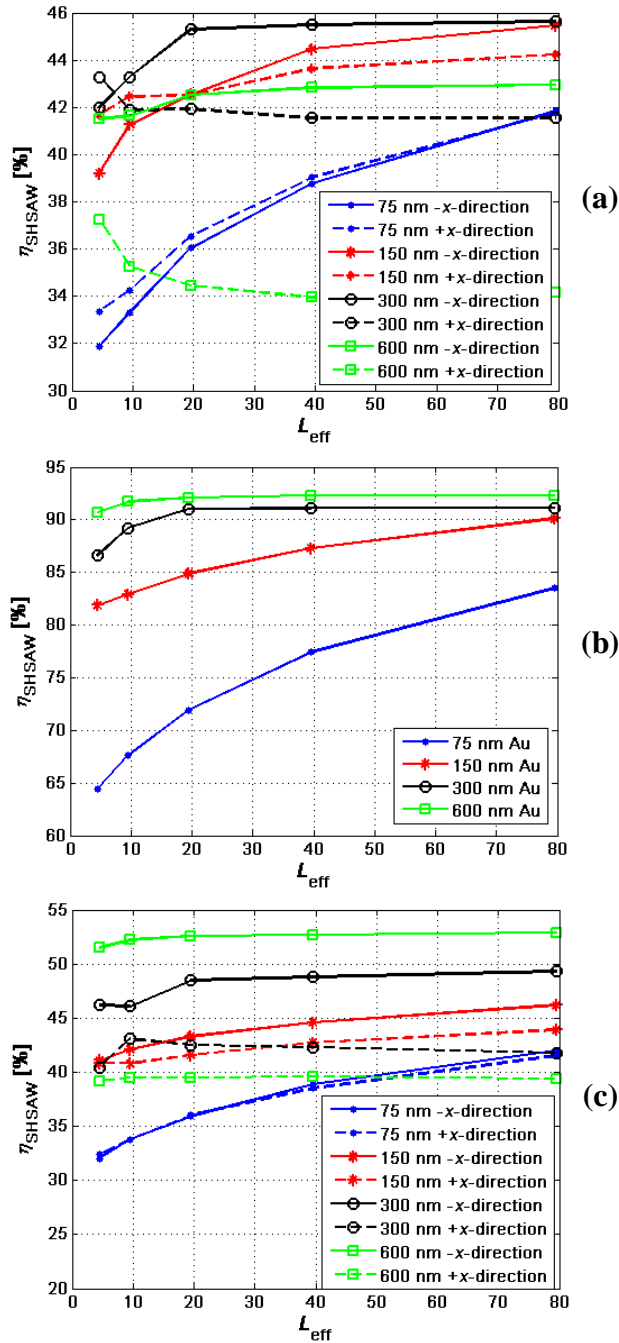
Figure 3.21. SHSAW excitation efficiency η_{SHSAW} [%] for split-finger IDTs of different lengths and metallization thicknesses under the matched condition: (a) single uniform guiding electrodes on the left and right side of IDT, (b) uniform guiding electrodes both sides of IDT and total left and right propagated SHSAW, and (c) uniform guiding electrodes both sides of IDT with separated left and right propagating SHSAW contributions.

147

Figure 3.21 shows the results of the computed η_{SHSAW} as a function of L_{eff} considering diverse electrode metallization thicknesses. In particular, Figure 3.21 (a) shows η_{SHSAW} for the structure represented case (ii) in Figure 3.16 where a single semi-infinite uniform electrode is on one side of the IDT, as well as the reverse situation. Figure 3.21 (b) gives η_{SHSAW} for the structure represented as case (ii) in Figure 3.16, where the guiding electrodes are on both sides of the IDT. Finally, Figure 3.21 (c) plots η_{SHSAW} split into both +x- and −x-propagating SHSAW contributions, again for the structure represented as case (ii) in Figure 3.16. The results shown in Figure 3.21 (b) indicate that the overall η_{SHSAW} considering excitation to both sides increases with IDT length towards an asymptotic value, and also increases with metallization thicknesses. Within assumed 1% uncertainty, Figure 3.21 (a) shows that η_{SHSAW} increases with thickness up to a 300 nm thick Au film, and then the efficiency decreases for the thicker 600 nm film. This behavior might be credited to the higher structural mismatch between the IDT region with thicker electrodes and the free region, which then leads to more power transduced into the SHBAW. Figure 3.21 (a) also reveals an interesting directivity effect which takes place for thicker films. For thinner films the placement of the long electrode on the left or the right of the IDT generates comparable η_{SHSAW} performance. For the thicker electrodes, in particular for 600 nm thick electrodes, about 9% difference in excitation between forward and backward propagation is identified when the electrodes are positioned on one side or the other of the IDT. Similar directivity effect for thicker electrode is observed on Figure 3.21 (c), where long electrodes are present on both sides of the IDT and split into contributions to each side. Comparing Figure 3.21 (a)

and Figure 3.21 (c), one can see that for a selected thickness the presence of long electrodes on both sides of the IDT increases the overall SHSAW excitation for both the forward and backward propagation directions when compared to having the electrodes on one side only. The effect is more pronounced for the thicker 600 nm electrode case. The higher overall η_{SHSAW} for the quartz Euler angles (0°, 132.75°, 90°) case where electrodes are present on both sides is justifiable by less SHBAW excitation and SHSAW excitation on both directions, as opposed to a single direction in the case of electrode on only one side.

In order to experimentally verify the proposed modeling technique, and in particular the directivity effect reported in the previous paragraph, a quartz Euler angles (0°, 132.75°, 90°) delay-line structure consisting of a regular two-electrodes per wavelength IDT, two identical split-finger IDTs, and long guiding uniform electrodes were fabricated as shown in Figure 3.22. The structure was simulated and the results were compared to measurements. The structure shown in Figure 3.22 allows the determination of P_{SHSAW} going to the left with respect to P_{SHSAW} going to the right excited by the Port 2 IDT; defined as directivity D_{solid}.
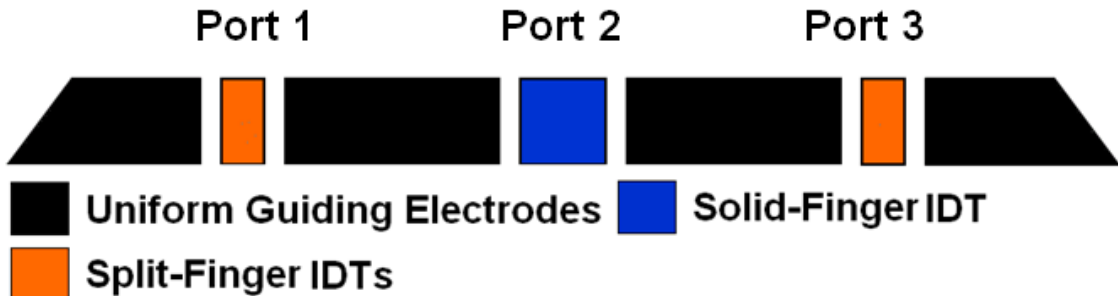
Figure 3.22. Layout of the SHSAW device fabricated.

The fabricated device consists of a two-electrode per wavelength input IDT having $L_{eff} = 79.5$, $\lambda_{IDT} = 32$ μm, 8 μm electrodes, and mark-to-space ratio = 1:1. Long uniform guiding electrodes, with 6 μm gaps between themselves and the extreme solid-finger IDT electrodes, extend 9596 μm in each direction. The split-finger IDTs have $L_{eff} = 39.5$, $\lambda_{IDT} = 32$ μm, 4 μm electrodes, mark-to-space ratio = 1:1, and 4 μm gaps between themselves and the guiding electrodes. On the other side of the split-finger IDTs, long uniform guiding electrodes approximately 6500 μm in length are placed 4 μm from the outer edge of each IDT. The guiding electrodes are terminated with a diagonal edge to scatter reflections. The acoustic aperture of the device is 1600 μm. The Au metallization layer is 287.5 nm thick atop a 10 nm Cr adhesion layer. Devices were fabricated at the Laboratory for Surface Science & Technology (LASST) cleanroom facility and tested at the Microwave Acoustics Laboratory, the University of Maine.

The input transducer, Port 2, was numerically analyzed using the technique described in this section considering uniform guiding electrodes on both side of the two-electrodes per wavelength IDT and inclusion of matching electrodes. Figure 3.23 shows the calculated $|T_4|$ at the interface after the matching (1V applied). The analysis and Figure 3.23 clearly reveals a directional behavior of the Port 2 IDT since P^+_{SHSAW} and P^-_{SHSAW} are both proportional to $|T_4|^2$ associated with the forward and backward propagating SHSAW. Based on the calculated P^+_{SHSAW} and P^-_{SHSAW} along the uniform guiding electrode/substrate interface, the directivity for the structure is determined to be 9.0 dB.
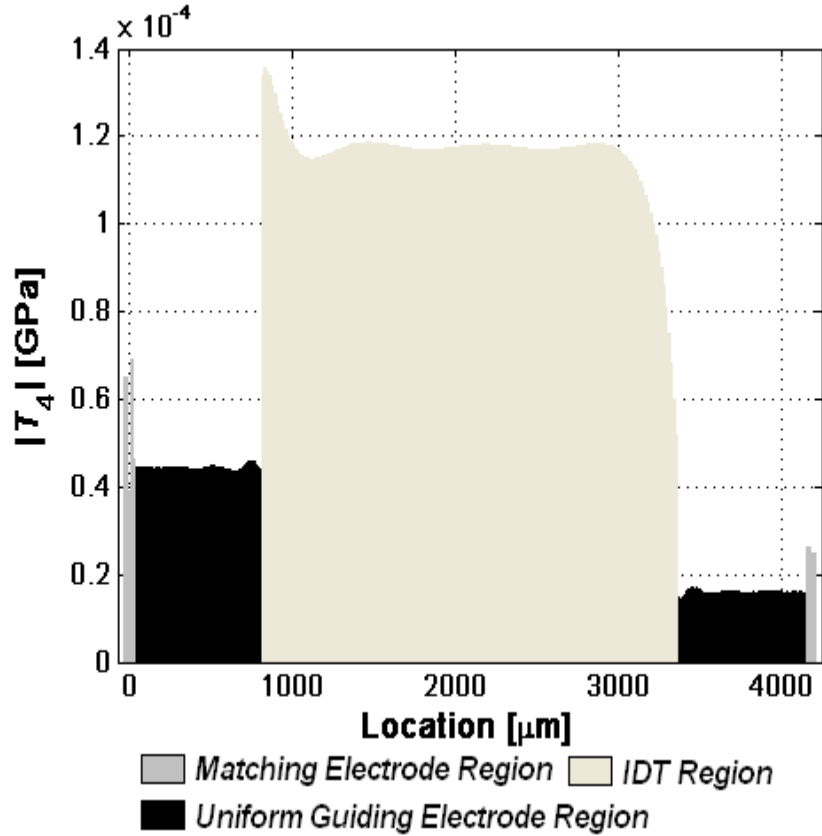
Figure 3.23. Calculated $|T_4|$ along electrode/substrate interface for the solid finger IDT including guiding and matching electrodes.

Figure 3.24 plots the measured $|S_{12}|$ and $|S_{32}|$ obtained for both the forward and backward delay-line propagation directions on quartz Euler angles (0°, 132.75°, 90°) with Au electrodes, $H_1/\lambda_{IDT}= 0.9\%$. As expected based on the previous analysis using the proposed model, the Natural Single Phase Unidirectional Transducer (NSPUDT) directivity effect is experimentally observed.
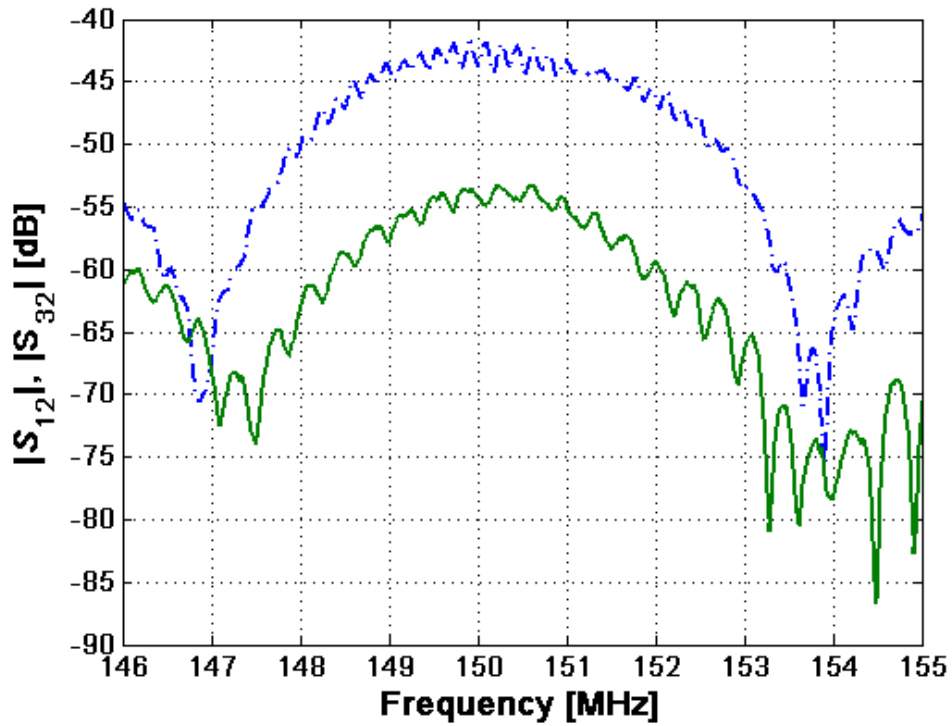
Figure 3.24. Experimentally measured $|S_{12}|$ (·-) and $|S_{32}|$ (solid) for the NSPUDT device fabricated demonstrating quartz Euler angles (0°, 132.75°, 90°) directionality. Port 2 is connected to the solid-finger IDT and Ports 1 and 3 are connected to the split-finger IDTs as shown in Figure 3.22.

To compare the experimental results shown in Figure 3.24 with predicted D_{solid} results, the finite directivity of the split finger detection IDTs, D_{split}, are considered and estimated from Figure 3.21 (c) to be 0.4 dB for a 300nm thick film. Minor differences in the $|S_{11}|$ and $|S_{33}|$ frequency responses for the two split-finger IDTs have been measured and are considered in the analysis. After time gating spurious reflections out, the minimum measured value of $|S_{11}|$ was about -0.71dB at 150MHz compared -0.63dB at 150.8MHz for $|S_{33}|$. These observed small variations in frequency response between the two IDTs (about 1 MHz in 150MHz) was credited to variations in the fabrication process,

namely the thin-film thickness and the patterned mark-to-space ratio for the structure

fabricated. To account for the observed fabrication variation towards the extraction of

D_{solid}, a relative port efficiency factor defined as $\delta = (1-|S_{11}|^2)/(1-|S_{33}|^2)$ was computed,

which relates the efficiency of acoustic excitation/detection between Port 1 and Port 3

IDTs. Finally D_{solid} is calculated by $D_{solid} = D_{split} \cdot (|S_{12}|^2/|S_{32}|^2)/\delta$ and at 150 MHz resulted

in 9.8 dB.

Therefore, the proposed model successfully predicts the experimentally observed

directivity effect for the pure SHSAW on quartz angles (0°, 132.75°, 90°) with Au

electrodes. The calculated and measured directivity agree to within 0.8dB of the 9dB

experimentally measured value, which is reasonable given the uncertainties and

variations in the fabricated structure parameters and choices for the extrapolated D_{split}

used in the calculations.

3.4.3. Surrounding Periodic Electrode IDT Analysis

Sections 3.4.1 and 3.4.2 showed that the addition of guiding electrodes placed

next to IDTs can dramatically improve excitation efficiency of the SHSAW mode. In

particular, it was seen that for the LGS orientation considered, for IDTs with surrounding

free surfaces, less than 3% of input IDT power is transduced to the SHSAW. For the

quartz orientation considered, 0% of IDT input power is transduced to a SHSAW mode

since a free surface SHSAW does not exist. However, it was shown for quartz that, with

use of uniform guiding electrodes composed of Au, η_{SHSAW} can approach 93% for the

number of IDT pairs and metal thicknesses considered. In this section the use of periodic

synchronous guiding electrode gratings placed next to finite IDTs is studied and the resulting η_{SHSAW} is investigated. It is shown that this guiding method is the most efficient in terms of η_{SHSAW} of the three IDT surrounding boundary conditions investigated, since the resulting η_{SHSAW} can approach 100% for various numbers of IDT pairs and electrode thicknesses. The improved η_{SHSAW} is attributed to the following: (i) absence of mechanical aperiodicity, thus reducing mode reflection and scattering, (ii) the fact that the mode supported in the IDT region is the same mode supported in the delay region (i.e. same slowness value), and (iii) the ability to further slow down the guided SHSAW mode by use of dense electrodes, thus separating the SHSAW grating slowness from the SHSBAW slowness region. The η_{SHSAW} extraction method and presented results in this section were reported first by the author of this dissertation in [60] while considering LGS Euler angles (0°, 22°, 90°), in [90] considering KNB Euler angles (0°, 90°, 0°), and in [52] considering quartz Euler angles (0°, 132.75°, 90°).

Using the periodic FEM/BEM model theory developed in Chapter 2 Section 2.7, a numerical simulation tool for a finite IDT structure surrounded by semi-infinite synchronous guiding gratings was implemented. The simulation tool uses (2.44) to compute the nth-period grating mutual admittance, $\mathbf{Y}_n(\omega)$, from which the IDT electrical properties are evaluated via discrete convolution, given the finite-length voltage distribution of IDT electrodes, using (2.45). Novel to this dissertation work is the extraction of η_{SHSAW} for the structure from the simulation results.

A discussion of the η_{SHSAW} extraction procedure follows. The authors in [59] first reported that the harmonic admittance function used in evaluation of the mutual admittance, (2.44), may be separated into two main contributions; in particular a portion due to SAW coupling, and a second portion representing all other contributions, i.e. electrostatic, evanescent, BAW, and PSAW. It appears the author's main motivation for separating the harmonic admittance function into two contributions was to permit numerical evaluation of (2.44). In particular the integrand of (2.44) will have simple poles on the axis of integration if a true guided SAW mode exists on a short-circuit grating and is electrically coupled. As the integral cannot be computed numerically due to the presence of poles on the axis of integration, the SAW contribution containing the simples poles is first subtracted out of the integrand, then integrated analytically, and finally added to the residual integral, which is obtained by numerical integration of the of the remaining portion. Thus the overall mutual admittance has two contributions, a SAW portion and a residual portion:

$$\mathbf{Y}_n(\omega) = \mathbf{Y}_n^{SHSAW}(\omega) + \mathbf{Y}_n^{residual}(\omega), \tag{3.26}$$

where:

- $\mathbf{Y}_n^{SHSAW}(\omega) = \int_{-1/2}^{1/2} \mathbf{Y}^{SHSAW}(\omega, \gamma) e^{-j2\pi\gamma n} d\gamma$,

- $\mathbf{Y}_n^{residual}(\omega) = \int_{-1/2}^{1/2} \left(\mathbf{Y}(\omega, \gamma) - \mathbf{Y}^{SHSAW}(\omega, \gamma) \right) e^{-j2\pi\gamma n} d\gamma$,

- and the mutual admittance, $\mathbf{Y}_n(\omega)$, is the current entering the nth electrode when a unit voltage is applied to the $n = 0$ electrode and all other electrodes are placed at zero voltage.

The authors of [59] showed that SAW portion of the harmonic admittance can be chosen as:

$$\mathbf{Y}^{SHSAW}(\omega,\gamma) = \frac{jY_{sc}(\omega)}{\tan(\pi\gamma_{sc}(\omega))} \cdot \frac{1-\cos(2\pi\gamma)}{\cos(2\pi\gamma_{sc}(\omega))-\cos(2\pi\gamma)}, \tag{3.27}$$

where:

- $\gamma_{sc}(\omega)$ is the value of γ at which the SAW pole occurs (corresponding to $+x$ propagation, another pole shows up at $-\gamma_{sc}(\omega)$ and corresponds to $-x$ propagation),

- and $\dfrac{Y_{sc}(\omega)}{-2\pi j}$ is the pole residue at $\gamma = \gamma_{sc}$.

Given that in reality all materials display finite loss, the location of the poles can be thought of being located infinitesimally off the real γ axis. Therefore integration of (3.27), as required for (3.26), can be evaluated using residue theory [78], resulting in:

$$\mathbf{Y}_n^{SHSAW}(\omega) = \begin{cases} Y_{sc}(\omega)\cdot e^{-j2\pi y_{sc}|n|} & |n| > 0 \\ Y_{sc}(\omega)\cdot\left(1+\dfrac{j}{\tan(\pi\gamma_{sc}(\omega))}\right) & n = 0 \end{cases}. \tag{3.28}$$

Given an applied voltage distribution on IDT electrodes, the IDT input admittance, $y_{in}(\omega)$, is determined by substituting (3.26) into (2.45), and then summing IDT input currents (unit voltage applied to IDT); resulting in:

$$y_{in}(\omega) = y_{in}^{SHSAW}(\omega) + y_{in}^{residual}(\omega), \tag{3.29}$$

where:

- $y_{in}^{SHSAW}(\omega) = \displaystyle\sum_{m=D}\sum_{n=D}\mathbf{Y}_{m-n}^{SHSAW}(\omega)$

- $y_{in}^{residual}(\omega) = \displaystyle\sum_{m=D}\sum_{n=D}\mathbf{Y}_{m-n}^{residual}(\omega)$

- D are the driven IDT electrode indices

156

Thus, for an applied voltage on the IDT, η_{SHSAW} is given by:

$$\eta_{SHSAW}(\omega) = \frac{\Re\{y_{in}^{SHSAW}(\omega)\}}{\Re\{y_{in}^{SHSAW}(\omega) + y_{in}^{residual}(\omega)\}}, \qquad (3.30)$$

Due to reciprocity it can be shown that $\mathbf{Y}_n = \mathbf{Y}_{-n}$ [59], which results in non-directional excitation for the structure considered, thus equal SHSAW power is excited for both forward and reverse propagation directions

Using (3.30) and the implemented periodic FEM/BEM model, η_{SHSAW} values were computed for split-finger type transducers with surrounding synchronous short-circuited periodic guiding gratings. In particular, η_{SHSAW} values were determined using the same number of IDT split-finger pairs and Au electrode metallization thicknesses considered in the two previous sections for the SHSAW orientations of quartz, Euler angles (0°, 132.75°, 90°), and LGS, Euler angles (0°, 22°, 90°). The IDTs considered have electrode finger width of 4 μm, 1:1 mark-to-space ratio, and rectangular electrodes composed of isotropic Au. The η_{SHSAW} value was determined at the frequency of maximum IDT conductance. Figure 3.25 shows results obtained for quartz, Euler angles (0°, 132.75°, 90°) and Figure 3.26 shows results obtained for LGS, Euler angles (0°, 22°, 90°). From the figures it is apparent that η_{SHSAW} increases with metallization thickness for a given IDT length. It also appears that, for increased IDT length, the use of guiding gratings results in η_{SHSAW} values approaching 100% for all metallization thicknesses considered. By contrast, when guiding uniform electrodes are considered, η_{SHSAW} appears to approach values less than 100% (cf. Figure 3.21 (b)). Thus the higher efficiency obtained with the guiding gratings is due to the uninterrupted structure

periodicity and matching slowness values of modes supported in both regions, resulting in less SHBAW scattering / acoustic reflections from otherwise structure discontinuities.
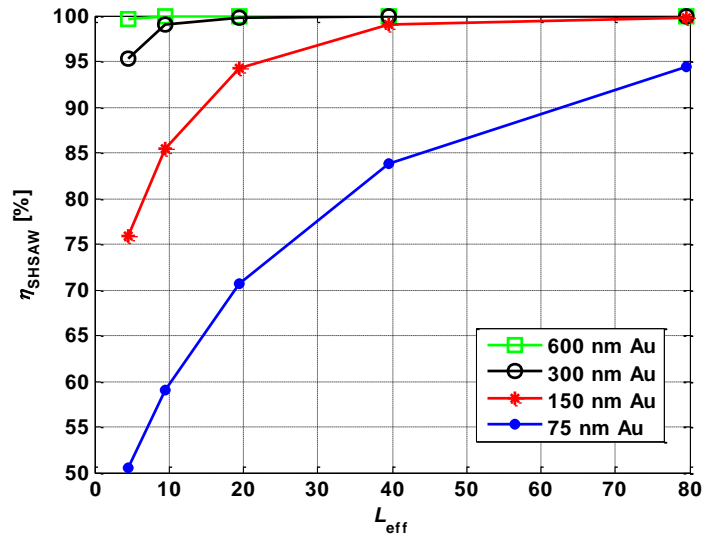
Figure 3.25. IDT SHSAW excitation efficiency, η_{SHSAW}, with surrounding synchronous periodic guiding electrodes for quartz, Euler angles (0°, 132.75°, 90°), as a function of IDT split finger pairs and Au electrode thicknesses.
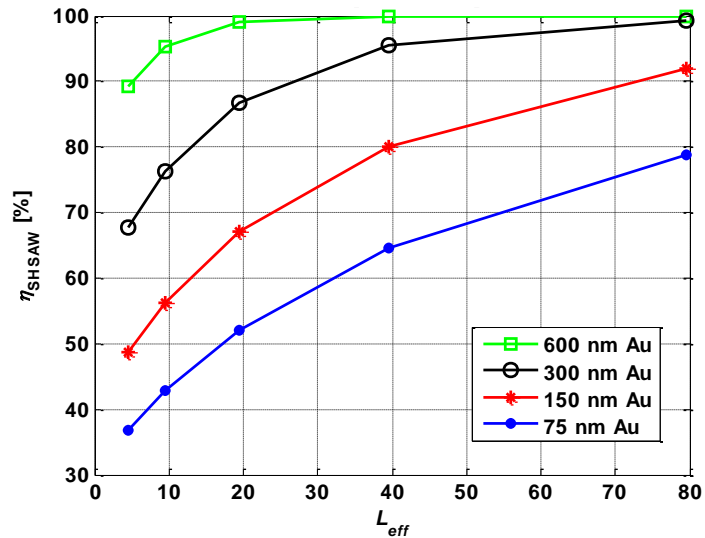
Figure 3.26. IDT SHSAW excitation efficiency, η_{SHSAW}, with surrounding synchronous periodic guiding electrodes for LGS, Euler angles (0°, 22°, 90°), as a function of IDT split finger pairs and Au electrode thicknesses.

CHAPTER 4

MONOLITHIC SHSAW/MICROFLUIDIC SENSOR PLATFORM DESIGN AND

FABRICATION

4.1. Introduction

This chapter discusses the development of SHSAW sensor packaging for liquid-phase sensing applications. Recall that the goal of sensor packaging is to only expose the delay path region of the device to the fluid analyte such that dielectric- or electric-shorting of IDTs is avoided. This goal is accomplished in this work via attachment of microfluidic chambers to SHSAW device surfaces. The chambers are designed with fluidic containment walls placed between IDT and delay-path regions, thus allowing only fluid exposure to the delay-path region while protecting IDT electrodes. Two main packaging techniques were investigated: (i) a method based on formation of microfluidic chambers directly on the SHSAW die using photolithographic techniques; and (ii) a method based on molding of polydimethylsiloxane (PDMS) microfluidic chambers, followed by dicing, aligning, and permanent bonding to SHSAW device surfaces. The latter proved to provide a more robust packaging technique and received most attention in this work. This chapter is outlined as follows. In Section 4.2 the initially employed packaging technique based on photolithographically patterning microfluidic structures direction on the SHSAW device using SU-8 is discussed. Next, Section 4.3 reports on the packaging techniques based on use of PDMS. Section 4.3 is broken down into subsections disussing: (i) the patterning of microfluidic features in PDMS via molding process; (ii) permanent bonding of PDMS to substrates; and (iii) chamber

alignment and bonding to SHSAW devices. Section 4.4 presents a series of hybrid SHSAW PDMS microfluidic device designs fabricated in this work. And lastly, Section 4.5 describes the performance of the related package, and compares the device response before and after attachment of the fluidic chamber. As a result of this work a novel packaging technique for SHSAW liquid-phase sensors has been developed. The packaging approach permits robust sealing of devices. In addition, it is shown that applying device packaging has minor negative affect on the overall SHSAW sensor platform response.

4.2. SU-8 Liquid Phase Packaging

Initial efforts regarding packaging of SHSAW sensor platforms for liquid-phase operation involved photolithographic patterning fluid containment structures directly on pre-fabricated SHSAW devices, followed by attachment of a chamber glass cap. The permanent photoresist incorporated in the formation of containment structures is the SU-8 2000 series available from MicroChem Corporation Newton, MA, USA (see Section 1.4 for a review of reported SU-8/SAW packaging approaches). A photograph of a packaged SHSAW device fabricated in this work taken after patterning SU-8 fluid containment structures and attachment of a glass cap is shown in Figure 4.1.
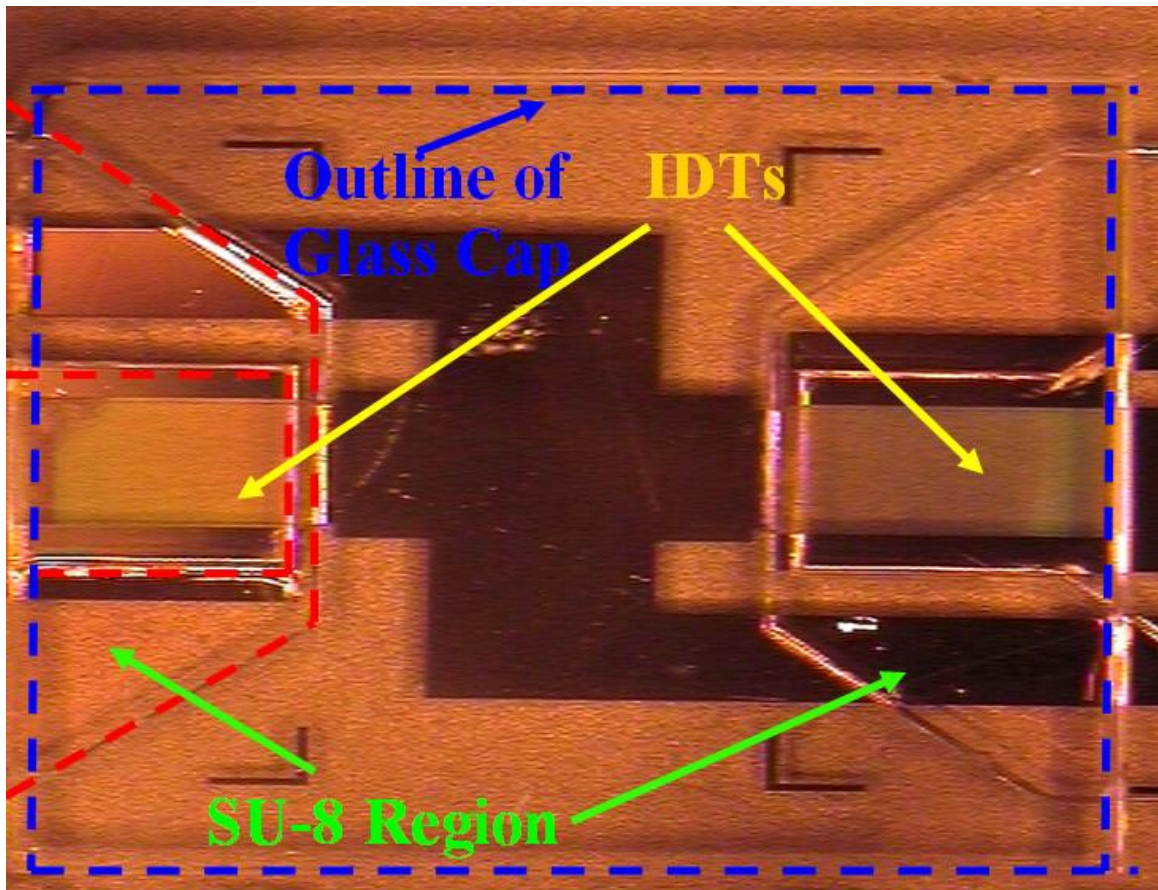
Figure 4.1. SHSAW/SU-8 liquid phase packaging configuration.

The device in Figure 4.1 consists of a SHSAW delay-line device fabricated along LGS Euler angles (0° 22° 90°) with a uniform Au guiding electrode located in the delay region to improve SHSAW transduction efficiency and allow selective attachment of bio-molecules for subsequent biological sensor proof-of-concept testing. The containment wall width separating the IDTs and delay region is 200 μm. A glass cap is attached to the SU-8 layer to form a fluid containment region in the device delay path. Additional details regarding the LGS SHSAW device include: Au metallization of 400 nm atop a 12.5 nm Cr adhesion layer; IDTs consist of 80 split-finger pairs with electrodes 4 μm in width and periodicity of 8 μm; IDT aperture is 1.600 mm; and the device IDT

center-to-center distance is 6.400 mm. All devices reported in this work were fabricated in the class 1000 cleanroom facility located at the Laboratory for Surface Science and Technology (LASST) University of Maine, Orono, ME USA.

The fabrication sequence of the SU-8 microfluidic chamber is shown step-by-step in Figure 4.2. After SHSAW device fabrication, samples are cleaned via acetone, methanol, isopropyl, and DI water rinses, followed by a nitrogen blow dry and dehydration bake on a 150°C hotplate for 10 minutes. Next, a layer of SU-8 2050 is applied to the device via direct pouring from a working bottle to avoid the generation of bubbles, which is typically observed if a syringe is used alternatively. Next the resist is spun at 1000 rpm for 30 seconds to achieve a layer approximately 170 μm thick.
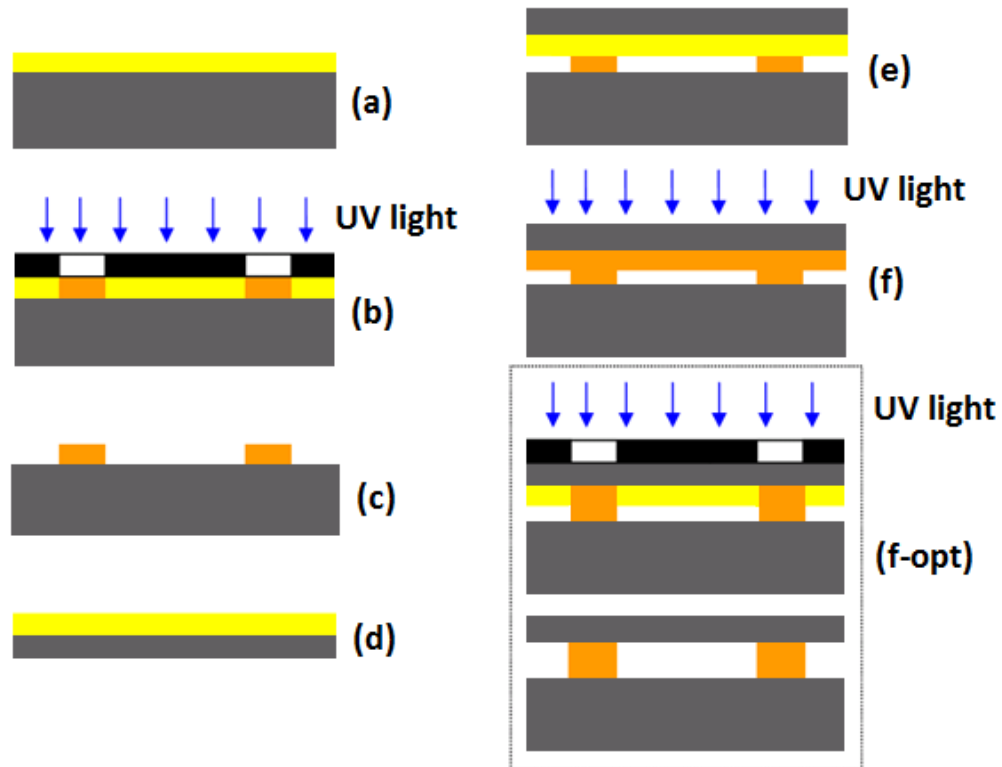
Figure 4.2. SHSAW/SU-8 liquid phase fabrication protocol steps.

The device is then soft-baked (solvent level reduction step) on a hotplate at 65°C for 4 hours, followed by a 1 hour bake at 95°C (Figure 4.2 a). This relatively long two step bake process resulted in improved film uniformity compared to the datasheet recommended bake process suggesting 65°C for 7 minutes, followed by 30 minutes at 95°C. After the layer is soft-baked, the SU-8 layer is exposed to UV light through a photomask (clear features become permanent SU-8) having the desired SU-8 pattern (~500 mJ/cm^2 dose), see Figure 4.2 b. Wavelengths below 350 nm were filtered out using an optical filter (not shown in Figure 4.2, but is placed in the path between UV source and the mask) to avoid resist 'T-topping'. The 'T-topping' effect results in over exposure of SU-8 at the top surface, as compared to that in the bulk SU-8, as the lower wavelength UV light (~250 nm) is highly absorbed near the SU-8 surface, which generates a local region of higher crosslinking acid concentration compared to that in the bulk. This concentration difference result in cross-linked features that display a 'T' shaped profile, as looking from a side, and reduces fine control of feature aspect ratio. Use of a filter is recommended by the manufacture for this reason. Following exposure, the device is post-exposure-baked at 65°C for 1 hour to promote polymer crosslinking. The temperature used for this process is lower and longer than the recommended bake profile of 65°C for 5 minutes, and 95°C for 12 minutes to reduce thermal induced interfacial stress at the SU-8 and LGS interface, which stems from the thermal coefficient of expansion mismatch between the SU-8 layer and the LGS substrate. The device is then allowed to cool to room temperature over a period of about 30 minutes to avoid thermal shock and SU-8 adhesion failure. Next the unexposed resist is developed away in SU-8 developer solution: first in used and then in a new bath for 5 minutes intervals under mild

ultrasonic agitation. Following the development step, the devices is rinsed with isopropyl alcohol and DI water and blown dry with nitrogen (Figure 4.2 c). Next a pre-diced glass microscope slide is cleaned with acetone, methanol, isopropyl, and DI water, followed by nitrogen blow dry and dehydration bake on a 150°C hotplate for 10 minutes. A layer of SU-8 2015 is then applied to the glass cap and spun at 3000 rpm for 30 seconds to form a layer ~15 μm thick (Figure 4.2 d). The glass cap is then soft-baked at 65°C for 5 minutes, followed by 5 minutes at 95°C. The cap is then flipped over and placed on top of the SHSAW/SU-8 structure in a period short enough that the cap film is still above the SU-8 glass transition temperature during the merging process to allow some slight SU-8 reflow around the containment wall interface. Next the sample is allowed to cool to room temperature (Figure 4.2 e). The entire device is then blanket exposed to filtered UV light to cure the unexposed resist (~200 mJ/cm^2 dose) causing the cap to attach to the pre-patterned SU-8 containment areas. Finally, cap sealing resist crosslinking is initiated by heating the device to 65°C for 1 hour and then allowed to cool to room temperature (Figure 4.2 f). An alternative step to Figure 4.2 f, is depicted in Figure 4.2 f-opt where the combined structure is again baked and exposed to UV, but now includes use of a photomask to cure SU-8 regions only in contact with the pre-patterned SU-8 walls. Next the device is post-exposure-baked, followed by SU-8 development. This modified step resulted in improved chamber liquid filling due to the increased hydrophilicity of the glass cap surface as compared to a glass surface covered with SU-8.

To demonstrate how SU-8 packaging affects the SHSAW platform device performance, the transmission coefficient, S_{21}, of the device in Figure 4.1 was measured

before attachment of the SU-8 chamber, and after attachment of the SU-8 chamber. Figure 4.3 plots the magnitude and phase results obtained. Comparing the magnitude of the responses around the frequencies in the device passband indicates that addition of SU-8 chamber walls placed along the delay path reduces the level of signal detected by the output IDT by about 7dB. This is attributed to SHSAW reflection from the SU-8 wall / substrate interface, as well as mode conversion loss to SHSBAW, which is scattered into the substrate bulk. Before application of the chamber the magnitude response is flat (less than 1 dB ripple) and the phase response is linear. After chamber attachment the magnitude begins to exhibit ~3 dB ripple in the passband, indicating increased detected spurious signal (a slight ripple in the phase response is also now present).
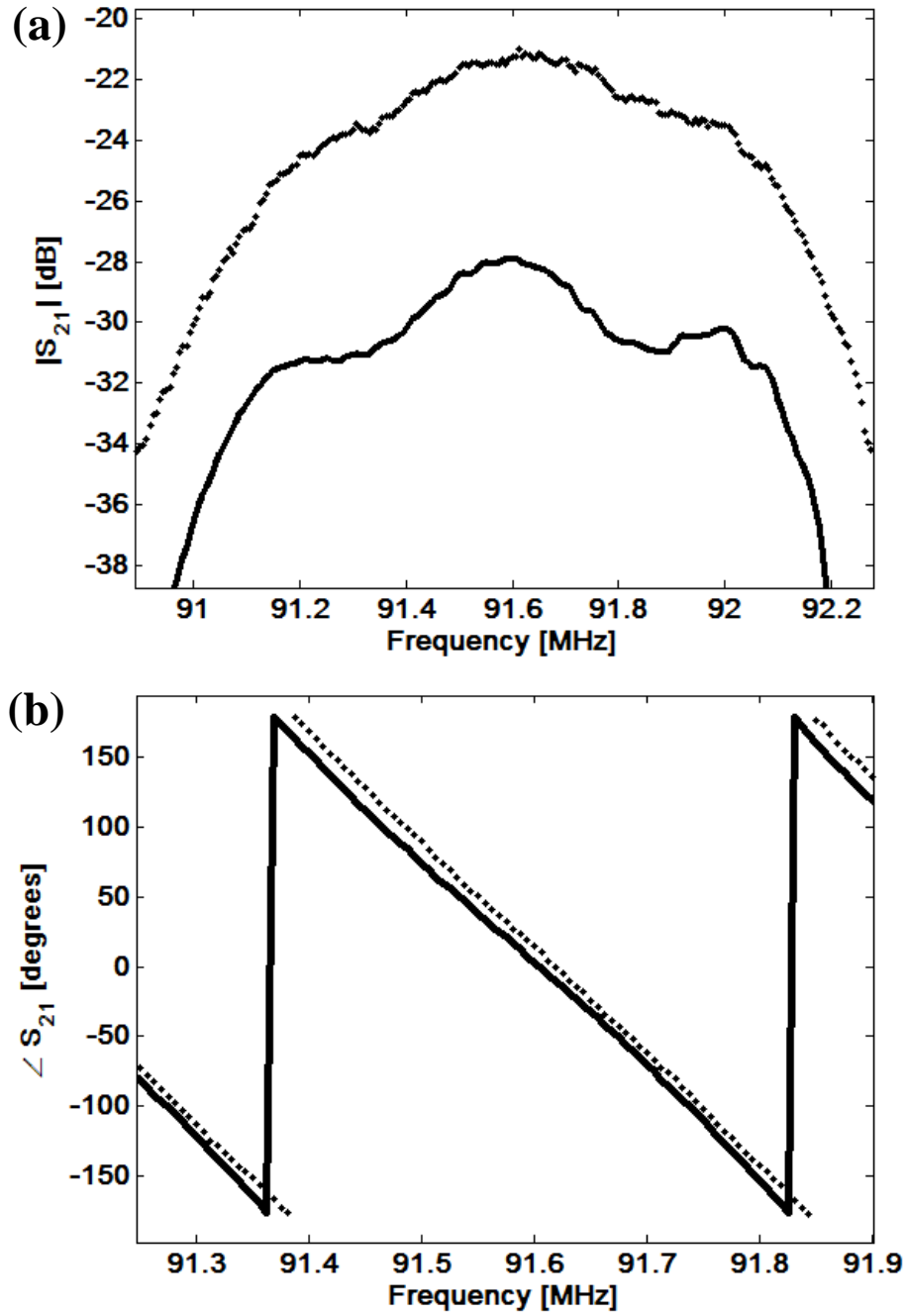
Figure 4.3. LGS liquid phase sensor platform transmission coefficient magnitude and phase without chamber (dotted), and with chamber, (a) magnitude, (b) phase.

166

The performance of the SU-8 packaging technique for liquid phase sensing applications was limited due to fluid containment problems. In particular, this device packaging technique was not very robust, as in some instances just picking up the devcies with tweezers caused the chamber to detach. In addition, attachment was also sensitive to temperature variation or shock. In response to these stimuli, chambers would begin to leak. This issue was attributed to the fact that SU-8 has poor adhesion to LGS due to being very brittle, and the large difference in thermal expansion coefficients between both materials (SU-8 expansion approximately 10-50X LGS expansion) [69, 93,94]. After many attempts to reduce these issues via improvement of substrate cleanliness during processing and reduction of processing temperature shock, this packaging technique was abandoned. Efforts were directed towards novel MEMs liquid-phase packaging techniques based on molding of silicone elastomers, namely polydimethylsiloxane (PDMS), and chamber bonding to substrate protocols reported in literature (see Section 1.4 for literature review regarding PDMS microfluidics). The new methods and techniques seemed very promising towards packaging of SHSAW devices and led to a change of course for this work, in terms of SHSAW liquid-phase sensor packaging. The next section describes the methods, techniques, and protocols investigated and developed based on PDMS and SU-8 technology that resulted in successful fabrication of a robust and easily interfaced packaged SHSAW liquid-phase sensor platform. To the best of the author's knowledge, the packaging method developed in this work and applied to SHSAW sensor platforms is first reported in this dissertation work.

4.3. PDMS Liquid Phase Packaging

An alternative to packaging the SHSAW platform devices by forming chambers on the device surface via photolithographically patterning SU-8 is packaging that is based on molding PDMS, followed by dicing individual chambers, and aligning and bonding to SHSAW devices. This latter technology was considered a better alternative and was further explored in this work.

A general discussion on the properties of PDMS and its application towards packaging of SHSAW devices for liquid phase applications follows. PDMS is a silicon-based polymer having many commercial uses including contact lenses, medical devices, shampoos, caulking, and lubrication. The chemical composition of PDMS is given as $CH_3[Si(CH_3)_2O]_nSi(CH_3)_3$ where n is the number of monomers in the polymer chain [1]; the structure of PDMS is shown in Figure 4.4.
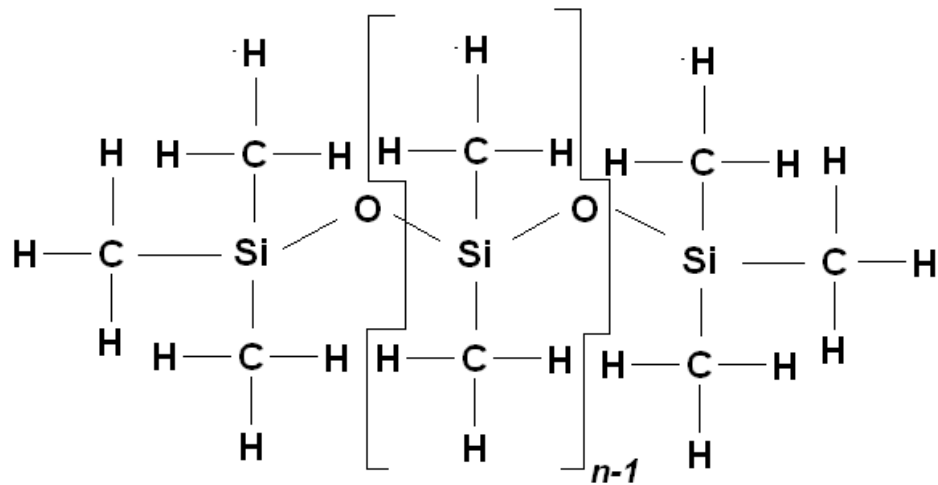
Figure 4.4. Chemical structure of polydimethylsiloxane.

Under long flow times or high temperature, PDMS behaves like a viscous liquid, e.g. honey, while for short flow times or low temperatures behaves like an elastic solid, e.g. rubber. Through a vulcanization process crosslinking of PDMS may be initiated, which attaches multiple polymer chains into a 3 dimension structure rendering the material to have properties of an elastic solid near room temperature. This process has been recently used in the formation of microfluidic structures for lab-on-a-chip applications [67]. Such a process can be initiated through addition of crosslinking agent mixed into the PDMS base which is activated, for example, via radiation, and/or temperature, depending on the curing agent chemistry. A commonly reported formulation used in the fabrication of microfluidic structures is the Slygard 184 Elastomer Kit available from Dow Corning. This kit consists of two parts, the base PDMS, and a curing agent which contains dimethyl, methylhydrogen siloxane and additional proprietary constituents. The two parts are generally mixed in mass ratio of 10:1 (base to curing agent, respectively), poured into a mold defining the desired final shape, and then allowed to cure via exposure to

169

temperatures (25°C–150°C) over a time period that depends on cure temperature; e.g. 48 hours at 25°C and 10 minutes at 150°C. Such a technique has been called softlithography by the MEMs community and allows replication of features down to the sub-micron scale. (Additional details on molding PDMS are discussed in Section 4.3.1.)

Another property of PDMS relevant to microfluidic devices is the ability to irreversibly bond to a variety of materials, e.g. glass, quartz, and Si, via low temperature surface oxidation treatment of mating surfaces. After treatment the surfaces are brought into contact and a covalent bond forms at the interface producing a strong hermetic seal which is sufficient for many lab-on-a-chip applications. (Details of this bonding mechanism are given in Section 4.3.2.) One disadvantage, in some instances, of this material in terms of microfluidic devices is that the surface properties of PDMS are hydrophobic by nature and therefore for experiments involving polar fluids, e.g. water, chamber filling problems may be encountered, such as formation of voids and entrapment of bubbles. These issues become problematic in cases such as biosensing where the fluids used consist mainly of water. Through proper design of fluidic channels and use of techniques such in situ grafting of hydrophilic groups onto PDMS surfaces [95], such problematic effects can be reduced. The following sub-sections of Section 4.3 describe the employed packaging techniques based on attaching PDMS micromolded chambers to SHSAW devices.

4.3.1. PDMS Micro-Molding

In the formation of microfluidic structures based on softlithography, traditional micro-featured PDMS molds are fabricated via patterning features on Si or glass substrates using MEMs techniques such as deep reactive ion etching (DRIE) or photolithographic patterning of SU-8. In terms of processing time and cost the latter method is probably more advantageous, while in terms of mold fidelity and robustness the former technique is probably a better choice. In this work many chamber designs needed to be evaluated quickly and inexpensively, therefore PDMS mold fabrication based on patterning SU-8 was utilized to quickly test new microfluidic chamber designs.

Initial efforts to generate microfluidic PDMS molds involved patterning structures on Si or glass substrates using SU-8 2050 (same resist used in Section 4.2 for on-chip chamber fabrication approach). A typical process flow used to generate PDMS molds and chambers is shown in Figure 4.5 (process details specific to this work are given in Appendix F). In step (a) a glass or Si substrate is cleaned, followed by application of SU-8, spinning, and soft-baking. Next, in step (b) the wafer is exposed to UV light with a photomask having the desired negative of the mold patterns. In step (c) the unexposed SU-8 is removed via submersion in a SU-8 developer solution bath under mild ultrasonic agitation. At this point the mold fabrication is complete and is ready for PDMS casting. After the mold is fabricated it is placed in a container and premixed PDMS and curing agent, after degassing in a desiccator to remove air bubbles, is poured over the mold. Next, the sample is placed in an oven to cure the PDMS, step (e). After the bake, the PDMS sample is carefully peeled up from the mold, step (f), and is ready be attached to

the SHSAW device. (Additional steps prior to bonding included boring small holes in the PDMS to allow attachment of microfluidic tubes used to fill the chamber during experiments).
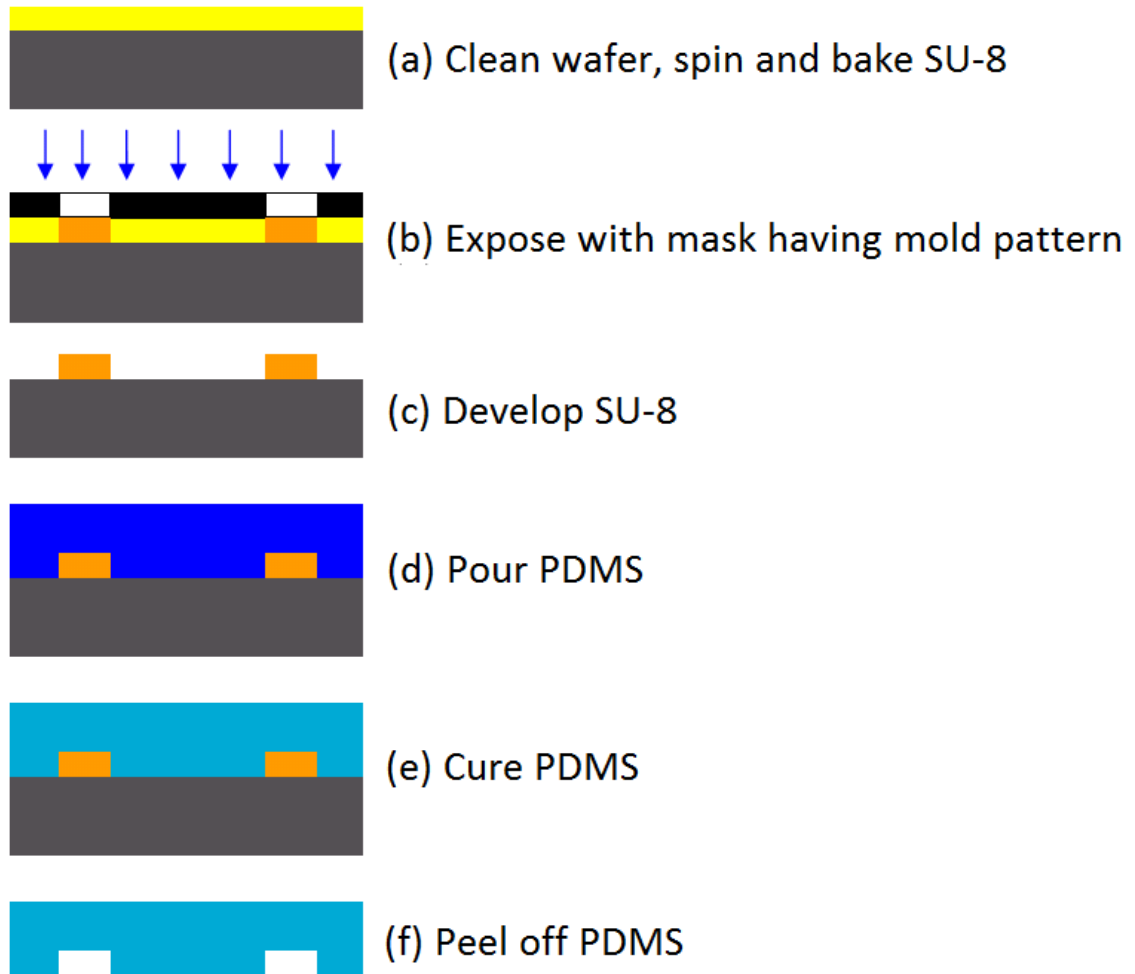
Figure 4.5. Process flow for SU-8 mold and PDMS chamber fabrication.

For the dimensions of the SU-8 structures considered, namely features having heights ~100 μm, adhesion of SU-8 to glass or Si substrates became problematic in terms of mold robustness and in many instances resulted in delimitation of mold features from the substrate. The literature mentions problems with mold robustness based on SU-8 features on Si or glass [69,63]. The adhesion problems stem from the fact that SU-8 and

glass or Si have large differences between coefficients of thermal expansion. This mismatch results in the generation of thermal interfacial stress upon heating and cooling, leading to delimitation from the surface and potential SU-8 cracking. This problem was encountered many times during mold fabrication and PDMS curing processes. In this work it was decided not to allocate additional time to adjust the SU-8/Si process protocols and mitigate the SU-8 delamination problems due to the large number of chamber designs required and the need to evaluate them quickly. For this reason, alternative substrate materials were sought out with coefficient of thermal expansion more similar to that of SU-8 in order to improve mold robustness. A search in the literature uncovered [69] and [64], which suggest poly(methyl methacrylate) (PMMA), also named Plexiglass, Perspex, or Acrylic, can be used as an alternative substrate for formation of SU-8 features. This was attractive since PMMA has chemistry that is more similar to SU-8 compared to Si or glass, and in particular has a thermal coefficient of expansion between 50-100 ppm/K [96] which is approximately the same range given for SU-8 in [69,93]. This property suggests the potential for improved overall adhesion of SU-8 to PMMA and therefore increased robustness of PDMS molds.

To implement the patterning of SU-8 on PMMA substrates, a PMMA rectangular sheet was purchased from a local hardware store and 4" diameter wafers were cut. After cutting wafers the edges were ground down to give a bevel along the outer wafer edge to reduce resist edge-bead effects resulting from the spinning process, and thus improve the resist film uniformity. Initial SU-8 patterning on PMMA followed the same protocol as done using Si or glass substrates. Two main problems were identified with the switch to

PMMA. First, the SU-8 softbake process resulted in wafer bowing during cure and poor SU-8 layer uniformity. To circumvent this problem a soft-bake process with increased time and lower temperature was devised that removed all visible wafer bowing. (All fabrication details are given in Appendix F.) In addition to the wafer bowing issue, the second issue encountered with the switch to PMMA substrate was that during SU-8 development the solvent used to remove unexposed SU-8 also attacked the PMMA, resulting in PMMA surface pitting. To avoid this problem an initial blanket layer of SU-8 was cured atop the PMMA prior to applying another layer used to form mold features. The blanket layer protected the PMMA from being attacked by the SU-8 developer, thus avoiding surface pitting. As expected the SU-8 molds based on PMMA substrate displayed superior adhesion and mold robustness compared to molds based on use of Si or glass substrates. These processing results were very encouraging and resulted in a method allowing rapid prototyping and testing of various microfluidic chamber designs, and the ability to reuse molds at least up to 10 times. The process flow for the finalized SU-8 / PMMA mold and PDMS fabrication process is shown in Figure 4.6. Lastly, it is important to mention that during the PDMS curing process, which typically takes place at 60-80°C, the PMMA mold expands due to thermal expansion. As the PDMS cures at this temperature and is brought back to room temperature the PDMS shrinks faster than the PMMA mold because its thermal expansion coefficient is larger than PMMA/SU-8. Upon removal from the mold the PDMS features are now smaller at room temperature than the mold. Similar problems have been reported using Si/SU-8 molds in [97], were the authors recommended scaling the mold by 1.07% when curing PDMS at 65°C in order to for achieve accurate-sized features on cured PDMS samples. In this work all PMMA/SU-8

174

mold masks were scaled by 1.017% to account for the shrinkage, which was estimated from measurement of a cured PDMS sample. As the cure temperature affects feature scaling, fine tuning of feature size was performed to achieve proper scaling of features by running various curing temperature experiments. Based on these tests it was determined that 75 °C resulted in correct feature size when using a 1.017% scaled mold mask.
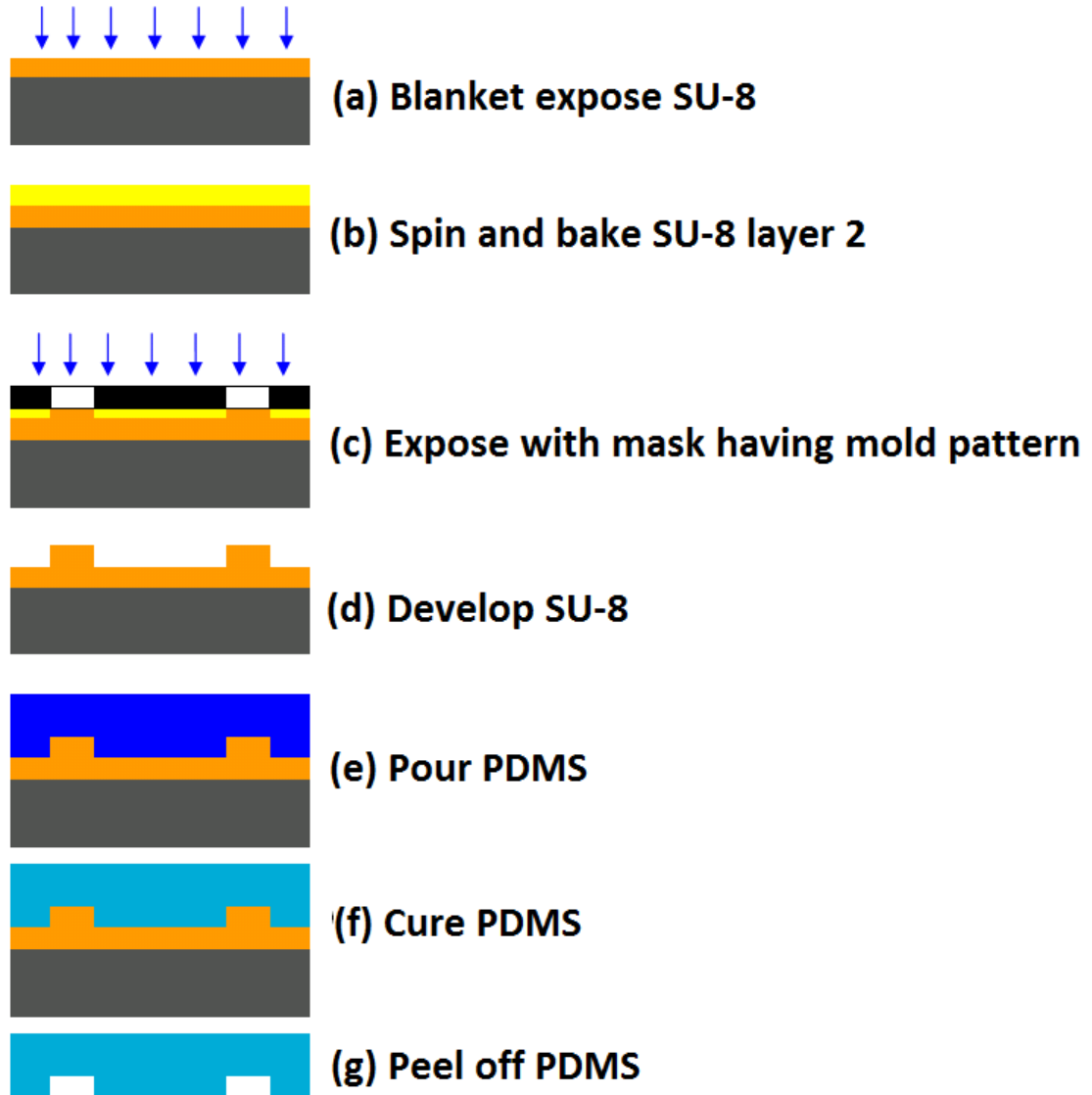
Figure 4.6. Process flow for SU-8 mold and PDMS chamber fabrication on PMMA.

4.3.2. PDMS/SHSAW Device Bonding

During the same period the PDMS mold process was being developed, experiments also began to take place regarding the attachment of PDMS chambers to SHSAW devices. It had been previously reported [67] that PDMS has the ability to irreversibly bond to a number of substrates e.g. PDMS, Si, glass, quartz, and silicon nitride via surface oxygen plasma treatment of mating surfaces before being contacted (no reference to bonding PDMS to LGS was not found in the literature). Initial experiments sought to reproduce such reported results prior to application of the technique to actual packaging SHSAW platforms. It had been reported [67] that the chemistry involved in irreversibly bonding PDMS via oxygen plasma treatment is based on removal of Si-methyl (Si-CH$_3$) groups from the PDMS surface, which become silanols (Si-OH) upon exposure humidity in air. The plasma treatment of, for instance, a glass substrate also results in a large concentration of silanols on the surface. When the two surfaces are then brought into contact, a reaction occurs giving off water as silicon atoms along each surface mate with individual oxygen atoms forming a covalent bond (Si-O-Si), linking the two bulk materials. The strength of this interfacial bond was observed in this work to be as strong as or stronger than the bulk PDMS; typical attempts to remove chambers from a substrate after bonding resulted in tearing of bulk PDMS.

Since this bonding techniques had been successfully reported using glass substrates, it was decided that initial SHSAW sensor platforms should be fabricated on quartz which has similar chemistry. No reports on successful bonding of PDMS to LGS substrates had been reported and initial attempts to bond PDMS to LGS were

unsuccessful. It is believed by that author that part of the problem regarding PDMS bonding to LGS is that the concentration of Si atoms at the surface of LGS that can be oxidized by plasma treatment is lower as compared to quartz; thus density of Si-O-Si bonds between the LGS is and PDMS is reduced. In Chapter 6 it is suggested that PDMS bonding to LGS should be further explored in future work. One potential solution discussed is the possibility of depositing a flash-layer (10's-100's nm) of SiO_2 on the LGS surface prior to electrode patterning via atomic layer deposition (ALD), electron-beam deposition, magnetron sputter deposition, or plasma-enhanced chemical vapor deposition (PECVD). Based on this approach, the concentration of surface bound Si should increase, thus the probability in achieving a sufficient PDMS bond should improve. Furthermore, the addition of a relatively thin (compared to the SHSAW wavelength) layer of SiO_2 on the LGS surface should still permit adequate piezoelectric coupling.

After deciding to use quartz as the substrate much time was then spent tuning the reactive ion etching (RIE) oxygen plasma settings for PDMS and quartz treatments in order achieve optimal bond strength. The parameters varied included oxygen plasma pressure, power, and exposure time. Many reports have stated that bonding of PDMS generally improves with higher plasma pressure, lower power, and shorter treatment times [98]. In this dissertation it was also confirmed that as the length of plasma treatment time increases further from the optimal, surface damage of the PDMS worsens as the concentration of glassy/brittle material at the surface increases, which is not firmly connected to the bulk PDMS. As for treatment of quartz surfaces, the amount of plasma

177

pressure, power, and time had little affect on bonding quality compared to the PDMS treatment. In order to determine the optimal RIE parameters, a number of bulk PDMS samples were cut into approximately 1 cm x 1 cm pieces and bonded to glass microscope slides under various plasma treatment conditions. After treating the glass and PDMS samples the two pieces were quickly and gently placed into contact by hand and allowed to sit overnight. The next day attempts to remove the PDMS glass slides were conducted and the degree of bond strength was qualitatively evaluated. Pressure ranges of RIE plasma varied from 250-1000 mTorr, power was varied from 15-200 Watts, and exposure time was varied from 10-120 s. Increased plasma pressure results in reducing the etch directionality due to increased ion bombardment and scattering as the ion mean-free-path reduces. Therefore, in terms of this effect on PDMS bonding, it is suspected that use of a more isotropic plasma due to increase plasma pressure reduces the PDMS bulk damage via shearing predominately surface rather than bulk methyl groups and thus improves the bonding surface quality. In terms of power, increasing it past an optimal it is thought that the PDMS polymer backbone can begin to be damaged resulting in poor bonding surface quality, while alternatively if the power is well below the optimal bonding may not even occur as not enough oxygen ion energy is present to shear surface methyl groups. It is thought that the effect of exposure time is also is important, such that if it is increased beyond an optimal, the PDMS bulk and surface backbone will become increasingly damaged, but if it is below the optimal, not enough few methyl groups along the surface will be sheared resulting in reduced covalent bond density. A matrix of PDMS bonding tests were performed and the best bonding protocol determined consisted of RIE pressure of 1000 mTorr, power of 50 Watts, and exposure time of 45 s. As for the glass substrate

178

treatment, the settings used were 1000 mTorr, 150 Watts, and exposure time of 60 s. It was observed that baking the samples at 65 °C for 4 hours, after allowing the samples to sit overnight at room temperature, also increased the bond strength. It should be noted that if the temperature was increased for example to 80 °C that occasional delimitation of certain micro-features occurred, which is thought to be caused by thermal interfacial stress due to expansion coefficient mismatch between PDMS and glass. Letting the sample sit overnight at room temperature prior to heating seemed to reduce this problem as more time was allowed for initial bond formation.

4.3.3. PDSM/SHSAW Alignment and Attachment

The PDMS containment walls separating IDT and delay-path regions of candidate SHSAW liquid phase sensor prototypes ideally should be as narrow as possible in order to minimally interact with the SHSAW mode and influence the overall sensor platform response. In particular, the containment walls may cause SHSAW attenuation, reflection, and scattering to bulk waves, which degrade the overall sensor platform performance. Two main issues arise as a consequence of reducing the wall thickness. One involves the strength of the bond, which obviously reduces with minimization of wall thickness and can result in fluid leakages. Another issue resulting from wall thickness reduction is the ability to accurately align the chamber to the SHSAW substrate. As the wall thicknesses and corresponding bonding surface gap thicknesses between IDTs and delay-path electrodes are reduced, the alignment placement accuracy requirement becomes stricter. In this work wall thicknesses which provided sufficient bond strength and acceptable modification of platform device response were determined to be on the order of 64-160

μm. In this work this distance corresponds to 2-5 SHSAW wavelengths for candidate SHSAW platforms having split-type IDT designs with wavelength of 32 μm (4 μm electrodes, and 4 per wavelength), which were able to be fabricated at the LASST facility cleanroom consistently. This design required chamber placement with respect to the SHSAW device to be within about 10 μm to make sure bonding PDMS wall surfaces landed on gaps between IDTs and the guiding electrode such that a covalent bond to can form between PDMS and quartz. Such a placement requirement does not allow alignment by eye. In order to address this challenge the literature available on alignment of PDMS and sequent bonding to substrates were reviewed. It was reported [99] that the use of a surfactant such as methanol or ethanol used to wet mating surfaces prior to bonding allows positioning of two pieces relative to each other prior to permanent attachment. The interfacial methanol layer prevents the silanol groups of the modified PDMS surface from migrating into the bulk layer, prevents instant bond formation and allows a few seconds to minutes of movement before evaporating such that features can be aligned. As the methanol evaporates the bond begins to form at the interface and any movement of chamber relative to substrate at this point will cause bonding not to occur in areas where dried interfaces had touched prior to movement. Use of methanol allowed chamber positioning to take place relative to the SHSAW platform succesfully, but a method to align the two devices was still required. Based on the previously developed experience in this work with patterning SU-8 on numerous substrates, an idea to align the PDMS chambers to SHSAW devices based on patterning SU-8 chamber locking features on the SHSAW device was investigated. A diagram of the entire alignment and bonding process is shown in Figure 4.7.

SHSAW with SU-8 Alignment Guides

IDT 1   IDT 2

quartz

Wall Bonding Gap   Guiding Electrode   SU-8 Alignment Guides
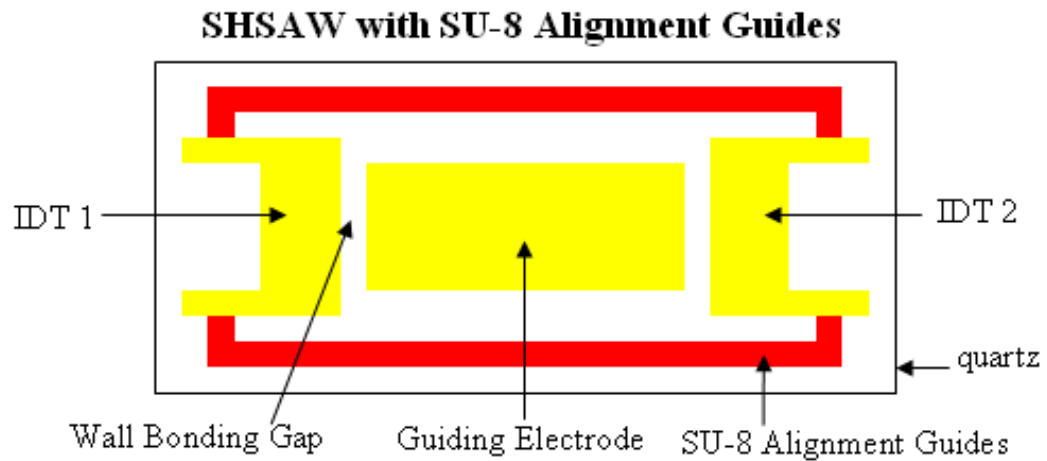
Diced PDMS Molded Chamber with Bored Holes

Microtube
Connection Holes

Surface Bonding Features   Bulk PDMS
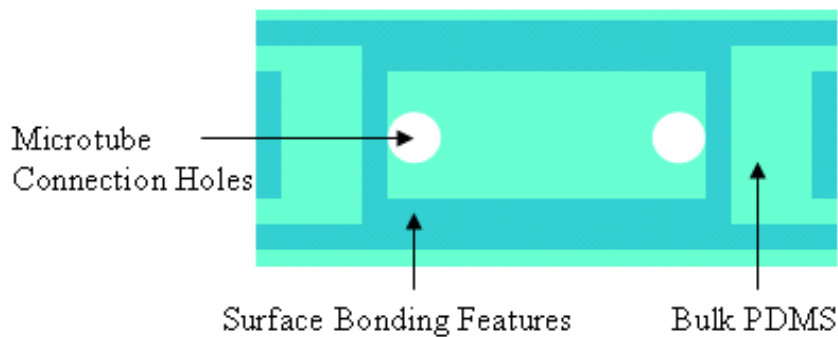
O_2 plasma treatment
PDMS dip in surfactant
Alignment
Dry / Heat

Hybrid PDMS SHSAW Packaged Platform
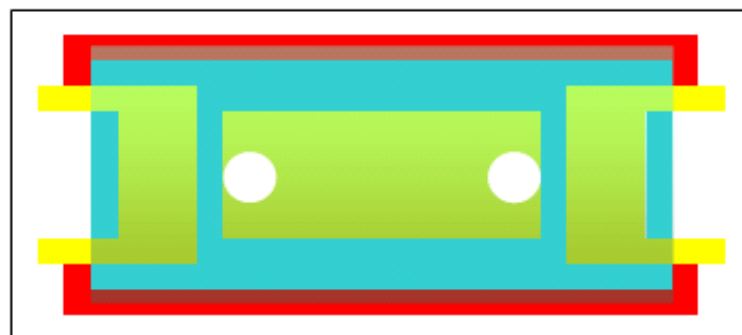
Figure 4.7. Fabrication of packaged hybrid PDMS SHSAW liquid phase sensor platform.

181

In Figure 4.7 a rectangular SU-8 framing structure, used for proper PDMS alignment of rectangular PDMS samples, is photographically patterned on the SHSAW wafer prior to dicing. Using a mask aligner the SU-8 features were able to be accurately positioned on the substrate relative to the SHSAW devices and within ±10 μm for the SU-8 thickness considered (~50 μm). The patterned SU-8 frame dimensions were designed slightly larger, 5 μm on each side, than the footprint of the PDMS chamber such that when the chamber is aligned the PDMS chip "snaps into place" within seconds through placement by hand. This alignment technique proved to be very quick and has batch fabrication compatibility, and provided very accurate alignment to SHSAW devices. The method proved to be much more advantageous than alignment by either microscope and micrometer.

An overview of the packaging process of the hybrid PDMS / SHSAW liquid phase sensor platform, shown in Figure 4.7, is further detailed next. The first step in the process involves patterning a quartz wafer with the desired SHSAW devices. After complete, SU-8 PDMS alignment guides are patterned on the SHSAW wafer and accurately aligned to the SHSAW wafer using a mask aligner. The SU-8 features extend approximately 50 μm above the quartz surface. The wafer is subsequently diced in to individual dies and is cleaned with solvents to prepare for chamber bonding. PMDS chambers are then prepared via the molding process described in Section 4.3.1 (SU-8 mold features are ~100 μm tall, therefore PDMS locking features are ~50 μm greater then than the top of the SU-8 alignment guides). After curing, holes are bored in the PMDS using a precision hole punch (Technical Innovations, Inc. Angleton, TX) to allow later

insertion of microfluidic tubes having connectors on opposites ends which are attachable to fluid systems such as syringes and valves (Upchurch Scientific, Oak Harbor, WA). After boring holes, individual PDMS chambers are diced using a razor blade which is first dragged flush against molded chamber framing features and then used to cut. Next, the merging and attachment process is initiated. If chambers had been diced a few days prior to bonding then the surface of PDMS was first cleaned in a room temperature bath of HCl:DI 1:5 for 5 minutes. Next the SHSAW wafer surface was activated via O_2 RIE treatment at 1000 mTorr, 150 Watts, for 1 minute. Afterwards, the PDMS and SHSAW were both treated at 1000 mTorr, 50 Watts, for 45 seconds. The SHSAW sample was then removed first and placed on a cleanroom wipe facing up. The PDMS wafer was then dipped in bath of prepared high purity 100% ethanol and allowed to dip dry for ~1 s (Care should be taken not to touch activated surfaces to be bonded with tweezers). Next the PDMS was gently laid down on the surface of the SHSAW device and positioned with tweezers to lock the chamber into place. Next a small piece of wipe was cut and placed on top of the chamber, followed by placement of a weight which applied uniform pressure to the device equal to ~0.25 psi. The use of the wipe allowed ethanol to evaporate out of the bored holes when covered by the weight. The packaged devices were left at room temperature overnight to allow ethanol evaporation and to initiate the bonding process. If the bond did not appear to be sufficient the next day, which is apparent by observing small bubbles at bonding surfaces, the chamber could still be peeled up allowing another bonding attempt to be performed (re-cleaning, O_2 RIE treatment, ethanol dip, alignment, drying) without sacrificing the SHSAW device. If the bond looked good, the sample was baked in an oven for 4 hours at 65 °C with the weight

183

on top rendering the bond irreversible. After the heat treatment the device packaging process is complete.

4.4. Improved Device Designs and Design Considerations

Over the course of 3 years about 10 different packaged device designs were evaluated based on the presented PDMS/SHSAW packaging technique. The design iterations sought to address issues such as best method to form fluidic connections to the device, optimal flow channel geometry and IDT / delay-path PDMS containment wall thickness, most advantageous number of devices on packaged chip, and removal of spurious responses. In terms of making fluidic connections to the devices, two main strategies were employed. In the first technique considered, microfluidic tubes were inserted into molded PDMS microfluidic channels and permanently sealed using glue or PDMS sealant. The outer diameter of the Teflon tubes was 360 μm (Upchruch Scientific, Part # 1932) and required SU-8/PMMA mold features to be about 280 μm tall to allow insertion of tubes into the packaged device; the ports were slightly smaller than the tubing outer diameter resulting in improved tube sealing. The use of this connection technique had the advantage of using tubes with very small fluidic volumes (less then 10 μL/m) which reduces the overall required analyte per experiment. One negative aspect was that very slow flow rates and high pressures are encountered as the flow resistance goes up as tube diameter is reduced. In addition this technique did not allow easy removal of inserted tubes, and if removed typically the device became damaged. A photograph of a device using this connection scheme is given in Figure 4.8.
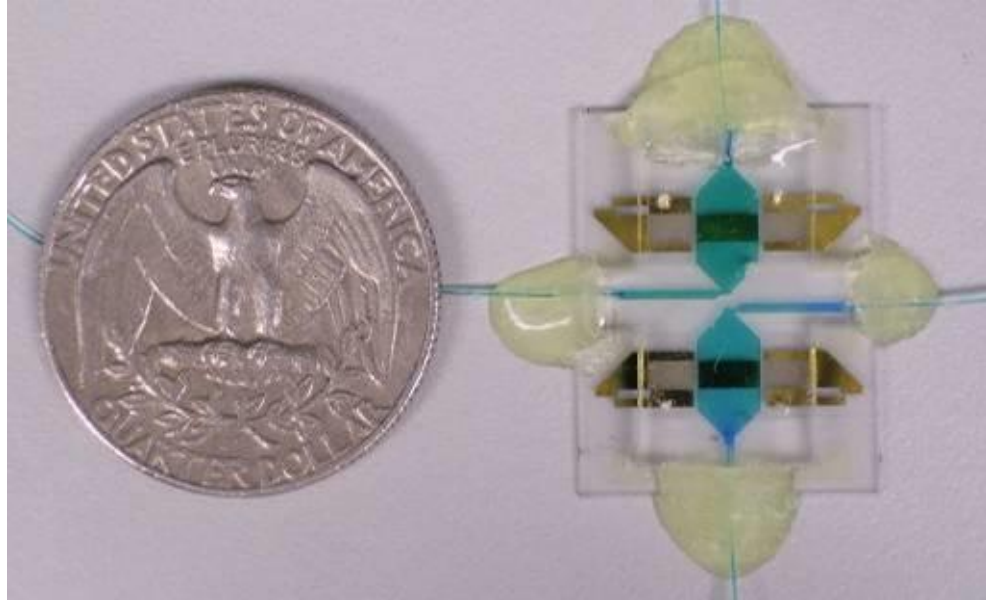
Figure 4.8. Packaged 1st generation SHSAW/PDMS device with fluidic chamber filled with dye-containing water.

The design of Figure 4.8 consists of two SHSAW device patterned on the Euler angle (0°, 132.75°, 90°) orientation of quartz on a single die, two independent fluidic channels, and tubing inserted and glued permanently. Dye-containing water was introduced into the device to demonstrate the chamber shape and to show that sealing is occurring. The chamber containment wall thickness in this instance was 200 μm or about 6.25 SHSAW wavelengths. Small pinholes were formed in the PDMS above IDT regions using a syringe needle to allow the alignment surfactant, in this case methanol, to evaporate out of the IDT regions during the bonding process. A diagram of the different device features is given in Figure 4.9.
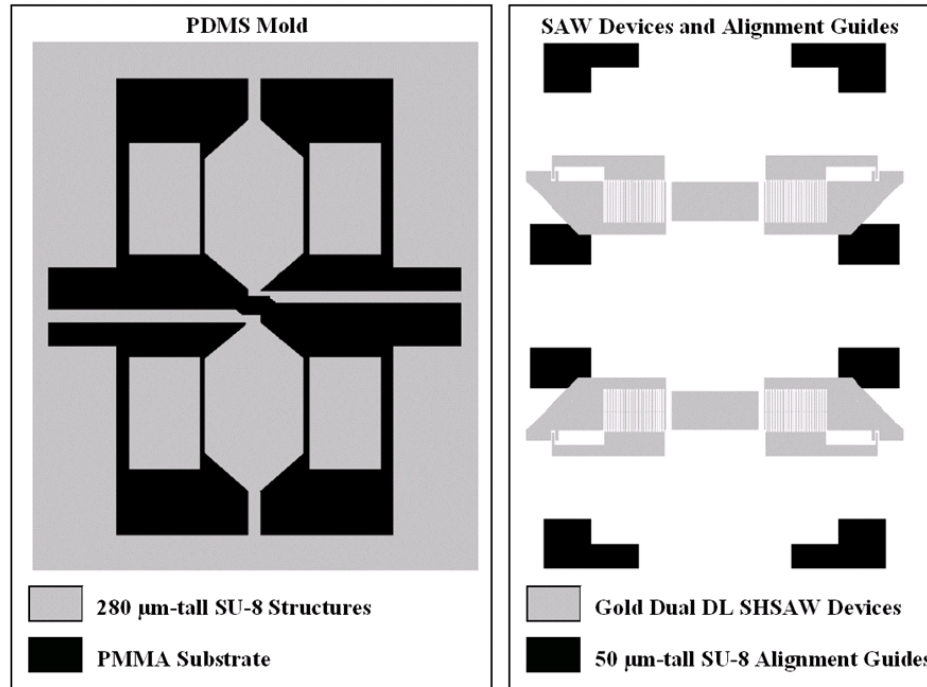
Figure 4.9. Diagram of fluidic, SHSAW, and alignment guide features of 1st generation design.

As an alternative fluidic connection method, the next approach involved punching holes in the bulk PDMS using precision machined hole punches, slightly smaller than 1/8" or 1/16" diameters, such that insertion of 1/8" and 1/16" outer diameter Teflon tubing could be firmly held in place without the need of a sealant or glue. This allowed tubes to be inserted from the top of the PDMS and removed repeatedly without causing damage to the device. Figure 4.10 shows a photograph of second generation packaged device having fluidic connections based on insertion of tubes through bored out holes in PDMS. The device in Figure 4.10 consists of 2 sets of 2 SHSAW delay-lines patterned on the $(0°, 132.75°, 90°)$ orientation of quartz with a redesigned PDMS microfluidic chamber. The fluidic interface consists of two 1/8" diameter inlet holes and a single 1/16" diameter outlet hole. A diagram of the design is shown in Figure 4.11.

186
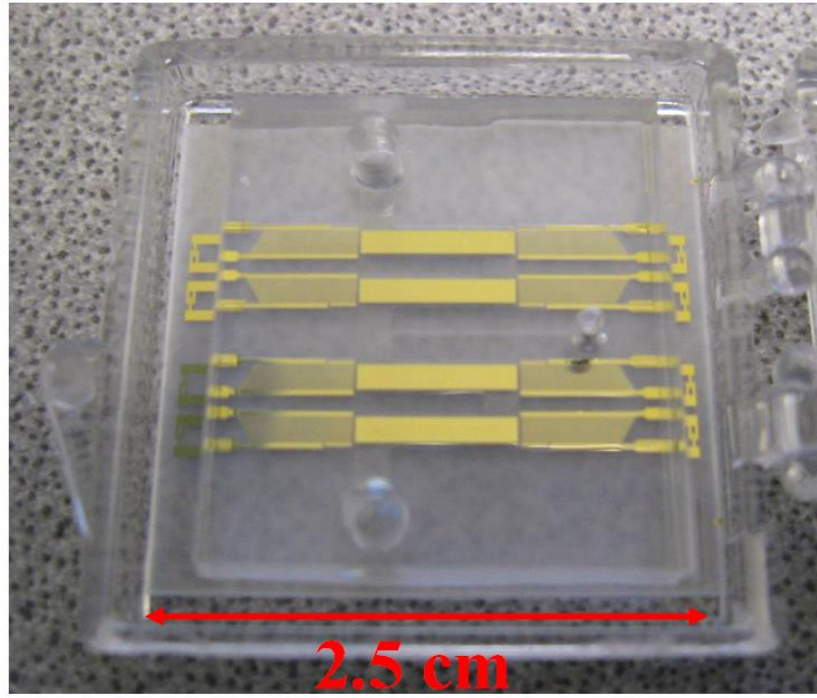
Figure 4.10. 2nd generation packaged SHSAW/PDMS device.
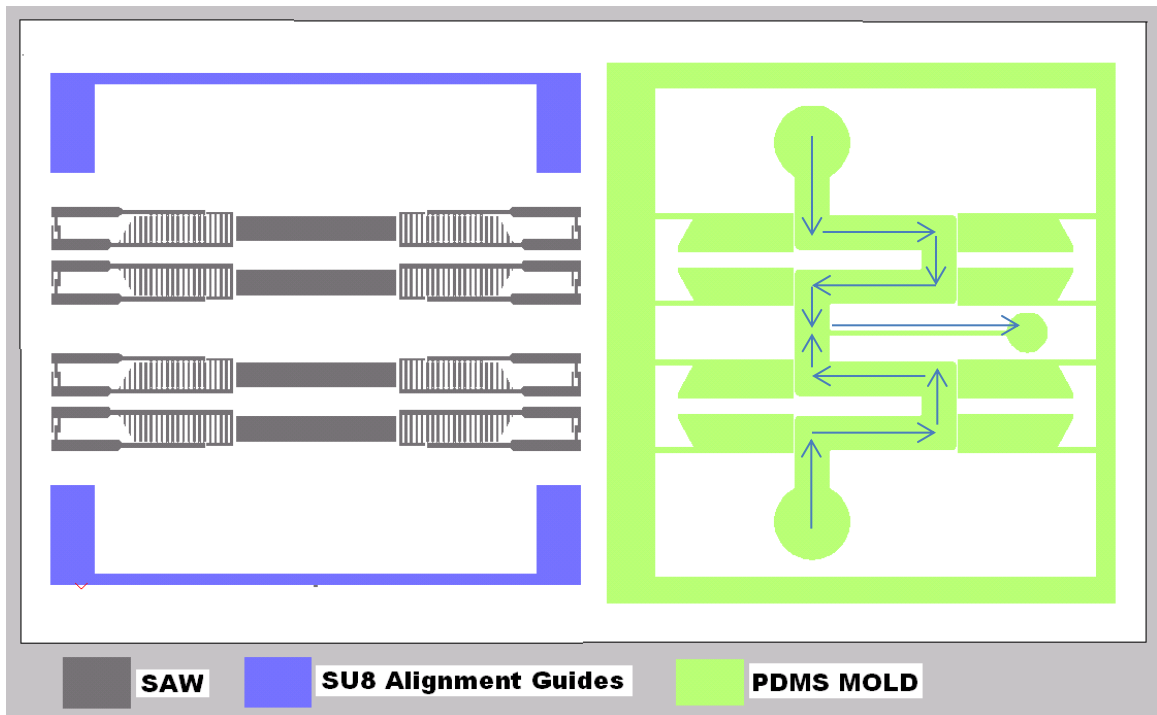
Figure 4.11. 2nd generation SHSAW/PDMS device design.

The design includes 4 overall SHSAW devices, the top two of which can be exposed to one analyte, while the bottom two can be exposed to a different analyte. Fluid is pulled into the chamber by applying suction to the common outlet port (central channel with smaller OD tube connection) (see arrows in Figure 4.11 indicating flow directions). Using valves on the tubing running into the inlet ports (larger OD tube connections) allows fluid to flow thru only one channel path or the other by closing a single valve. To prevent mixing between each channel, fluid is continuously drawn through the device by applying continuous section to the outlet port. During the design process it was thought that having a common output port may reduce the potential of sensing fluid pressure differences, which may result if using two independent suction sources; one for each channel. The design could be easily modified to include independent fluidic channels if desired. In this design, the fluidic containment walls separating the IDT and delay-path regions were reduced from 200 μm to 60 μm (1.875 acoustic wavelengths) due to improvement in mold processing capability resulting from practice, which was anticipated to reduce SHSAW reflection and attenuation and still provided adequate chamber sealing. The microfluidic channel geometry was completely redesigned to have rounded corners and more uniform channel width throughout. This reduced bubble nucleation, entrapment, and occurrence of fluid voids during experiments as compared to the 1st generation design, which is advantageous given that the presence of voids/bubbles along the delay path can affect the sensor response.

A 3rd and final generation device was designed and fabricated and is shown in Figure 4.12. The features of the device design are shown in a diagram in Figure 4.13.
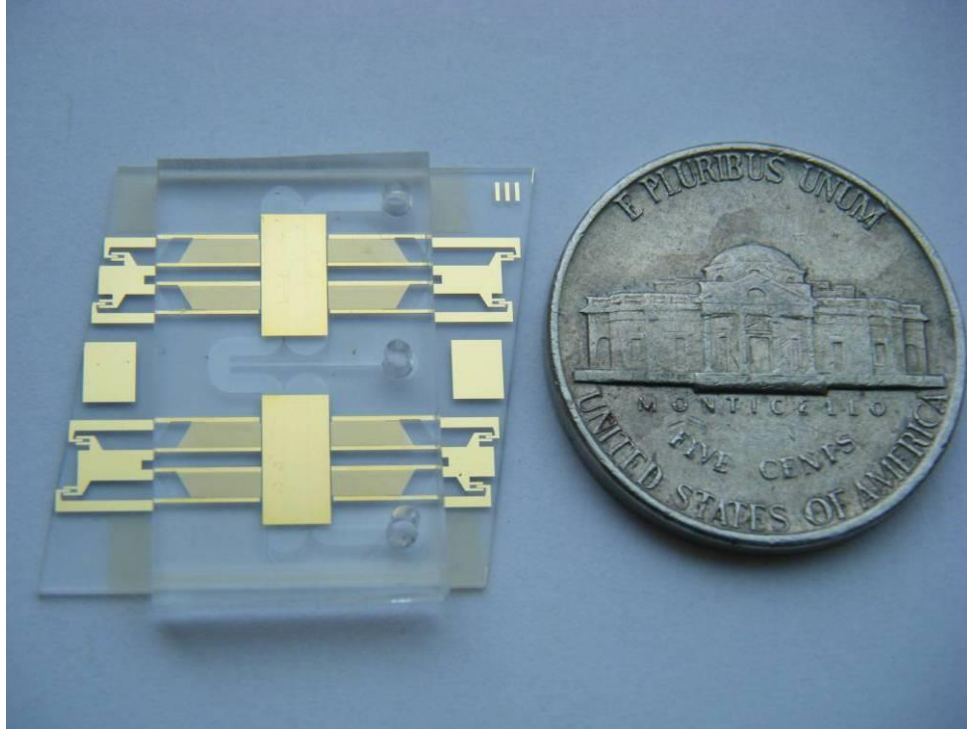
Figure 4.12. 3rd generation packaged SHSAW/PDMS device.
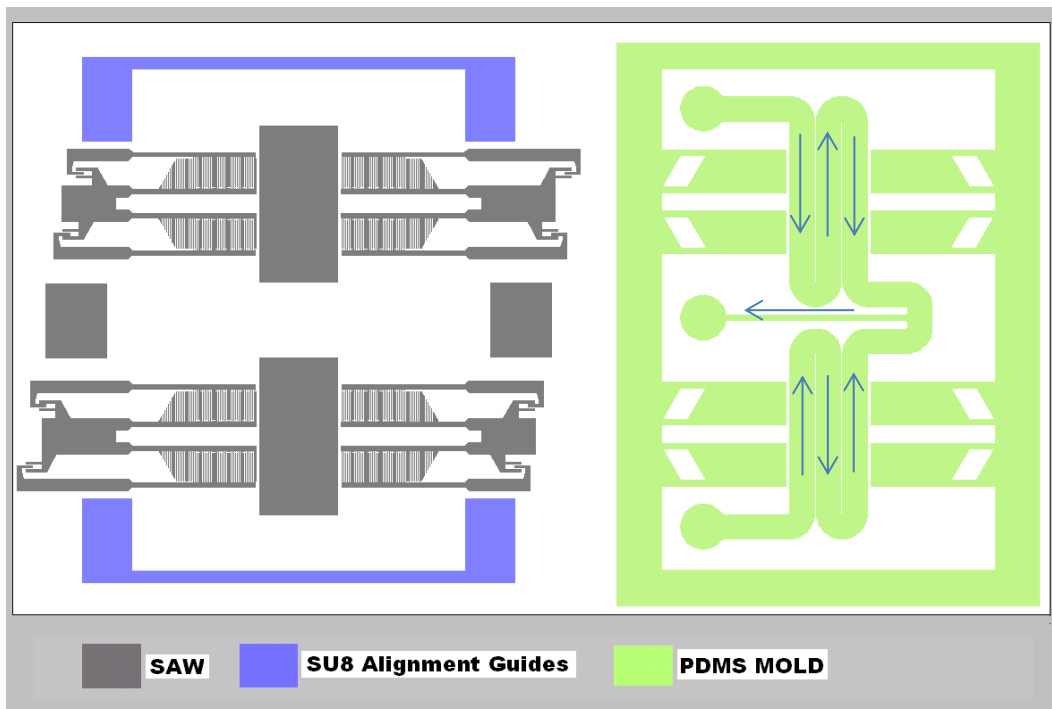
Figure 4.13. 3rd generation SHSAW/PDMS device design.

Major changes with respect to the 2nd generation design include: (i) the ability to dice individual die at an angle with respect to the SHSAW propagation direction which reduced the SHSAW spurious edge reflection; and (ii) the modified microfluidic chamber design. Rather than using a combination of 1/8" and 1/16" diameter tubing connections, the 3rd generation used strictly 1/16" connections. This reduced the total required analyte volume per experiment via reducing tubing dead volume. In addition, the fluidic channels are the same width as the tubing inner diameter and are constant throughout the flow path. The smaller width channels further improved chamber liquid filling and flow characteristics, such as reducing instances of bubble nucleation and entrapment, compared to 1st and 2nd generation designs. As a consequence of using narrower flow channels the channels themselves had to be looped back and forth to expose the entire delay path region to a fluid analyte, which did not seem to affect device response significantly, as discussed in the next section. The chamber fluidic containment walls between IDT and delay regions were slightly increased from 60 μm to 100 μm to improve bond strength without causing any significant effect on the device response because with the previous generation design leaks occasionally occurred due to reduced overall bond strength. In addition, channel walls in the middle of the delay path were designed to be 32 μm to minimally interfere with the propagating SHSAW; this dimension was chosen to be smaller than the other containment walls since a robust seal here is not required but is only used to guide the fluid along a proper path. In addition it should be noted that PDMS does not covalently bond to a gold surface using the bonding protocol employed. Lastly, the delay-path length of the 3rd generation device was shrunk

to 100 acoustic wavelengths from 225 to improve the dynamic range of the sensor via reduction of overall insertion loss under viscous fluid loading.

4.5. Packaged SHSAW Platform Performance

This section presents the performance comparison of the 3 packaged device designs previously discussed in this chapter. In particular, for each generational device the transmission coefficient, S_{21}, is presented and measured before and after attachment of the PDMS microfluidic chamber. A comparison is given in terms of device passband ripple and phase linearity. Improved S_{21} phase linearity and reduced passband ripple indicate that the direct SHSAW response from port 1 to port 2 dominates the measured response and that the liquid-phase theoretical sensing evaluation developed in Chapter 3 is applicable. Non-linear phase distortion and passband ripple indicate significant spurious signal being detected by the output transducer, which may stem from signals such as spurious SHSAW reflections, electromagnetic feed-through, and SHSBAW scattering and reflection. It is shown that the 3rd generation device design exhibits best phase linearity and reduced passband ripple, and verifies that the packaged devices are applicable to liquid-phase testing.

Figure 4.14 shows the measured S_{21} magnitude and phase responses of the 1st generation design before attachment of the PDMS chamber, and after attachment of the PDMS chamber. It is observed that before attachment of the chamber, both the passband ripple and phase linearity are very good indicating little effect of spurious responses.

Figure 4.14. 1st generation design transmission coefficient without PDMS '.', and with PDMS 'solid', magnitude (a), phase (b).

192

After attachment of the chamber it is observed that the average magnitude drops about 3 dB and some phase non-linearity effects become present in the response. This indicates that the 200 μm PDMS walls causes some SHSAW reflection and potential SHBAW scattering or finite propagation loss. To overcome the issues related to spurious signal detection, the 2nd generation device sought to reduce the chamber wall thickness between IDT and delay-path regions. It was anticipated that reducing the wall thickness would reduce the effects introduced after chamber attachment.

Figure 4.15 shows the measured S_{21} magnitude (a) and phase response (b) of the 2nd generation design before attachment of the PDMS chamber, and after attachment of the PDMS chamber. Compared to the 1st generation device this design had a chamber wall thickness of 60 μm rather than 200 μm. In addition, the 2nd generational device also replaced the ground plane electrode on the outsides of each IDT, sides opposite to the delay-path, with a short-circuit guiding grating to reduce mechanical discontinuities, i.e. reduce SHSAW reflection from the outer IDT edge. From Figure 4.15 (a) and (b) is apparent that attachment of the PDMS has little effect on the magnitude response, but strong ripple of about 5 dB is present in the passband. Using Fourier transform time-domain techniques this ripple was shown to originate from SHSAW reflection from the perpendicularly diced edge of the crystal. The phase does show some ripple as well and was removed by time-gating analysis verifying interference from the edge reflection. To overcome this problem the 3rd generation design included the ability to dice individual sensor die at a slightly inclined angle with respect to SHSAW propagation direction

193

perpendicular, as shown in Figure 4.12. Due to this dicing angle reflected SHSAW is scattered away from the detection IDT, thus reducing the overall level of spurious signal.

(a)

(b)
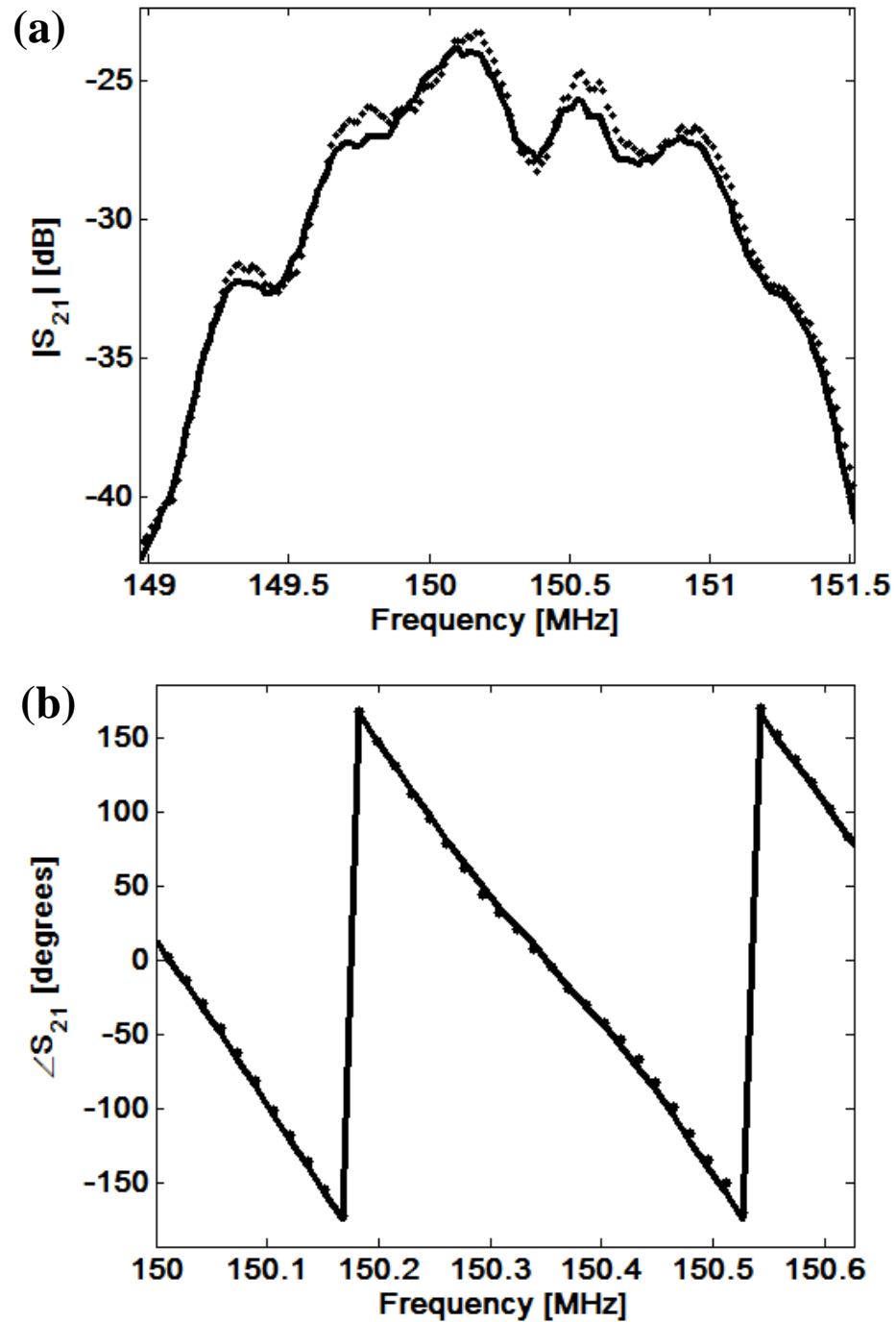
Figure 4.15. 2nd generation design transmission coefficient without PDMS '.', and with PDMS 'solid', magnitude (a), phase (b).

Figure 4.16 shows the measured S_{21} magnitude (a) and phase responses (b) of the 3rd generation design before attachment of the PDMS chamber, and after attachment of the PDMS chamber. Major differences between this design and the 2nd generation are the incorporation of a wafer dicing angle and a compromise in PDMS wall thickness that balances bond strength and level of spurious signal, which in this case is 100 μm. As apparent from Figure 4.16 (a) the passband ripple is greatly reduced as a result of dicing the wafer at an angle of about 10° with respect to the SHSAW propagation direction normal. In addition, the design displayed best phase linearity out of all generational designs. This design was chosen to be the final in this work and was used for subsequent liquid-phase sensing proof-of-concept demonstrations.

195
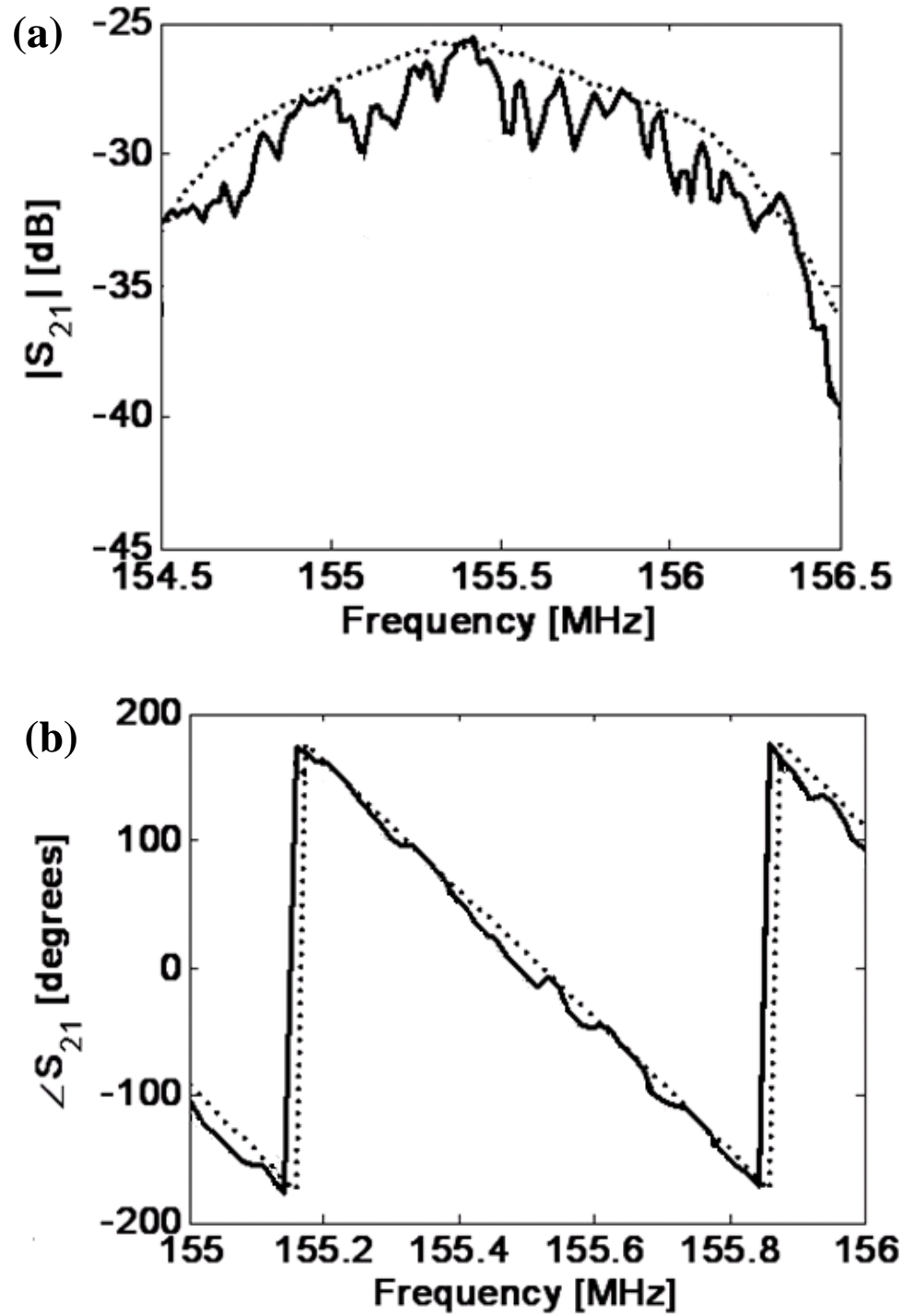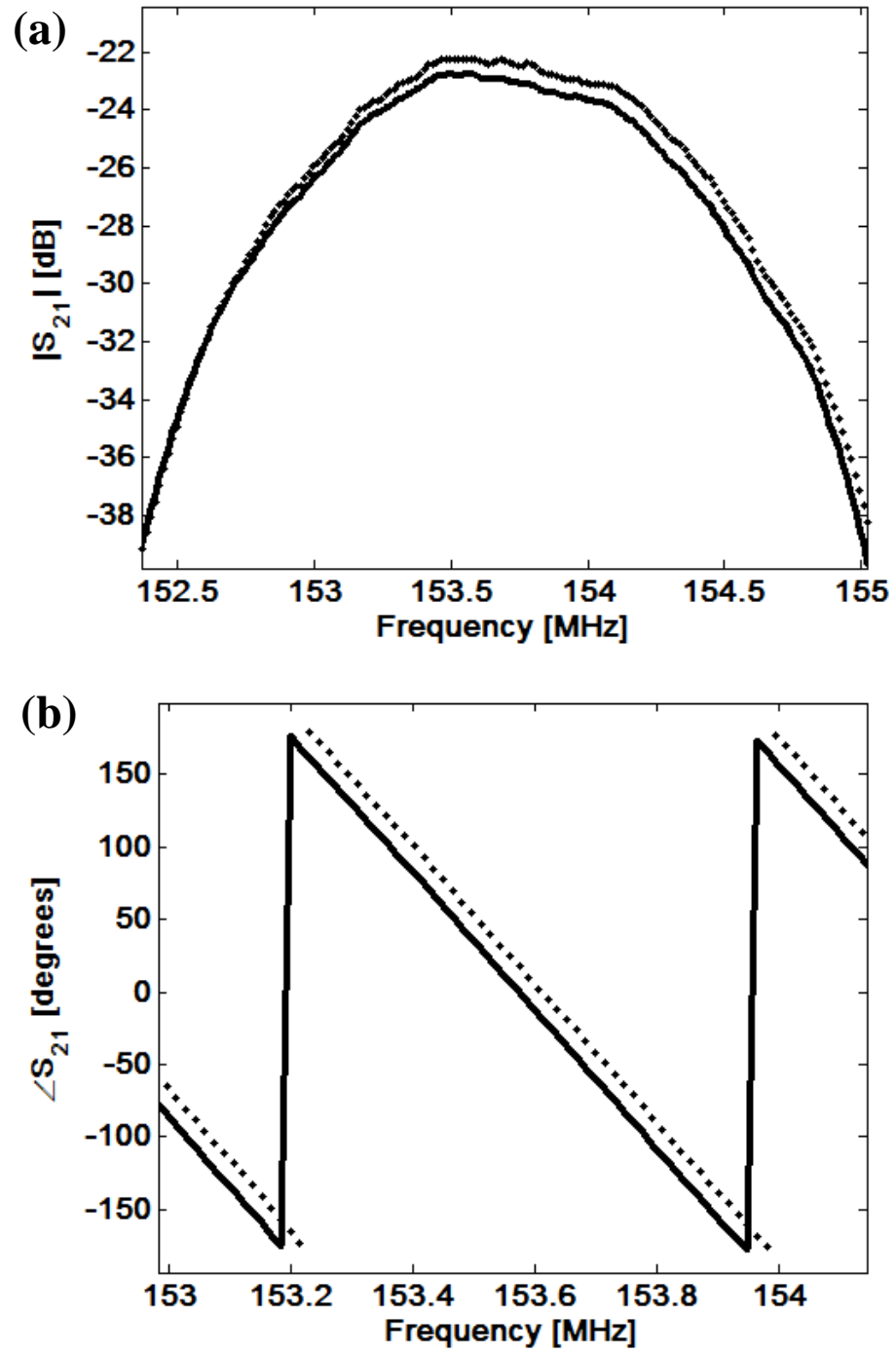
Figure 4.16. 3rd generation design transmission coefficient without PDMS '.', and with PDMS 'solid', magnitude (a), phase (b).

CHAPTER 5

PACKAGED SHSAW LIQUID-PHASE SENSOR EXPERIMENTAL RESULTS

5.1. Introduction

This chapter presents experimental results and analysis of fabricated SHSAW liquid-phase sensors based on the designs presented in Chapter 4. In Section 5.2 the experimental setup used is presented. The setup consists of various sub-systems such as SHSAW device temperature controlling hardware; radio frequency (RF) switches used interrogate individual delay lines; an interface to external fluid handling components; computer software routines; and data acquisition instruments. In Section 5.3 the performance of the 3rd generation SHSAW design is experimentally evaluated by measuring device responses upon exposure to various concentrations of glycerol-water mixtures that display a range of viscosities. The device transmission coefficient phase and attenuation shifts resulting from fluid loading of the device surface are shown and compared to theoretical shifts determined using the numerical propagation characterization model presented in Chapter 3. From the data the mode sensitivity parameter to viscosity is extracted and compared to the theoretical values given in Chapter 3. In addition, the viscosity detection resolution is extracted and presented. The values for extracted sensitivity and detection limit are compared with reported results of other liquid-phase acoustic wave devices. Next, in Section 5.4 multi-analyte sensing using the 3rd generation SHSAW design is experimentally evaluated. In particular, two of the four sensors on the device are exposed to varying glycerol/DI water concentrations, while the other two devices are exposed to only DI water. Lastly,in Section 5.5 an

197

experiment is presented in cooperation with a UMaine Ph.D. candidate to demonstrate the applicability of the devices designed and fabricated towards biosensor applications.

5.2. Experimental Setup

The fundamental component of the experimental liquid-phase SHSAW sensor measurement system is a packaged 3rd generation SHSAW/PDMS platform. Recall that this design consists of a single die with 4 SHSAW devices; 2 of which are contained in one fluidic flow path, and the other 2 are contained in another flow path. Therefore two separate analytes can be measured on the same die, and for each analyte, two independent SHSAW measurements can be made. This is achieved using a microfluidic chamber design with two fluidic inlets and common single outlet as detailed in Chapter 4. Upon placing the outlet port under suction, fluid flows through the channels and prevents intermixing. Under no suction, channels may begin to mix as a result of diffusion. In order to measure all four of the SHSAW devices using a single two-port network analyzer, switching electronics were required to be incorporated into the experimental apparatus. Figure 5.1 shows a block diagram of the electronic switching system constructed. The system consists of two radio frequency (RF) 4:1 multiplexing switches which are controlled via external electronics, in this case a computer running a LabView virtual instrument (VI). Port 1 and Port 2 nodes are connected to the ports of a network analyzer for individual SHSAW device measurement.
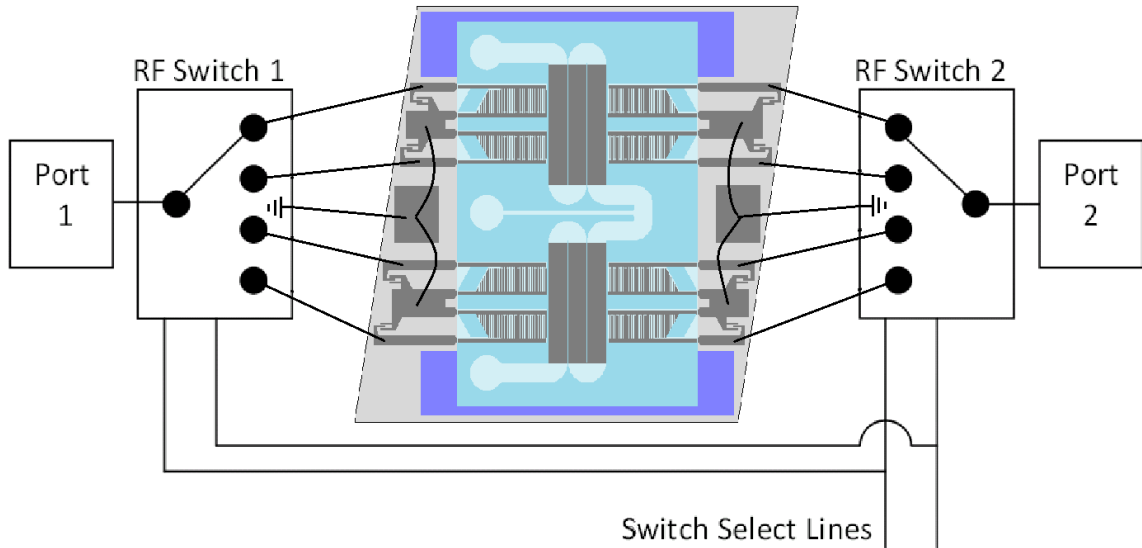
Figure 5.1. Switching electronics block diagram used to measure 4 SHSAW devices.

In addition to controlling which SHSAW devices are to be measured at a particular time, it was also desirable to control the temperature of the SHSAW devices precisely to minimize the response of sensors to environmental temperature variations. A similar temperature control setup to that used by [100] was constructed and consists of a resistance temperature device (RTD) probe to monitor temperature and a Peltier device to heat or cool the SHSAW devices. The two components were connected to an Omega temperature controller which was interfaced to a computer running LabView.

Figure 5.2 shows a diagram of the SHSAW device mounting and testing fixture. The fixture provides a method for sensor mounting, temperature control, and electrical connection to RF switches and a network analyzer. In particular, a Peltier device is sandwiched between a heat sink and a machined aluminum block that contains a small pre-drilled hole to allow insertion of a cylindrical shaped RTD. The SHSAW device is glued to a small printed circuit board (PCB) and wire-bonded to pads, of which are also

connected to header pins mounted on the PCB. The top of the Al block is in direct contact with the backside of the SHSAW PCB. The header pins of the SHSAW PCB are inserted into header sockets mounted on another PCB containing the RF switches and SMA connections. The header sockets have three main functions: (i) provide electrical contact to the sensor; (ii) provide mechanical support for the RF switch PCB; and (iii) allow easy removal or replacement of SHSAW PCBs. The switch PCB is not in direct thermal contact with temperature controlled Al block. Due to the relatively large thermal mass of the SHSAW PCB and Al block, as compared to the SHSAW device, the actual temperature of the SHSAW should be very close to that of the PCB and Al block, especially around room temperature. Photographs of the device fixture are shown in Figure 5.3. Appendix G contains documentation for the RF switch and sensor bonding PCBs.
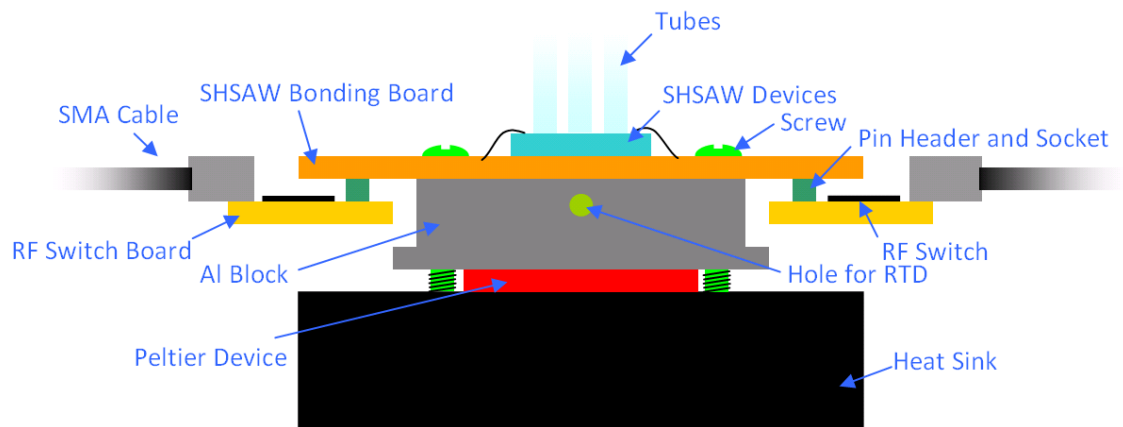
Figure 5.2. Temperature control hardware and RF switch setup.
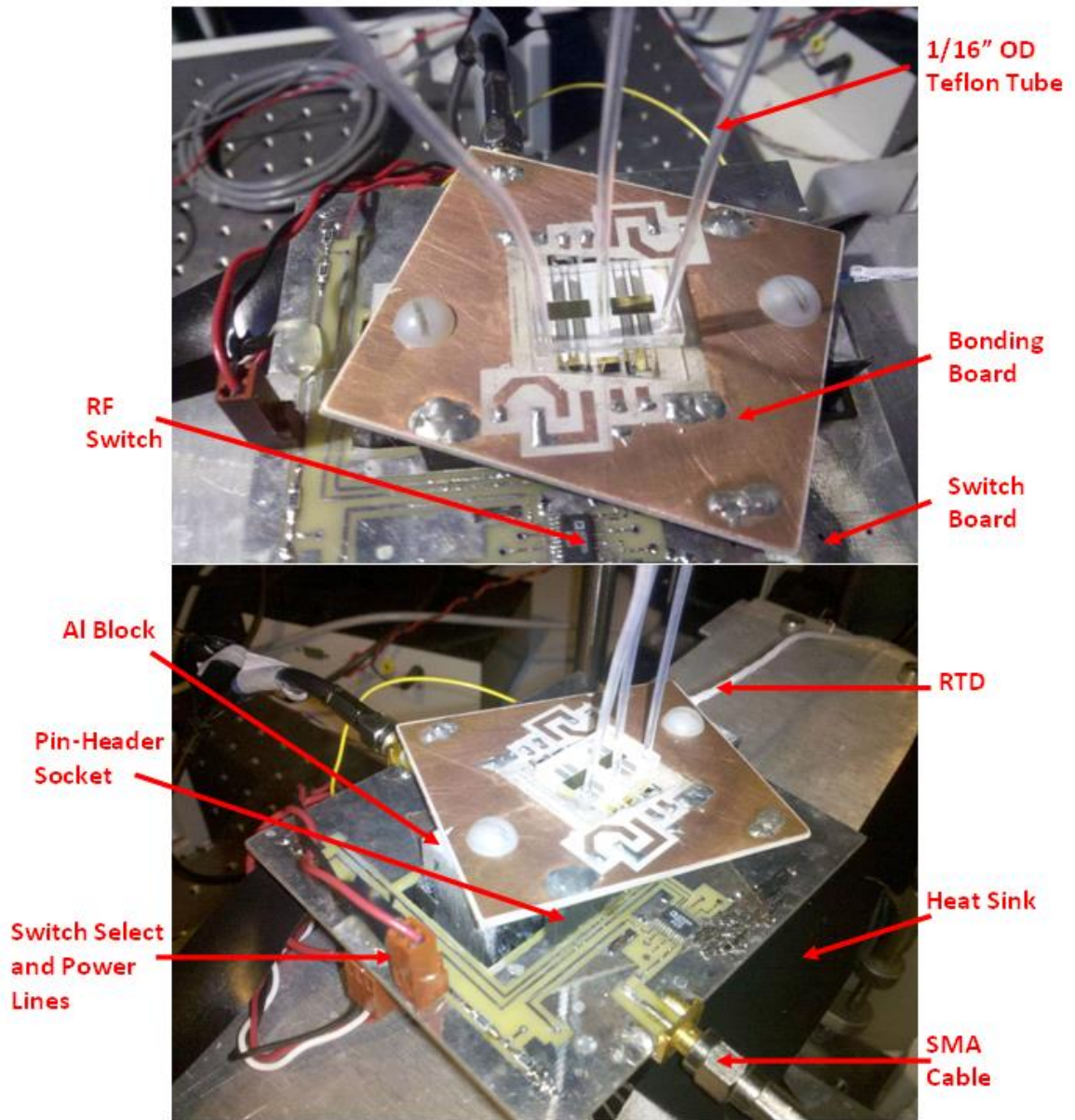
Figure 5.3. Photographs of the setup depicted in Figure 5.2.

A diagram of the fluid system is shown in Figure 5.4. The setup consist of two syringes with plungers removed, which are mounted on a ring stand (not shown in figure) that are used as fluid analyte reservoirs. The ends of the syringes are connected to microfluidic valves (also mounted on the ring stand) with tubing, and permit on/off

control of each flow path. The other sides of the valves are connected to the PDMS inlet

port with tubing. The PDMS outlet port is connected to another microfluidic valve with

tubing, and allows suction on/off control. The other end of this valve is connected to a

Erlenmeyer flask with tubing that is inserted into a one of two holes in the a rubber

stopper. The flask is used for fluid waste collection. To generate suction, the flask is

brought under partial vacuum using an air pump. A needle valve is used to control overall

flow rate of pumped air and fluid. A pressure gauge is also installed to indicate indirectly

the flow-rate (actual flow rate is analyte dependent as it depends on fluid viscosity and

pressure and must be calibrated if accurate flow-rate information is desired).
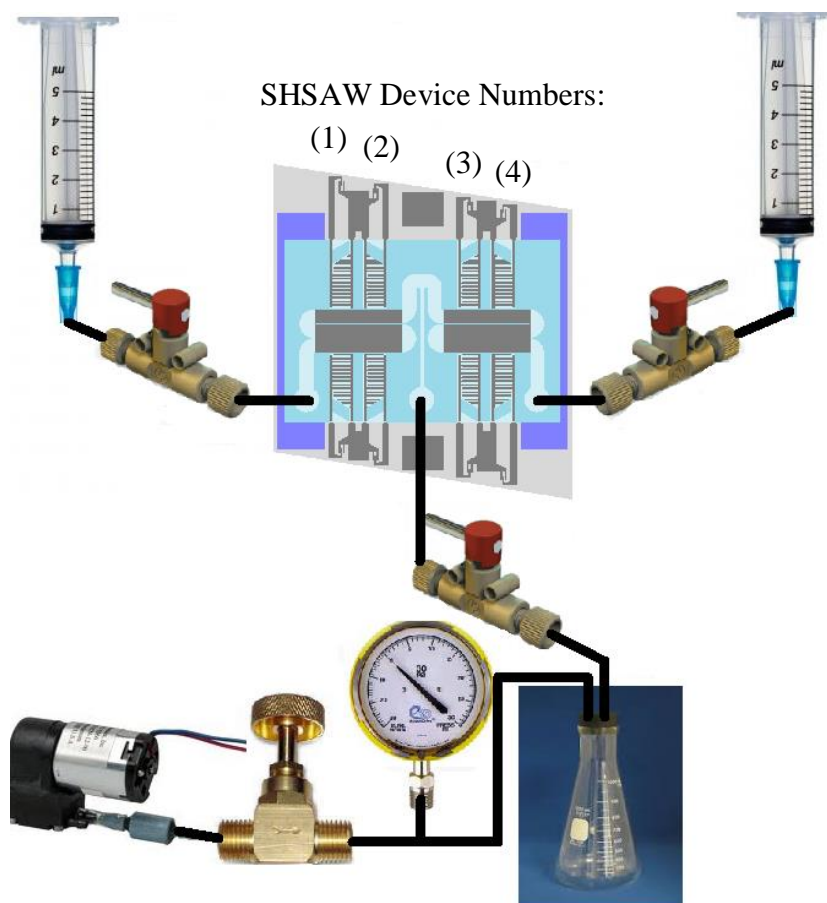
Figure 5.4. Fluids setup (note the SHSAW device numbering convection).

A LabView program was written and used to control the device temperature, set the state of RF switches, and initiate and retrieve measurement data from an Agilent 4396B two-port network analyzer. The RF switches are digitally controlled by an Ontrak Control Systems Inc. ADR2100 Analog/Digital/RS232/RS485 interface board (http://www.ontrak.net/adr2100.htm) having 32 digital I/O lines which are setup and controlled using LabView program over RS232. A block diagram of the LabView code routine is shown in Figure 5.5.
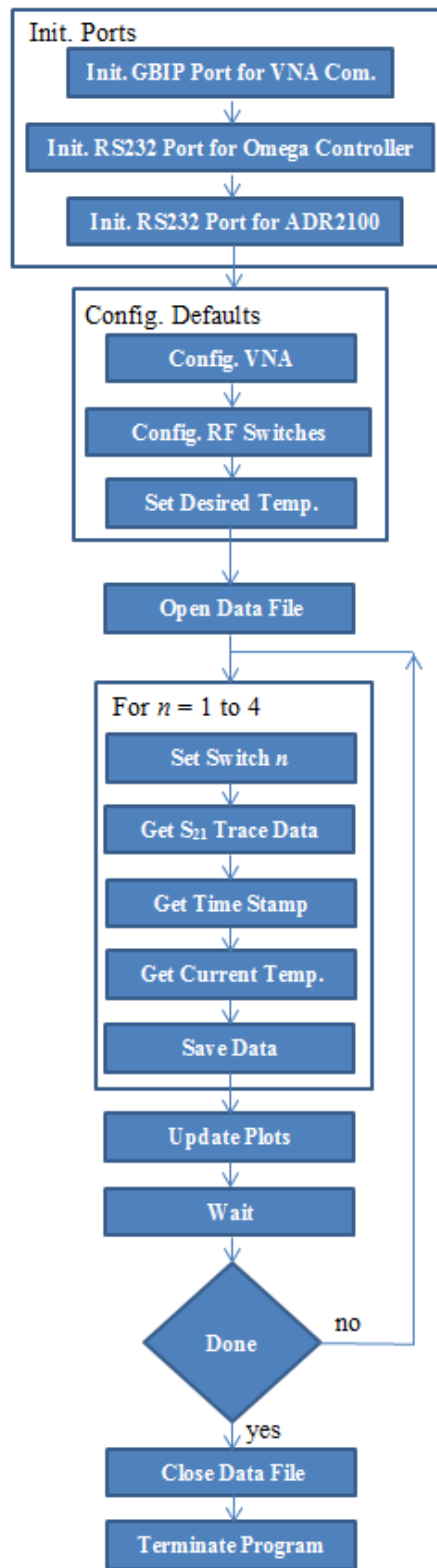
Figure 5.5. Block diagram of the LabView code routine.

5.3. Viscosity Sensing: Measurements of Glycerol Water Dilutions

To demonstrate the use of the SHSAW platform towards liquid-phase sensor applications and verify the sensor sensitivity analysis in Chapter 3, initial experiments were designed to characterize the device performance in terms of viscosity sensing. Seven liquid sample analytes used to characterize the 3rd generation SHSAW platform were obtained [101]. The samples consisted of dilutions of glycerol in DI water with concentrations, measured densities, and viscosities given in Table 5.1. The densities were measured using 1 mL samples and a precision scale, while the viscosities were determined using a Cannon-Fenske Routine Viscometer.

% weight Glycerol in DI	Density (g/mL)	Dynamic Viscosity (cP)
0	0.9860	0.9542
1	1.0005	0.9959
3	1.0116	1.0629
10	1.0190	1.1431
15	1.033	1.4240
25	1.07	2.3119
30	1.097	3.2065

Table 5.1. Properties of samples used for the SHSAW device viscosity experiments.

Over the range of increasing glycerol concentrations the viscosity increases by 236% while the density only increases 11%. Therefore use of such a fluid analyte is very good for viscosity characterization as the viscosity change dominates the variation in fluid physical properties. For pure shear bulk-wave liquid-phase sensing devices the theoretical response of the fluid interaction with the device only depends on the viscosity-density

product for a short-circuit condition, which can be shown using the equation for the isotropic half-space Green's Function (given on page 63 in Chapter 2) evaluated when there is no-field variation along the surface, i.e. $s_x = 0$, and $c_{44} = j\omega\eta$ for the fluid. In the case of a SAW devices $s_x \neq 0$. As a result, the half-space Green's functions for the isotropic fluid, assuming a single shear displacement u_2, depends on $\rho\,c_{44} - c_{44}^2 s_x^2$, and not just $\rho\,c_{44}$ as in the case of a bulk-wave device; s_x is the slowness of the x-directed spatial variation of fields along the interface and $c_{44} = j\omega\eta$ for a Newtonian fluid. Therefore two fluids having the same viscosity-density products but unequal densities would theoretically have equal sensor responses using the same bulk-wave device. Alternatively if using a SHSAW devices, the responses would theoretically be unequal, although potentially very similar, due to the additional effect resulting from finite field variation of $-j\omega s_x x$ along the interface.

The design and fabrication characteristics of the 3rd generation SHSAW devices used in the experiment included: two 80.5 split-finger pair IDTs having 4.5 μm electrode width and 3.5 μm gaps (32 μm IDT periodicity) and aperture equal to 1150 μm; 110 μm gaps between last IDT electrodes and guiding electrodes; delay-path length of 3120 μm (97.5 IDT periodicities); metallization consisting of 165 nm Au atop a 15 nm Cr adhesion layer, where $\omega h = 159$ m/s at device center frequency of 153.43 MHz. The length of the delay path exposed to the fluid after packaging is 3066 μm. Using the measured guiding electrode thickness, the SHSAW velocity for a uniform guiding electrode was numerically computed at the operating frequency and determined to be 4760 m/s, which

was used to determine the approximate wavelength of the SHSAW on the delay path electrode, equal to 31 μm. Therefore the fluid-exposed delay path length normalized to wavelength was approximately 99.

The first experiment involved loading the PDMS chamber with increasing concentrations of glycerol over time. For each concentration tested the fluid was allowed to sit under zero flow-rate for 10 minutes while measurements of individual device S_{21} phase and magnitude responses at a constant frequency located in the device passband were taken, here 153.43 MHz. Figure 5.6 (a) and (b) show the phase and magnitude shifts respectively of the 4 devices over the extent of the experiment; the last step involved testing DI water again to see effect of any potential drift. The magnitude and phase responses are shifted to reference values obtained at the start of the experiment where DI water was loaded into the chamber. The initial magnitude and phase response at 153.43 MHz is given in Table 5.2 before addition of fluid, and after loading DI water.

Device #	Init. Mag. [dB]	Init. Phase [degrees]	DI Mag. [dB]	DI Phase [degrees]	Delta Mag. [dB]	Delta Phase [degrees]
1	-22.395	-0.27	-26.828	-25.26	-4.433	-25.53
2	-23.256	20.60	-27.723	-5.60	-4.467	-26.20
3	-23.472	37.59	-27.927	11.10	-4.455	-26.49
4	-23.136	34.86	-27.342	9.85	-4.206	-25.01
Mean	-23.065	23.20	-27.455	-2.48	-4.390	-25.81
Std. Dev.	0.468	17.33	0.483	16.98	0.124	0.67

Table 5.2. Magnitude and phase response for empty chamber and DI water filled chamber.

207
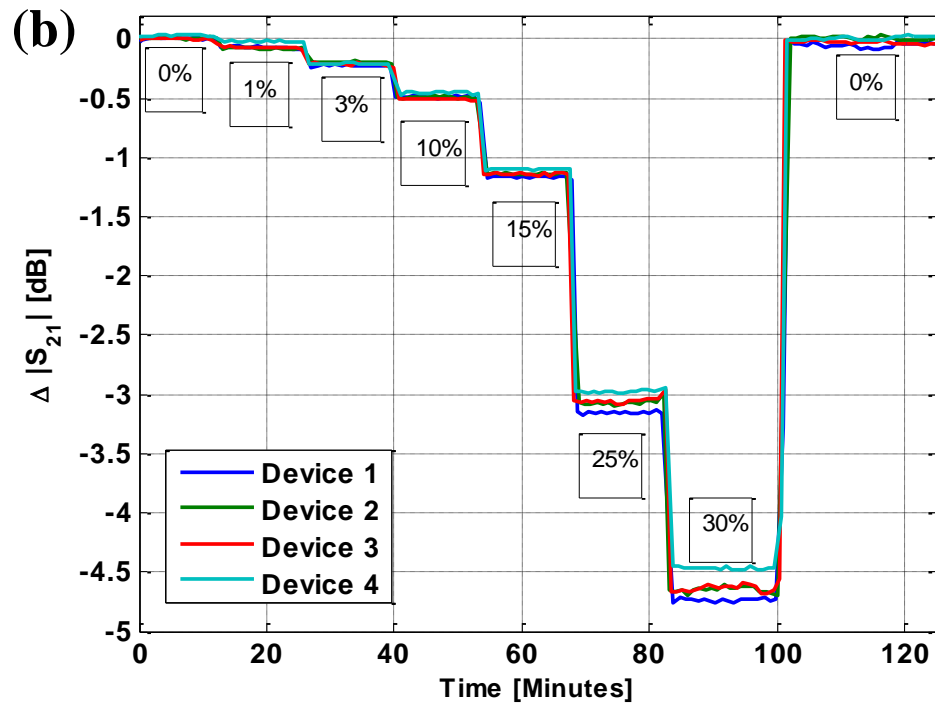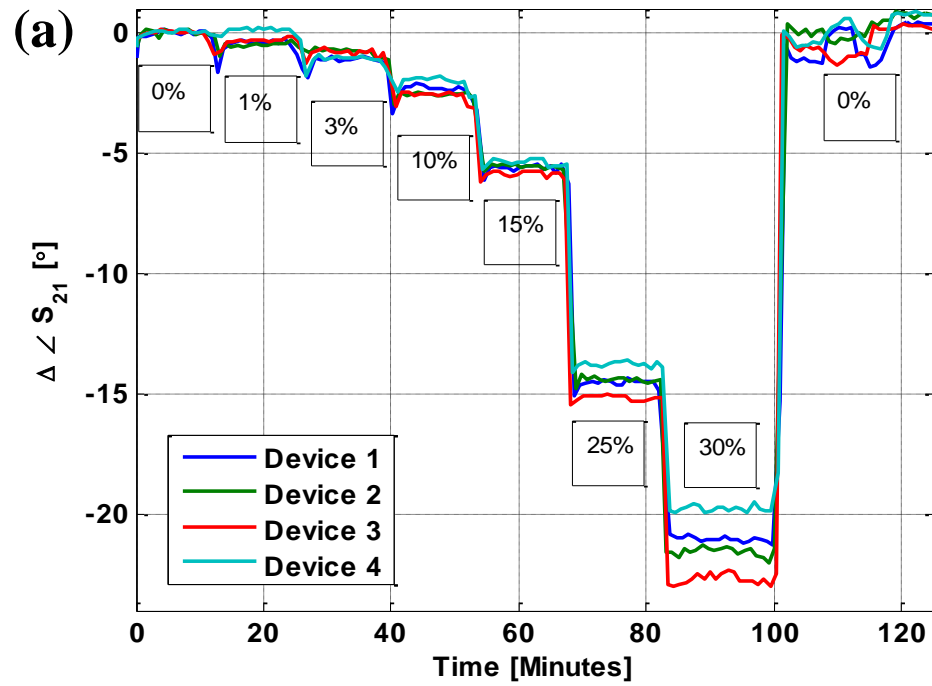
Figure 5.6. 3rd generation design response to various concentrations of glycerol (% weight) solutions in DI water; (a) S_{21} phase response, (b) S_{21} magnitude response.

208

The sensor is clearly able to distinguish the varying solutions. It was observed that the signal-to-noise ratio (defined as the shift in response, phase or magnitude, resulting from changing from DI water to 30% glycerol, divided by the amplitude of response variation, phase or magnitude, observed during exposure to 30% glycerol) is about 110 for the phase response, and 310 for the magnitude response. The noise signals are expected to be due to the fact that devices were fabricated on the Euler angle (0°, 132.75°, 90°) orientation of quartz which exhibits finite temperature coefficient of delay (TCD). It was measured that the temperature variation of the SHSAW devices is about ±0.1 °C over the course of the experiment. In a previous experiment the TCD of the device was measured using a temperature controllable chuck and Cascade Microtech probe station with the chamber empty. The data extracted showed a phase response with temperature equal to 2.2°/°C. Using (3.8) the TCD was determined to be about -30 ppm/°C. Using this value of TCD the expected phase variation for the measured temperature variation of ±0.1°C is about ±0.22°, which explains the signal variation in Figure 5.6 (a) of ±0.19°. Given that the chamber was empty during the extraction of TCD, the addition of 30% glycerol into the chamber may explain this slight discrepancy as viscosity of fluids are sensitive to temperature as well.

In terms of the sensor insertion loss, given that the extracted signal-to-noise ratio of the measurement data is about 3 times larger for the magnitude signal as compared to the phase signal, magnitude tracking rather than phase tracking may be more advantageous, if devices are fabricated on the non-temperature compensated quartz Euler angle (0°, 132.75°, 90°) orientation. Towards trying to explain this result, using the same

set of data collected in the device TCD extraction, the temperature coefficient of magnitude (TCM) was also extracted. Over the device passband frequency the TCM value extracted was -0.09 dB/°C. Given the ±0.1 °C temperature variation observed during the glycerol experiments, variation of the magnitude response was expected to be of ±0.009 dB. The actual measured variation of the magnitude response during the glycerol experiments Figure 5.6 (b) was about ±0.014 dB, which is only about 1.5 times larger than expected. Again, given that the chamber was empty during the extraction of TCM, the addition of 30% glycerol into the chamber may explain this slight discrepancy as viscosity of fluids are sensitive to temperature as well.

Taking the average phase and attenuation shifts resulting from exposure to the various solution concentrations, the normalized changes in complex propagation constants were determined as a function of the square-root of radian frequency-viscosity-density product and are shown in Figure 5.7. Such a plot is shown for acoustic wave liquid-phase sensors in [86, 102] and is used to characterize the device sensitivity parameter, S, in (3.17). In addition, the expected responses assuming both Newtonian and Maxwell models are shown which were computed using the rigorous numerical software tool discussed in Chapter 3 and the parameters given in Table 5.1. The Maxwell model is evaluated in the same way as the Newtonian model with the exception that the fluid shear modulus, c_{44}^{fluid}, is replaced by a complex quantity given by (5.1), which is based on a Maxwell viscoelastic model [86].
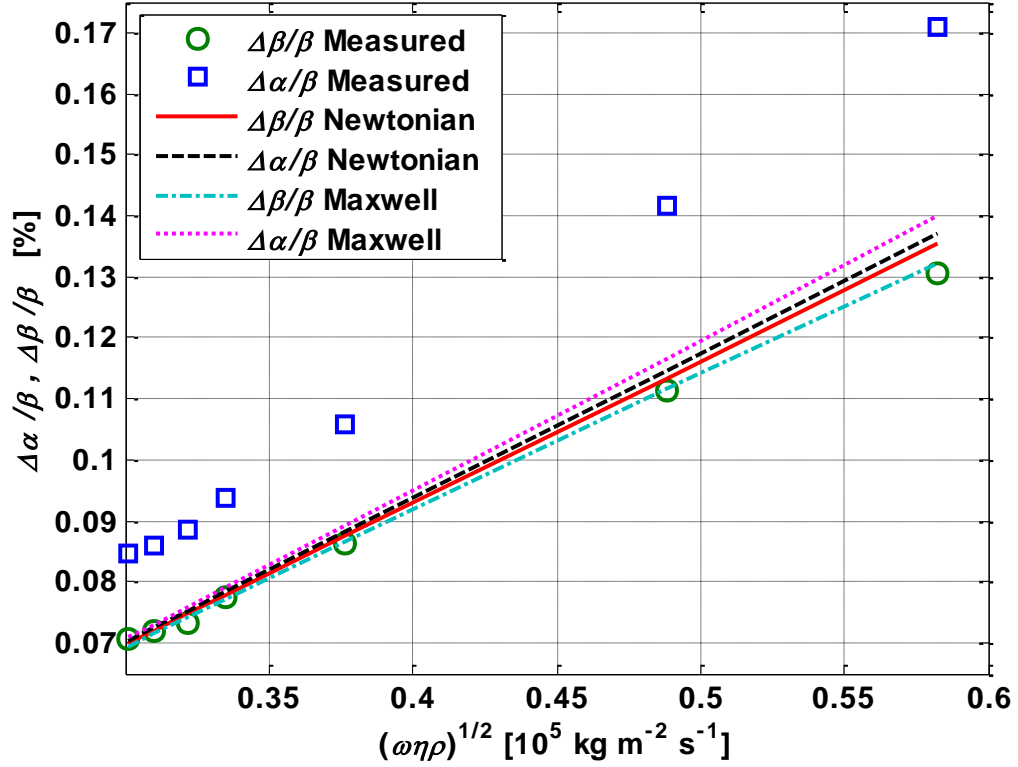
Figure 5.7. Experimental and theoretical normalized changes in complex propagation constant in percent for the six glycerol-water solutions considered.

$$c_{44}^{fluid} \rightarrow \frac{j\omega\eta}{1 + j\omega\eta \Big/ \mu_\infty} \qquad (5.1)$$

where:

- η is the low frequency fluid viscosity determined by the viscometer,

- μ_∞ is the shear modulus of the fluid at very high frequency.

The parameter η/μ_∞ is defined as the characteristic relaxation time of the fluid. In this work a constant value of $\mu_\infty = 0.07$ GPa was assumed as in [102]. Given (3.17) from [86] which is based on a perturbation theory, it is expected that both the normalized change in attenuation and wavenumber should be equal to each other. Based on the data obtained with the rigorous model used in this Section 3.3.2, shown in Figure 5.7, this is confirmed to be quite an accurate assumption over the range of radian frequency-viscosity-density product values considered. It is observed that the normalized change in attenuation and wavenumber values begin to diverge as the radian frequency-viscosity-density product increases, with the Maxwell model diverging faster as compared to the Newtonian model. The experimental wavenumber data fits well to the Newtonian model over the range of radian frequency-viscosity-density, with only a slight slope deviation from the numerically predicted. Regarding the attenuation data, the measured values compared to the numerically predicted do not agree as well, as there seems to be an offset and a slope deviation. Looking at the Maxwell model data it is apparent that use of this model better accounts for the wavenumber and attenuation slope discrepancy, but it still does not account for the observed attenuation offset. This additional attenuation offset has been observed in [86] and the authors tested to see if the offset could be a result of any of the following second order effects: surface roughness, non-Newtonian behavior, interfacial slip, or interfacial double layer. None of the methods could explain the observed offset. In this work two potential reasons for the observed offset are hypothesized. One potential reason for the additional observed attenuation is that the equivalent acoustic impedance seen by the IDT looking into the propagation path

212

region may be changing slightly upon fluid loading, which can be expected given that the SHSAW phase velocity reduces further compared to the IDT region velocity with increased loading. This may cause an additional mismatch between IDT and delay path impedances resulting in less power being delivered to the mode along the delay path region, thus reducing the detected power by the other IDT which appears as additional insertion loss. Another potential reason for the additional observed attenuation follows. Given that physical IDTs do not generate a pure plane wave, as the theory assumes, due to diffraction, the actual displacement components along the surface may not be entirely shear. As a result additional energy loss will occur via excitation of a compression wave into the fluid or potentially via leakage of energy outside the effective device aperture. In any case the observed offset only equates to and extra 0.81 dB and 1.6 dB of insertion loss in the device response for the 0% and 30% solutions respectively, which corresponds to 9% and 17% of additional power being lost. The power lost can potentially be accounted for by reasons indicated above. Since the wavenumber response of Figure 5.7 fits the expected data much better then the attenuation parameter, it was chosen to be used for fitting the measured data to (3.17) for extraction of the device sensitivity parameter. The result of the referred fit resulted in $S = 3.3 \cdot 10^{-8}$ m^2·s/kg for this particular design. Given the discussion on page 127 regarding mass sensitivity, this value of S corresponds to a mass sensitivity of $S_m = 318$ cm^2/g. Using (3.18) and (3.15) the sensitivity parameters towards viscosity and radian frequency-viscosity product were determined to be $S_\eta = 37$ ppm/mP and $S_{\omega\eta} = 0.38$ 1/GPa, respectively and agree very well with predicted value of 0.395 1/GPa extracted (at 154.3 MHz) using software written for the numerical sensitivity analysis described in 3.3.2. Using (3.13) and assuming only the

temperature dependent term is non-zero the resolution of the sensor towards a viscosity perturbation of DI water is at least 0.3 mP. When also including the second term of (3.13) and assuming a phase resolution of 0.1° and that the level of spurious detected signal is at least 50 dB below the main signal, which was verified via time gating analysis, the resolution of the sensor towards a viscosity perturbation of DI water is better than 0.72 mP. The data in Figure 5.6 (a) shows that the 1% glycerol solution can just barely be detected, which has a 0.42 mP increase in viscosity with respect to the 0% solution, thus verifying the predicted viscosity resolution. In terms of a sensitivity comparison with other reported surface acoustic wave devices, [103] gives their own, and cited values, of S equal to $8.2 \cdot 10^{-9}$ m^2·s/kg, and $4.8 \cdot 10^{-8}$ m^2·s/kg and $2.6 \cdot 10^{-8}$ m^2·s/kg, respectively for their developed SHSAW device based on an AlN-on-sapphire substrate, and two reported Love mode devices consisting of devices fabricated using an SiO_2 layer atop Euler angle (0°, 132.75°, 90°) quartz. In addition the authors report a mass sensitivity for their AlN/sapphire device given as S_m = 131 cm^2/g. For quartz crystal microbalance (QCM) devices the mass sensitivity is proportional to the operating frequency by a factor of about $2.26 \cdot 10^{-6}$ s·cm^2/g for AT-cut quartz according to the well known Sauerbrey Equation [12]. For typical QCM devices operating at the fundamental harmonic, the device operating frequency is between 1-30 MHz. Therefore the achievable mass sensitivity of QCM based devices is typically between 2 and 68 cm^2/g; a factor of about 5 less than the device reported here for the best QCM mass sensitivity at 30 MHz.

5.4. Multi-Analyte Sensing

To demonstrate the ability of the developed device to simultaneously analyze two separate fluid analytes, another experiment was conducted which consisted of exposing two of the four devices to the same viscous solutions used in the previous experiment, while exposing the other two devices to DI water. As opposed to the previous experiment, where fluids were allowed to sit under no flow rate during measurement, this experiment required a continuous flow rate to mitigate solution mixing during the experiment. This was achieved by connecting the fluidic chamber's common outlet to a flow control valve and pump providing constant vacuum and fluid suction as detailed in Figure 5.4 (note the SHSAW device numbering convention). Through experimentation the needle valve and vacuum level were altered to achieve a flow rate at the output port of about 20 µL/min (calibrated with DI water in both reservoirs). During the course of the experiment varying glycerol concentration solutions were exposed to two of the four devices for about 10 minutes at a time. Upon changing the solution, the majority of residual fluid in the syringe reservoir was removed leaving behind just enough to prevent air from entering the system. Within a minute after fluid removal the next sample was added to the reservoir. Figure 5.8 (a) and (b) show the devices phase and magnitude responses, respectively of all 4 devices. The response curves are shifted to zero at time zero as was done in the experiment described in the previous section (see Table 5.2 for un-shifted initial response properties of each device).

(a)

(b)
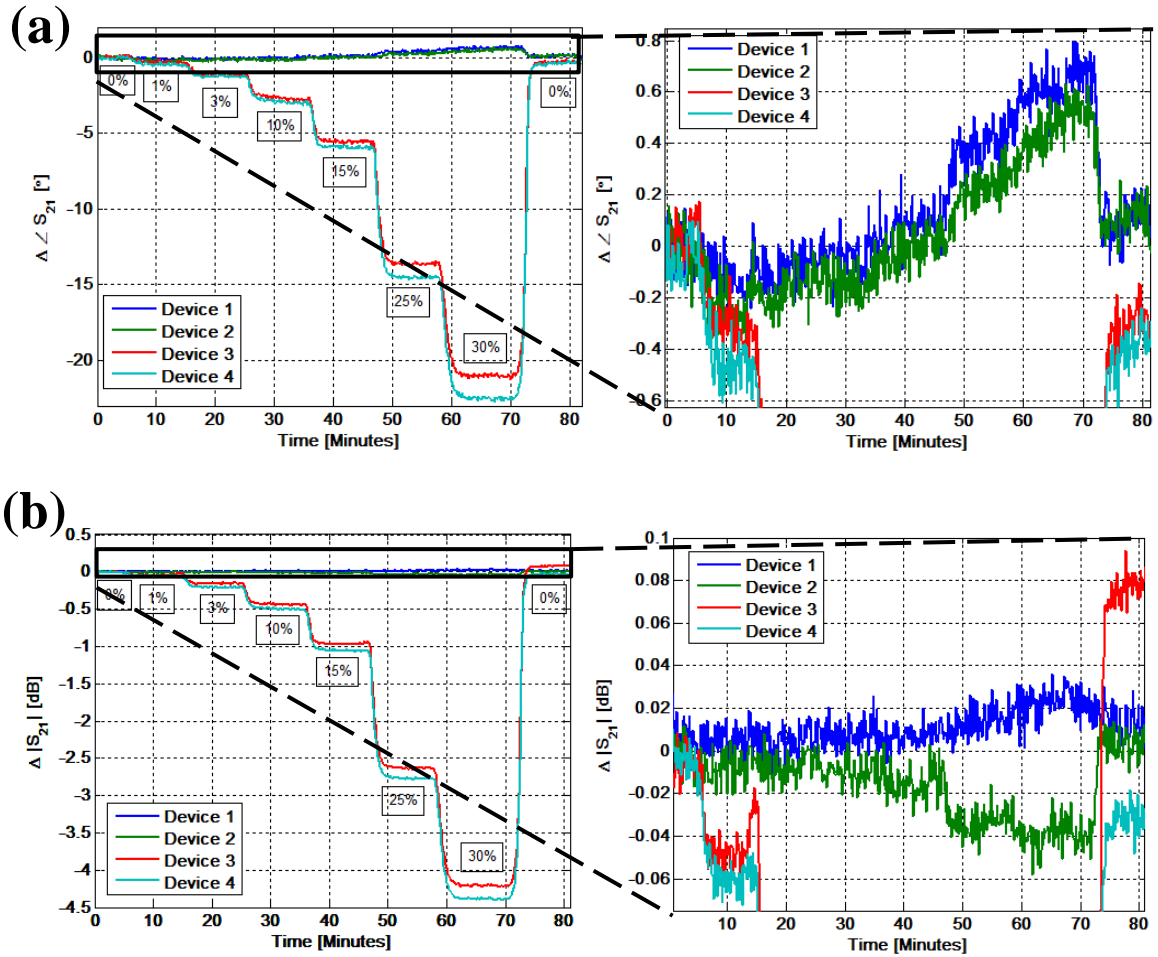
Figure 5.8. 3rd generation design response. Devices 1 and 2 exposed continuously to DI water while devices 3 and 4 are exposed to varying glycerol/DI concentrations; (a) S_{21} phase response, (b) S_{21} magnitude response.

For both the magnitude and phase responses in Figure 5.8 it is observed that the responses for devices 1 and 2 (DI water) are relatively unchanged as compared to devices 3 and 4 (glycerol solutions) over the course of the experiment. Closer examination of the response of devices 1 and 2 as seen in the zoomed-in inset plot of the phase response, (a), reveals an increasing phase response trend with increasing glycerol concentration for devices 1 and 2; with device 2 on average shifted less from the baseline than device 1.

Upon introduction of DI water into both flow paths, at the end of the experiment, it is observed that the phase response of each device returns near the baseline response at time zero; devices 3 and 4 appear to still be exposed to some residual glycerol in DI water as the response has not fully recovered. The full scale phase shift of device 1 and 2 at time 70 minutes (local average), relative to the shift of the devices 3 and 4 that are exposed to 30% glycerol is approximately only -3.3% and -2.6%, respectively. In regards to the inset plot for the magnitude response, (b), device 1 has an increasing trend with increasing glycerol concentration, while device 2 has a decreasing trend with increasing glycerol concentration. The full-scale magnitude shift of device 1 and 2 at time 70 minutes (local average), relative to the shift of the devices 3 and 4 that are exposed to 30% glycerol is approximately only -0.47% and +0.93%, respectively, which are also less in magnitude that the relative shift of the phase response signals of device 1 and 2 by a factor of at least 3. Upon introduction of DI water into both flow paths at the end of the experiment it is observed that the magnitude response of device 1 and 2 returns near the baseline response at time zero; device 4 appears to still be exposed to some residual glycerol in DI water as the response has not fully recovered, and device 3 overshoots the baseline. One possible reason why this device overshoots the baseline may be that a bubble(s) became trapped along the device delay path, which may also explain the rapid increase in the magnitude of device 4 at time 15 minutes, as observed in the inset plot of (b), given that air displays less loss than the glycerol solution. In any case it is very interesting to see that devices 1 and 2 in the inset plot of the phase response (a) show an increasing trend, while in the magnitude plot inset (b) of device 1 shows an increasing trend and device 2 shows a decreasing trend. The author has a theory that two competing effects are simultaneously

occurring, which can explain theses observed results as the glycerol concentration of devices 3 and 4 increases: (i) there is an increase in pressure applied to the PDMS walls sealing devices 1 and 2; and (ii) a degree solution mixing takes place in the region of the device 2 delay path near the fluid common outlet port. Considering (i), as the viscosity of the solution in the flow path of devices 3 and 4 increases, the flow rate in the flow path of devices 1 and 2 must increase given that the same suction pressure is applied to the fluidic system. This effect results in increased pressure being applied to the sealing PDMS walls located in between IDTs and the delay path of devices 1 and 2. The author believes that the stiffness at the PDMS/substrate interface as a result increases, thus accelerating the wave, and results in an upward trend in the phase response of device 1 and 2 as the pressure increases. Considering (ii), given that the flow path along the delay path of device 2 is closer to the common outlet port than device 1, it is believed that a degree of the glycerol is present in the solution near the outlet region of the device 2 delay-path. Such a scenario will cause the phase and magnitude response of device 2 to have a decreasing trend. Given that the magnitude response shift of devices 1 and 2, relative to full-scale shift of devices 3 and 4 at 30% glycerol, is less than the phase response shifts of devices 1 and 2, it is thought that the pressure effect more strongly affects the phase response as compared to the magnitude response. Regarding the magnitude response it is believed that the solution mixing effect dominates the response of device 2, while the pressure effect dominates the response of device 1. Regarding the phase response, it is believed the pressure effect dominates the response of devices 1 and 2, while the solution mixing effect only slightly affects device 2. Given the response levels of devices 3 and 4 shown in the inset plots of (a) and (b) at 1% glycerol, it is

believed that the degree of solution mixing results in a local glycerol concentration for device 2 near the outlet port of <3% when device 3 and 4 are exposed to 30% glycerol. This was calculated using that fact that this region makes up only 1/3 of the total device delay and that the equivalent shift in the magnitude response of device 2 corresponds almost to that of a device exposed to 1% glycerol solution, as seen with device 3 and 4 under exposure to the 1% solution. The author is only presenting this reasoning as an initial theory. It should be understood that the observed signals for devices 1 and 2 are relatively very small and are only slightly above the magnitude and phase response noise levels, although on average local trends do seem to be present. The question regarding whether these signals are a result of systematic errors or are an actual phenomena, can be addressed in future work if desired. It should be mentioned that at this time if it is required that absolutely no chance of solution mixing can be tolerated then another chamber design should be implemented, which includes two independent flow paths and outlet ports.

5.5. Biological Sensing: Measurements of a Bio-Assay

A current Electrical Engineering Ph.D. student at UMaine, Dana Tucker, has been working on Improving the Sensitivity of a DNA-Probe Based Surface Acoustic Wave Biosensor, and has been using the 2nd generation SHSAW sensing platform devices developed in this dissertation to perform some of her experimental measurements. She has been kind enough to let me present some of her data here to demonstrate the applicability of the devices developed in this work towards biological sensing applications.

The experiment she performed was designed to study the sensitivity of SHSAW devices towards DNA crosslinking of surface bound molecules. It has been well known for many years that SAW devices are very sensitive platforms for detection of surface mass loading. Alternatively, little work has been done in distinguishing responses caused by mass loading and responses resulting by interfacial stiffness variations. To test the effects of changing just the relative surface stiffness, experiments were devised which sought to keep the surface attached mass constant while only changing the equivalent stiffness. In particular one of the experiments she performed, which is presented here, involved attachment of NeutrAvidin (NA) to the SHSAW surface, which is known to non-specifically bind to a Au surface. Next, two complementary single stranded DNA (ssDNA), each with a single biotin molecule attached to their 5' end, are hybridized in solution. Afterwards the complex is loaded into the device and the biotin molecules, which have a very strong affinity to NA, attach to the NA crosslinking the surface bound NA via the double stranded DNA (dsDNA) complex. The experiment consisted of 5 main

steps. In the first step the device was exposed to DI water to establish a baseline response, set the fluid flow rate, and remove air bubbles from the device. In the second step, the device was exposed to a NA buffer solution (50mM TRIS, 10mM $MgCl_2$, 10mM KCl, pH 7.5), again to form a baseline response used to study NA attachment. In the third step a solution of NA with a concentration of 100µg/ml in NA buffer was then inserted into the device. As a fourth step a blocking buffer (BB) solution consisting of 0.5% bovine serum albumin (BSA) in saline-sodium citrate (SSC) buffer (150mM NaCl, 15mM sodium citrate, pH 7.5) was loaded into the device and used to block non-specific attachment of DNA and to form a baseline for the crosslinking event. Finally the pre-prepared dsDNA complex (dsTri) at a concentration of 80nM in SSC buffer was inserted into the device to initiate the crosslinking event. The biotinylated ssDNA sequences used to form the dsTri complex is given in Table 5.3.

96 base pair biotinylated ssDNA molecules
5'- biotin – TCTTGCTGGGGGTTATCGATGGGAAAAAACACGAAAAAAAGCAAAAAAA GAATTCAGCCAAAAAACACAAAAAAAATCGATGTAGGCCATGCTGTCC – 3'
5' – biotin – GGACAGCATGGCCTACATCGATTTTTTTTGTGTTTTTTGGCTGAATTCTT TTTTTGCTTTTTTTCGTGTTTTTTCCCATCGATAACCCCAGCAAGA – 3'

Table 5.3. Biotinylated complementary ssDNA used to form dsTri complex.

The results of the experiment, which involved testing two of the four available devices, are shown in Figure 5.9 (a) and (b). In particular, Figure 5.9 (a) and (b) show the phase and magnitude shifts observed, respectively for each step over the course of the experiment. It should be noted the main difference between the 3rd and 2nd generation devices designs, in terms the SHSAW device layout, is that the delay path length of the 2nd generation is about 2.25X longer than the 3rd generation design. Thus it is expected that both the phase and magnitude shifts observed for a similar experiment using the 3rd generation design alternatively would be about 2.25X less. The data clearly shows that the device is able to detect the attachment of bio-molecules on the device surface. A more thorough explanation of the experimental details and the data will be given in Dana Tucker's dissertation under preparation. In addition, she intends to show additional experimental biological sensing data obtained from other experiments which were performed using devices developed in this work.

(a)

(b)

DI NA Buffer NA BSA dsTri
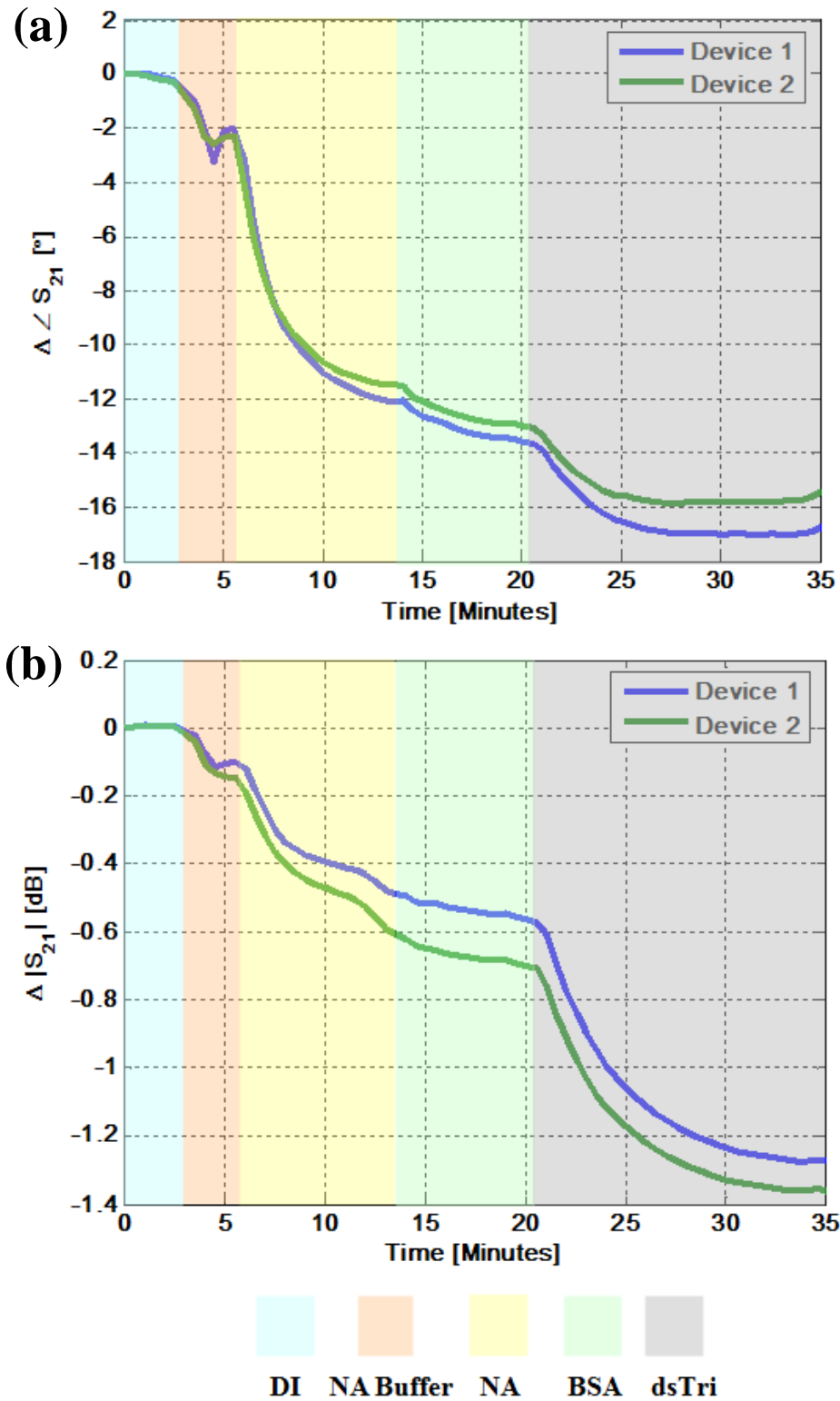
Figure 5.9. 2nd generation response to crosslinking NA with biotinylated dsTri; (a) S_{21} phase response, (b) S_{21} magnitude response.

223

CHAPTER 6

CONCLUSION

6.1. Summary

Successful modeling, design, packaging, and experimental evaluation of pure shear horizontal surface acoustic wave (SHSAW) liquid-phase sensor platforms has been performed in this work and has been presented in this dissertation. In particular, this work introduced novel methods to: (i) model SHSAW liquid-phase sensors; (ii) quantify sensor performance in terms of key design parameters (e.g. IDT center-to-center length, sensing region length, SHSAW mode temperature and analyte sensitivities, SHSAW complex slowness, and ratio of spurious signal detected to desired signal); (iii) numerically extract the key parameters for candidate designs; and (iv) form robust and reproducible packaging of devices for liquid-phase operation. Experimental liquid-phase measurement data presented obtained via testing the candidate liquid-phase sensor platforms designed and fabricated in this work verify the modeling analysis, design, and packaging methods proposed in the this work.

In Chapter 1 an overview of liquid-phase sensors was presented. The discussion addressed current methods used to measure properties of liquid-phase materials and alternative acoustic wave sensor platforms based on use of bulk-wave, Lamb, Love, acoustic plate, and pseudo surface acoustic wave modes. Next, the state-of-the-art in surface acoustic wave device modeling with emphasis on the analysis on interdigital transducers (IDTs) and interaction of the device substrate with a fluid analyte were

224

discussed. Lastly a discussion was presented on reported techniques used for packaging acoustic wave devices for liquid-phase operation.

Chapter 2 presented the theoretical approach used to model candidate device designs. This included a theoretical development of a full-wave simulation tool used to model finite and infinite electrode structures atop a piezoelectric substrate and subsequent methods for extraction of parameters relevant to sensor performance. Based on use of the implemented model, and presented for the first time in this dissertation work, was the extraction of IDT SHSAW mode excitation efficiency for various surrounding IDT boundary condition situations, while including the mass/stiffness loading effect of all electrodes in the structure. It was shown that the excitation efficiency can depend strongly on the mass/stiffness effect of surrounding electrodes. Therefore to achieve accurate efficiency extraction the considerations of such effects are required and are considered for the first time using the methods presented in this dissertation. In addition to the device simulation model, a theoretical model was presented which was used to characterize modes propagating in a semi-infinite piezoelectric substrate with *n* finite-thickness uniform layers, followed by a semi-infinite fluid.

In Chapter 3 an analytical sensor response model was presented, which was derived in terms of key sensor design parameters (IDT center-to-center length, sensing region length, SHSAW mode temperature and analyte sensitivities, SHSAW complex slowness, and ratio of spurious signal detected to desired signal). Quantifiable expressions were shown which indicate that the expected sensor signal-to-noise level and resolution for a particular analyte can be improved by reducing the ratio of SHSAW

temperature coefficient of delay (TCD) to SHSAW sensitivity to the fluid measurand, and through reduction of detected spurious signals via improvement of the IDT SHSAW excitation efficiency, η_{SHSAW}. Theoretical methods and modeling tools were developed and presented for the first time which allowed extraction of the aforementioned important performance parameters of SHSAW device designs. Using the developed modeling tools it was numerically verified that sensitivity of the SHSAW mode to changes in fluid physical properties, such as viscosity, can be improved via use of a uniform electrode finite-thickness guiding layer placed between device IDTs. In particular, through use of electrode materials with relatively high density, such as Au, and of appropriate thickness, the sensitivity of the SHSAW was shown be able to approach or in some cases exceed that of more complex Love mode configurations that incorporate dielectric, and possibly also metallic over-layers in addition to IDT electrodes. In addition, it was shown using a model simulation, which considers the fluid interaction, that mode sensitivity to fluid viscosity and attenuation in dB per wavelength are highly correlated. It was quantitatively shown that if the sensitivity is too high the overall sensor performance may degrade as the level of detected spurious signal increases. Lastly, for the first time the η_{SHSAW} parameter of a particular device design has been quantified for finite length IDTs surrounded by finite-thickness uniform and periodic guiding electrodes. These results have been achieved through use of an implemented full-wave model accounting for spurious mode excitation (e.g. BAW), which is based on implementation of boundary element and finite element methods. For the uniform electrode guiding condition, the technique implemented introduced the concept of an acoustic matching electrode. The use of the matching electrode allowed far-field parameters to be extracted, such as

η_{SHSAW}, by removing IDT spurious responses due to SHSAW reflection from a truncated structure edge, which can be redetected by the IDT and interfere with the extraction process. It was quantitatively verified that the use of a uniform guiding electrode of proper material and thickness not only improves SHSAW sensitivity, but also improves η_{SHSAW}. For example, it was verified that by using Au electrodes w for a device on ST-90° quartz (79.5 split finger pairs, and 32 μm IDT periodicity) with uniform guiding electrodes on both sides of the IDT, η_{SHSAW} is improved by about 11% and S_η by about 216% when using electrodes 600 nm thick instead of 75 nm . It was also shown that use of finite-thickness periodic guiding electrodes placed synchronously alongside the IDT can further improve $\eta_{SHSAW,}$ which was shown to approach 100% when employing denser and thicker electrodes.

Chapter 4 presented the packaging technique developed in this work to allow the operation of liquid-phase SHSAW sensors, and also discussed different generations of device designs. The reported packaging technique prevents fluids from coming in contact with the device IDTs, thus avoiding potential dielectric and/or conductive electrical-shorting of signals, while only affecting the overall device response slightly. The packaging method consists of molding poly(dimethyl siloxane) (PDMS) microfluidic chambers via softlithography techniques, dicing and alignment of individual chambers to a SHSAW device, and permanent bonding to the device surface. A process for fabrication of micro-featured PDMS molds on a poly(methyl methacrylate) (PMMA) substrate using SU-8 resist has been developed and presented in this work, which exhibits greatly improved mold robustness compared to traditionally used mold substrates such as glass

and silicon. In addition, a novel technique was developed and presented which was used to align PDMS chamber to SHSAW device rapidly and precisely, within ±10 μm, prior to permanent attachment to the surface. This process was made possible via use of lock-and-key features patterned on a SHSAW device with SU-8 resist and use of a surfactant, such as ethanol, allowing slight positioning before evaporation and subsequent bonding occurs. Lastly, three generations of complete packaged devices designs are reported.

Chapter 5 presented experimental results of candidate liquid-phase surface acoustic wave devices for two potential sensor applications. The fist set of experiments involved testing various concentrations of glycerol-water mixtures with the reported devices. Characteristic properties of the sensor are extracted, such as sensitivity and detection resolution, and are compared to other reported devices. The comparison showed that the device reported here has sensitivity within 31% of one reported device and 27% higher than another, which used a SiO_2 layer on quartz. In addition, it was shown that the device reported here has sensitivity 300% higher than a reported high-velocity AlN/Sapphire SHSAW devices. It is shown that the sensitivity of the device reported in this work could be increased by about 75% by increasing the guiding electrode thickness by a factor of about 3 (without addition of SiO_2 under the electrode), which then transfers more energy into the liquid and causes a 75% increase in signal propagation loss (an effect which is shown independent of material in this work, i.e. devices with equal viscosity sensitivities will have equal propagation loss due to viscous loading). In addition to viscosity sensing, the developed device was used in a bioassay test to

228

demonstrate the applicability as a biosensor to detect DNA crosslinking of surface bound molecules.

6.2. Contributions

The following is a bulleted list of contributions resulting from this work.

- Developed new SHSAW sensor response model; key design parameters identified and their effect on devices performance quantified.

- Expanded Green's function theories and improved their computation.

  - GF expanded to n-layers for layered excitation and propagation problems.

  - Provided additional insight into proper partial mode selection for half-spaces.

  - Improved partial mode analytical continuation into complex slowness plane using a numerical eigen-value/-vector partial derivative computation method.

  - Improved numerical stability for acoustically thick layers.

- Applied new Green's function model to the following SHSAW propagation problems.

  - Presented novel layered sensitivity analysis with fluid loading – optimum configurations identified.

- Performed analysis of new materials/orientations.

- Verified, without any perturbation theory constraint, that the SHSAW mode sensitivity is strongly correlated to the viscous attenuation under acoustically thick layered configurations.

- New finite FEM/BEM model computational models developed.

  - Incident mode analysis implemented for FEM/BEM S- or P-matrix extraction that considers electrode thickness.

  - Allows for the choice of different basis functions without loss of generality for the finite FEM/BEM model.

  - Alternate numerical integration method developed – electrostatic pole cancelation, new contours defined.

  - Post processing model developed for calculation of BAW radiation w.r.t. PFA in addition to the existing k-vector angle theory in the literature.

- Additional periodic FEM/BEM model computational models developed.

  - Allows for the choice of different basis functions without loss of generality for the periodic FEM/BEM model.

  - Arbitrary period electrode configurations covered – multiple electrodes, floating electrodes.

- SHSAW excitation efficiency quantified for first time for various surrounding IDT guiding configuration considering electrode thickness.

  - Uniform electrode guiding, and periodic electrode guiding covered.

- SHSAW 'matching' electrode shown possible; potential other applications in filtering (periodic tuned electrodes analogous to coupled line filter).

- Enhanced SHSAW liquid-phase packaging developed.

  - New PDMS combination alignment/bonding method for SHSAW – ± 10 μm alignment.

  - Enhanced PDMS mold robustness with low temperature PMMA/SU-8 process.

6.3. Suggestions for Future Work

As a result of this dissertation, future work relevant to further improving SHSAW liquid-phase sensor device design and understanding has been identified.

It would be interesting to see the results of a numerical study of how the value η_{SHSAW} for an IDT changes with respect to the length of the free-surface gap between IDT and the uniform guiding electrode. In particular, in the actual fabricated device the gap between the IDT and the uniform guiding electrode was required to be on the order a few wavelengths to permit enough room for PDMS sealing to the quartz surface. Alternatively in the presented simulation data the gap was assumed only 1/8 of a

wavelength. It would be interesting to see how the increased gap spacing affects the achievable IDT η_{SHSAW}. In addition, it would be interesting to include in the model the influence of the presence of a PDMS containment wall via including a FEM model of the PDMS (maybe treat it acoustically only and neglect the electrical influence for simplicity). This would require the material constants of cured PDMS to be obtained (viscosity constants would also be desired), which the author has yet to find. Lastly, in order to verify that observed attenuation offset in Chapter 5 experimental results concerning the glycerol-water measurements, it would be interesting to see if the numerical model could explain the observed results, which were suggested to be caused by a reduction in η_{SHSAW} as a result of fluid loading.

The next generation device should be fabricated on a material and orientation that is less sensitive to temperature variation, such as the LGS orientation initially considered. Initial experiments attempting to bond PDMS chambers to LGS were unsuccessful and prompted the use of quartz for development. It had been reported that PDMS is able to permanently attach to silicon-nitride through the same mechanism as attachment to quartz. Therefore it may be feasible to deposit a very thin (in terms of device wavelength) layer of silicon-nitride or silicon-oxide on the LGS surface via PECVD, ALD, e-beam, or sputter process prior to electrode patterning. This may permit PDMS bonding to the surface and still present low device TCD. In an initial experiment in this work to prove feasibility, a layer silicon-nitride (~13 nm) was deposited on the surface of a scrap piece of LGS crystal via PECVD process at UMaine. Next bonding of scrap pieces of clean PDMS to the LGS sample was attempted using the same bonding protocol developed in

this work for quartz/PDMS. It was observed that PDMS appeared to bond sufficiently to the coated LGS sample after attempting to pull samples apart. Future work should include fabricating a LGS SHSAW device with an initial pre-layer of silicon-nitride or silicon-oxide and then PDMS sample attachment should be tested. If successful, the device should be tested and characterized with and without fluid analytes and compared to the performance of the reported quartz device in this dissertation.

Given the knowledge obtained resulting from this dissertation work, alternative designs to the PDMS fluid containment structure and SHSAW delay line structure implemented, which incorporates a uniform guiding electrode, should be considered. In particular, it would be interesting to study a delay-line or resonator device consisting of periodic electrodes and a dielectric over-layer and shielding film over the entire device. It was shown that periodic electrode guiding permits the highest achievable η_{SHSAW} due to the structure being absent of mechanical discontinuities or aperiodicities. Thus such a design may demonstrate reduced spurious signal detection and improved overall sensor performance. In addition via use of dielectric over-layer and shielding film, packaging for liquid-phase operation may be simpler since no containment wall between IDT and guiding structure would be required; therefore less alignment precision would also be required. In addition, the electrode, dielectric layer, and shielding electrode layer thicknesses could be tailored to improve devices sensitivity. For instance, in Section 3.3.2 it was shown that a Love wave configuration with a SiO_2 layer and top surface shorting electrode can achieve higher sensitivity than the configuration employed in this work, which consists of only a uniform electrode at the substrate surface. Although a

device configuration based on the layered situation sounds promising, it is anticipated that much work will be required towards its realization. For instance models must be expanded to include the ability to simulate structures with finite thickness dielectric and top electrode layers positioned over finite thickness grating electrodes. This would require the FEM treatment of the non-homogeneous structure regions (including the electrical effects) and coupling to the BEM model of the semi-infinite homogeneous regions; i.e. substrate and air/vacuum/fluid regions. The current model employed in this work is not able to model such a situation. In addition, fabrication of such a configuration is may be challenging due to the increased number of process steps required.

6.4. List of Publications

The following is a list of publications originating from this work.

T. B. Pollard, J. F. Vetelino, and M. Pereira da Cunha, "Pure SH SAW on single crystal $KNbO_3$ for liquid sensing applications," in *Proc. IEEE Ultrason. Symp.*, 2003, pp. 1125-8.

T. D. Kenny, T. B. Pollard, E. J. Berkenpass, and M. P. da Cunha, "FEM/BEM impedance and power analysis for measured LGS SH-SAW devices," in *Proc. IEEE Ultrason. Symp.*, 2004, pp. 1371-4.

T. B. Pollard, T. D. Kenny, and M. P. da Cunha, "SH-SAW transducer analysis on single crystal $KNbO_3$ for liquid sensors," in *Proc. IEEE Ultrason. Symp.*, 2004, pp. 390-5.

T. B. Pollard, and M. Pereira da Cunha, "Improved pure SH SAW transduction efficiency on LGS using finite thickness gratings," in *Proc. IEEE Ultrason. Symp.*, 2005, pp. 1048-1051.

T. B. Pollard, T. D. Kenny, J. F. Vetelino, and M. Pereira da Cunha, "Pure SH-SAW propagation, transduction and measurements on $KNbO_3$," *IEEE Trans. Ultrason. Ferroelect. Freq. Contr.*, vol. 53, no. 1, pp. 199-208, Jan. 2006.

T. D. Kenny, T. B. Pollard, E. Berkenpas, and M. Pereira da Cunha, "FEM/BEM impedance and power analysis of measured LGS SH-SAW devices," *IEEE Trans. Ultrason., Ferroelect., Freq. Contr.*, vol. 53, pp. 402-411, Feb. 2006.

T. B. Pollard, and M. P. da Cunha, "Pure shear horizontal SAW network model for periodic structures including bulk scattering," in *Proc. IEEE Ultrason. Symp.*, 2006, pp. 88-91.

T. B. Pollard, and M. P. da Cunha, "Improved SHSAW transduction efficiency using gratings and uniform electrode guiding," in *Proc. IEEE Ultrason. Symp.*, 2009, pp. 835-8.

T. B. Pollard, M. P. da Cunha, "Improved SHSAW transduction efficiency using grating and uniform electrode guiding," *IEEE Trans. Ultrason. Ferroelect. Freq. Contr.*, vol. 58, no. 5, pp. 1087-1096, May 2011.

REFERENCES

[1]   J. R. Fried, *Polymer Science and Technology*. Upper Saddle River, NJ: Prentice Hall, 2003.

[2]   J. Cazes, Ewing's Analytical Instrumentation Handbook, Third Edition, New York, NY: Marcel Dekker, 2005.

[3]   D. J. Harrison, A. Manz, Z. Fan, H. Luedi, and H. M. Widmer, "Capillary electrophoresis and sample injection systems integrated on a planar glass chip," *Anal. Chem.*, vol. 64, no. 17, p. 1926-1932, Sept. 1992.

[4]   E. M. Purcell, "Life at low Reynolds number," *Am. J. Phys.*, vol. 45, no. 1, pp. 3-11, Jan. 1977.

[5]   K. K. Kanazawa, and J. G. Gordan, "Frequency of a quartz microbalance in contact with a liquid," *Anal. Chem.*, vol. 57, no. 8, pp. 1770-1771, Jul. 1985.

[6]   D. Royer, and E. Dieulesaint, *Elastic Waves in Solids I: Free and Guided Propagation*. New York, NY: Springer-Verlag, 2000.

[7]   M. Trainer, "Kelvin and piezoelectricity," *Eur. J. Phys.*, vol. 24, no. 5, pp. 535-542, Sept. 2003.

[8]   A. Ballato, "Piezoelectricity: history and new thrusts," in *Proc. IEEE Ultrason. Symp.*, 1996, pp. 575-583.

[9]   D. P. Morgan, *Surface Wave Devices for Signal Processing*. Amsterdam, The Netherlands: Elsevier, 1985.

[10]   C. Campbell, Surface acoustic wave devices and their signal processing applications. CA, USA: Academic Press, 1989.

[11]   C. Ruppel, "SAW devices for consumer communication applications," *IEEE Trans. Ultrason. Ferroelec. Freq. Contr.*, vol. 40, no. 5, pp. 438-452, Sep. 1993.

[12]   G. Sauerbrey, "Verwendung von Schwingquarzen zur Wägung dünner Schichten und zur Mikrowägung," *Z. Phys.* vol. 155, no. 2, pp. 206-222, Apr. 1959.

[13]   P. L. Konash, and G. J. Bastiaans, "Piezoelectric crystals as detectors in liquid chromatography," *Anal. Chem.*, vol. 52, no. 12, pp. 1929-1931, 1980.

[14]   F. Josse, and Z. Shana, "Analysis of shear horizontal surface waves at the boundary between a piezoelectric crystal and a viscous fluid medium," *J. Acoust. Soc. Amer.*, vol. 84, no. 3, pp. 978-984, Sept. 1988.

[15]   J. J. Campbell, and W. R. Jones, "Propagation of surface waves at the boundary between a piezoelectric crystal and a fluid medium," *IEEE Trans. Sonics Ultrason.*, vol. SU-17, no. 2, pp. 71-76, Apr. 1970.

[16]   Z. A. Shana, D. E. Radtke, U. R. Kelkar, D. T. Hanworth, and F. Josse, "Theory and applications of quartz resonators as sensors for viscous conductive liquids," in *Proc. IEEE Ultrason. Symp.*, 1989, pp. 567-571.

[17]   Y. Hu, L. A. French, K. Radecsky, M. P. da Cunha, P. Millard, and J. F. Vetelino, "A lateral field excited liquid acoustic wave sensor," *IEEE Trans. Ultrason., Ferroelect., Freq. Contr.*, vol. 51, no. 11, pp. 1373-1380, Nov. 2004.

[18]   D. F. McCann, L. A. French, M. S. Wark, and J. F. Vetelino, "Recent advances in lateral field excited and monolithic spiral coil acoustic transduction bulk acoustic wave sensor platforms," *Meas. Sci., Technol.*, vol. 20, no. 12, pp. 124001, 2009.

[19]   S. V. Krishnaswamy, J. Rosenbaum, S. Horwitz, C. Vale, and R. A. Moore, "Film bulk acoustic wave resonator technology," in *Proc. IEEE Ultrason. Symp.*, 1990, pp. 529-536.

[20]   G. Wingqvist, J. Bjurstrrom, L. Liljehom, I. Katardjiev, and A. L. Spetz, "Shear mode AlN thin film electroacoustic resonator for biosensing applications," in *Proc. IEEE Sens.*, 2005, pp. 492-495.

[21]   J. Weber, W. M. Albers, J. Tuppurainen, M. Link, R. Gabl, W. Wersing, and M. Schreiter, "Shear mode FBARs as highly sensitive liquid biosensors," *Sens. Actuators, A*, vol. 128, no. 1, pp. 84-88, Mar. 2006.

[22]   Lord Rayleigh, "On waves propagated along the plane surface of an elastic solid," *Proc. London Math. Soc.*, vol. 17, pp. 4–11, 1885.

[23]   H. Lamb, "On waves in an elastic plate," *Proc. Roy. Soc.*, vol. A93, pp. 114-128, 1917.

[24]   R. Stoneley, "Elastic waves at the surface of separation of two solids," *Proc. Roy. Soc.*, vol. A106, pp. 416–428, 1924.

[25]   A. E. H. Love, *Some Problems of Geodynamics.* London: Cambridge University Press, 1911, Dover, 1967.

[26]   R. M. White and F. W. Voltmer, "Direct piezoelectric coupling to surface elastic waves," *Appl. Phys. Lett.*, vol. 7, pp. 314–316, 1965.

[27]   J. L. Bleustein, "A new surface wave in piezoelectric materials," *Appl. Phys. Lett.*, vol. 13, no. 12, pp. 412-413, Dec. 1968.

[28]   F. S. Hickernell, "Shear horizontal BG surface acoustic waves on piezoelectrics: a historical note," *IEEE Trans. Ultrason. Ferroelect. Freq. Contr.*, vol. 52, no. 5, pp. 809-811, May 2005.

[29]   Y. V. Gulyaev, "Electroacoustic surface waves in solids," *Zh. Eksper. i Teor. Fiz. Piz. v Red.*, vol. 9, pp. 63–65, Jan. 1969, (Sov. Phys. JETP Lett., vol. 9, pp. 37–38, Jan. 1969). (in Russian)

[30]   Y. Ohta, K. Nakamura, and H. Shimizu, "Piezoelectric surface shear waves," in *Proc. Ultrason. Committee Inst. Electron. Commun. Eng. Japan*, Apr. 1969. (in Japanese)

[31]   G. W. Farnell, E. L. Adler, "Elastic wave propagation in thin layers," in *Phys. Acout.*, vol. 9. W. P. Mason and R. N. Thurston, Ed. New York: Academic Press, 1972, pp. 35-127.

[32]   C. Lardat, C. Maerfeld, and P. Tournois, "Theory and performance of acoustical dispersive surface wave delay lines," Proc. IEEE, vol. 59, no. 3, pp. 355-368, Mar. 1971.

[33]   T. Moriizumi, Y. Unno, and S. Shiokawa, "New sensor in liquid using leaky saw," in *Proc. IEEE Ultrason. Symp.*, 1987, pp. 579-582.

[34]   R. M. White, "Fluid loading of a Lamb-wave sensor," *Appl. Phys. Lett.*, vol. 52, no. 20, pp. 1653-1655, 1988.

[35]   J. C. Andle, J. F. Vetelino, R. Lec, and D. J. McAllister, "An acoustic plate mode immunosensor," in *Proc. IEEE Ultrason. Symp.*, 1989, pp. 579-584.

[36]   E. Gizeli, A. C. Stevenson, N. J. Goddard, and C. R. Lowe, "A novel Love-plate acoustic sensor utilizing polymer overlayers," *IEEE Trans. Ultrason., Ferroelect., Freq. Contr.*, vol. 39, no. 5, pp. 657-659, Sept. 1992.

[37]   J. Kondoh, and S. Shiokawa, "Measurements of conductivity and pH of liquid using surface acoustic wave devices," *Jpn. J. Appl. Phys., Suppl.*, suppl. 31-1 vol. 31, pp. 82-84, 1992.

[38]   E. L. Adler, "SAW and pseudo-SAW properties using matrix methods," *IEEE Trans. Ultrason. Ferroelec. Freq. Contr.*, vol. 41, no. 6, pp. 876-882, Nov. 1994.

[39]   C. Zhang, J. J. Caron, and J. F. Vetelino, "The Bleustein-Gulyaev wave for liquid sensing applications," *Sens. Actuators, B*, vol. 76, no. 1-3, pp.64-68, Jun. 2001.

[40] M. Pereira da Cunha, D. C. Malocha, D. W. Puccio, J. Thiele, and T. B. Pollard, "LGX pure shear horizontal SAW for liquid sensor applications," *IEEE Sens. J.*, vol. 3, no. 5, Oct. 2003.

[41] T. Kikuchi, and T. Moriizumi, "Effects of liquid viscosity on ultrasonic propagation in liquid/solid structre," *Jpn. J. Appl. Phys.*, *Supplement*, vol. 25, suppl 25-1, 1985, pp. 43-45.

[42] L. A. Francis, J. -M. Friedt, R. De Palma, C. Zhou, C. Bartic, A. Campitelli, and P. Bertrand, "Techniques to evaluate the mass sensitivity of love mode surface acoustic wave biosensors," in *Proc. IEEE Freq. Contr. Symp.*, 2005, pp. 241-249.

[43] S. Ballandras, A. Reinhardt, A. Khelif, M. Wilm, V. Laude, W. Daniau, and V. Blondeau-Patissier, "Theoretical analysis of damping effects of guided elastic waves at solid/fluid interfaces," *J. Appl. Phys.*, vol. 99, no. 5, p. 054907-1-9, Mar. 2006.

[44] K. Hashimoto, Surface Acoustic Wave Devices in Telecommunications: modeling and simulation. New York, NY: Springer-Verlag, 2000.

[45] R. F. Milsom, N. H. C. Reilly and M. Redwood, "Analysis of generation and detection of surface and bulk acoustic wave by interdigital transducers," *IEEE Trans. Sonics Ultrason.*, vol. SU-24, no. 3, pp. 147-166, May 1977.

[46] P. Ventura, J. M. Hodé, B. Lopes, "Rigorous analaysis of finite SAW devices with arbitrary electorde goemetries," in *Proc. IEEE Ultrason. Symp.*, 1995, pp. 257-262.

[47] R. Lerch, "Simulation of piezoelectric devices by two- and three-dimensional finite elements," *IEEE Trans. Ultrason. Ferroelect. Freq. Contr.*, vol. 37, no. 3, pp. 233-247, May 1990.

[48] P. M. Smith, and W. Ren, "Finite-difference time-domain techniques for SAW device analysis," in *Proc. IEEE Ultrason. Symp.*, 2002, pp. 325-328.

[49] R. C. Peach, "A general green function analysis for SAW devices," in *Proc. IEEE Ultrason. Symp.*, 1995, pp. 221-225.

[50] T. B. Pollard, T. D. Kenny, J. F. Vetelino, and M. Pereira da Cunha, "Pure SH-SAW propagation, transduction and measurements on $KNbO_3$," *IEEE Trans. Ultrason. Ferroelect. Freq. Contr.*, vol. 53, no. 1, pp. 199-208, Jan. 2006.

[51] T. D. Kenny, T. B. Pollard, E. Berkenpas, and M. Pereira da Cunha, "FEM/BEM impedance and power analysis of measured LGS SH-SAW devices," *IEEE Trans. Ultrason., Ferroelect., Freq. Contr.*, vol. 53, pp. 402-411, Feb. 2006.

[52] T. B. Pollard, M. P. da Cunha, "Improved SHSAW transduction efficiency using grating and uniform electrode guiding," *IEEE Trans. Ultrason. Ferroelect. Freq. Contr.*, vol. 58, no. 5, pp. 1087-1096, May 2011.

[53] G. Xu, "Direct finite-element analysis of the frequency response of a Y-Z lithium niobate SAW filter," *Smart Mater. Struct.*, vol. 9, no. 6, pp. 973-980, Dec. 2000.

[54] G. Xu, and Q. Jaian, "A finite element analysis of second order effects on the frequency response of a SAW device," *J. Intell. Mater. Syst. Struct.*, vol. 12, no. 2, pp. 69-77, Feb. 2001.

[55] S. Ballandras, D. Gachon, J. Masson, and W. Daniau, "Development of absorbing conditions for the analysis of finite demension elastic wave-guids," in *Proc. IEEE Freq. Contr. Symp.*, 2007, pp. 729-732.

[56] K. Y. Wong, and W. Y. Tam, "Analysis of the frequency response of SAW filters using finite-difference time-domain method," *IEEE Trans. Microwave Theory Tech.*, vol. 53, no. 11, pp. 3364-2270, Nov. 2005.

[57] V. P. Plessky, T. Thorvaldsson, "Periodic green's funciton analysis of SAW and leaky SAW propagation in a periodic system of electrodes on a piezoelectric crystal," *IEEE Trans. Ultrason. Ferroelect. Freq. Contr.*, vol. 42, no. 2, pp. 280-293, Mar. 1995.

[58] P. Ventura, J. M. Hodé, J. Desbois, and M. Solal, "Combined FEM and green's function analysis of periodic SAW structure, application to the calculation of reflection and scatting parameters," *IEEE Trans. Ultrason. Ferroelect. Freq. Contr.*, vol. 48, no. 5, pp. 1259-1274, Sep. 2001.

[59] Y. Zhang, J. Desbois, L. Boyer, "Characteristic parameters of surface acoustic waves in a periodic metal grating on a piezoelectric substrate," *IEEE Trans. Ultrason. Ferroelect. Freq. Contr.*, vol. 40, pp. 183-192, May 1993.

[60] T. B. Pollard, and M. Pereira da Cunha, "Improved pure SH SAW transduction efficiency on LGS using finite thickness gratings," in *Proc. IEEE Ultrason. Symp.*, 2005, pp. 1048-1051.

[61] L. A. Francis, J. –M. Friedt, C. Bartic, and A. Campitelli, "A SU-8 liquid cell for surface acoustic wave biosensors," *Proc. SPIE*, vol. 5455, pp. 353-363, Aug. 2004.

[62] J. –M. Friedt, L. el Fissi, F. Cherioux, B. Guichardaz, V. Blondeau-Patissier, and S. Ballandras, "Design and use of a wafer level fluidic packaging for surface acoustic wave sensors," in *Proc. IEEE Freq. Contr. Symp.*, 2007, pp. 369-373.

[63]   B. Li, M. Liu, and Q. Chen, "Low-stress ultra-thick SU-8 UV photolithography process for MEMS," *J. Microlith.*, *Microfab.*, *Microsyst.*, vol. 4, no. 4, p 43008-1-6, Dec. 2005.

[64]   D. A. Karla, A. S. Holland, G. Rosengarten, K. K. Zadeh, "Fabrication of an integrated microfluidic and surface acoustic wave device for fluid analysis," *Proc. SPIE*, vol. 5650, no. 1, pp. 189-199, Feb. 2005.

[65]   K. Länge, G. Blaess, A. Voigt, R. Götzen, and M. Rapp, "Integration of surface acoustic wave biosensor in a microfluidic polymer chip," *Biosens. Bioelectron.*, vol. 22, no. 2, pp. 227-232, Aug. 2006.

[66]   I. Stoyanov, M. Tewes, S. Glasss, M. Koch, and M. Leöhndorf, "Low-cost and chemical resistant microfluidic devices based on thermoplastic elastomers for a novel biosensor system," *Mat. Res. Soc. Spring Meeting Proc.*, vol. 872, pp. 169-174, 2005.

[67]   J. C. McDonald, D. C. Duffy, J. R. Anderson, D. T. Chiu, H. Wu, O. J. A. Schueller, and G. M. Whitesides, "Fabrication of microfluidic systems in poly(dimethylesiloxane)," *Electrophoresis*, vol. 21, no. 1, pp 27-40, Jan. 2003.

[68]   J. N. Lee, C. Park, and G. M. Whitesides, "Solvent compatibility of poly(dimethylsiloxane)-based microfluidic devices," *Anal. Chem.*, vol. 75, no. 23, pp 6544-6554, Dec. 2003.

[69]   T. Q. Truong, N. T. Nguyen, "SU-8 on PMMA – a new technology for microfluidics," *Int. J. Comput. Eng. Sci.*, vol. 4, no. 3, pp 667-670, Sep. 2003.

[70]   V. Raimbault, D. Rebiere, C. Dejous, M. Guirardel, and V. Conedera, "Acoustic love wave platform with PDMS microfluidic chip," *Sens. Actuators, A*, vol. 142, no. 1, pp.160-165, Mar. 2008.

[71]   K. Mitsakakis, A. Tserepi, and E. Gizeli, "Integration of microfluidics with love wave sensor for the fabrication of multisample analytical microdevice," *J. Microelectromech. Syst.*, vol. 17, no. 4, pp 1010-1019, Aug. 2008.

[72]   S. V. Biryukov, and M. Weihnacht, "Real-space field of sources and the problem of fast leaky wave generation in the piezoelectric half-space," *J. Appl. Phys.*, vol. 83, no. 6, p. 3276-87, Mar. 1998.

[73]   B. A. Auld, *Acoustic Fields and Waves in Solids: volume I*. New York, NY: John Wiley & Sons, Inc., 1973.

[74]   C. Moler, and C. V. Loan, "Nineteen dubious ways to compute the exponential of a matrix, twenty-five years later," *SIAM Rev.*, vol. 45, no. 1, pp 3-49, Mar. 2003.

[75]   M. Pereira da Cunha, "Extended investigation on high velocity psuedo surface waves," *IEEE Trans. Ultrason., Ferroelect., Freq. Contr.*, vol. 45, no. 3, pp. 604-613, May 1998.

[76]   N. P. Van Der AA, H. G. Morsche, and R. R. M. Mattheij, "Computation of eigenvalue and eigenvector derivatives for a general complex-valued eigensystem," *Electronic. J. Linear Algebra*, vol. 16, pp. 300-314, Oct. 2007.

[77]   M. Fogiel, Handbook of Mathematical, Scientific, and Engineering: Formulas, Tables, Functions, Graphs, Transforms. Piscataway, New Jersey: Research & Education Association, 2001, pg. 313.

[78]   G. B. Arfken, and H. J. Weber, *Mathematical Methods for Physicists, Sixth Edition*. New York, NY: Elsevier Academic Press, 2005.

[79]   R. V. Goldstein, and G. A. Maugin, Surface Waves in Anisotropic and Laminated Bodies and Defect Detection: NATO Science Series, II. Mathematics, Physics, and Chemistry - Vol. 163. New York, NY: Springer 2008.

[80]   V. V. Aleksandrov, and A. V. Gladkevitch, "Evidence for exceptional bulk waves on (110) and (111) surfaces of GaAs from Brillouin spectroscopy," *J. Phys. Condens. Matter*, vol. 6, no. 18, pp. 3359-68, Mar. 1994.

[81]   F. S. Hickernell, "The application of dielectric thin films to enhance the properties of SAW devices," in *2001 IEEE MTT-S Int. Microwave Symp. Digest*, 2001, pp. 363-366.

[82]   K. J. Gamble, and D. C. Malocha, "Simulation of short LSAW transducers including electrode mass loading and finite finger resistance," *IEEE Trans. Ultrason. Ferroelect. Freq. Contr.*, vol. 49, no. 1, pp. 47-56, Jan. 2002.

[83]   M. Pereira da Cunha, and E. L. Adler, "A network model for arbitrarily oriented IDT structures," *IEEE Trans. Ultrason. Ferroelect. Freq. Contr.*, vol. 40, no. 6, pp. 622-629, Nov. 1993.

[84]   S. A. Sauter, and C. Schwab, *Boundary Element Methods*. New York, NY: Springer-Verlag, 2011.

[85]   E. W. Weisstein, "Law of Sines." From *MathWorld*--A Wolfram Web Resource. http://mathworld.wolfram.com/LawofSines.html.

[86]   G. Kovacs, M. J. Vellekoop, R. Haueis, G. W. Lubking, and A. Venema, "A Love wave sensor for (bio)chemical sensing in liquids," *Sens. Actuators*, *A*, vol. 43, no. 1-3, pp. 38-43, May. 1994.

[87] T. B. Pollard, J. F. Vetelino, and M. Pereira da Cunha, "Pure SH SAW on single crystal $KNbO_3$ for liquid sensing applications," in *Proc. IEEE Ultrason. Symp.*, 2003, pp. 1125-8.

[88] T. D. Kenny, T. B. Pollard, E. J. Berkenpass, and M. P. da Cunha, "FEM/BEM impedance and power analysis for measured LGS SH-SAW devices," in *Proc. IEEE Ultrason. Symp.*, 2004, pp. 1371-4.

[89] T. B. Pollard, T. D. Kenny, and M. P. da Cunha, "SH-SAW transducer analysis on single crystal $KNbO_3$ for liquid sensors," in *Proc. IEEE Ultrason. Symp.*, 2004, pp. 390-5.

[90] T. B. Pollard, T. D. Kenny, J. F. Vetelino, and M. P. da Cunha, "Pure SH-SAW propagation, transduction, and measurements on $KNbO_3$," *IEEE Trans. Ultrason. Ferroelect. Freq. Contr.*, vol. 53, no. 1, pp. 199-208, Jan. 2006.

[91] T. B. Pollard, and M. P. da Cunha, "Improved SHSAW transduction efficiency using gratings and uniform electrode guiding," in *Proc. IEEE Ultrason. Symp.*, 2009, pp. 835-8.

[92] E. W. Weisstein, "Associated Laguerre Polynomial." From *MathWorld*--A Wolfram Web Resource. http://mathworld.wolfram.com/AssociatedLaguerrePolynomial.html.

[93] R. Feng, and J. Farris, "Influence of processing conditions on the thermal and mechanical properties of SU8 negative photoresist," *J. Micromech. Microeng.*, vol. 13, no. 1, pp. 37629-6, Jan. 2003.

[94] O. M. Kugaenko, S. S. Uvarova, S. A. Krylov, B. R. Senatulin, V. S. Patrakov, O. A. Buzanov, V. N. Egorov, and S. A. Sakharov, "Basic thermophysical parameters of langasite ($La_3Ga_5SiO_{14}$), langatate ($La_3Ta_{0.5}Ga_{5.5}O_{14}$), and catangasite ($Ca_3TaGa_3Si_2O_{14}$) single crystals in a temperature range of 25 to 1000C," *Bull. Russ. Acad. Sci. Phys.*, vol. 76, no. 11, pp. 1258-1263, Nov. 2012.

[95] B. Wang, L. Chen, z. Abdulali-Kanji, J. H. Horton, and R. D. Oleschuk, "Aging effects on oxidized and amine-modified poly(dimethylsiloxane) surfaces studied with chemical force titirations: effects on electroosmotic flow rate in microfluidic channels," *Langmuir*, vol. 19, no. 23, pp. 9792-8, Oct. 2003.

[96] Tangram Technology Ltd., "Polymer data file: polymethyl methacrylate – PMMA (acrylic)," http://www.tangram.co.uk/TI-Polymer-PMMA.html.

[97] S. W. Lee, and S. S. Lee, "Shrinkage ratio of PDMS and its alignment method for the wafer level process," *Microsyst. Technol.*, vol. 14, no. 2, pp. 205-208, Feb. 2008.

[98] S. Bhattacharya, A. Datta, J. M. Berg, and S. Gangopadhyay, "Studies on surface wettability of poly(dimethyl) siloxane (PDMS) and glass under oxygen-plasma treatment and correlation with bond strength," *J. Microelectromech. Syst.*, vol. 14, no. 3, pp. 590-597, Jun. 2005.

[99] B. Jo, L. M. Van Lerberghe, K. M. Motsegood, and D. J. Beebe, "Three-dimensional mirco-channel fabrication in polydimethylsiloxane (PDMS) elastomer," *J. Microelectromech. Syst.*, vol. 9, no. 1, pp. 76-81, Mar. 2000.

[100] E. Berkenpas, P. Millard, and M. Pereira da Cunha, "Detection of Escherichia coli 0157:H7 with langasite pure shear horizontal surface acoustic wave sensor," *Biosens. Bioelectron.*, vol. 21, no. 12, pp. 2255-2262, Jun. 2006.

[101] D. McCann, "A monolithic spiral coil acoustic transduction sensor for chemical and biological analytes." Ph.D. dissertation, University of Maine, U.S.A, 2010.

[102] B. Jakoby, M. J. Vellekoop, "Viscosity sensing using a Love-wave device," *Sens. Actuators, A*, vol. 68, no. 1-3, pp. 275-281, Jun. 1998.

[103] G. Hu, J. Xu, G. W. Auner, J. Smolinski, and H. Ying, "Viscosity response of shear horizontal surface acoustic wave on AlN/sapphire structure," *Electron. Lett.*, vol. 43, no. 18, pp. 1006-1007, Aug. 2007.

[104] E. W. Weisstein, "Legendre-Gauss Quadrature." From *MathWorld*--A Wolfram Web Resource. http://mathworld.wolfram.com/Legendre-GaussQuadrature.html.

[105] D. Burnett, *Finite Element Analysis*. Reading, MA: Addison-Wesley Publishing Co., 1987.

[106] B. James, "A new measurement of the basic elastic and dielectric constants of quartz," in *Proceedings of the IEEE Frequency Control Symposium*, 1988, pp. 146–154.

[107] B. P. Sorokin, P. P. Turchin, S. I. Burkov, D. A. Glushkov and K. S. Aleksandrov, "Influence of static electric field, mechanical pressure and temperature on the propagation of acoustic waves in $La_3Ga_5SiO_{14}$ piezoelectric single crystals," in *Proceedings of the IEEE Frequency Control Symposium*, 1996, pp. 161-169.

[108] M. Zgonik, R. Schlesser, I. Biaggio, E. Voit, J. Tscherry, P. Günter, "Material constants of $KNbO_3$ relevant for electro- and acousto-optics," *J. Appl. Phys.*, vol. 74, pp. 1287-1297, Jul. 1993.

[109] *CRC Handbook of Chemistry and Physics*, 86th ed. Lide, D.R., Ed.; CRC Press: Boca Raton, FL, 2005; Chapter 12, p 33-34.

[110] O. L. Anderson, "Determination and some uses of isotropic elastic constants of polycrystalline aggregates using single-crystal data," in *Physical Acoustics*. vol. 3, Part B, New York: Academic, 1965, pp. 77–83.

[111] G. Carlotti, L. Doucet, and M. Dupeux, "Elastic properties of silicon dioxide films deposited by chemical vapour deposition from tetraethylorthosilicate," *Thin Solid Films*, vol. 296, pp. 102-105, Mar. 1997.

[112] G. C. Schwartz, Y. S. Huang, and W. J. Patrick, "The effective dielectric Constant of silicon dioxides deposited in the spaces between adjacent conductors," *J. Electrochem. Soc*. vol. 139, no. 12, pp. L118-L122, Dec. 1992.

[113] D. P. Fernández, Y. Umlev, A. R. H. Goodwin, and J. M. H. Levelt Sengers, "A database for the static dielectric constant of water and steam," *J. Phys. Chem. Ref. Data*. vol. 24, no. 1, pp. 33-69, Jan.-Feb. 1995.

APPENDIX A

DERIVATION OF THE 2D "A"-MATRIX

The purpose of Appendix **A** is to detail the derivation of the 2D (in terms of slowness-space) **A** matrix represented in Equation (2.6). The work presented here expanded that presented by [38] (1D analysis) to include, to the best of the author's knowledge for the first time, a 2D slowness-space derivation. In the case of purely real values of slowness for s_x and s_y, the same results using [38] may be obtained by pre-rotating the material constants around the $+z$-axis by an amount $\psi = \tan^{-1}(s_y/s_x)$ (four quadrant inverse tangent of ratio). Under the case where s_x and s_y are complex and independent quantities, only the method here can be used, since $s_x = s_r \cos(\psi)$ and $s_y = s_r \sin(\psi)$ (hence $s_y/s_x = \tan(\psi)$), where s_r is the s_x complex slowness value evaluated in the method presented in [38] after material constant rotation about the $+z$-axis by ψ. This method may prove useful in implementation of future more accurate full-3D FEM/BEM models as computation power improves, which will require 2D Fourier analysis in the s_x and s_y complex slowness-space. This method combined with the eigen-partial-derivative analysis presented in Section 2.3 may prove to be very useful towards the numerical implementation of such future tools. The derivation of the 2D **A** matrix follows.

Step 1: Substituting (2.2) and (2.4) into (2.1) and factoring partial derivative terms yields:

$$
\begin{bmatrix} T_1 \\ T_2 \\ T_3 \\ T_4 \\ T_5 \\ T_6 \end{bmatrix} = \begin{bmatrix} c_{11} & c_{12} & c_{13} & c_{14} & c_{15} & c_{16} \\ c_{12} & c_{22} & c_{23} & c_{24} & c_{25} & c_{26} \\ c_{13} & c_{23} & c_{33} & c_{34} & c_{35} & c_{36} \\ c_{14} & c_{24} & c_{34} & c_{44} & c_{45} & c_{46} \\ c_{15} & c_{25} & c_{35} & c_{45} & c_{55} & c_{56} \\ c_{16} & c_{26} & c_{36} & c_{46} & c_{56} & c_{66} \end{bmatrix} \left[\frac{\partial}{\partial x} \begin{bmatrix} u_1 \\ 0 \\ 0 \\ 0 \\ u_3 \\ u_2 \end{bmatrix} + \frac{\partial}{\partial y} \begin{bmatrix} 0 \\ u_2 \\ 0 \\ u_3 \\ 0 \\ u_1 \end{bmatrix} + \frac{\partial}{\partial z} \begin{bmatrix} 0 \\ 0 \\ u_3 \\ u_2 \\ u_1 \\ 0 \end{bmatrix} \right] + \begin{bmatrix} e_{11} & e_{21} & e_{31} \\ e_{12} & e_{22} & e_{32} \\ e_{13} & e_{23} & e_{33} \\ e_{14} & e_{24} & e_{34} \\ e_{15} & e_{25} & e_{35} \\ e_{16} & e_{26} & e_{36} \end{bmatrix} \left[\frac{\partial}{\partial x} \begin{bmatrix} \phi \\ 0 \\ 0 \end{bmatrix} + \frac{\partial}{\partial y} \begin{bmatrix} 0 \\ \phi \\ 0 \end{bmatrix} + \frac{\partial}{\partial z} \begin{bmatrix} 0 \\ 0 \\ \phi \end{bmatrix} \right]
\tag{A.1}
$$

and

$$
\begin{bmatrix} D_1 \\ D_2 \\ D_3 \end{bmatrix} = - \begin{bmatrix} \varepsilon_{11} & \varepsilon_{12} & \varepsilon_{13} \\ \varepsilon_{12} & \varepsilon_{11} & \varepsilon_{23} \\ \varepsilon_{13} & \varepsilon_{23} & \varepsilon_{33} \end{bmatrix} \left[\frac{\partial}{\partial x} \begin{bmatrix} \phi \\ 0 \\ 0 \end{bmatrix} + \frac{\partial}{\partial y} \begin{bmatrix} 0 \\ \phi \\ 0 \end{bmatrix} + \frac{\partial}{\partial z} \begin{bmatrix} 0 \\ 0 \\ \phi \end{bmatrix} \right] + \begin{bmatrix} e_{11} & e_{12} & e_{13} & e_{14} & e_{15} & e_{16} \\ e_{21} & e_{22} & e_{23} & e_{24} & e_{25} & e_{26} \\ e_{31} & e_{32} & e_{33} & e_{34} & e_{35} & e_{36} \end{bmatrix} \left[\frac{\partial}{\partial x} \begin{bmatrix} u_1 \\ 0 \\ 0 \\ 0 \\ u_3 \\ u_2 \end{bmatrix} + \frac{\partial}{\partial y} \begin{bmatrix} 0 \\ u_2 \\ 0 \\ u_3 \\ 0 \\ u_1 \end{bmatrix} + \frac{\partial}{\partial z} \begin{bmatrix} 0 \\ 0 \\ u_3 \\ u_2 \\ u_1 \\ 0 \end{bmatrix} \right].
\tag{A.2}
$$

Step 2: Define the vector $\boldsymbol{\tau}_u$ as:

$$
\boldsymbol{\tau}_u = \begin{bmatrix} u_1 \\ u_2 \\ u_3 \\ \phi \end{bmatrix}.
\tag{A.3}
$$

Step 3: Factoring out (A.3) from (A.1) and (A.2), and grouping particular stress and electric displacement components yields:

$$
\begin{bmatrix} T_5 \\ T_4 \\ T_3 \end{bmatrix} = \begin{bmatrix} c_{15} & c_{56} & c_{55} & e_{15} \\ c_{14} & c_{46} & c_{45} & e_{14} \\ c_{13} & c_{36} & c_{35} & e_{13} \end{bmatrix} \frac{\partial \boldsymbol{\tau}_u}{dx} + \begin{bmatrix} c_{56} & c_{25} & c_{45} & e_{25} \\ c_{46} & c_{24} & c_{44} & e_{24} \\ c_{36} & c_{23} & c_{34} & e_{23} \end{bmatrix} \frac{\partial \boldsymbol{\tau}_u}{dy} + \begin{bmatrix} c_{55} & c_{45} & c_{35} & e_{35} \\ c_{45} & c_{44} & c_{34} & e_{34} \\ c_{35} & c_{34} & c_{33} & e_{33} \end{bmatrix} \frac{\partial \boldsymbol{\tau}_u}{dz} \quad \text{(A.4)}
$$

and

$$
\begin{bmatrix} T_1 \\ T_6 \\ T_5 \end{bmatrix} = \begin{bmatrix} c_{11} & c_{16} & c_{15} & e_{11} \\ c_{16} & c_{66} & c_{56} & e_{16} \\ c_{15} & c_{56} & c_{55} & e_{15} \end{bmatrix} \frac{\partial \boldsymbol{\tau}_u}{dx} + \begin{bmatrix} c_{16} & c_{12} & c_{14} & e_{21} \\ c_{66} & c_{26} & c_{46} & e_{26} \\ c_{56} & c_{25} & c_{45} & e_{25} \end{bmatrix} \frac{\partial \boldsymbol{\tau}_u}{dy} + \begin{bmatrix} c_{15} & c_{14} & c_{13} & e_{31} \\ c_{56} & c_{46} & c_{36} & e_{36} \\ c_{55} & c_{45} & c_{35} & e_{35} \end{bmatrix} \frac{\partial \boldsymbol{\tau}_u}{dz} \quad \text{(A.5)}
$$

and

$$
\begin{bmatrix} T_6 \\ T_2 \\ T_4 \end{bmatrix} = \begin{bmatrix} c_{16} & c_{66} & c_{56} & e_{16} \\ c_{12} & c_{26} & c_{25} & e_{12} \\ c_{14} & c_{46} & c_{45} & e_{14} \end{bmatrix} \frac{\partial \boldsymbol{\tau}_u}{dx} + \begin{bmatrix} c_{66} & c_{26} & c_{46} & e_{26} \\ c_{26} & c_{22} & c_{24} & e_{22} \\ c_{46} & c_{24} & c_{44} & e_{24} \end{bmatrix} \frac{\partial \boldsymbol{\tau}_u}{dy} + \begin{bmatrix} c_{56} & c_{46} & c_{36} & e_{36} \\ c_{25} & c_{24} & c_{23} & e_{32} \\ c_{45} & c_{44} & c_{34} & e_{34} \end{bmatrix} \frac{\partial \boldsymbol{\tau}_u}{dz} \quad \text{(A.6)}
$$

and

$$
\begin{bmatrix} D_1 \\ D_2 \\ D_3 \end{bmatrix} = \begin{bmatrix} e_{11} & e_{16} & e_{15} & -\varepsilon_{11} \\ e_{21} & e_{26} & e_{25} & -\varepsilon_{12} \\ e_{31} & e_{36} & e_{35} & -\varepsilon_{13} \end{bmatrix} \frac{\partial \boldsymbol{\tau}_u}{\partial x} + \begin{bmatrix} e_{16} & e_{12} & e_{14} & -\varepsilon_{12} \\ e_{26} & e_{22} & e_{24} & -\varepsilon_{22} \\ e_{36} & e_{32} & e_{35} & -\varepsilon_{23} \end{bmatrix} \frac{\partial \boldsymbol{\tau}_u}{\partial y} + \begin{bmatrix} e_{15} & e_{14} & e_{13} & -\varepsilon_{13} \\ e_{25} & e_{24} & e_{23} & -\varepsilon_{23} \\ e_{35} & e_{34} & e_{24} & -\varepsilon_{33} \end{bmatrix} \frac{\partial \boldsymbol{\tau}_u}{\partial z}. \quad \text{(A.7)}
$$

Step 4: Define the vectors $\boldsymbol{\tau}_{Px}$, $\boldsymbol{\tau}_{Py}$, and $\boldsymbol{\tau}_N$ as:

$$
\boldsymbol{\tau}_{Px} = \begin{bmatrix} T_1 \\ T_6 \\ T_5 \\ D_1 \end{bmatrix}, \quad \text{(A.8)}
$$

and

$$
\boldsymbol{\tau}_{Py} = \begin{bmatrix} T_6 \\ T_2 \\ T_4 \\ D_2 \end{bmatrix}, \quad \text{(A.9)}
$$

and

$$\boldsymbol{\tau}_N = \begin{bmatrix} T_5 \\ T_4 \\ T_3 \\ D_3 \end{bmatrix}. \tag{A.10}$$

Step 5: Substituting appropriate rows from Equations (A.4) through (A.7) into Equations (A.8) through (A.10) yields:

$$\boldsymbol{\tau}_{Px} = -s_x \boldsymbol{\Gamma}^{11} j\omega \, \boldsymbol{\tau}_u - s_y \boldsymbol{\Gamma}^{12} j\omega \, \boldsymbol{\tau}_u + \boldsymbol{\Gamma}^{13} \frac{\partial \boldsymbol{\tau}_u}{\partial z}, \tag{A.11}$$

and

$$\boldsymbol{\tau}_{Py} = -s_x \boldsymbol{\Gamma}^{21} j\omega \, \boldsymbol{\tau}_u - j\omega \, s_y \boldsymbol{\Gamma}^{22} j\omega \, \boldsymbol{\tau}_u + \boldsymbol{\Gamma}^{23} \frac{\partial \boldsymbol{\tau}_u}{\partial z}, \tag{A.12}$$

and

$$\boldsymbol{\tau}_N = -s_x \boldsymbol{\Gamma}^{31} j\omega \, \boldsymbol{\tau}_u - s_y \boldsymbol{\Gamma}^{32} j\omega \, \boldsymbol{\tau}_u + \boldsymbol{\Gamma}^{33} \frac{\partial \boldsymbol{\tau}_u}{\partial z}, \tag{A.13}$$

since $\quad \dfrac{\partial \boldsymbol{\tau}_u}{\partial x} = -j\omega \, s_x \boldsymbol{\tau}_u$ and $\dfrac{\partial \boldsymbol{\tau}_u}{\partial y} = -j\omega \, s_y \boldsymbol{\tau}_u,$

where

$$\boldsymbol{\Gamma}^{ik} = \begin{bmatrix} c_{1i1k} & c_{1i2k} & c_{1i3k} & e_{k1i} \\ c_{2i1k} & c_{2i2k} & c_{2i3k} & e_{k2i} \\ c_{3i1k} & c_{3i2k} & c_{3i3k} & c_{k3i} \\ e_{i1k} & e_{i2k} & e_{i3k} & -\varepsilon_{ik} \end{bmatrix}. \tag{A.14}$$

Step 6: Combining (2.3) and (2.5) and factoring terms defined in (A.8) through (A.10) yields:

$$j\omega \, s_x \boldsymbol{\tau}_{Px} + j\omega \, s_y \boldsymbol{\tau}_{Py} - \frac{\partial \boldsymbol{\tau}_N}{\partial z} = \omega^2 \rho \, \mathbf{I}_4 \boldsymbol{\tau}_u, \tag{A.15}$$

where

$$\mathbf{I}_4 = \begin{bmatrix} 1 & 0 & 0 & 0 \\ 0 & 1 & 0 & 0 \\ 0 & 0 & 1 & 0 \\ 0 & 0 & 0 & 0 \end{bmatrix}.$$

Step 7: Solving (A.13) for jω times the z-partial-derivative term yields:

$$\frac{\partial\, j\omega\,\boldsymbol{\tau}_u}{\partial z} = j\omega\!\left(\mathbf{X}\boldsymbol{\tau}_N + \left(s_x\mathbf{X}\boldsymbol{\Gamma}^{31} + s_y\mathbf{X}\boldsymbol{\Gamma}^{32}\right)j\omega\,\boldsymbol{\tau}_u\right), \qquad (\text{A.16})$$

where

$$\mathbf{X} = \left[\boldsymbol{\Gamma}^{33}\right]^{-1}.$$

Step 8: Solving (A.15) for the z-partial-derivative term yields:

$$\frac{\partial\boldsymbol{\tau}_N}{\partial z} = j\omega\!\left(s_x\boldsymbol{\tau}_{Px} + s_y\boldsymbol{\tau}_{Py} + \rho\,\mathbf{I}_4\, j\omega\boldsymbol{\tau}_u\right). \qquad (\text{A.17})$$

Step 9: Dividing both side of (A.16) by $j\omega$ and substituting into (A.11) through (A.12) yields:

$$\boldsymbol{\tau}_{Px} = \boldsymbol{\Gamma}^{13}\mathbf{X}\boldsymbol{\tau}_N + \left(s_x\!\left(\boldsymbol{\Gamma}^{13}\mathbf{X}\boldsymbol{\Gamma}^{31} - \boldsymbol{\Gamma}^{11}\right) + s_y\!\left(\boldsymbol{\Gamma}^{13}\mathbf{X}\boldsymbol{\Gamma}^{32} - \boldsymbol{\Gamma}^{12}\right)\right)j\omega\,\boldsymbol{\tau}_u, \qquad (\text{A.18})$$

and

$$\boldsymbol{\tau}_{Py} = \boldsymbol{\Gamma}^{23}\mathbf{X}\boldsymbol{\tau}_N + \left(s_x\!\left(\boldsymbol{\Gamma}^{23}\mathbf{X}\boldsymbol{\Gamma}^{31} - \boldsymbol{\Gamma}^{21}\right) + s_y\!\left(\boldsymbol{\Gamma}^{23}\mathbf{X}\boldsymbol{\Gamma}^{32} - \boldsymbol{\Gamma}^{22}\right)\right)j\omega\,\boldsymbol{\tau}_u. \qquad (\text{A.19})$$

Step 9: Substitution of (A.18) and (A.19) into (A.17) yields:

$$\frac{\partial\boldsymbol{\tau}_N}{\partial z} = j\omega\!\left(s_x\boldsymbol{\Gamma}^{13}\mathbf{X} + s_y\boldsymbol{\Gamma}^{23}\mathbf{X}\right)\boldsymbol{\tau}_N +$$
$$j\omega\!\left(\rho\,\mathbf{I}_4 - s_x^2\!\left(\boldsymbol{\Gamma}^{11} - \boldsymbol{\Gamma}^{13}\mathbf{X}\boldsymbol{\Gamma}^{31}\right) - s_x s_y\!\left(\boldsymbol{\Gamma}^{12} - \boldsymbol{\Gamma}^{13}\mathbf{X}\boldsymbol{\Gamma}^{32} - \boldsymbol{\Gamma}^{23}\mathbf{X}\boldsymbol{\Gamma}^{31} + \boldsymbol{\Gamma}^{22}\right) - s_y^2\!\left(\boldsymbol{\Gamma}^{22} - \boldsymbol{\Gamma}^{23}\mathbf{X}\boldsymbol{\Gamma}^{32}\right)\right)j\omega\,\boldsymbol{\tau}_u. \qquad (\text{A.20})$$

Step 10: Combining (A.20) and (A.16), (2.6) follows.

APPENDIX B

EVALUATION OF Y$_{\text{MN}}$ INTERGRALS

The purpose of Appendix B is to present the methods used in this work for the evaluation of the $\mathbf{Y}_{mn}$ matrix elements defined in (2.34); shown here as (B.1):

$$Y_{mn}^{rs} = \frac{2\pi}{j\omega} \int_{-\infty}^{\infty} G_{mn}\left(\frac{k_x}{\omega}\right) f_m^r(-k_x) f_n^s(k_x) dk_x = -2\pi j \int_{-\infty}^{\infty} G_{mn}(s_x) f_m^r(-\omega s_x) f_n^s(\omega s_x) ds_x. \qquad \text{(B.1)}$$

In Chapter 2 Section 2.4 it was shown that the Green's functions for a semi-infinite piezoelectric/vacuum half-space display the following properties: (i) possible simple poles at $\pm s^{SAW}$, which represent contributions for $\pm x$-directed SAW excitation, respectively; (ii) possible additional simple poles at complex $\pm s_n^{PSAW}$, which represent contributions for the nth $\pm x$-directed PSAW/HVPSAW mode excitation, respectively; (iii) branch cut-lines extending from the bulk-wave cut-off slowness points, $\pm s_n^{BAW}$, to $\left(\pm s_n^{BAW} \mp j\infty\right)$; and (iv) a branch cut-line extending to from $-j\infty$ to $+j\infty$ due to use of the quasi-static approximation. In addition, branch-cut singularities may appear at $\pm s_n^{BAW}$; a branch-cut singularity always appears at the origin of $G_{44}(s_x)$ where

$G_{44}(s_x) \propto \dfrac{1}{\sqrt{s_x^2}}$; and all Green's functions follow $G_{mn}(s_x) \propto \dfrac{1}{s_x}$ as $|s_x|$ goes to infinity.

Before proceeding on the description of methods in this work to evaluate (B.1), a novel modification to the integrand in (B.1) is presented which allows the singularity at the origin of $G_{44}(s_x)$ to be effectively cancelled-out, thus making the numerical integration more practical. The following analysis demonstrates this method.

Recall c_4^r from (2.34) and define the portion due to charge sources as:

$$c_{\sigma 4}{}^r = \sum_{s=1}^{N_4} w_4^s Y_{44}^{rs} = -j2\pi \int_{-\infty}^{\infty} G_{44}(s_x) \left(\sum_{s=1}^{N_4} w_4^s f_4^r(-\omega\, s_x) f_4^s(\omega\, s_x) \right) ds_x \ .$$

(B.2)

It was shown in Chapter 2 that charge conservation requires:

$$0 = \sum_{s=1}^{N_4} w_4^s f_4^s(\omega\, s_x = 0).$$

(B.3)

Adding a constant-scaled (w.r.t s) instance of (B.3) (say multiplying by b) to the summation term in (B.2) therefore does not modify the l.h.s of the equation. Performing this operation, combining summation terms, and interchanging the order of integration and summation results in:

$$c_{\sigma 4}{}^r = \sum_{s=1}^{N_4} w_4^s \left(-j2\pi \int_{-\infty}^{\infty} G_{44}(s_x) \left(f_4^r(-\omega\, s_x) f_4^s(\omega\, s_x) + b\, f_4^s(0) \right) ds_x \right).$$

(B.4)

By choosing an appropriate value for b we can effectively cancel the singularity at $s_x = 0$, and in addition preserve good integral convergence when evaluating numerically. A good choice for b that satisfies the desired aforementioned properties is $b = -f_4^r(0) \left(-\dfrac{s_p^2}{s_x^2 - s_p^2} \right)^{v}$

, where $s_p = |s_p| \dfrac{(1-j)}{\sqrt{2}}$, and v is some integer greater than 1. Applying this method to (B.4) results in:

$$c_{\sigma 4}{}^r = \sum_{s=1}^{N_4} w_4^s \left(-j2\pi \int_{-\infty}^{\infty} G_{44}(s_x) \left(f_4^r(-\omega\, s_x) f_4^s(\omega\, s_x) - f_4^r(0) f_4^s(0) \left(-\frac{s_p^2}{s_x^2 - s_p^2} \right)^{v} \right) ds_x \right).$$

(B.5)

Therefore the $m = 4$, $n = 4$ portion of (B.1) is equivalent to:

$$Y_{44}^{rs} = -j2\pi \int_{-\infty}^{\infty} G_{44}(s_x) \left(f_4^r(-\omega s_x) f_4^s(\omega s_x) - f_4^r(0) f_4^s(0) \left(-\frac{s_p^2}{s_x^2 - s_p^2} \right)^v \right) ds_x. \qquad \text{(B.6)}$$

Note that under this modification, additional complex simple poles are introduced in the integrand of (B.6) in the complex slowness plane at $\pm s_p$. In this work $|s_p|$ is chosen to be less then the maximum of the set of bulk-wave cut-off slowness points.

Given the aforementioned characteristics of the Green's functions, appropriate integrations contours in the complex slowness plane will now be defined, which allow evaluation of (B.1) and (B.6) via the complex analysis residue theorem [78].

In theory of complex analysis, the residue theorem, (B.7), states that the close contour integral over a region in the complex plane where the arbitrary complex integrand $g(s_x)$ is analytic with possibly a finite number of enclosed isolated singularities, is equal to 2π multiplied by the sum of singularity residues enclosed by the contour (in counter-clockwise path sense, for a clockwise path sense the contour integral is equal to -2π multiplied by the sum of residues enclosed by the contour).

$$\oint g(s_x) ds_x = \left[\begin{array}{cc} j2\pi \sum (Enclosed\ Residues) & counter\text{-}clockwise\ path \\ -j2\pi \sum (Enclosed\ Residues) & clockwise\ path \end{array} \right] \qquad \text{(B.7)}$$

Before explicitly showing the integration contours used in this work, it proves usefully to define the properties of the integrals along the radial contour in the complex slowness plane as the radius, R, tends toward infinity over a range of angles given by $\theta = \text{Arg}[s_x]$.

Inserting the integrands of (B.1) and (B.6) into a complex integral of s_x, I, and making the

following substitutions $s_x = Re^{j\theta}$ and $ds_x = jRe^{j\theta}$ results in, respectively:

$$I = 2\pi \int_\theta Re^{j\theta} G_{mn}\left(Re^{j\theta}\right) f_m^r\left(-\omega Re^{j\theta}\right) f_n^s\left(\omega Re^{j\theta}\right) d\theta ,$$

(B.8)

or

$$I = 2\pi \int_\theta Re^{j\theta} G_{44}\left(Re^{j\theta}\right) \left(f_4^r\left(-\omega Re^{j\theta}\right) f_4^s\left(\omega Re^{j\theta}\right) - f_4^r(0) f_4^s(0)\left(-\frac{s_p^2}{R^2 e^{j2\theta} - s_p^2} \right)^v \right) d\theta .$$

(B.9)

Recalling that all Green's functions in the limit of large slowness magnitude (large R) are

proportional to $1/s_x$ allows further simplification of (B.8) and (B.9) in the limit R goes to

infinity, and results in, respectively:

$$I = C_{mn} \int_\theta f_m^r\left(-\omega Re^{j\theta}\right) f_n^s\left(\omega Re^{j\theta}\right) d\theta ,$$

(B.10)

or

$$I = C_{44} \int_\theta \left(f_4^r\left(-\omega Re^{j\theta}\right) f_4^s\left(\omega Re^{j\theta}\right) - f_4^r(0) f_4^s(0)\left(-\frac{s_p^2}{R^2 e^{j2\theta} - s_p^2} \right)^v \right) d\theta ,$$

(B.11)

where C_{mn} are constants.

Clearly the magnitude of the second term in the integrand of (B.11) vanishes in the limit

as R goes to infinity; hence only (B.10) needs to be considered from here on as the form

of each integral become identical. Using (2.15), (B.10) maybe expressed as:

$$I = \frac{C_{mn}}{4\pi^2} \int_\theta \int_{\Gamma_{mr}} \int_{\Gamma_{ns}} \overline{f}_m^r(x_r) \overline{f}_n^s(x_s) e^{-j\omega R \cos(\theta)(x_r - x_s)} e^{\omega R \sin(\theta)(x_r - x_s)} dx_r dx_s d\theta ,$$

(B.12)

where

$\Gamma_{(m,n)(r,s)}$ represents the non-zero domain of the corresponding basis

functions.

254

Using an integral triangle inequality on the magnitude of (B.12) results in:

$$|I| \leq \left|\frac{C_{mn}}{4\pi^2}\right| \int_\theta \int_{\Gamma_{mr}} \int_{\Gamma_{ns}} \left|\overline{f}\,_m^r(x_r)\right| \left|\overline{f}\,_n^s(x_s)\right| e^{\omega R \sin(\theta)(x_r - x_s)} dx_r dx_s d\theta .$$

(B.13)

We will now examine (B.13) under various conditions on Γ_{mr}, Γ_{ns}, and θ : case 1 is defined to be when $\Gamma_{mr} > \Gamma_{ns}$ and $\theta \in [-\pi/2, 0]$; case 2 is defined to be when $\Gamma_{mr} > \Gamma_{ns}$ and $\theta \in [-\pi, -\pi/2]$; case 3 is defined to be when $\Gamma_{mr} < \Gamma_{ns}$ and $\theta \in [0, \pi/2]$; and case 4 is defined to be when $\Gamma_{mr} < \Gamma_{ns}$ and $\theta \in [\pi/2, \pi]$. Under case 1 and case 2 the $(x_r - x_s)$ term in exponent of the integrand is always positive over the integration domains, while under case 3 and case 4 the $(x_r - x_s)$ term in exponent of the integrand is always negative over the integration domains. Furthermore: for case 1, $\sin(\theta) \leq 2\theta/\pi$, for case 2, $\sin(\theta) \leq -2\theta/\pi - 2$; for case 3, $\sin(\theta) \geq 2\theta/\pi$; and for case 4, $\sin(\theta) \geq -2\theta/\pi + 2$. By using the aforementioned characteristics of the each specific case, (B.13), and setting $|d_{min}|$ as the minimum absolute value of the term $(x_r - x_s)$ over the domains of integrands in each case, the following inequalities result:

$$|I| \leq |Q| \left(\int_{\theta_l}^{\theta_u} e^{\omega R \frac{2\theta}{\pi} |d_{\min}|} d\theta \right) = |Q| \frac{\pi}{2|d_{\min}|\omega R} \left(e^{\omega R \frac{2\theta_u}{\pi} |d_{\min}|} - e^{\omega R \frac{2\theta_l}{\pi} |d_{\min}|} \right), \qquad \text{(case 1)} \qquad \text{(B.14)}$$

$$|I| \leq |Q| \left(\int_{\theta_l}^{\theta_u} e^{\omega R \left(\frac{2\theta}{\pi} - 2 \right) |d_{\min}|} d\theta \right) = |Q| \frac{\pi}{2|d_{\min}|\omega R} \left(e^{-\omega R \frac{2(\pi+\theta_l)}{\pi} |d_{\min}|} - e^{-\omega R \frac{2(\pi+\theta_u)}{\pi} |d_{\min}|} \right), \qquad \text{(case 2)} \qquad \text{(B.15)}$$

$$|I| \leq |Q| \left(\int_{\theta_l}^{\theta_u} e^{-\omega R \frac{2\theta}{\pi} |d_{\min}|} d\theta \right) = |Q| \frac{\pi}{2|d_{\min}|\omega R} \left(e^{-\omega R \frac{2\theta_l}{\pi} |d_{\min}|} - e^{-\omega R \frac{2\theta_u}{\pi} |d_{\min}|} \right), \qquad \text{(case 3)} \qquad \text{(B.16)}$$

$$|I| \leq |Q| \left(\int_{\theta_l}^{\theta_u} e^{-\omega R \left(-\frac{2\theta}{\pi} + 2 \right) |d_{\min}|} d\theta \right) = |Q| \frac{\pi}{2|d_{\min}|\omega R} \left(e^{\omega R \frac{2(-\pi+\theta_u)}{\pi} |d_{\min}|} - e^{\omega R \frac{2(-\pi+\theta_l)}{\pi} |d_{\min}|} \right), \qquad \text{(case 4)} \qquad \text{(B.17)}$$

where:

$$|Q| = \left| \frac{C_{mn}}{4\pi^2} \right| \left(\int_{\Gamma_{ns}} \left| \overline{f}_n^s(x_s) \right| dx_s \right) \left(\int_{\Gamma_{mr}} \left| \overline{f}_m^r(x_r) \right| dx_r \right), \qquad \text{(B.18)}$$

and

θ_u and θ_l are the upper and lower limits of integration for the contour of interest, respectively, which must fall within each corresponding case's defined θ range.

Therefore, as long as the integrals of (B.18) are finite it is seen in (B.14)-(B.17) that the magnitude of the contour integral under each case goes to zero as R tends towards infinity.

Appropriate complex contours for numerical evaluation of (B.1) and (B.6) are now defined given (B.7) and the outcomes for the previous derivation regarding integrals of (B.1) and (B.6) along radial contours in the complex slowness plane in the limit as R goes to infinity. In particular, Figure B.1 shows the evaluated contour integral paths chosen for the three possible situations: (i) $\Gamma_{mr} < \Gamma_{ns}$; (ii) $\Gamma_{mr} > \Gamma_{ns}$; and (iii) $\Gamma_{mr} = \Gamma_{ns}$.

Situation 1

$\Gamma_{mr} < \Gamma_{ns}$

Situation 2

$\Gamma_{mr} > \Gamma_{ns}$

Situation 3

$\Gamma_{mr} = \Gamma_{ns}$
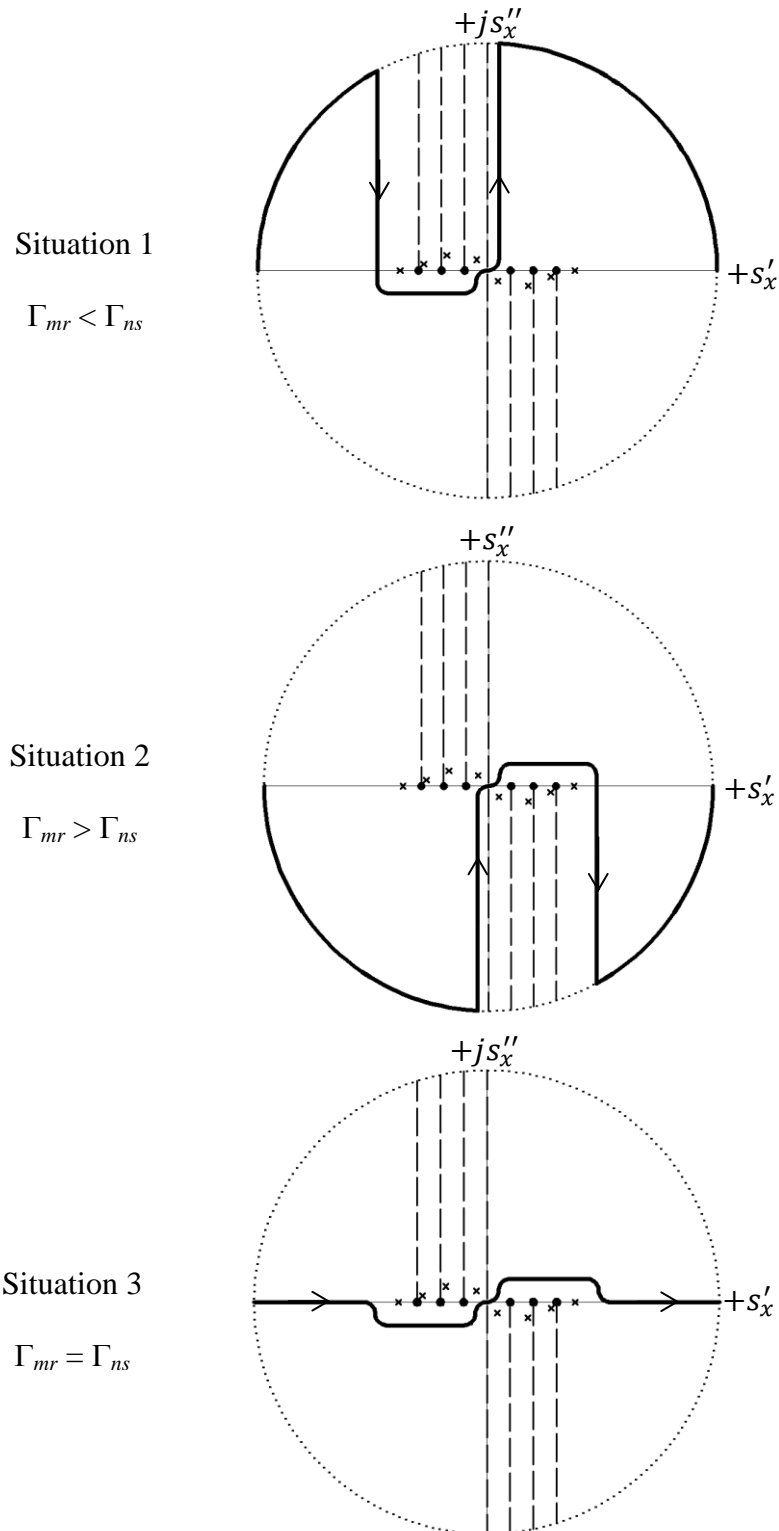
Figure B.1. Complex s_x plane integration contours (bold) used for evaluation of (B.1) and (B.6) for three potential basis function domain situations.

Figure B.1 also shows the corresponding regions in the complex slowness plane where the integrands in (B.1) and (B.6) display branch-cut lines, possible branch-cut singularities, and possible simple poles. Note that the representation of these features is not exact as presented here, but is characteristic of the behavior seen for various orientations and piezoelectric materials, where if the true SAW solution occurs it is at greater slowness magnitude than bulk-wave transition points, and if PSAW/HVPSAW modes exist they fall in between bulk-wave cut-off slowness points. It is also assumed that the spectrum of the basis functions is analytic everywhere except for possibly at complex infinity. The number of branch-cut lines, branch-cut singularities, and simple poles depends on the specific crystal orientation and material. In addition, since all materials exhibit some finite losses, the locations of bulk-wave transition points, and simple poles can in reality be shifted infinitesimally off the real slowness access (towards $-js_x''$ for $+js_x'$ points, and towards $+js_x''$ for $-s_x'$ points) as additional propagation loss must be accounted for. Using this technique allows defining what the value of the enclosed residues is when integrand singularities appear on the integration contour (before applying shifting).

Numerical estimation of (B.1) and (B.6) is performed via integrating the integrands of (B.1) and (B.6) along the contours show in Figure B.1, for a "large" finite value of R. It should be noted that integrating along the first two contours in Figure B.1 (situations 1 and 2) converges much faster with increasing R compared to integration along the last contour in Figure B.1 (situation 3). In most cases (where the pole cancelation is not required at the origin) this is true since the integrands will contain an

258

inherent factor of $e^{-j\omega s_x \Delta_{rs}}$, where Δ_{rs} is the difference of midpoints for Γ_{mr} and Γ_{ns} respectively, which results in rapid decay of the integrand along the vertical running contours in Figure B.1 (under situations 1 and 2) as evaluation moves away from the real slowness axis. The contours for situation 3 shown in Figure B.1 where chosen because it was not possible to show convergence for radial contour integrals as R goes to infinity, since $|d_{min}| = 0$ under this situation. It should be noted that the situation 3 contour can be used in situations 1 and 2, but it is not as efficient in terms of convergence. To achieve better convergence for situation 3, it can be helpfully to subtract out asymptotic approximations for the integrand on each side of the contour after some large R, then evaluate their contribution analytically if possible, and finally add the result to the numerically integrated residual contribution.

In this work the basis functions used for representation of stress fields and charge density at the electrode/substrate interface are given as:

$$\bar{f}_p^s(x) = \begin{cases} \dfrac{T_{n_s}\left(\dfrac{x - x_s^c}{a_s}\right)}{\sqrt{1 - \left(\dfrac{x - x_s^c}{a_s}\right)^2}} & \left(x_s^c - a_s\right) \le x \le \left(x_s^c + a_s\right) \\ 0 & otherwise \end{cases}, \tag{B.19}$$

where:

    T_{n_s} is the Chebyshev polynomial of the first kind of order n_s,

    x_s^c is the center postilion of the electrode that the basis function is applied to,

    a_s is the ½ the width of the electrode the basis function is applied to,

    and p is 1,2,3, or 4 (same basis functions used for charge and stress).

Applying (2.15) to (B.19) and making the following substitutions, $x' = \dfrac{x - x_s^c}{a_s}$ and

$dx' = \dfrac{dx}{a_s}$, results in:

$$f_p^s(k_x) = \frac{a_s e^{jk_x x_s^c}}{2\pi} \int_{-1}^{1} \frac{T_{n_s}(x') e^{jk_x a_s x'}}{\sqrt{1 - x'^2}} dx' . \tag{B.20}$$

Making the following substations into (B.20), $x' = \cos(\theta)$ and $dx' = -\sin(\theta) d\theta$, using the

identity $T_{n_s}(\cos(\theta)) = \cos(n_s \theta)$, and then simplifying results in:

$$f_p^s(k_x) = \frac{a_s e^{jk_x x_s^c}}{2\pi} \int_{0}^{\pi} \cos(n_s \theta) e^{jk_x a_s \cos(\theta)} d\theta , \tag{B.21}$$

Given the following identity for an nth order Bessel function of the first kind:

$$J_n(z) = \frac{j^{-n}}{\pi} \int_{0}^{\pi} \cos(n\theta) e^{jz \cos(\theta)} d\theta , \tag{B.22}$$

(B.21) is now given as:

$$f_p^s(k_x) = j^{n_s} \frac{a_s}{2} J_{n_s}(a_s k_x) e^{jk_x x_s^c} . \tag{B.23}$$

Given that even order Bessel functions of the first kind are even, and odd orders are odd:

$$f_p^r(-k_x) = (-1)^{n_r} j^{n_r} \frac{a_r}{2} J_{n_r}(a_r k_x) e^{-jk_x x_r^c} . \tag{B.24}$$

With (B.23) and (B.24) defined, (B.1) and (B.6) are now given as:

$$Y_{mn}^{rs} = c_{rs} \int_{-\infty}^{\infty} G_{mn}(s_x) J_{n_r}(a_r \omega s_x) J_{n_s}(a_s \omega s_x) e^{-j\omega s_x \Delta_{rs}} ds_x, \qquad \text{(B.25)}$$

and

$$Y_{44}^{rs} = c_{rs} \int_{-\infty}^{\infty} G_{44}(s_x) \left(J_{n_r}(a_r \omega s_x) J_{n_s}(a_s \omega s_x) e^{-j\omega s_x \Delta_{rs}} - \delta_{n_r} \delta_{n_s} \left(-\frac{s_p^2}{s_x^2 - s_p^2} \right)^\nu \right) ds_x, \qquad \text{(B.26)}$$

where: $c_{rs} = (-1)^{n_r} \dfrac{\pi}{2} a_r a_s j^{n_r + n_s - 1}$,

δ is the Kronecker delta function,

and $\Delta_{rs} = x_r^c - x_s^c$.

When $\Delta_{rs} < 0$, numerical integration of the situation 1 contour shown in Figure B.1 is used for evaluation of (B.25) and (B.26). When $\Delta_{rs} > 0$, numerical integration of the situation 2 contour shown in Figure B.1 is used for evaluation of (B.25) and (B.26). For these situations, and when the pole cancelation term is not required ($m \neq 4$ or $n \neq 4$ or $n_s \neq 0$ or $n_r \neq 0$), the magnitude of the integrand falls off at approximately $\dfrac{e^{-\omega R(|\Delta_{rs}| - a_r - a_s)}}{R^2}$ as R goes to infinity, given the known asymptotic behavior of Bessel functions and the Green's functions. For these situations, and when the pole cancelation term is required ($m = 4$ and $n = 4$ and $n_s = 0$ and $n_r = 0$) the magnitude of the integrand falls off slower, but sufficiently, at $\dfrac{1}{R^{2\nu+1}}$. In this work $\nu = 2$ was chosen to be sufficient (too large of a value may cause integral in the neighborhood of s_p to become numerically unstable). Under the case when $\Delta_{rs} = 0$ numerical integration of the situation 3 contour shown in Figure B.1 is used for evaluation of (B.25) and (B.26). Under this situation the magnitude of the integrand falls at approximately $1/R^2$, which is at a much slower rate compared to

the previous two situations. In order to improve the convergence rate, approximations of the integrand at large R are subtracted out of the integrand, integrated analytically, and finally added to the result of numerically integrated residual integrand. The following are used to approximate the integrand of (B.25) and (B.26) under the $\Delta_{rs} = 0$ situations:

$$\frac{c_{mn}^+}{s_x}\left(J_{n_r}(a_r\omega s_x)J_{n_s}(a_s\omega s_x) - \delta_{n_r}\delta_{n_s}\left(-\frac{s_p^2}{s_x^2 - s_p^2} \right)^v \right), \text{ for } \Re\{s_x\} > 0 \tag{B.27}$$

and

$$\frac{c_{mn}^-}{s_x}\left(J_{n_r}(a_r\omega s_x)J_{n_s}(a_s\omega s_x) - \delta_{n_r}\delta_{n_s}\left(-\frac{s_p^2}{s_x^2 - s_p^2} \right)^v \right), \text{ for } \Re\{s_x\} < 0 \tag{B.28}$$

where: $\quad c_{mn}^+ = \lim_{s_x \to \infty} \{s_x G_{mn}(s_x)\}$, and $c_{mn}^- = \lim_{s_x \to -\infty} \{s_x G_{mn}(s_x)\}$.

Note that under $\Delta_{rs} = 0$ situations, $a_r = a_s$. Using the Wolfram Mathematica® software package, the contributions of (B.25) and (B.26) resulting from subtracting off (B.27) and (B.28) from the integrands, were determined to be:

$$c_{rs}(c_{mn}^+ - c_{mn}^-)\left(\log(2) - \gamma - j\frac{\pi}{4} - \log(a_r\omega|s_p|) + \frac{1}{2}\sum_{k=1}^{v-1}\frac{1}{k} \right), \text{ for } n_r = n_s = 0, \tag{B.29}$$

$$\frac{c_{rs}(c_{mn}^+ - c_{mn}^-)}{2n_r}, \text{ for } n_r = n_s \neq 0, \text{ and} \tag{B.30}$$

$$\frac{2c_{rs}(c_{mn}^+ - c_{mn}^-(-1)^{n_s+n_r})}{\pi}\frac{\sin\left(\frac{\pi}{2}(n_s - n_r) \right)}{n_s^2 - n_r^2}, \text{ for } n_r \neq n_s, \tag{B.31}$$

where γ is the Euler-Mascheroni constant.

This concludes the presentation regarding computation of $\mathbf{Y}_{mn}$ integrals.

APPENDIX C

FAR-FIELD AND POWER PARTITIONING ANALYSIS

The purpose of Appendix C is to present the methods used in this work for the evaluation of the scattered or directly transduced fields far away from a finite length electrode structure located at the interface of a piezoelectric and vacuum (see Figure 2.3). In the first part of this appendix it is shown that integration of the Poynting vector along far away contours allows the total radiated SAW and BAW contributions to be determined individually. In the second part of this appendix the theory used in this work for computing far-field BAW radiation patterns is presented.

The first step of the analysis is to draw and imaginary square box of dimensions $2R$ X $2R$ centered at $z = 0$ and $x =$ (center position of the structure under consideration). Sides with outward normal facing $\pm x$ represent contours for integration of x-directed Poynting vector, while sides of the box with outward normal facing $\pm z$ represent contours for integration of z-directed Poynting vector. In the limit as R goes to infinity only Poynting vector associated with the $\pm x$-traveling SAW mode is finite on the $\pm x$-directed outward normal sides, respectively, while Poynting vector associated with only the BAW modes is finite on the side with outward normal facing the $-z$-direction (Poynting vector magnitude is zero for the side with outward normal facing the $+z$-direction). Therefore, normal-directed Poynting vector integrations along the sides of the box allow the determination and separation of power transduced or scattered to $\pm x$-traveling SAW and the BAWs dissipating energy to the crystal bulk.

The next step in the analysis to determine the fields associated with the $\pm x$-traveling SAW mode in the far-field, given the solution of the charge and stress at the electrode/substrate interface. Extraction begins given the relationship for the time-derivative of electric potential at the interface in terms of the spectral domain Greens functions, and the determined spectral domain surface normal stress components and surface charge density resulting from the FEM/BEM analysis (determined by applying (2.33) to the determined basis function weights):

$$j\omega\bar{\phi}(x) = \int_{-\infty}^{\infty}\left(G_{41}\left(\frac{k_x}{\omega}\right)T_5(k_x) + G_{42}\left(\frac{k_x}{\omega}\right)T_4(k_x) + G_{43}\left(\frac{k_x}{\omega}\right)T_3(k_x) + G_{44}\left(\frac{k_x}{\omega}\right)\sigma(k_x)\right)e^{-jk_x x}dk_x =$$

$$j\omega\bar{\phi}(x) = \omega\int_{-\infty}^{\infty}\left(G_{41}(s_x)T_5(\omega s_x) + G_{42}(s_x)T_4(\omega s_x) + G_{43}(s_x)T_3(\omega s_x) + G_{44}(s_x)\sigma(\omega s_x)\right)e^{-j\omega s_x x}ds_x, \quad \text{(C.1)}$$

which can be shown by applying (2.15) to the forth equation of (2.16). Using (B.7) to evaluate (C.1) in the limit $|x|$ gets large indicates that only the simple pole behavior of the Green's functions contribute to the integral, which in turn are only associated with the SAW contribution. This makes sense as the SAW mode in a lossless media situation displays no propagation loss, whereas the magnitude of fields associated with BAW at the surface decay at some factor of $1/x^p$ ($p > 0$) as energy is spread into the bulk, and as the magnitudes of PSAW and HVPSAW modes decay with distance along the surface. The result of applying (B.7) to (C.1) in the limit $|x|$ gets large results in:

$$\lim_{x \to -\infty} j\omega\bar{\phi}(x) = j\omega\phi^{-} e^{j\omega s_o x},$$

(C.2)

where:

$$j\omega\phi^{-} = j\omega 2\pi \left(R_{41}^{-s_o} T_5(-\omega s_o) + R_{42}^{-s_o} T_4(-\omega s_o) + R_{43}^{-s_o} T_3(-\omega s_o) + R_{44}^{-s_o} \sigma(-\omega s_o) \right),$$

and

$$\lim_{x \to +\infty} j\omega\bar{\phi}(x) = j\omega\phi^{+} e^{-j\omega s_o x},$$

(C.3)

where:

$$j\omega\phi^{+} = -j2\omega\pi \left(R_{41}^{+s_o} T_5(\omega s_o) + R_{42}^{+s_o} T_4(\omega s_o) + R_{43}^{+s_o} T_3(\omega s_o) + R_{44}^{+s_o} \sigma(\omega s_o) \right),$$

and the residues are defined as:

$$R_{mn}^{\pm s_o} = \lim_{s_x \to \pm s_o} \left\{ G_{mn}(s_x)(s_x \mp s_o) \right\}.$$

Note that in the cases where incident SAW modes are used as excitation sources, and therefore used to generate the values of the basis function weights, the total far-fields are the sum of the incident fields and the SAW far-fields generated by the basis weights ((C.2) and (C.3)). It should be noted that this far-field analysis method presented here also permits extraction of P-matrix-type model parameters for the structure, which rely on the magnitude and phase parameters of scattered / transmitted / and excited SAW in the far-field.

Given $j\omega\phi^{-}$ and $j\omega\phi^{+}$ at the surface in the far-field, the *x*-directed Poynting vectors as a function of depth into the substrate will now be determined and integrated analytically to obtain the total power crossing the boundary. The first step is to determine the normal mode weights for the valid partial modes, **c**, from (2.19), which results in:

$$\mathbf{c}^\pm = \begin{bmatrix} c_1^\pm & c_2^\pm & c_3^\pm & c_4^\pm \end{bmatrix}^\mathrm{T} = \mathbf{C}^\pm j\omega\phi^\pm, \tag{C.4}$$

where:

$$\mathbf{C}^\pm = \begin{bmatrix} C_1^\pm & C_2^\pm & C_3^\pm & C_4^\pm \end{bmatrix}^\mathrm{T} = \left[\mathbf{P}^\pm([1,2,3,8],:) \right]^{-1} \begin{bmatrix} 0 & 0 & 0 & 1 \end{bmatrix}^\mathrm{T},$$

and

$$\mathbf{P}^\pm = \mathbf{P}_{8x4} \text{ evaluated at } \pm s_o.$$

Note that the "$\pm$" notation is used to represent whether considering the $\pm x$ far-fields, respectively. Using (C.4) with (2.10) results in:

$$\overline{\boldsymbol{\tau}}^\pm (z \le 0) = \mathbf{P}^\pm \mathbf{C}^\pm(z) j\omega\phi^\pm e^{\mp jk_o x}, \tag{C.5}$$

where:

$$\mathbf{C}^\pm(z) = \begin{bmatrix} e^{j\omega\lambda_1^\pm z} C_1^\pm & e^{j\omega\lambda_2^\pm z} C_2^\pm & e^{j\omega\lambda_3^\pm z} C_3^\pm & e^{j\omega\lambda_4^\pm z} C_4^\pm \end{bmatrix}^\mathrm{T}.$$

and $\lambda_n^\pm$ is the nth valid partial mode eigenvalue corresponding to the nth partial mode weight obtained at $s_x \pm s_o$.

Given (A.18), fields $\boldsymbol{\tau}_{Px}(z)$ or $(T_1(z), T_6(z), T_5(z), \text{ and } D_1(z), \text{ respectively})$ are given as:

$$\overline{\boldsymbol{\tau}}_{Px}^\pm (z \le 0) = \mathbf{T}_{Px}^\pm \mathbf{P}^\pm \mathbf{C}^\pm(z) j\omega\phi^\pm e^{\mp jk_o x}, \tag{C.6}$$

where:

$$\mathbf{T}_{Px}^\pm = \left(\mathbf{T}_{Px} = \begin{bmatrix} \boldsymbol{\Gamma}^{23}\mathbf{X} & \left(s_x \left(\boldsymbol{\Gamma}^{23}\mathbf{X}\boldsymbol{\Gamma}^{31} - \boldsymbol{\Gamma}^{21} \right) + s_y \left(\boldsymbol{\Gamma}^{23}\mathbf{X}\boldsymbol{\Gamma}^{32} - \boldsymbol{\Gamma}^{22} \right) \right) \end{bmatrix} \text{ at } s_x = \pm s_o, s_y = 0 \right).$$

Given (C.5), (C.6) and (2.12) the $\pm$x-directed time average Poynting vector is given as:

$$\overline{S}_{\pm x}(z \le 0) = \mp \frac{1}{2} \left| j\omega\phi^\pm \right|^2 \Re \left\{ \left[\mathbf{C}^\pm(z) \right]^\mathrm{H} \mathbf{K}^\pm \mathbf{C}^\pm(z) \right\}, \tag{C.7}$$

where:

$$\mathbf{K}^\pm = \left[\mathbf{P}_{low}^\pm \right]^\mathrm{H} \mathbf{T}_{Px}^\pm \mathbf{P}^\pm,$$

and $\mathbf{P}_{low}^\pm = \mathbf{P}^\pm([5,6,7,8],:)$ (Matlab index notation).

Using an alternative summation notation, (C.7) is may be given as:

$$\overline{S}_{\pm x}(z \leq 0) = \mp \frac{1}{2} \left| j\omega\phi^{\pm} \right|^2 \sum_{i=m}^{4}\sum_{j=n}^{4} \Re\left\{ C_m^{\pm}(z)^* C_n^{\pm}(z) K_{mn}^{\pm} \right\},$$
(C.8)

Integrating (C.8) from $z = -h$, to the surface, $z = 0$, results in:

$$\int_{-h}^{0} \overline{S}_{\pm x}(z)dz = \mp \frac{1}{2}\frac{1}{\omega} \left| j\omega\phi^{\pm} \right|^2 \sum_{m=1}^{4}\sum_{n=1}^{4} \Im\left\{ C_m^{\pm *} C_n^{\pm} K_{mj}^{\pm} \frac{\left(1 - e^{j\omega\left(\lambda_n^{\pm} - \lambda_m^{\pm *} \right)h} \right)}{\left(\lambda_n^{\pm} - \lambda_m^{\pm *} \right)} \right\}.$$
(C.9)

Give that all valid partial modes must decay with depth in the case of a true SAW mode, the total integrated time average Poynting vector in the substrate is given as:

$$\int_{-\infty}^{0} \overline{S}_{\pm x}(z)dz = \mp \frac{1}{2}\frac{1}{\omega} \left| j\omega\phi^{\pm} \right|^2 \sum_{m=1}^{4}\sum_{n=1}^{4} \Im\left\{ \frac{C_m^{\pm *} C_n^{\pm} K_{mn}^{\pm}}{\left(\lambda_n^{\pm} - \lambda_m^{\pm *} \right)} \right\}.$$
(C.10)

Note that the summation terms are independent of frequency. As the fields are assumed to be uniform and along the device aperture, W, the total structure input power converted SAW power crossing the $\pm x$-directed sides of the box in the substrate is:

$$P_{SAW}^{\pm Substrate} = \mp \frac{1}{2}\frac{W}{\omega} \left| j\omega\phi^{\pm} \right|^2 \sum_{m=1}^{4}\sum_{n=1}^{4} \Im\left\{ \frac{C_m^{\pm *} C_n^{\pm} K_{mn}^{\pm}}{\left(\lambda_n^{\pm} - \lambda_m^{\pm *} \right)} \right\}.$$
(C.11)

We now turn our attention to the fields along the $\pm x$-directed sides of the box above the substrate, or in the vacuum. Given the analysis of Chapter 2 Section 2.4 regarding the valid partial mode for the vacuum, it can be shown that the time-derivative of the electric potential above the interface can be given as:

$$\overline{j\omega\phi}^{\pm}(z \geq 0) = j\omega\phi^{\pm}e^{-\omega|s_o|z}e^{\mp jk_o x} . \tag{C.12}$$

Using (2.4) and (C.12) D_1 may be expressed as:

$$\overline{D}_1^{\pm}(z \geq 0) = \pm\varepsilon_o|s_o|\,j\omega\phi^{\pm}e^{-\omega|s_o|z}e^{\mp jk_o x} . \tag{C.13}$$

Therefore from (2.12) the $\pm x$-directed time average Poynting vector in the vacuum is:

$$\overline{S}_{\pm x}(z \geq 0) = \mp\frac{1}{2}\varepsilon_o|s_o|\left|j\omega\phi^{\pm}\right|^2 e^{-2\omega|s_o|z} . \tag{C.14}$$

A very interesting observation from (C.14) is that the positive Poynting vector direction is opposite to that for which one might expect (i.e. it is opposite to the propagation direction). The author was unable to find an error in the derivation after much iteration. It is now believed that this non-intuitive result may have developed from use of the quasi-static approximation. Assuming this result is correct, the total structure input power converted SAW power crossing the $\pm x$-directed sides of the box in the vacuum is:

$$P_{SAW}^{\pm Vacuum} = W\int_0^{\infty}\overline{S}_{\pm x}(z)dz = \mp\frac{1}{2}\frac{W}{\omega}\frac{\varepsilon_o}{2}\left|j\omega\phi^{\pm}\right|^2 . \tag{C.15}$$

Combining (C.14) and (C.15) the total structure input power converted SAW power crossing the $\pm x$-directed sides of the box is:

$$P_{SAW}^{\pm} = \mp\frac{1}{2}\frac{W}{\omega}\left|j\omega\phi^{\pm}\right|^2\left(\frac{\varepsilon_o}{2} + \sum_{m=1}^{4}\sum_{n=1}^{4}\,\Im\left\{\frac{C_m^{\pm *}C_n^{\pm}K_{mn}^{\pm}}{\left(\lambda_n^{\pm} - \lambda_m^{\pm *}\right)}\right\}\right) . \tag{C.16}$$

Attention is now focused on the analysis of the far-field BAW generated by the structure via direct electrical excitation or incident modes. The analysis begins by

defining the total BAW power as the integral of the $-z$-directed Poynting vector on the side of box with outward normal facing in the $-z$-direction, and by (2.12) is given as:

$$P_{BAW}(z) = W \int_{-\infty}^{\infty} \overline{S}_z(z) dx, \tag{C.17}$$

where:

$$\overline{S}_z(z) = -\frac{1}{2} \Re\left\{ \begin{bmatrix} \overline{T}_5(z) & \overline{T}_4(z) & \overline{T}_3(z) & \overline{D}_3(z) \end{bmatrix} \begin{bmatrix} \overline{j\omega u}_1(z) & \overline{j\omega u}_2(z) & \overline{j\omega u}_3(z) & \overline{j\omega\phi}(z) \end{bmatrix}^H \right\}.$$

Applying (2.15) to each term in the integrand of (C.17), interchanging the order of integrations, and then simplifying allows the total BAW power to be express as:

$$P_{BAW}(z) = W \int_{-\infty}^{\infty} S_z(z) dk_x, \tag{C.18}$$

where spectral domain Poynting vector is given as

$$S_z(z) = -\pi \Re\left\{ \begin{bmatrix} T_5(z) & T_4(z) & T_3(z) & D_3(z) \end{bmatrix} \begin{bmatrix} j\omega u_1(z) & j\omega u_2(z) & j\omega u_3(z) & j\omega\phi(z) \end{bmatrix}^H \right\}. \tag{C.19}$$

Given (2.10) and (2.19) permits (C.19) to be written as:

$$S_z(z) = -\pi \Re\left\{ \mathbf{C}^H(z) \mathbf{K} \, \mathbf{C}(z) \right\}_{s_x = \frac{k_x}{\omega}}, \tag{C.20}$$

where:

$$\mathbf{C}(z) = \begin{bmatrix} e^{j\omega \tilde{k}_1 z} c_1 & e^{j\omega \tilde{k}_2 z} c_2 & e^{j\omega \tilde{k}_3 z} c_3 & e^{j\omega \tilde{k}_4 z} c_4 \end{bmatrix}^T,$$

$$\mathbf{K} = \mathbf{P}_{low}^H \mathbf{P}_{up},$$

and

$$\mathbf{P}_{up} = \mathbf{P}_{8x4}([1,2,3,4],:) \text{ and } \mathbf{P}_{low} = \mathbf{P}_{8x4}([5,6,7,8],:) \text{ (Matlab index notation)}.$$

The normal mode weights, c_i, are determined at each value of k_x by applying (2.33) to the determined basis function weights and using of (2.20) and (2.21); resulting in:

$$\begin{bmatrix} c_1 & c_2 & c_3 & c_4 \end{bmatrix}^T = \mathbf{M}_{up}^{-1} \begin{bmatrix} T_5 & T_4 & T_3 & \sigma \end{bmatrix}^T_{z=0, s_x = \frac{k_x}{\omega}}. \tag{C.21}$$

Using an alternative summation notation, (C.20) is also given by:

$$S_z(z) = -\pi \sum_{m=1}^{4} \sum_{m=1}^{4} \Re \left\{ K_{mn} \, c_m^* c_n e^{j\omega(\lambda_n - \lambda_m^*)z} \right\}.$$

(C.22)

For any term in the sum with n or m corresponding to a decaying partial mode, the corresponding term in the summation goes to zero as R goes to infinity. Alternatively, when n and m correspond to BAW type partial modes, where the λ are purely real, the fields are finite. When $n \neq m$ and n and m correspond to BAW type partial modes with different values of λ, the overall value of (C.22) will oscillate w.r.t. z, as the BAW-type partial modes beat. In order to deal with this situation, the time average power crossing the plane is defined in a different way. In particular, given the fact that (C.17) approaches a constant, or a constant plus an oscillating beating term as z goes to -infinity, we can redefine the total time average power as:

$$P_{BAW} = W \lim_{R \to \infty} \left\{ \frac{1}{R} \int_{-2R}^{-R} \int_{-\infty}^{\infty} \overline{S}_z(z) dx dz \right\},$$

(C.23)

which simply averages the total Power crossing planes as a function of distance (note that the distance averaged also approaches infinity as R goes to infinity). Using this new definition of total time average power, (C.18) becomes:

$$P_{BAW} = W \int_{-\infty}^{\infty} \lim_{R \to \infty} \left\{ \frac{1}{R} \int_{-2R}^{-R} S_z(z) dz \right\} dk_x.$$

(C.24)

Substituting (C.22) into (C.24) and interchanging the order of the limiting integral with the summations terms and $\Re$ operator results in:

$$P_{BAW} = W \int\limits_{-\infty}^{\infty} S_z' dk_x \ , \tag{C.25}$$

where:

$$S_z' = -\pi \sum_{m=1}^{4} \sum_{m=1}^{4} \Re\left\{ K_{mn} \, c_m^* c_n \lim_{R \to \infty} \left\{ \frac{1}{R} \int\limits_{-2R}^{-R} e^{j\omega(\lambda_n - \lambda_m^*)z} dz \right\} \right\} . \tag{C.26}$$

Performing the integration and taking the limit results in:

$$\lim_{R \to \infty} \left\{ \frac{1}{R} \int\limits_{-2R}^{-R} e^{j\omega(\lambda_n - \lambda_m^*)z} dz \right\} \tag{C.27}$$

$= 0$; if n or m correspond to a decaying partial modes,

$= 0$; if n and m correspond to BAW-type partial modes with unequal λ,

$= 1$; if n and m correspond to BAW-type partial modes with equal λ.

Furthermore, in potential cases where n and m correspond to separate BAW-type partial modes ($n \neq m$), but have equal purely real λ, then the two partial modes must be uncoupled (e.g. transverse shear modes), and therefore K_{mn} must equal zero. Therefore (C.26) is alternatively given by:

$$S_z' = -\pi \sum_{n=1}^{4} |c_n|^2 \Re\{K_{nn}\}(\Im\{\lambda_n\} == 0). \tag{C.28}$$

(note the use of a Boolean term in the summation; 'true'$\to$1 and 'false'$\to$ 0)

Given that all partial modes will decay with depth for all $|k_x| > k_c$, where $k_c = \omega \max\{s_c^p\}$ and s_c^p ($p = 1$ to N_c) is the set of sorted values of s_x where partial mode transitions from a decaying type partial mode to BAW-type partial mode, or vice versa, (C.25) becomes equivalent to:

$$P_{BAW} = W \int_{-k_c}^{k_c} S_z'(k_x) dk_x \quad .$$

(C.29)

This integral is approximated numerically in this work for the computation of total BAW power.

The calculation of far-field BAW radiation pattern is now presented. Examination of (C.28) and (C.29) indicate that the product of W and S_z' represents a sum of partial mode power spectral density distributions w.r.t. k_x; given as:

$$\frac{\partial P_{BAW}^n}{\partial k_x} = -\pi W |c_n|^2 \Re\{K_{nn}\}(\Im\{\lambda_n\} == 0) \quad ,$$

(C.30)

where:

$$P_{BAW} = \sum_{n=1}^{4} \int_{-k_c}^{k_c} \frac{\partial P_{BAW}^n}{\partial k_x} dk_x \ .$$

Using the chain-rule the power spectral density distributions w.r.t. the partial mode power flow angle, $\theta^n - \tan^{-1}\left(\frac{S_z^n}{S_x^n}\right)$, where S_z^n and S_x^n are the z- and x-directed Poynting vectors associated with the nth partial mode, respectively, are given as:

$$\frac{\partial P_{BAW}^n}{\partial \theta^n} = \frac{\partial P_{BAW}^n}{\partial k_x} \frac{\partial k_x}{\partial \theta^n} = \omega \frac{\partial P_{BAW}^n}{\partial k_x} \left[\frac{\partial \theta^n(s_x)}{\partial s_x} \right]_{s_x = \frac{k_x}{\omega}}^{-1},$$

(C.31)

where:

$$P_{BAW} = \sum_{n=1}^{4} \int_{-\pi}^{0} \frac{\partial P_{BAW}^n}{\partial \theta^n} d\theta_x \ .$$

The power flow angle derivative term in (C.31) associated with each partial mode can be is computed using the following formulas, where the $'$ symbol denotes differentiation w.r.t. s_x:

$$\left(\theta^n\right)' = \frac{S_x^n\left(S_z^n\right)' - S_z^n\left(S_x^n\right)'}{\left(S_x^n\right)^2 + \left(S_z^n\right)^2},$$

(C.32)

where:

$$S_x^n = -\frac{1}{2}\left|c_n\right|^2 \left[\mathbf{P}_{low}^n\right]^{\mathrm{H}} \mathbf{T}_{Px} \mathbf{P}^n,$$

$$\left(S_x^n\right)' = -\frac{1}{2}\left|c_n\right|^2 \left(\left[\mathbf{P}_{low}^n\right]^{\mathrm{H}} \mathbf{T}_{Px}\left(\mathbf{P}^n\right)' + \left[\mathbf{P}_{low}^n\right]^{\mathrm{H}}\left(\mathbf{T}_{Px}\right)' \mathbf{P}^n + \left[\left(\mathbf{P}_{low}^n\right)'\right]^{\mathrm{H}} \mathbf{T}_{Px} \mathbf{P}^n\right),$$

$$S_z^n = -\frac{1}{2}\left|c_n\right|^2 \left[\mathbf{P}_{low}^n\right]^{\mathrm{H}} \mathbf{P}_{up}^n,$$

$$\left(S_z^n\right)' = -\frac{1}{2}\left|c_n\right|^2 \left(\left[\mathbf{P}_{low}^n\right]^{\mathrm{H}}\left(\mathbf{P}_{up}^n\right)' + \left[\left(\mathbf{P}_{low}^n\right)'\right]^{\mathrm{H}} \mathbf{P}_{up}^n\right),$$

$$\mathbf{T}_{Px} = \left[\mathbf{\Gamma}^{23}\mathbf{X} \quad s_x\left(\mathbf{\Gamma}^{23}\mathbf{X}\mathbf{\Gamma}^{31} - \mathbf{\Gamma}^{21}\right)\right],$$

$$\left(\mathbf{T}_{Px}\right)' = \left[\mathbf{0}_{4x4} \quad \left(\mathbf{\Gamma}^{23}\mathbf{X}\mathbf{\Gamma}^{31} - \mathbf{\Gamma}^{21}\right)\right],$$

$\mathbf{P}^n$ is the eigen-vector of $\mathbf{A}(s_x)$ associated with nth partial mode,

$\left(\mathbf{P}^n\right)'$ is computed based on Chapter 2 Section 2.3,

$\mathbf{P}_{low}^n = \mathbf{P}^n$ ([5,6,7,8],1) (Matlab index notation),

$\mathbf{P}_{up}^n = \mathbf{P}^n$ ([1,2,3,4],1) (Matlab index notation),

(note that $-\frac{1}{2}\left|c_n\right|^2$ factors need not be included as they cancel in the (C.32)).

The term $\dfrac{\partial P_{BAW}^n}{\partial \theta^n}$ may be directly computed as a function of k_x, given (C.31), but computation of radiation patterns requires evaluation of this term as a function of θ.

Therefore, the mapping, $k_x^n(\theta) = \omega\, s_x^n(\theta)$, needs to be established, which returns the nth partial mode x-directed wavenumber as a function of power flow angle. In general, $s_x^n(\theta)$ can be a multivalued-function, as a partial mode may have the same θ at multiple values of s_x. Additionally, in practice, the numerically returned eigen-value/-vectors of $\mathrm{A}(s_x)$ are not guaranteed to follow any particular order w.r.t. s_x. Therefore, $\dfrac{\partial P_{BAW}^n}{\partial \theta^n}$ at any two consecutive k_x points are not guaranteed to both be associated with n^{th} partial mode. It therefore becomes apparent that for the calculation of far-field radiation patterns, partial mode numerical tracking as a function of $s_x = \dfrac{k_x}{\omega}$ is required. The word 'tracking' is meant to imply that the numerically computed eigen-values/–vectors of $\mathbf{A}(s_x)$ are sorted such that the partial modes corresponding to a particular index are analytically continued w.r.t. s_x over at least regions between consecutive BAW cutoff slowness points, s_c^p, where $p = 1$ to N_c, and N_c is the total number of unique BAW cutoff slowness points. In this work the continuation process is performed via stepping s_x in small increments and comparing the set of eigen-values/–vectors to a predicted set, which is based on information at the previously evaluated point. In particular, at each evaluation point the eigen-values/–vectors at the next point are approximated using a truncated Taylor series, with coefficients determined using the method presented in Chapter 2 Section 2.3 regarding computation of eigen-value/–vector derivatives. All permutations at the next evaluation point, in terms of the eigen-value/-vector order, are compared to the predicted set. The permutation that gives the least error (sum of absolute normalized difference of

each eigen-values/–vectors) is considered to be the properly constructed analytically continued eigen-value/-vector set.

Given the ability to track partial modes, extraction of the functional behavior of $s_x^n(\theta)$ will now be discussed. Recall that in general $s_x^n(\theta)$ can be a multivalued function over the range $s_c^p \leq s_x \leq s_c^{p+1}$, therefore in this work consecutive regions of the s_x axis are further discretized such $s_x^n(\theta)$ is single valued over any particular s_x region. This is accomplished via identification of unique points $s_x = s_d^m$ where $\dfrac{\partial \theta^n(s_x)}{\partial s_x} = 0$ $(n = 1$ to $4)$, $m = 1$ to N_d, and N_d is the total number of unique points identified. The consecutive $(N_q$ - $1)$ regions of s_x are given as $s_x^q \leq s_x \leq s_x^{q+1}$, $q = 1$ to $(N_q - 1)$, where s_x^q is the qth element of the sorted unique set of containing the points s_c^p and s_d^m, whose length is equal to N_q. Therefore over any of the defined regions of s_x, the function $s_x^n(\theta)$ is continuous and single valued. In this work, for each s_x range, $s_x^n(\theta)$ is interpolated at discrete θ by spline fitting to the inverse set of discrete point pairs obtained via evaluation of $\theta^n(s_x)$. Given (C.31), (C.32), and the extraction of $s_x^n(\theta)$, the BAW power spectral density w.r.t. θ for the nth partial mode over the qth region, $\omega\, s_x^q \leq k_x \leq \omega\, s_x^{q+1}$, is computed using:

$$\frac{\partial P_{BAW}^{nq}}{\partial \theta^n}(\theta) = \begin{cases} \left(\omega \frac{\partial P_{BAW}^n}{\partial k_x} \left[\frac{\partial \theta^n(s_x)}{\partial s_x} \right]^{-1}_{s_x = \frac{k_x}{\omega}} \right) & \theta \in \theta^n\left(s_x^q \le s_x \le s_x^{q+1} \right) \\ 0 & \theta \notin \theta^n\left(s_x^q \le s_x \le s_x^{q+1} \right) \end{cases}, \qquad \text{(C.33)}$$

evaluated at $k_x = \omega \, s_x^{nq}(\theta),$

where:

$s_x^{nq}(\theta)$ is the interpolated function, $s_x^n(\theta)$, over the range $s_x^q \le s_x \le s_x^{q+1}$.

Therefore the total BAW power spectral density w.r.t. θ is given by:

$$\frac{\partial P_{BAW}}{\partial \theta}(\theta) = \sum_{n=1}^{4} \sum_{q=1}^{N_q - 1} \frac{\partial P_{BAW}^{nq}}{\partial \theta^n}(\theta), \qquad \text{(C.34)}$$

where:

$$P_{BAW} = \int_{-\pi}^{0} \frac{\partial P_{BAW}}{\partial \theta}(\theta) \, d\theta.$$

This concludes Appendix C.

APPENDIX D

FEM ANALYSIS OF FINITE-THICKNESS ELECTRODES AND FEM/BEM MODEL COUPLING

The purpose of Appendix D is to describe the finite element method model implemented in this work, which was used to account for the mass/stiffness effects of finite thickness electrodes in the overall simulation model. Initially, the finite element method model of the electrode is presented, which allows node displacement to be computed as a function of node forces. Afterwards, a discussion is presented regarding merging the FEM analysis of the electrode with the BEM analysis of the substrate.

The analysis begins by defining the surface-normal stress component vectors for the infinitesimal elastic cube; see Figure D.1.
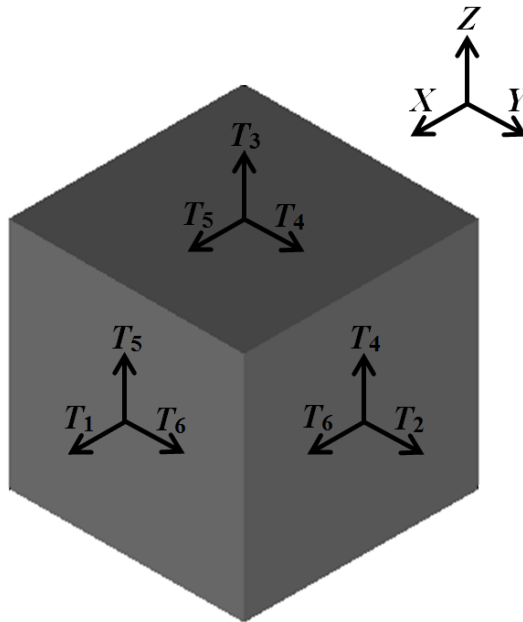

Figure D.1. Surface-normal stress component vectors for the infinitesimal elastic cube.

Based on the definitions of stress components in Figure D.1, the familiar acoustic wave equation, given as (D.1), can be derived by balancing forces and taking the limit as the dimensions become infinitely small.

$$\nabla \cdot \tilde{\mathbf{T}}_i = \rho \frac{\partial^2 u_i}{\partial t^2} \quad (i = 1, 2, \text{ or } 3),$$ (D.1)

where:

$$\tilde{\mathbf{T}}_i = T_{i1}\hat{x} + T_{i2}\hat{y} + T_{i3}\hat{z} .$$

and the stress components follow Voigt notation:

$11 \rightarrow 1, 22 \rightarrow 2, 33 \rightarrow 3, 12 \rightarrow 6, 21 \rightarrow 6, 13 \rightarrow 5, 31 \rightarrow 5, 23 \rightarrow 4, 32 \rightarrow 4.$

If one discretizes the body of interest, here a single electrode, into small elements, then over the volume of each element (D.1) is also valid. Multiplying both sides of (D.1) by a test function, $w_n(x, y, z)$, and then integrating over the element volume result in:

$$\int_V w_n \nabla \cdot \tilde{\mathbf{T}}_i \, dV = \rho \int_V w_n \frac{\partial^2 u_i}{\partial t^2} \, dV .$$ (D.2)

Substituting the vector calculus identity, $w_n \nabla \cdot \tilde{\mathbf{T}}_i = \nabla \cdot \left(w_n \tilde{\mathbf{T}}_i \right) - \nabla w_n \cdot \tilde{\mathbf{T}}_i$, into the integrand of the l.h.s of (D.2) gives:

$$\int_V \nabla \cdot \left(w_n \tilde{\mathbf{T}}_i \right) dV - \int_V \nabla w_n \cdot \tilde{\mathbf{T}}_i \, dV = \rho \int_V w_n \frac{\partial^2 u_i}{\partial t^2} \, dV .$$ (D.3)

Applying the Divergence theorem to first term of the l.h.s. of (D.3) and rearranging terms results in:

$$\int_V \nabla w_n \cdot \tilde{\mathbf{T}}_i \, dV + \rho \int_V w_n \frac{\partial^2 u_i}{\partial t^2} \, dV = \oint_S \left(w_n \tilde{\mathbf{T}}_i \right) \cdot d\,\mathbf{S}, \tag{D.4}$$

where:

$\mathbf{S}$ is the outward normal vector along the surface of the element.

Assuming a non-piezoelectric body, combining (D.4) for $i = 1$ to 3, assuming $e^{j\omega t}$ time variation, and including (2.1) and (2.2) results in:

$$\int_V
\begin{bmatrix}
\dfrac{\partial w_n}{\partial x} & 0 & 0 & 0 & \dfrac{\partial w_n}{\partial z} & \dfrac{\partial w_n}{\partial y} \\[2mm]
0 & \dfrac{\partial w_n}{\partial y} & 0 & \dfrac{\partial w_n}{\partial z} & 0 & \dfrac{\partial w_n}{\partial x} \\[2mm]
0 & 0 & \dfrac{\partial w_n}{\partial z} & \dfrac{\partial w_n}{\partial y} & \dfrac{\partial w_n}{\partial x} & 0
\end{bmatrix}
\mathbf{c}^E
\begin{bmatrix}
\dfrac{\partial}{\partial x} & 0 & 0 \\[2mm]
0 & \dfrac{\partial}{\partial y} & 0 \\[2mm]
0 & 0 & \dfrac{\partial}{\partial z} \\[2mm]
0 & \dfrac{\partial}{\partial z} & \dfrac{\partial}{\partial y} \\[2mm]
\dfrac{\partial}{\partial z} & 0 & \dfrac{\partial}{\partial x} \\[2mm]
\dfrac{\partial}{\partial y} & \dfrac{\partial}{\partial x} & 0
\end{bmatrix}
\mathbf{u}^e \, dV \tag{D.5}$$

$$- \rho \omega^2 \int_V w_n \mathbf{u}^e \, dV = \oint_S w_n
\begin{bmatrix}
\tilde{\mathbf{T}}_1 \\
\tilde{\mathbf{T}}_2 \\
\tilde{\mathbf{T}}_3
\end{bmatrix}
\cdot d\,\mathbf{S}\,.$$

where:

$$\mathbf{u}^e = \left[u_1(x, y, z) \quad u_2(x, y, z) \quad u_3(x, y, z) \right]^{\mathrm{T}}.$$

(over the domain of the element)

Within the element the displacement components are approximated using the displacement components at a finite number of M points within the element by M shape functions such that:

$$u_p(x, y, z) \approx \sum_{m=1}^{M} N_m(x, y, z) u_p^m \, , \tag{D.6}$$

where:

$p = 1, 2, \text{ or } 3,$

N_m are the shape functions,

and u_p^m is the pth displacement at the mth point.

Expressing (D.6) in matrix notation gives:

$$\mathbf{u}^e = \mathbf{N} \, \tilde{\mathbf{u}}^e \, , \tag{D.7}$$

where:

$$\tilde{\mathbf{u}}^e = \begin{bmatrix} u_1^1 & u_2^1 & u_3^1 & u_1^2 & u_2^2 & u_3^2 & \cdots & u_1^M & u_2^M & u_3^M \end{bmatrix}^{\text{T}} \, ,$$

$$\mathbf{N} = \begin{bmatrix} N_1 & 0 & 0 & N_2 & 0 & 0 & \cdots & N_M & 0 & 0 \\ 0 & N_1 & 0 & 0 & N_2 & 0 & \cdots & 0 & N_M & 0 \\ 0 & 0 & N_1 & 0 & 0 & N_2 & \cdots & 0 & 0 & N_M \end{bmatrix} \, .$$

Inserting (D.7) into (D.5) results in:

$$
\left(\int_V \begin{bmatrix} \dfrac{\partial w_n}{\partial x} & 0 & 0 & 0 & \dfrac{\partial w_n}{\partial z} & \dfrac{\partial w_n}{\partial y} \\[2ex] 0 & \dfrac{\partial w_n}{\partial y} & 0 & \dfrac{\partial w_n}{\partial z} & 0 & \dfrac{\partial w_n}{\partial x} \\[2ex] 0 & 0 & \dfrac{\partial w_n}{\partial z} & \dfrac{\partial w_n}{\partial y} & \dfrac{\partial w_n}{\partial x} & 0 \end{bmatrix} \mathbf{c}^E \, \mathbf{B} \; dV \right) \tilde{\mathbf{u}}^e
$$

(D.8)

$$
- \rho \omega^2 \left(\int_V w_n \mathbf{N} \; dV \right) \tilde{\mathbf{u}}^e = \oint_S w_n \begin{bmatrix} \tilde{\mathbf{T}}_1 \\ \tilde{\mathbf{T}}_2 \\ \tilde{\mathbf{T}}_3 \end{bmatrix} \cdot d\,\mathbf{S} .
$$

where:

$$
\mathbf{B} = \begin{bmatrix} \mathbf{B}_1 & \mathbf{B}_2 & \cdots & \mathbf{B}_M \end{bmatrix},
$$

and

$$
\mathbf{B}_m = \begin{bmatrix} \dfrac{\partial N_m}{\partial x} & 0 & 0 \\[2ex] 0 & \dfrac{\partial N_m}{\partial y} & 0 \\[2ex] 0 & 0 & \dfrac{\partial N_m}{\partial z} \\[2ex] 0 & \dfrac{\partial N_m}{\partial z} & \dfrac{\partial N_m}{\partial y} \\[2ex] \dfrac{\partial N_m}{\partial z} & 0 & \dfrac{\partial N_m}{\partial x} \\[2ex] \dfrac{\partial N_m}{\partial y} & \dfrac{\partial N_m}{\partial x} & 0 \end{bmatrix} .
$$

Using the M shape functions as the test functions in (D.8) (Galerkin method) results in a square matrix system, given as:

$$
\left(\int_V \mathbf{B}^{\mathrm{T}} \mathbf{c}^E \, \mathbf{B} \; dV \right) \tilde{\mathbf{u}}^e - \rho \omega^2 \left(\int_V \mathbf{N}^{\mathrm{T}} \mathbf{N} \, dV \right) \tilde{\mathbf{u}}^e = \oint_S \mathbf{N}^{\mathrm{T}} \begin{bmatrix} \tilde{\mathbf{T}}_1 \\ \tilde{\mathbf{T}}_2 \\ \tilde{\mathbf{T}}_3 \end{bmatrix} \cdot d\,\mathbf{S} .
$$

(D.9)

Evaluation of the integrals in (D.9) is now presented, which begins by defining the shape functions. The shape and nodes of an arbitrary element in the (x, y, z) coordinate system is shown in the l.h.s of Figure D.2.
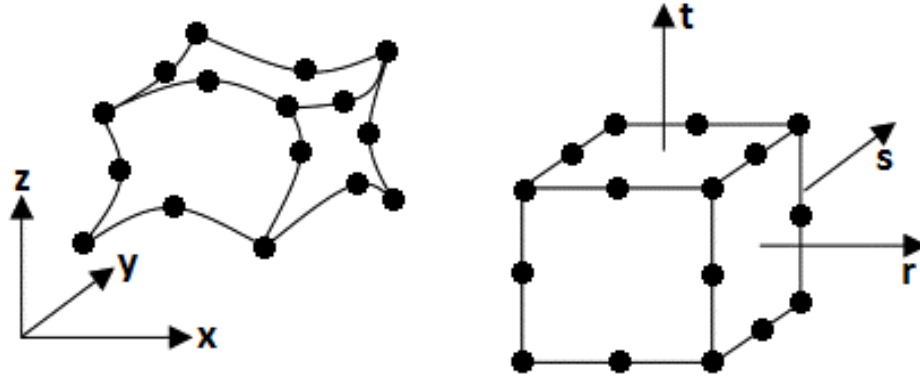

Figure D.2. Element in (x, y, z) space mapped to isoparametric element in (r, s, t) space.

The right-hand side of Figure D.2 shows the equivalent isoparametric element in another coordinate system, (r, s, t). The mapping of one point in the (r, s, t) coordinate system to the (x, y, z) coordinate system is given by (D.10), (D.11), and (D.12).

$$x = \sum_{m=1}^{M} x_m N_m(r, s, t) \tag{D.10}$$

$$y = \sum_{m=1}^{M} y_m N_m(r, s, t) \tag{D.11}$$

$$z = \sum_{m=1}^{M} z_m N_m(r, s, t) \tag{D.12}$$

The (x, y, z) coordinate system shape functions are now defined in terms of the (r, s, t) coordinate system shape functions, such that:

$$N_m(x, y, z) \equiv N_m(r(x, y, z), s(x, y, z), t(x, y, z)). \tag{D.13}$$

Clearly, evaluation of the integrals in (D.9) is easier in (r, s, t) coordinate system as compared to the (x, y, z) coordinate system, because the element shape is much simpler, and the fact the shape functions are typically defined in the (r, s, t) coordinate system. In order to switch the integration domains however, mapping of the dV term to the equivalent term, $drdsdt$, term must be determined. The mapping is accomplished using the concept of the Jacobian, $\mathbf{J}$, defined as:

$$\begin{bmatrix} dx \\ dy \\ dz \end{bmatrix} = \mathbf{J} \begin{bmatrix} dr \\ ds \\ dt \end{bmatrix},$$

(D.14)

where:

$$\mathbf{J} = \begin{bmatrix} \dfrac{\partial x}{\partial r} & \dfrac{\partial x}{\partial s} & \dfrac{\partial x}{\partial t} \\ \dfrac{\partial y}{\partial r} & \dfrac{\partial y}{\partial s} & \dfrac{\partial y}{\partial t} \\ \dfrac{\partial z}{\partial r} & \dfrac{\partial z}{\partial s} & \dfrac{\partial z}{\partial t} \end{bmatrix},$$

and

$$\mathbf{J}^{-1} = \begin{bmatrix} \dfrac{\partial r}{\partial x} & \dfrac{\partial r}{\partial y} & \dfrac{\partial r}{\partial z} \\ \dfrac{\partial s}{\partial x} & \dfrac{\partial s}{\partial y} & \dfrac{\partial s}{\partial z} \\ \dfrac{\partial t}{\partial x} & \dfrac{\partial t}{\partial y} & \dfrac{\partial t}{\partial z} \end{bmatrix}.$$

Given that an infinitesimal cube in (r, s, t) maps to parallelepiped in (x, y, z), the well know expression relating differential volumes may be derived, and given as:

$$dV = \left| \det\{\mathbf{J}\} \right| dr\, ds\, dt .$$

(D.15)

Given (D.10), (D.11), and (D.12) the elements of the Jacobian are:

$$J_{11} = \frac{\partial x}{\partial r} = \sum_{m=1}^{M} x_m \frac{N_m(r,s,t)}{\partial r}, \tag{D.16}$$

$$J_{12} = \frac{\partial x}{\partial s} = \sum_{m=1}^{M} x_m \frac{N_m(r,s,t)}{\partial s}, \tag{D.17}$$

$$J_{13} = \frac{\partial x}{\partial t} = \sum_{m=1}^{M} x_m \frac{N_m(r,s,t)}{\partial t}, \tag{D.18}$$

$$J_{21} = \frac{\partial y}{\partial r} = \sum_{m=1}^{M} y_m \frac{N_m(r,s,t)}{\partial r}, \tag{D.19}$$

$$J_{22} = \frac{\partial y}{\partial s} = \sum_{m=1}^{M} y_m \frac{N_m(r,s,t)}{\partial s}, \tag{D.20}$$

$$J_{23} = \frac{\partial y}{\partial t} = \sum_{m=1}^{M} y_m \frac{N_m(r,s,t)}{\partial t}, \tag{D.21}$$

$$J_{31} = \frac{\partial z}{\partial r} = \sum_{m=1}^{M} z_m \frac{N_m(r,s,t)}{\partial r}, \tag{D.22}$$

$$J_{32} = \frac{\partial z}{\partial s} = \sum_{m=1}^{M} z_m \frac{N_m(r,s,t)}{\partial s}, \tag{D.23}$$

$$J_{33} = \frac{\partial z}{\partial t} = \sum_{m=1}^{M} z_m \frac{N_m(r,s,t)}{\partial t}. \tag{D.24}$$

Regarding the terms in **B** using the chain rule, the shape function derivatives are given as:

$$\frac{\partial N_m}{\partial x} = \frac{\partial N_m}{\partial r} \frac{\partial r}{\partial x} + \frac{\partial N_m}{\partial s} \frac{\partial s}{\partial x} + \frac{\partial N_m}{\partial t} \frac{\partial t}{\partial x}, \tag{D.25}$$

$$\frac{\partial N_m}{\partial y} = \frac{\partial N_m}{\partial r} \frac{\partial r}{\partial y} + \frac{\partial N_m}{\partial s} \frac{\partial s}{\partial y} + \frac{\partial N_m}{\partial t} \frac{\partial t}{\partial y}, \tag{D.26}$$

$$\frac{\partial N_m}{\partial z} = \frac{\partial N_m}{\partial r} \frac{\partial r}{\partial z} + \frac{\partial N_m}{\partial s} \frac{\partial s}{\partial z} + \frac{\partial N_m}{\partial t} \frac{\partial t}{\partial z}. \tag{D.27}$$

Given the definition of the inverse Jacobian from (D.14) and grouping equations results in:

$$\left[\frac{\partial N_m}{\partial x} \quad \frac{\partial N_m}{\partial y} \quad \frac{\partial N_m}{\partial z}\right] = \left[\frac{\partial N_m}{\partial r} \quad \frac{\partial N_m}{\partial s} \quad \frac{\partial N_m}{\partial t}\right]\mathbf{J}^{-1}.$$

(D.28)

Transforming the integration domain for the $\mathbf{k}^e$ and $\mathbf{m}^e$ terms of (D.9) results in:

$$\mathbf{k}^e = \int_{-1}^{1}\int_{-1}^{1}\int_{-1}^{1}[\mathbf{B}(r,s,t)]^t\,\mathbf{c}^E\,\mathbf{B}(r,s,t)\big|\det\{\mathbf{J}(r,s,t)\}\big|\,ds\,dr\,dt\,,$$

(D.29)

and

$$\mathbf{m}^e = \rho\int_{-1}^{1}\int_{-1}^{1}\int_{-1}^{1}[\mathbf{N}(r,s,t)]^t\,\mathbf{N}(r,s,t)\big|\det\{\mathbf{J}(r,s,t)\}\big|\,ds\,dr\,dt$$

(D.30)

,

where:

$\mathbf{J}$ is computed using (D.16) thru (D.24),

and $\mathbf{B}(r,s,t)$ is computed using by substituting (D.28) into its definition

given in (D.8).

The integrals of (D.29) and (D.30) are computed using Gauss-Legendre quadrature [104], and are given as:

$$\mathbf{k}^e = \sum_{a=1}^{N_g}\sum_{b=1}^{N_g}\sum_{c=1}^{N_g}w_a w_b w_c [\mathbf{B}(r_a,s_b,t_c)]^t \mathbf{c}^E\, \mathbf{B}(r_a,s_b,t_c)\big|\det\{\mathbf{J}(r_a,s_b,t_c)\}\big|,$$

(D.31)

$$\mathbf{m}^e = \rho\sum_{a=1}^{N_g}\sum_{b=1}^{N_g}\sum_{c=1}^{N_g}w_a w_b w_c [\mathbf{N}(r_a,s_b,t_c)]^t\, \mathbf{N}(r_a,s_b,t_c)\big|\det\{\mathbf{J}(r_a,s_b,t_c)\}\big|.$$

(D.32)

The N_g evaluations points $r_i = s_i = t_i = x_i$ satisfy:

$$P_{N_g}(x_i) = 0,$$

(D.33)

where:

$P_n(x)$ is the nth order Legendre polynomial, and

$$P_n(x) = \frac{2n-1}{n} x P_{n-1}(x) - \frac{n-1}{n} P_{n-2}(x),$$

$$P_0(x) = 1,$$

$$P_1(x) = x,$$

and the respective weights are given as:

$$w_i = \frac{2(1-x_i^2)}{(N_g+1)^2 P_{N_g+1}(x_i) P_{N_g+1}(x_i)}.$$

(D.34)

It should be noted that this integration result is exact if integrands are polynomials of order equal to $2N_g$-1 or less, which in this work is true given that the shape function employed are polynomials, as will be discussed.

Up to this point in the analysis, we have considered the problem to be in 3 dimensions. For this dissertation work, an equivalent 2 dimensional FEM analysis was performed since in the BEM model it was assumed $\partial/\partial y$ for all fields. The 3D analysis was only presented here for completeness. Assuming a 2D problem at the start and performing the same steps results in the equivalent system of equations:

$$\mathbf{k}^e\ \tilde{\mathbf{u}}^e - \omega^2 \mathbf{m}^e\ \tilde{\mathbf{u}}^e = \mathbf{f}^e, \tag{D.35}$$

where:

$$\mathbf{k}^e = \int_{-1}^{1}\int_{-1}^{1}[\mathbf{B}(r,t)]^t\,\mathbf{c}^E\,\mathbf{B}(r,t)|\det\{\mathbf{J}(r,t)\}|\,ds\,dt = \sum_{a=1}^{N_g}\sum_{c=1}^{N_g}w_a w_c[\mathbf{B}(r_a,t_c)]^t\mathbf{c}^E\,\mathbf{B}(r_a,t_c)|\det\{\mathbf{J}(r_a,t_c)\}|,$$

$$\mathbf{m}^e = \rho\int_{-1}^{1}\int_{-1}^{1}[\mathbf{N}(r,t)]^t\,\mathbf{N}(r,t)|\det\{\mathbf{J}(r,t)\}|\,ds\,dt = \rho\sum_{a=1}^{N_g}\sum_{c=1}^{N_g}w_a w_c[\mathbf{N}(r_a,t_c)]^t\mathbf{N}(r_a,t_c)|\det\{\mathbf{J}(r_a,t_c)\}|,$$

$$\mathbf{f}^e = \oint_{\Gamma}\mathbf{N}^t\begin{bmatrix}\tilde{\mathbf{T}}_1\\\tilde{\mathbf{T}}_2\\\tilde{\mathbf{T}}_3\end{bmatrix}\cdot d\,\mathbf{\Gamma},$$

$$\mathbf{J} = \begin{bmatrix}J_{11} & J_{13}\\J_{31} & J_{33}\end{bmatrix}.$$

For the 2D case, the main difference from the 3D analysis is that the volume integrals become surface integrals, the surface integrals become contour integrals, where $\mathbf{\Gamma}$ is the outward normal vector along the contour of the element, and the Jacobian is instead 2 x 2.

The specific element shape function employed in this work will now be described. In this work 2D 8 node bi-quadratic isoparametric shape functions were used. Figure D.3 shows the representation of the element in (x, y, z) and (r, s, t) coordinate system, along with node numbering scheme.
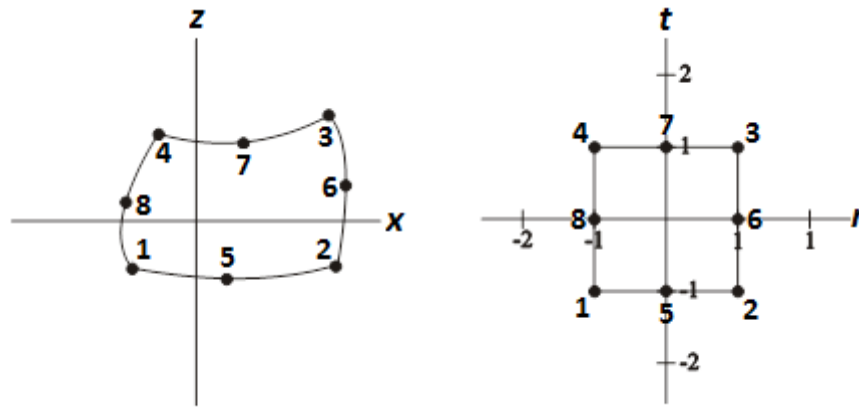
Figure D.3. Element in (x, z) space and corresponding isoparametric element in (r, t) space.

The mathematical definition of the isoparametric shape function and the respective partial derivatives are presented in Table D.1 [105].

Node	Shape Function	$\partial N_m/\partial r$	$\partial N_m/\partial t$
1	$N_1(r,t) = \frac{1}{4}(1-r)(1-t)(-r-t-1)$	$\frac{\partial N_1}{dr}(r,t) = \frac{1}{4}(1-t)(2r+t)$	$\frac{\partial N_1}{dt}(r,t) = \frac{1}{4}(1-r)(r+2t)$
2	$N_2(r,t) = \frac{1}{4}(1+r)(1-t)(r-t-1)$	$\frac{\partial N_2}{dr}(r,t) = \frac{1}{4}(1-t)(2r-t)$	$\frac{\partial N_2}{dt}(r,t) = \frac{1}{4}(1+r)(-r+2t)$
3	$N_3(r,t) = \frac{1}{4}(1+r)(1+t)(r+t-1)$	$\frac{\partial N_3}{dr}(r,t) = \frac{1}{4}(1+t)(2r+t)$	$\frac{\partial N_3}{dt}(r,t) = \frac{1}{4}(1+r)(r+2t)$
4	$N_4(r,t) = \frac{1}{4}(1-r)(1+t)(-r+t-1)$	$\frac{\partial N_4}{dr}(r,t) = \frac{1}{4}(1+t)(2r-t)$	$\frac{\partial N_4}{dt}(r,t) = \frac{1}{4}(1-r)(-r+2t)$
5	$N_5(r,t) = \frac{1}{2}(1-r^2)(1-t)$	$\frac{\partial N_5}{dr}(r,t) = -r(1-t)$	$\frac{\partial N_5}{dt}(r,t) = -\frac{1}{2}(1-r^2)$
6	$N_6(r,t) = \frac{1}{2}(1+r)(1-t^2)$	$\frac{\partial N_6}{dr}(r,t) = \frac{1}{2}(1-t^2)$	$\frac{\partial N_6}{dt}(r,t) = -t(1+r)$
7	$N_7(r,t) = \frac{1}{2}(1-r^2)(1+t)$	$\frac{\partial N_7}{dr}(r,t) = -r(1+t)$	$\frac{\partial N_7}{dt}(r,t) = \frac{1}{2}(1-r^2)$
8	$N_8(r,t) = \frac{1}{2}(1-r)(1-t^2)$	$\frac{\partial N_8}{dr}(r,t) = -\frac{1}{2}(1-t^2)$	$\frac{\partial N_8}{dt}(r,t) = -t(1-r)$

Table D.1. Isoparametric element shape functions and corresponding partial derivatives.

Before proceeding to the section regarding FEM/BEM coupling, construction of the global electrode FEM equations will now be described. Recall that (D.35) only represents one element in the overall discretized electrode. Given that (D.5) could be written as a sum of integrations of smaller volumes, each of which can represent a single element, it suffices to say that summing together (D.35) terms for each element in the electrode represents the total electrode system of equations; keeping in mind that multiple elements can share nodes, in a global sense. In addition, regarding the closed contour integrals of (D.35), the regions along paths of the contour touching other adjacent elements will cancel as the surface normal for the adjacent element points in an opposite direction and the fact that stress is continuous in the electrode. Therefore only normal stress components along outer surface of the electrode contribute to the contour integrals. Furthermore, because the outer contour of the electrode which is not in contact with the piezoelectric surface is stress free, then only the stress at the interface of the piezoelectric material and electrode contribute to the contour integrals. The rest of this appendix describes determining the contour integrals for elements with surfaces located at the interface of the piezoelectric and electrode, which allows FEM/BEM model coupling.

The analysis begins by assigning the surface elements at the interface of the kth electrode an index value, n, of 1 to N_e^k, which are sorted in order along x in terms of center positions of the elements within the electrode. For simplicity, in this work the 5th node of each element is forced to be at equal distance from the 1st and 2nd nodes, and each element at the interface is forced to equal x dimensional width given as Δ_k. Recall from the BEM analysis that the surface normal stress components at the interface of the

piezoelectric and the electrode are given as a weighted sum of basis functions. Therefore over the domain of a single surface element the contour integral of (D.35) may be set to:

$$f_i^{mnk} = \sum_{s=0}^{N_{ch}-1} w_i^{sk} f^{mnsk} \tag{D.36}$$

where:

- i is the index of the field component: $i = 1 \rightarrow T_5$; $i = 2 \rightarrow T_4$; $i = 3 \rightarrow T_4$,
- m is the shape function index in the **N** term,
- n is the element index along the interface of the electrode,
- k is the index of the current electrode under consideration,
- s is the basis function index for the ith field component,
- w_i^{ks} is the corresponding basis function weight,
- N_{ch} is the number of Chebyshev polynomial basis functions per electrode,

and

$$f^{mnsk} = -\int_{x_c^k - a_k + (n-1)\Delta_k}^{x_c^k - a_k + n\Delta_k} \frac{T_s\left(\dfrac{x - x_c^k}{a_k}\right)}{\sqrt{1 - \left(\dfrac{x - x_c^k}{a_k}\right)^2}} N_m(r(x))dx , \tag{D.37}$$

where:

- $a_k = \dfrac{\Delta_k N_e^k}{2}$ is the ½ the width of the kth electrode,
- x_c^k is the center x-position of the kth electrode
- $x_1^n = x_c^k - a_k + (n-1)\Delta_k$ (x-position of first node),
- $x_2^n = x_c^k - a_k + n\Delta_k$ (x-position of second node)
- and $T_s(x)$ is the sth order Chebyshev polynomial of the first kind.

Notice that the shape function in (D.37) is now only a function of $r(x)$, since along the interface side of the element $t = -1$. Furthermore, from (D.10) and Table D.1 it can be seen that along the interface ($z = 0$, $t = -1$) that:

$$x = N_1(r,t=-1)x_1^n + N_2(r,t=-1)x_2^n + N_5(r,t=-1)x_5^n .$$

(D.38)

Simplifying (D.38) results in:

$$x = x_c^k + \frac{1}{2}\Delta_k\left(r + 2n - 1 - N_e^k\right),$$

(D.39)

and solving for r, gives:

$$r = 1 - 2n + N_e^k + \frac{2}{\Delta_k}\left(x - x_c^k\right).$$

(D.40)

Turning our attention back to evaluation of the integral in (D.37), making the substitution

$x' = \dfrac{x - x_c^k}{a_k}$, results in:

$$f^{mnsk} = -a_k \int_{\frac{2(n-1)}{N_e^k}-1}^{\frac{2n}{N_e^k}-1} \frac{T_s(x')}{\sqrt{1-(x')^2}} N_m\left(r\left(a_k x' + x_c^k\right)\right)dx' .$$

(D.41)

Making another substitution, $x' = \cos(\theta)$, results in:

$$f^{mnsk} = a_k \int_{\theta_1^{nk}}^{\theta_2^{nk}} \cos[s\theta]N_m\left(r\left(a_k \cos(\theta) + x_c^k\right)\right)d\theta ,$$

(D.42)

where:

$$\theta_1^{nk} = \cos^{-1}\left[\frac{2(n-1)}{N_e^k} - 1\right], \text{ and } \theta_2^{nk} = \cos^{-1}\left[\frac{2n}{N_e^k} - 1\right].$$

Using (D.40) it can be shown that:

$$r\left(a_k\cos(\theta)+x_c^k\right)=1-2n+N_e^k\left(1+\cos[\theta]\right),\tag{D.43}$$

and therefore using Table D.1 for $m = 1, 2,$ or 5 at $t = -1,$

$$N_m\left(r\left(a_k\cos(\theta)+x_c^k\right)\right)=p_{m2}^{nk}\cos^2[\theta]+p_{ma}^{nk}\cos[\theta]+p_{m0}^{nk}\tag{D.44}$$

where the coefficients are given as:

- $p_{10}^{nk}=\dfrac{1}{2}\left(2n-N_e^k-1\right)\left(2n-N_e^k\right);\ \ p_{11}^{nk}=\dfrac{1}{2}N_e^k\left(1-4n+2N_e^k\right);\ \ p_{12}^{nk}=\dfrac{\left(N_e^k\right)^2}{2};$

- $p_{20}^{nk}=\dfrac{1}{2}\left(2n-N_e^k-2\right)\left(2n-N_e^k-1\right);\ \ p_{21}^{nk}=\dfrac{1}{2}N_e^k\left(3-4n+2N_e^k\right);\ \ p_{22}^{nk}=\dfrac{\left(N_e^k\right)^2}{2};$

- $p_{50}^{nk}=4n\left(1+N_e^k\right)-N_e^k\left(2+N_e^k\right)-4n^2;\ \ p_{51}^{nk}=2N_e^k\left(2n-N_e^k-1\right);\ \ p_{52}^{nk}=-\left(N_e^k\right)^2.$

Substitution of (D.44) into (D.42) results in:

$$f^{mnsk}=a_k\left[I_m^{nsk}\left(\theta_2^{nk}\right)-I_m^{nsk}\left(\theta_1^{nk}\right)\right],\tag{D.45}$$

where:

$$I_m^{nsk}(\theta)=\int\cos[s\theta]\left(p_{m2}^{nk}\cos^2[\theta]+p_{m1}^{nk}\cos[\theta]+p_{m0}^{nk}\right)d\theta,$$

and according the Wolfram Mathematica® software package:

- $I_m^{nsk}(\theta)_{s=0}=\dfrac{1}{2}[\theta+\cos(\theta)\sin(\theta)]p_{m2}^{nk}+\sin(\theta)p_{m1}^{nk}+\theta\,p_{m0}^{nk},$

- $I_m^{nsk}(\theta)_{s=1}=\dfrac{1}{12}[9\sin(\theta)+\sin(3\theta)]p_{m2}^{nk}+\dfrac{1}{2}[\theta+\cos(\theta)\sin(\theta)]p_{m1}^{nk}+\sin(\theta)p_{m0}^{nk},$

- $I_m^{nsk}(\theta)_{s=2}=\dfrac{1}{16}[4(\theta+\sin(2\theta))+\sin(4\theta)]p_{m2}^{nk}+\dfrac{1}{6}[3\sin(\theta)+\sin(3\theta)]p_{m1}^{nk}+\cos(\theta)\sin(\theta)p_{m0}^{nk},$

- $I_m^{nsk}(\theta)_{s>2}=\dfrac{1}{4}\left[\dfrac{\sin[(s-2)\theta]}{s-2}+\dfrac{2\sin[s\theta]}{s}+\dfrac{\sin[(s+2)\theta]}{s+2}\right]p_{m2}^{nk}+$

$\dfrac{s\cos(\theta)\sin(s\theta)-\cos(s\theta)\sin(\theta)}{s^2-1}p_{m1}^{nk}+\dfrac{\sin[s\theta]}{s}p_{m0}^{nk}.$

With (D.45) and (D.36) the global element displacement components can be calculated, given the stress basis function weights. In order to combine the FEM and BEM models, the integrals of the displacement components multiplied by the same stress basis function need to be evaluated at the electrode/substrate interface, as was performed in the BEM analysis. Recall that from (D.7) that the ith component of displacement at the kth electrode/substrate interface for the nth surface element is given by

$$u_i^{nk}(x, z = 0) = N_1(r(x))u_i^{1nk} + N_2(r(x))u_i^{2nk} + N_5(r(x))u_i^{5nk}, \tag{D.46}$$

where:

u_i^{hnk} is the ith component of displacement at the hth node of surface element n for the kth electrode.

Considering (D.46) the **c** terms corresponding to the displacement components of (2.34) are given as:

$$c_i^{sk} = \sum_{n=1}^{N_e^k} c_i^{nsk} \tag{D.47}$$

where:

$$c_i^{nsk} = c^{1nsk}u_i^{1nk} + c^{2nsk}u_i^{2nk} + c^{5nsk}u_i^{5nk},$$

and

$$c^{mnsk} = \int_{x_c^k - a_k + (n-1)\Delta_k}^{x_c^k - a_k + n\Delta_k} \frac{T_s\left(\dfrac{x - x_c^k}{a_k}\right)}{\sqrt{1 - \left(\dfrac{x - x_c^k}{a_k}\right)^2}} N_m(r(x)) dx,$$

which upon comparison to (D.37) indicates that:

$$c^{mnsk} = -f^{mnsk}. \tag{D.48}$$

293

Given that global system of equations for the kth electrode is given by:

$$\left(\mathbf{k}^k - \omega^2 \mathbf{m}^k\right)\tilde{\mathbf{u}}^k = \mathbf{f}^k,$$ (D.49)

where:

- $\mathbf{f}^k = \mathbf{F}^k \mathbf{w}^k$,

- $\mathbf{w}^k = \begin{bmatrix} w_1^{1k} & w_1^{2k} & \cdots & w_1^{N_{ch}k} & w_2^{1k} & w_2^{2k} & \cdots & w_2^{N_{ch}k} & w_3^{1k} & w_3^{2k} & \cdots & w_3^{N_{ch}k} \end{bmatrix}^{\mathrm{T}}$,

- and $\mathbf{F}^k$ is the matrix constructed from (D.45),

and

$$\mathbf{c}^k = -\left[\mathbf{F}^k\right]^{\mathrm{T}}\tilde{\mathbf{u}}^k,$$

where

$$\mathbf{c}^k = \begin{bmatrix} c_1^{1k} & c_1^{2k} & \cdots & c_1^{N_{ch}k} & c_2^{1k} & c_2^{2k} & \cdots & c_2^{N_{ch}k} & c_3^{1k} & c_3^{2k} & \cdots & c_3^{N_{ch}k} \end{bmatrix}^{\mathrm{T}},$$

then

$$\mathbf{c}^k = \mathbf{F}_{FEM}^k \mathbf{w}^k$$ (D.50)

where:

$$\mathbf{F}_{FEM}^k = -\left[\mathbf{F}^k\right]^{\mathrm{T}}\left[\mathbf{k}^k - \omega^2 \mathbf{m}^k\right]^{-1}\mathbf{F}^k.$$ (D.51)

By mapping the matrix of (D.51) for each electrode into (2.35), the FEM/BEM models are coupled, and the overall system can be solved. This concludes Appendix D.

APPENDIX E

MATERIALS CONSTANTS USED IN THIS WORK

The purpose of Appendix E is to list the values and sources of all material constants used in this dissertation work regarding simulations. The lists include values for un-rotated material elastic, density, piezoelectric, dielectric, and where applicable viscosity constants. In addition, the structure of material constant matrices for crystalline and isotropic materials is listed.

E.1. Structure of Material Constant Matrices

In this section, the structure of material constant matrices for crystalline and isotropic materials is listed, which are taken from [73].

Three main crystalline classes of materials were studied in this work: Trigonal Class 32, of which langasite and quartz are members; Orthorhombic Class mm2, which includes potassium niobate; and Isotropic, which was assumed for all electrode materials, and fluids. The overall structure of the stiffness, piezoelectric, and dielectric matrices are now presented for these three classes.

E.1.1. Structure of Elastic Constant Matrix $\mathbf{c}^E$

$$
\mathbf{c}^E = \begin{bmatrix}
c_{11} & c_{12} & c_{13} & c_{14} & 0 & 0 \\
c_{12} & c_{11} & c_{13} & -c_{14} & 0 & 0 \\
c_{13} & c_{13} & c_{33} & 0 & 0 & 0 \\
c_{14} & -c_{14} & 0 & c_{44} & 0 & 0 \\
0 & 0 & 0 & 0 & c_{44} & c_{14} \\
0 & 0 & 0 & 0 & c_{14} & \frac{1}{2}(c_{11} - c_{12})
\end{bmatrix}
\tag{E.1}
$$

Trigonal Class 32

$$
\mathbf{c}^E = \begin{bmatrix}
c_{11} & c_{12} & c_{13} & 0 & 0 & 0 \\
c_{12} & c_{22} & c_{23} & 0 & 0 & 0 \\
c_{13} & c_{23} & c_{33} & 0 & 0 & 0 \\
0 & 0 & 0 & c_{44} & 0 & 0 \\
0 & 0 & 0 & 0 & c_{55} & 0 \\
0 & 0 & 0 & 0 & 0 & c_{66}
\end{bmatrix}
\tag{E.2}
$$

Orthorhombic

$$
\mathbf{c}^E = \begin{bmatrix}
c_{11} & c_{11} - 2c_{44} & c_{11} - 2c_{44} & 0 & 0 & 0 \\
c_{11} - 2c_{44} & c_{11} & c_{11} - 2c_{44} & 0 & 0 & 0 \\
c_{11} - 2c_{44} & c_{11} - 2c_{44} & c_{11} & 0 & 0 & 0 \\
0 & 0 & 0 & c_{44} & 0 & 0 \\
0 & 0 & 0 & 0 & c_{44} & 0 \\
0 & 0 & 0 & 0 & 0 & c_{44}
\end{bmatrix}
\tag{E.3}
$$

Isotropic

E.1.2. Structure of Piezoelectric Constant Matrix e

$$\mathbf{e} = \begin{bmatrix} e_{11} & -e_{11} & 0 & e_{14} & 0 & 0 \\ 0 & 0 & 0 & 0 & -e_{14} & -e_{11} \\ 0 & 0 & 0 & 0 & 0 & 0 \end{bmatrix}$$

(E.4)

Trigonal Class 32

$$\mathbf{e} = \begin{bmatrix} 0 & 0 & 0 & 0 & e_{15} & 0 \\ 0 & 0 & 0 & e_{24} & 0 & 0 \\ e_{31} & e_{32} & e_{33} & 0 & 0 & 0 \end{bmatrix}$$

(E.5)

Orthorhombic

$$\mathbf{e} = \begin{bmatrix} 0 & 0 & 0 & 0 & 0 & 0 \\ 0 & 0 & 0 & 0 & 0 & 0 \\ 0 & 0 & 0 & 0 & 0 & 0 \end{bmatrix}$$

(E.6)

Isotropic

E.1.3. Structure of Dielectric Constant Matrix ε^s

$$\boldsymbol{\varepsilon}^s = \begin{bmatrix} \varepsilon_{11} & 0 & 0 \\ 0 & \varepsilon_{11} & 0 \\ 0 & 0 & \varepsilon_{33} \end{bmatrix} \qquad (E.7)$$

Trigonal Class 32

$$\boldsymbol{\varepsilon}^s = \begin{bmatrix} \varepsilon_{11} & 0 & 0 \\ 0 & \varepsilon_{22} & 0 \\ 0 & 0 & \varepsilon_{33} \end{bmatrix} \qquad (E.8)$$

Orthorhombic

$$\boldsymbol{\varepsilon}^s = \begin{bmatrix} \varepsilon_{11} & 0 & 0 \\ 0 & \varepsilon_{11} & 0 \\ 0 & 0 & \varepsilon_{11} \end{bmatrix} \qquad (E.9)$$

Isotropic

E.2. Material Constants

Quartz, Trigonal 32, [106]			
c_{mn} [GPa]	e_{mn} [C/m^2]	ε_{mn} [nF/m]	ρ [k-kg/m^3]
$c_{11} = 86.79$	$e_{11} = 0.1711$	$\varepsilon_{11} = 0.03916$	$\rho = 2.64838$
$c_{12} = 6.7901$	$e_{14} = -0.0406$	$\varepsilon_{33} = 0.04104$	
$c_{13} = 12.009$			
$c_{14} = -18.116$			
$c_{33} = 105.79$			
$c_{44} = 58.212$			

Table E.1. Material constants for quartz.

Langasite, Trigonal 32, [107]			
c_{mn} [GPa]	e_{mn} [C/m^2]	ε_{mn} [nF/m]	ρ [k-kg/m^3]
$c_{11} = 188.75$	$e_{11} = -0.44$	$\varepsilon_{11} = 0.16752$	$\rho = 5.743$
$c_{12} = 104.75$	$e_{14} = 0.08$	$\varepsilon_{33} = 0.44891$	
$c_{13} = 95.89$			
$c_{14} = 14.12$			
$c_{33} = 261.40$			
$c_{44} = 53.50$			

Table E.2. Material constants for langasite.

Potassium Niobate, Orthorhombic mm2, [108]			
c_{mn} [GPa]	e_{mn} [C/m^2]	ε_{mn} [nF/m]	ρ [k-kg/m^3]
$c_{11} = 226$	$e_{15} = 5.16$	$\varepsilon_{11} = 0.37$	$\rho = 4.63$
$c_{12} = 96$	$e_{24} = 11.7$	$\varepsilon_{22} = 7.8$	
$c_{13} = 68$	$e_{31} = 2.46$	$\varepsilon_{33} = 0.24$	
$c_{22} = 270$	$e_{32} = -1.1$		
$c_{23} = 101$	$e_{33} = 4.4$		
$c_{33} = 186$			
$c_{44} = 74.3$			
$c_{55} = 25$			
$c_{66} = 95.5$			

Table E.3. Material constants for potassium niobate.

Gold, Isotropic, (from [109] and transformed to isotropic using [110])			
c_{mn} [GPa]	e_{mn} [C/m^2]	ε_{mn} [nF/m]	ρ [k-kg/m^3]
$c_{11} = 209.62$	N/A	N/A	$\rho = 19.283$
$c_{44} = 27.61$			

Table E.4. Material constants for gold.

SiO$_2$, Isotropic, (c and ρ [111]), (ε [112])			
c_{mn} [GPa]	e_{mn} [C/m^2]	ε_{mn} [nF/m]	ρ [k-kg/m^3]
$c_{11} = 76$ $c_{44} = 25.5$	N/A	$\varepsilon_{11} = 0.03621$	$\rho = 2.2$

Table E.5. Material constants for SiO$_2$.

DI Water 25° C, Isotropic			
c_{mn} [GPa]	e_{mn} [C/m^2]	ε_{mn} [nF/m]	ρ [k-kg/m^3]
$c_{11} = \dfrac{1}{\chi} + j\omega\left(\dfrac{4}{3}\eta + \xi\right)$ [43] $c_{44} = j\omega\eta$ [43] $\xi = 2.8\eta$ [43] $\eta = 0.89 \cdot 10^{-12}$ [TcP] [41] ω = radian frequency [1/s] $\dfrac{1}{\chi} = 2.24$ [GPa] [41]	N/A	$\varepsilon_{11} = 78.4$ [113]	$\rho = 0.99704$ [41]

Table E.6. Material constants for DI water.

This concludes Appendix E.

SU-8 MOLD FABRICATION ON PMMA SUBSTRATES

The following procedure details the fabrication of PDMS molds used in this dissertation, which is based on patterning SU-8 photoresist on a PMMA substrate. For the process given here, the final thickness of mold features is ~280 μm. If a reduced thickens is desired, SU-8 should be spun faster as described in the product data sheet. I would suggest that the exposure dose be reduced in proportion with the layer thickness reduction factor as a starting point. In addition, I would recommend the same soft-bake time of ~17 hours as a starting point. The protocol used in this work is given below.

1. Rinse wafer with methanol then isopropyl soaked cleanroom cloths

2. Rinse wafer with isopropyl from squirt bottle

3. Dehydrate @ 95C on hotplate 5 min, remove hot (not allowed to fully cool before spin)

4. Pour SU-8 2050 from bottle or vial, do not use syringe to avoid bubbles (best approach is to pour in center of wafer and let it spread by spinning slowly by hand or very low RPM)

5. Spin 10s @ 500 RPM, then pop any visible bubbles with tweezers

6. Spin 35s @ 3k RPM (~50 um layer)

7. Hotplate bake 65C for 5 min. (pop any visible bubbles)

8. Ramp to 95C and hold for 15 min.

9. Cool to 65C on hotplate

10. Cool under cover by placing wafer metal table for 5 min.

11. Blanket expose through UV filter (>350 nm passed) for a 350 mJ/cm^2 dose (assuming average 365 nm and 405 nm intensity after filter in time calculation)

12. Ramp to 95C and hold for 7 min.

13. Remove and spin 2050 on hot wafer ~10s @ 300 RPM

14. Pop any visible bubbles

15. Spin 35s @ 690 RPM (~280 um layer)

16. 65C hotplate bake for ~17 hours

17. Remove and cool under cover at least 15 min. on metal table prior to exposure

18. Expose through UV filter (>350 nm passed) and mask for a 700 mJ/cm^2 dose (assuming average 365 nm and 405 nm intensity after filter in time calculation)

19. Do not move mask w.r.t. wafer one initial contact made, resist is still slightly soft and can result in ripples if moved

20. Remove wafer after exposure by manually separating wafer from mask (pull slightly down on chuck if sticks)

21. Hotplate bake wafer at 65C for 5 min.

22. Ramp to 90C and hold for 10 min.

23. Remove wafer after cooling to 65C

24. Develop in two cycles of SU-8 developer for 5 min. with mildest ultrasonic agitation. First bath in 'used' SU-8 developer, followed by bath in new developer

25. Rinse with isopropyl while still wet to avoid having powder form on surface (SU-8 developer attacks unprotected back side of PMMA and can leave a residue)

APPENDIX G

PCB DETAILS

This appendix documents the RF switch and sensor bonding PCBs used in the experimental setup discussed in Section 5.2. The circuit schematic, top copper geometry, top silkscreen, bottom copper geometry, and bottom silkscreen, are presented. In addition, the circuit components values are listed. The PCB was fabricated by ExpressPCB (http://www.expresspcb.com/) and designed using their free software tools. All components were populated by hand soldering.
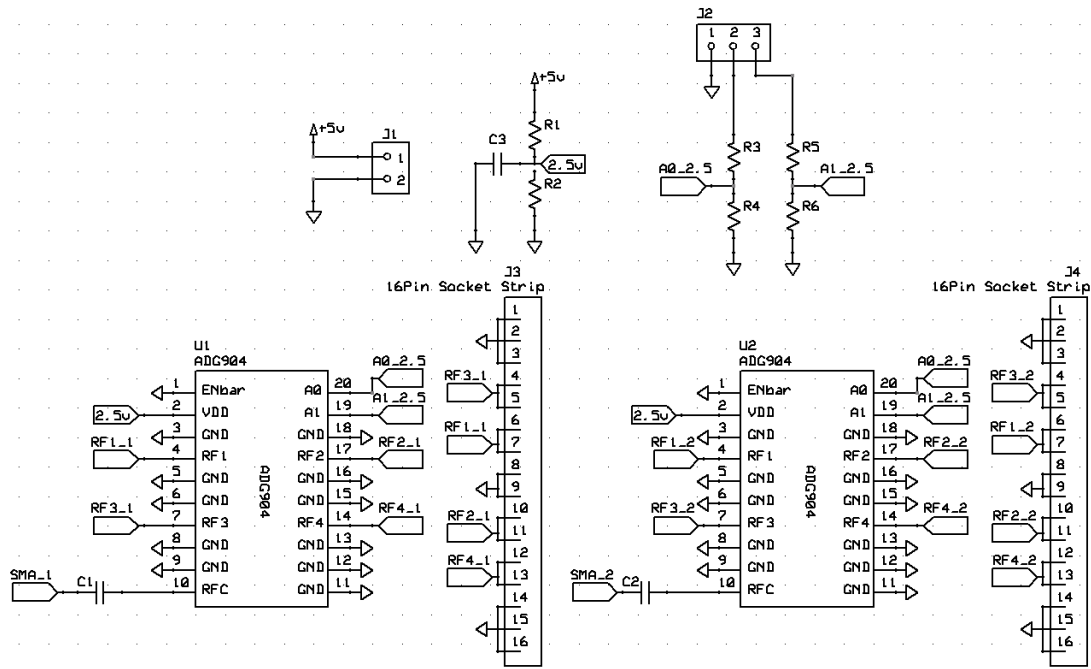
Figure G.1. Schematic of the RF switch PCB.

Component	R1	R2	R3	R4	R5	R6	C1	C2	C3
Value	1k	1k	1k	1k	1k	1k	10nF	10nF	0.1uF

Table G.1. RF switch PCB component values.
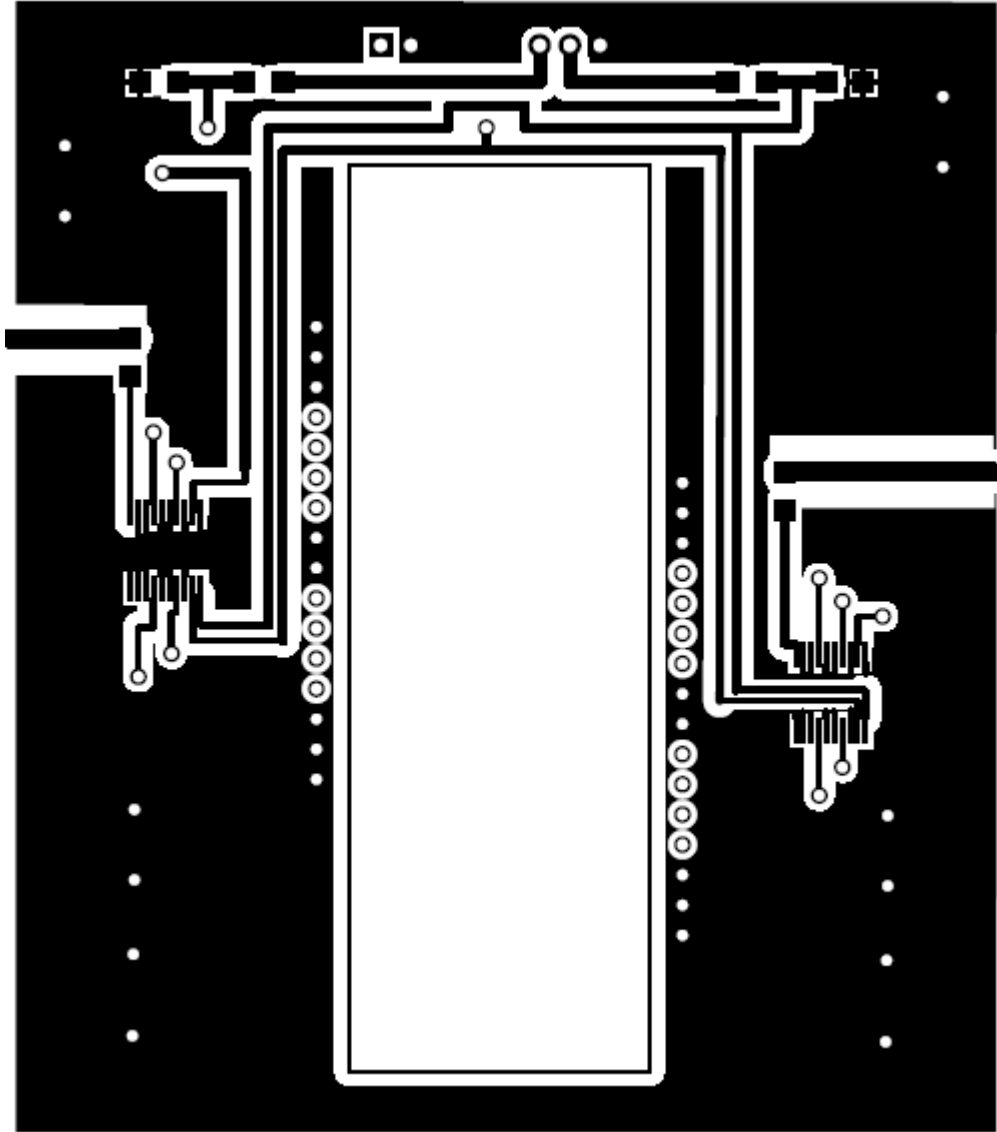
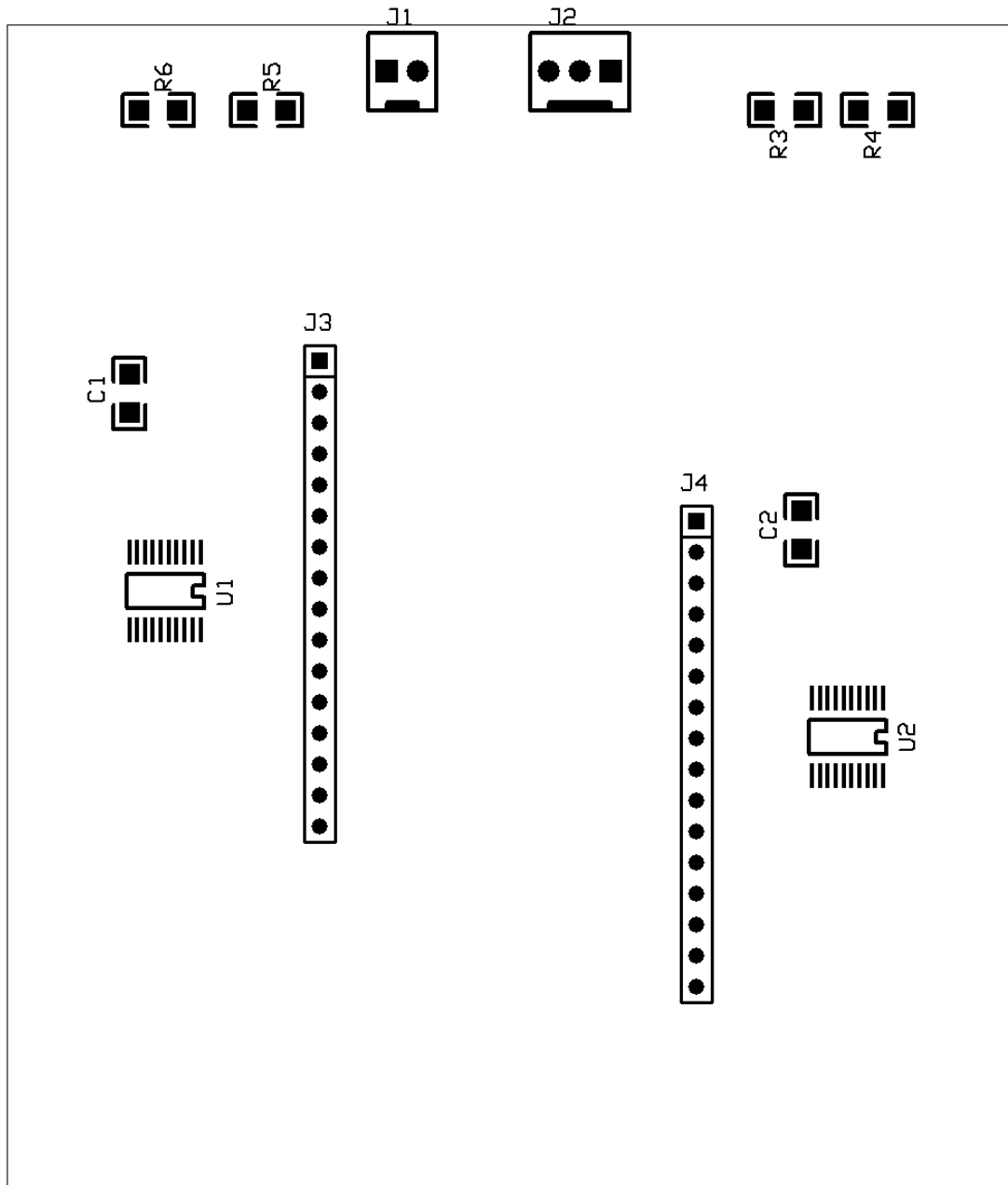Figure G.2. RF switch PCB top copper layer (large rectangular central region is a hole).

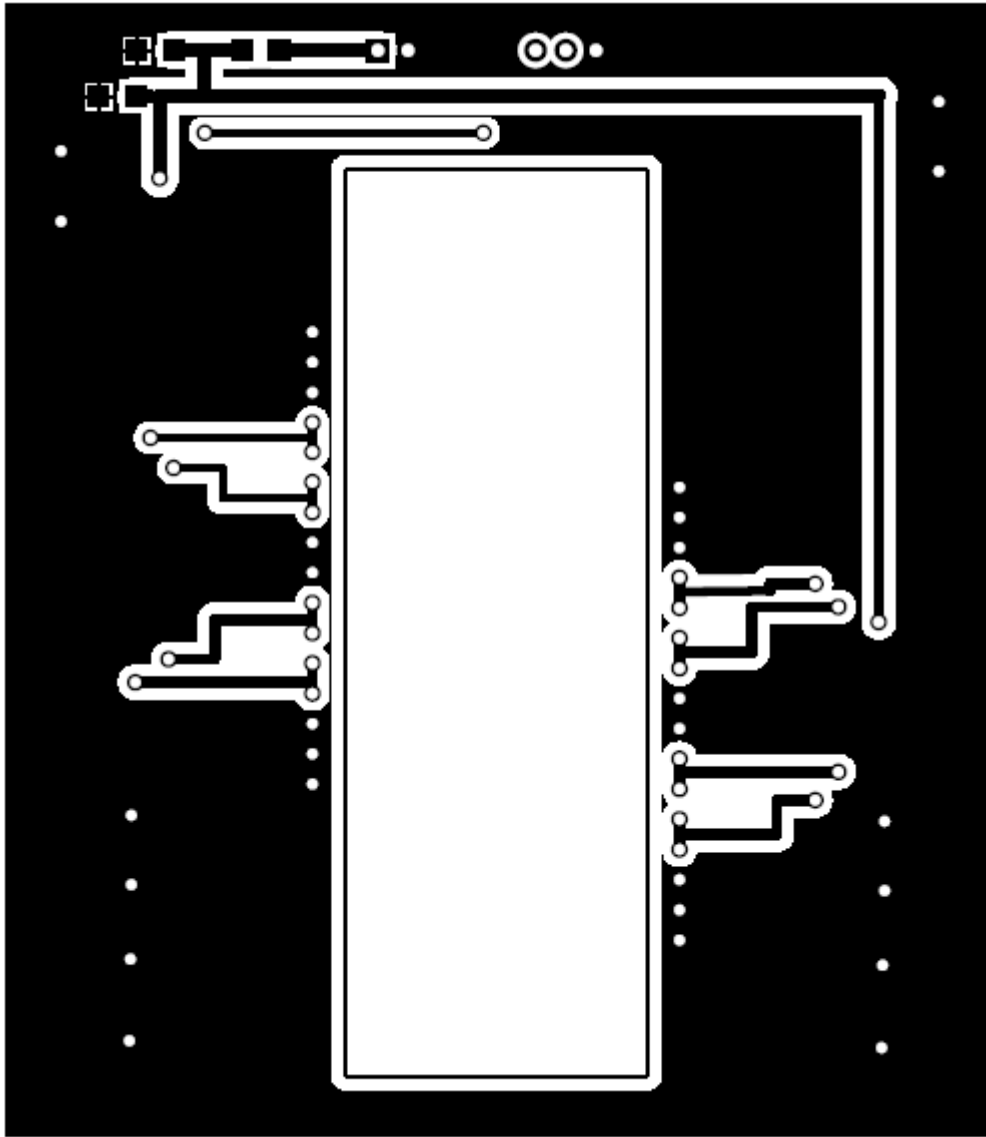Figure G.3. RF switch PCB top silkscreen layer.

Figure G.4. RF switch PCB bottom copper layer (large rectangular central region is a hole).
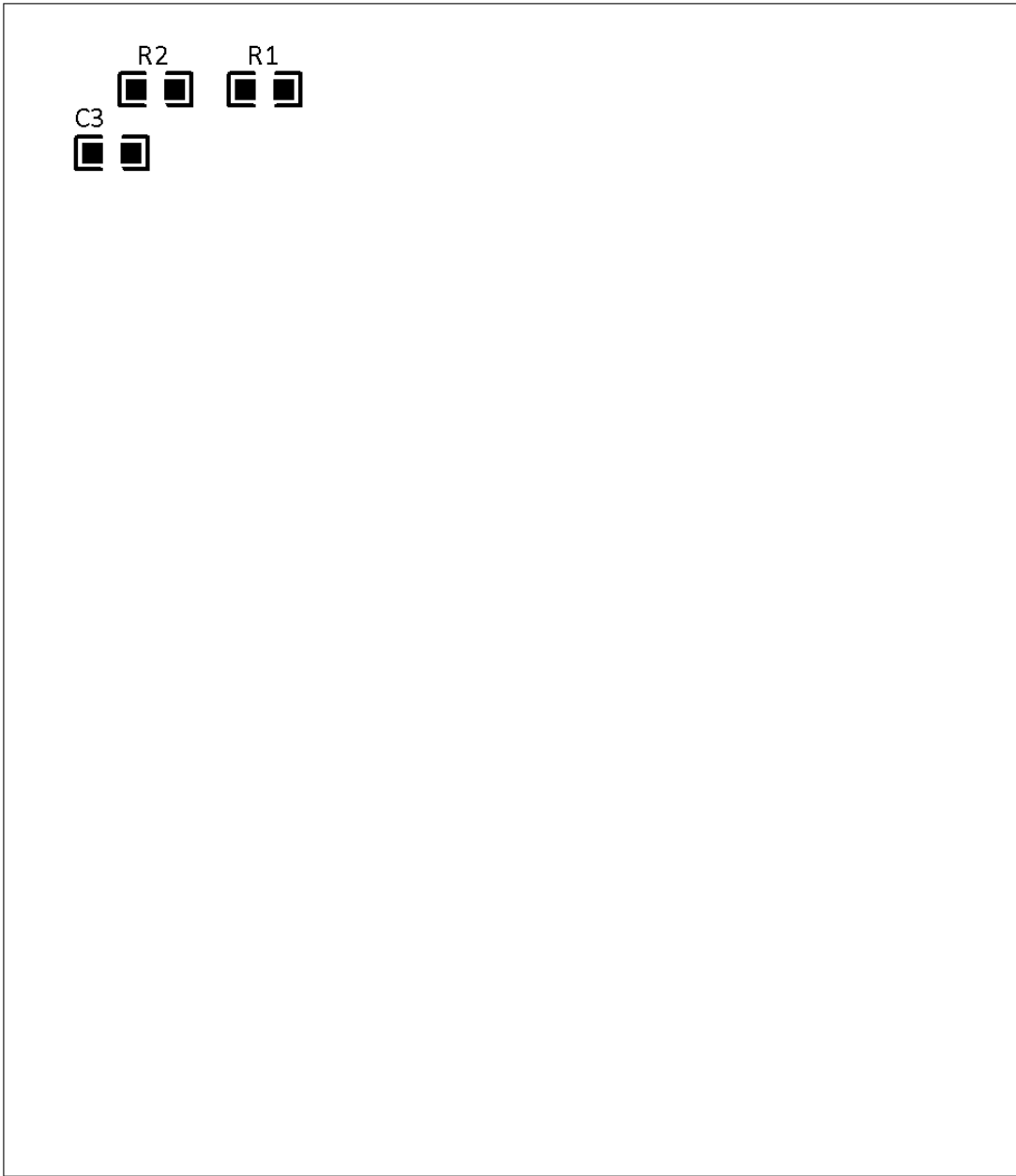
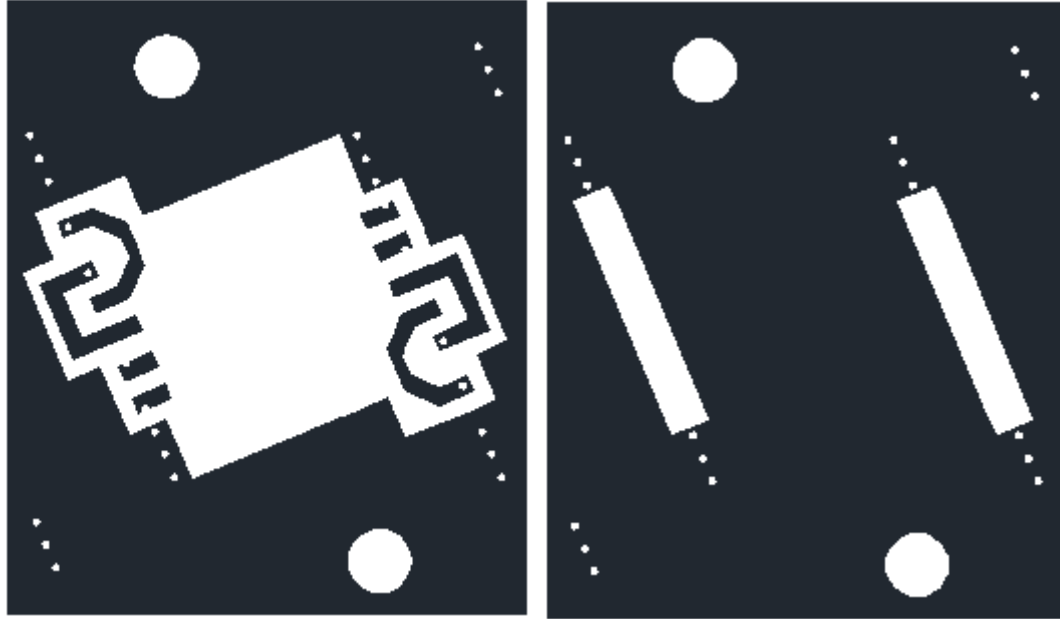Figure G.5. RF switch PCB bottom silkscreen layer.

Figure G.6. Sensor bonding PCB, top layer (left), bottom layer (right).

BIOGRAPHY OF THE AUTHOR

Thomas Pollard was born in Blue Hill, Maine on October 29, 1979. He was raised in Bucksport, Maine and graduated from Bucksport High School in 1998. He attended the University of Maine and graduated in 2003 with a Bachelor's degree in Computer Engineering. Shortly after Thomas entered the University of Maine graduate program and earned his Master's degree in Electrical Engineering in 2010. He worked on microwave acoustics research at the Microwave Acoustics Laboratory at the University of Maine Laboratory for Surface Science and Technology (LASST) from 1999 to 2010. As an undergraduate student, he was a three-time participant in the National Science Foundation Research Experience for Undergraduates (NSFREU) summer program at the University of Maine. Since 2009 Thomas has worked for Environetix Technologies Corporations, Orono, ME, as Principal Engineer, where his efforts are focused on commercial development of wireless and passive SAW-based harsh environment sensors and systems.

Thomas is a candidate for the Doctor of Philosophy degree in Electrical & Computer Engineering from the University of Maine in December, 2013.